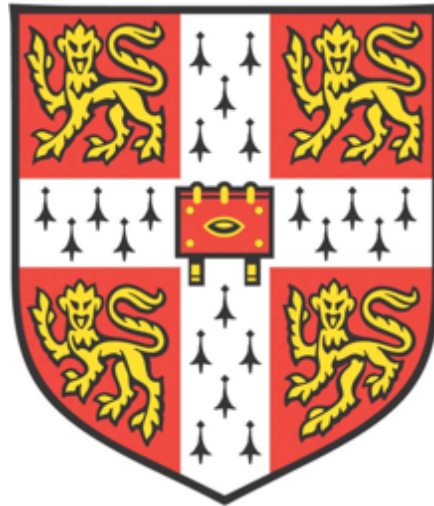


*DEVELOPMENT OF NOVEL THERAPIES  
FOR MARFAN SYNDROME USING A HUMAN  
IPSC-DERIVED DISEASE MODEL*



**Madeline McNamara**

**Darwin College**

**Anne McLaren Laboratory for Regenerative Medicine**

**Department of Medicine**

**University of Cambridge**

**This dissertation is submitted for the degree of Doctor of Philosophy**

**October 2018**

**Revised March 2019**

Development of Novel Therapies for Marfan Syndrome using a human iPSC-derived Disease Model - Madeline McNamara – October 2018

*To my grand-father (1925-2018)*

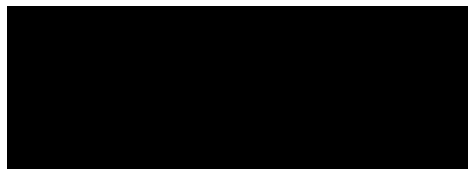
*“I can do this all through Him who gives me strength”*

*Philippian 4:13*

## DECLARATION

This dissertation is the result of my own work and includes nothing, which is the outcome of work done in collaboration except where specifically indicated in the text. It has not been previously submitted, in part or whole, to any university or institution for any degree, diploma, or other qualification.

In accordance with the Department of Medicine guidelines, this thesis does not exceed 65,000 words, and it contains less than 150 figures.



Signed: \_\_\_\_\_

Date: 25 March 2019 \_\_\_\_\_

Madeline McNamara and full qualifications

Cambridge

# SUMMARY

Madeline McNamara

Development of Novel Therapies for Marfan Syndrome using an iPSC-disease model

Marfan syndrome (MFS) is a connective tissue disorder caused by mutations in fibrillin-1, a matrix component encoded by the gene *FBNI*, with pleiotropic manifestations including severe cardiovascular complications, such as aortic aneurysms and dissection. Current treatments focus on surgically removing the aneurysm or on minimising aortic wall stress by controlling haemodynamics, but neither of these strategies tackle the underlying pathology. Although MFS is caused by fibrillin-1 mutations, it remains unclear how these lead to the pleiotropic manifestations seen in patients. Defective fibrillin-1 is thought to lead to excessive release of TGF- $\beta$  in the extracellular environment, which will increase TGF- $\beta$  signalling activity. Substantial efforts observed that angiotensin II receptor (AngIIIR) blockade is able to rescue promiscuous TGF- $\beta$  signalling and aortic complications in a MFS mouse model. However, results of AngII receptor blockade in patients have been disappointing and it is increasingly apparent that there is a need to develop better disease models for MFS to improve therapy development. In addition to abnormal TGF- $\beta$  signalling, matrix degradation is a likely crucial component for pathology development as most clinical studies show extracellular matrix degradation and increased matrix proteolytic enzyme levels in diseased aortas. In this work, I speculate that there are multiple disease perturbations downstream of the *FBNI* mutations and that there is a need to develop novel strategies to identify new putative disease mediators and signalling pathways that participate in the pathogenicity. Here, I use a patient iPSC-derived *in vitro* disease model that recapitulates the complexity of the patient abnormalities to develop two potential therapeutic strategies (i) directly interfering at the level of the pathological mutation using an exon skipping approach and (ii) designing an unbiased phenotypic drug screen to identify putative compounds able to rescue abnormal proteolysis in our disease model. These complementary techniques have enabled the identification of novel disease-causing pathways and offer strategies for clinical intervention using our *in vitro* disease model as a platform for drug discovery.

## ACKNOWLEDGEMENTS

The work presented in this thesis would not have been possible without my supervisor, Dr Sanjay Sinha. From our first meeting during a Ph.D scholarship panel interview to the final stages of shaping my thesis, Sanjay has offered me unlimited guidance, support, motivation, understanding and an immense source knowledge. I could not have imagined having a better mentor for my scientific experience as a PhD student and for preparing me for my next professional step.

Needless to say, I would like to thank everyone in my research group, especially Dr Alessandra Granata and Dr William Bernard, who taught me to be rigorous in my scientific thinking and to question my research from various perspectives.

My sincere gratitude goes to the entire Anne McLaren Laboratory for Regenerative Medicine who provided an environment of genuine support and gave me the opportunity to make long-lasting friendships that I will cherish beyond these four years.

I would like to thank Dr Thorsten Boroviak and Prof Austin Smith who gave me my first glance at stem cell research and initiated my experience at the University of Cambridge.

A special thanks goes to all of my friends, especially Oslo. It would take a lot more than a page to thank you deservedly. You all know who you are and what you have done to get me to where I am now. I'll always remember a certain boat trip...

I would also like to thank my parents, Michael and Colette, and my sister, Olivia. I naively threw myself into the world of academic research, but I knew that your support, love and encouragements would never leave me. A great amount of gratitude goes to my late grand-father whose sense of curiosity has guided me, and will continue to do so, throughout my life.

Last but not least, I would like to thank Thomas. This experience has made me grow into a better version of myself and I am beyond happy to be able to share it with you.

*Deos gratias*

# Contents

<b>1</b>	<b>Introduction.....</b>	<b>1</b>
1.1	Overview of the Introduction Chapter.....	2
1.2	Early Embryogenesis.....	3
1.3	Development of the vasculature .....	5
1.3.1	Pharyngeal aortic arches.....	5
1.3.2	Structure and maturation of blood vessels.....	6
1.4	Origins of vascular smooth muscle cells .....	9
1.4.1	SMC lineage diversity .....	9
1.4.2	Relation of SMC diversity to vascular disease.....	10
1.5	Vascular ECM and arterial mechanics in vascular disease .....	12
1.6	Marfan Syndrome: a disease with multiple facets.....	14
1.7	Fibrillin-1.....	16
1.7.1	Molecular structure and function of fibrillin-1 .....	16
1.7.2	The bi-functionality of fibrillin-1 .....	18
1.7.3	The pathophysiological effects of defective fibrillin-1 .....	19
1.8	Mouse models of Marfan Syndrome .....	21
1.9	Hyperactive TGF- $\beta$ signalling in MFS.....	23
1.9.1	TGF- $\beta$ as a driver of MFS .....	23
1.9.2	Controversy over role of TGF- $\beta$ in aneurysm development.....	23
1.9.3	Losartan: an alternative therapy .....	24
1.10	hiPSCs as a research tool to study disease pathology .....	27
1.10.1	Human Pluripotent Stem Cells .....	27
1.10.2	Generation of Induced Pluripotent Stem Cells .....	27
1.10.3	Differentiation of Human Pluripotent Stem Cells for Disease Modelling.....	28
1.11	Generation of a human iPSC derived model of MFS.....	30
1.11.1	Characterisation of MFS-specific hiPSC .....	30
1.11.2	Differentiation of MFS hiPSC in SMC intermediate and mature populations .....	31
1.11.3	MF <sup>C1242Y</sup> NC-SMC recapitulate the human MFS aortic phenotype .....	33
1.12	CRISPR-correction of MF <sup>C1242Y</sup> iPSC.....	39
1.13	Potential of MFS disease model to develop novel therapeutic strategies.....	42
1.13.1	AON-mediated exon-skipping to target and correct genetic diseases .....	42
1.13.2	Complementary unbiased strategies to identify novel disease-causing pathways.....	43
1.14	Hypothesis and Objectives of This Thesis .....	44
1.14.1	Hypothesis .....	44

1.14.2	Current Challenges and Objectives.....	44
<b>2</b>	<b>Materials and Methods .....</b>	<b>45</b>
2.1	Cell Culture.....	46
2.1.1	Patient human iPSC Derivation and Culture Conditions.....	46
2.1.2	Humans iPSC Differentiation Protocols .....	49
2.2	AON-Mediated Exon-Skipping .....	50
2.2.1	AON Design.....	50
2.2.2	AON Transfection.....	50
2.3	CRISPR/Cas9-mediated Exon 30 Skipping.....	52
2.3.1	Construction and Cloning Strategy of CRISPR guide RNA/Cas9 plasmid.....	52
2.3.2	Exon 30 Targeting in MF <sup>C1242Y</sup> human iPSC using CRISPR/Cas9 .....	52
2.4	RNA extraction, RT cDNA synthesis and Quantitative PCR Analysis.....	53
2.4.1	RNA Extraction and Reverse Transcription cDNA Synthesis.....	53
2.4.2	Polymerase Chain Reaction and Agarose Gel Run.....	55
2.4.3	Quantitative RT PCR Analysis .....	56
2.5	Western Blotting Analysis .....	59
2.6	Cell Fractionation.....	62
2.7	Immunocytochemistry .....	64
2.8	Luciferase Activity Assay.....	65
2.9	Phenotypic Assays .....	66
2.9.1	Cell Proliferation Assay .....	66
2.9.2	Apoptosis and Cell Death Assays .....	66
2.9.3	Matrix Degradation Assay .....	67
2.10	Cyclic Stretching of MF <sup>C1242Y</sup> NC-SMC.....	68
2.11	RNA Sequencing .....	69
2.12	Drug Screen .....	70
2.12.1	Drug-Screen Format and Cell-Density.....	70
2.12.2	MMP-Activity Detection Assay.....	70
2.13	Statistics .....	71
<b>3</b>	<b>Removing the Disease-Causing Mutation in MFS SMC using AON-Mediated Exon-Skipping .....</b>	<b>72</b>
3.1	Objectives of this Chapter.....	73
3.2	AON-mediated removal of exon 30 in FBN1 .....	76
3.2.1	In-silico design of AONs with exon-skipping potential .....	76

3.2.2	AON-mediated exon skipping leads to exon 30 exclusion in FBN1 .....	83
3.3	Phenotypic evaluation of removal of mutation-containing exon 30 in FBN1 .....	97
3.3.1	Evaluation of AONe30 transfection on SMC proliferation rates .....	97
3.3.2	AONe30 cocktail restores abnormal matrix degradation properties .....	99
3.3.3	AONe30 potentially restores elongated SMC morphology .....	103
3.3.4	Transcription evaluation of targets downstream of the FBN1 mutation .....	104
3.4	CRISPR/Cas9-mediated deletion of exon 30 in MF <sup>C1242Y</sup> NC-SMCs .....	106
3.4.1	CRISPR/Cas9 strategy to remove exon 30 .....	106
3.4.2	Characterisation of exon-skipped MF <sup>C1242Y</sup> iPSC lines .....	108
3.4.3	Off-target activity in exon-skipped hiPSC clones .....	111
3.5	Conclusions .....	112
<b>4</b>	<b>RNA-Sequencing Identifies Potential Disease-Causing Pathways in MFS</b>	<b>114</b>
4.1	Objectives of this Chapter .....	115
4.2	Characterisation of CRISPR-targeted MF <sup>C1242Y</sup> hiPSC-derived NC-SMCs at different maturation stages .....	116
4.3	RNA-Sequencing .....	119
4.3.1	Quality control of total RNA samples .....	120
4.3.2	DESeq2 statistical analysis of RNA-sequencing data .....	124
4.3.3	Identification of differentially expressed genes at early and late SMC differentiation stages ...	125
4.3.4	Identification of potential disease-causing pathways based on DE gene panel .....	131
4.4	Conclusions .....	138
<b>5</b>	<b>Phenotypic Drug Screen to Identify Putative Novel Disease Drivers in MFS</b>	<b>139</b>
5.1	Objectives of this Chapter .....	140
5.2	Optimisation of phenotypic assay based on MF <sup>C1242Y</sup> NC-SMCs proteolytic properties .....	141
5.3	Designing a drug screen based on the proteolytic properties of MF <sup>C1242Y</sup> NC-SMCs .....	145
5.4	Pilot screen of 100 compounds from phenotypic drug library .....	150
5.5	Expanding the drug-screen assay to 1000 compounds using a read-out based on MMP activity .....	156
5.6	GSK3 $\beta$ target validation .....	160
5.6.1	A short introduction to GSK3 $\beta$ .....	160
5.6.2	GSK3 $\beta$ is abnormally expressed in Marfan-uncorrected NC-SMCs .....	162
5.6.3	GSK3 $\beta$ inhibition restores MMP activity and cell-death in Marfan-uncorrected NC-SMCs ....	165
5.6.4	Abnormal $\beta$ -catenin signalling in Marfan-uncorrected NC-SMCs .....	169
5.6.5	A hypothesised GSK3 $\beta$ mechanistic model in Marfan Syndrome .....	172

5.7	Conclusions.....	175
<b>6</b>	<b>Discussion and Future Directions .....</b>	<b>176</b>
6.1	Gene-correcting therapy for MFS.....	177
6.2	Transcriptome Profiling for Pathway Analysis in Human iPSC-derived Complex Disease Models 183	
6.3	Improving Drug screening of Complex Disease Platforms for Pre-clinical Purposes.....	188
6.4	Future Directions .....	192
<b>7</b>	<b>References .....</b>	<b>195</b>
<b>8</b>	<b>Appendices .....</b>	<b>212</b>
	<b>Appendix 8.1 Table of Significantly Differentially Expressed Genes comparing Marfan-Uncorrected and CRISPR-corrected NC-SMCs at both Early and Late Stages of Differentiation Respectively .....</b>	<b>213</b>
	<b>Appendix 8.2 Differential Expression of SMC Genes comparing Early and Late Differentiation Stages for both Marfan-Uncorrected and CRISPR-corrected NC- SMCs respectively .....</b>	<b>214</b>
	<b>Appendix 8.3 Percentage of Gene Targets in Selection of Pathways for 100- compound Pilot Screen .....</b>	<b>215</b>
	<b>Appendix 8.4 Raw MMP Activity Values (RFU) for 1000 compounds Drug Screen .....</b>	<b>216</b>

## LIST OF TABLES

TABLE 2.1 COMPOSITION OF MEDIA USED FOR MAINTAINING HUMAN iPSCs .....	48
TABLE 2.2 AONS USED THROUGHOUT THIS STUDY .....	51
TABLE 2.3 MRNA cDNA SYNTHESIS MAXIMA MASTER MIX COMPOSITION .....	53
TABLE 2.4 MRNA cDNA SYNTHESIS SUPERSRIPT III MASTER MIX COMPOSITION .....	54
TABLE 2.5 MRNA cDNA SYNTHESIS THERMOCYCLING CONDITIONS FOR MAXIMA KIT	54
TABLE 2.6 MRNA cDNA SYNTHESIS THERMOCYCLING CONDITIONS FOR SUPERSRIPT III KIT.....	55
TABLE 2.7 cDNA AMPLIFICATION FASTSTART MASTER MIX COMPOSITION .....	55
TABLE 2.8 MRNA qRT-PCR MASTER MIX COMPOSITION .....	56
TABLE 2.9 MRNA qRT-PCR THERMOCYCLING CONDITIONS.....	56
TABLE 2.10 LIST OF PRIMER SEQUENCES USED FOR qRT-PCR.....	58
TABLE 2.11 BUFFERS USED FOR WESTERN BLOTTING.....	60
TABLE 2.12 LIST OF ANTIBODIES USED FOR WESTERN BLOTTING.....	61
TABLE 2.13 BUFFERS USED FOR CELL FRACTIONATION.....	63
TABLE 2.14 LIST OF ANTIBODIES USED FOR IMMUNOCYTOCHEMISTRY .....	64
TABLE 2.15 LIST OF INHIBITORS USED AS POSITIVE CONTROLS FOR DRUG SCREEN .....	70
TABLE 3.1 IDENTIFICATION OF ESE-RICH REGIONS IN EXON 30 FOR SPLICING MACHINERY DISRUPTION.....	78
TABLE 3.2 AON PARAMETERS SHOWING THE BINDING SEQUENCE OF THE AON, THE SEQUENCE OF THE AON (REVERSE COMPLEMENT), THE ANNEALING TEMPERATURE (T <sub>m</sub> ) AND THE GUANINE AND CYSTEINE PERCENTAGE IN EACH BINDING SEQUENCE (GC%). .....	81
TABLE 3.3 STERIC ENERGY VALUES (KCAL/MOL) FOR EACH STRUCTURE TYPE AS WELL AS EXON 30 ALONE WITH ASSOCIATED BINDING ENERGY (RNASTRUCTURE VERSION 6.0.1). .....	83
TABLE 3.4 EXON-SKIPPING PERCENTAGE .....	88
TABLE 3.5 APOPTOTIC PERCENTAGES MEASURED BY FITC <sup>+</sup> POSITIVE CELLS .....	102

TABLE 5.1 DESCRIPTION OF THE RANGE OF $Z'$ -FACTOR VALUES LIKELY TO BE USABLE IN A HIGH-THROUGHPUT CONTEXT. ....	148
TABLE 5.2 SUMMARY OF MMP ACTIVITY-REDUCING NON-CYTOTOXIC AZ COMPOUNDS AND THEIR RESPECTIVE GENE TARGETS. ....	154
TABLE 5.3 INFORMATION ON GSK3B SMALL MOLECULE INHIBITORS .....	158
TABLE 5.4 LIST OF SECONDARY TARGETS OF GSK3B INHIBITORY AZ COMPOUNDS AND RESPECTIVE PIC50 .....	159

## LIST OF FIGURES

FIGURE 1.1 PRIMITIVE STREAK FORMATION AND GASTRULATION.....	4
FIGURE 1.2 VASCULAR NETWORK DEVELOPMENT FROM THE PHARYNGEAL ARCHES .....	6
FIGURE 1.3 STRUCTURE OF THE VESSEL WALL .....	7
FIGURE 1.4 EMBRYONIC ORIGINS OF SMCs AND THEIR DISTRIBUTION IN THE VASCULATURE.....	10
FIGURE 1.5 STRUCTURE OF FIBRILLIN-1 AND ASSEMBLY OF MICROFIBRILS.....	17
FIGURE 1.6 SEQUESTRATION OF TGF- $\beta$ BY FIBRILLIN-1 MOLECULE.....	19
FIGURE 1.7 CHARACTERISATION OF HUMAN INDUCED PLURIPOTENT STEM CELL MARFAN MODEL. ....	30
FIGURE 1.8 DIFFERENTIATION OF hiPSC INTO NC-DERIVED SMC. ....	33
FIGURE 1.9 FIBRILLIN-1 PHENOTYPE IN MF <sup>C1242Y</sup> SMC. ....	34
FIGURE 1.10 INCREASED TGF- $\beta$ SIGNALLING CORRELATES WITH MMP EXPRESSION AND MATRIX DEGRADATION IN MF <sup>C1242Y</sup> NC-SMC.....	36
FIGURE 1.11 MF <sup>C1242Y</sup> NC-SMC EXHIBIT FUNCTIONAL ABNORMALITIES CONSISTENT WITH THE HUMAN DISEASE PHENOTYPE.....	38
FIGURE 1.12 CORRECTION STRATEGY FOR FBN1 MUTATION C1242Y USING CRISPR/CAS9 TECHNOLOGY. ....	40
FIGURE 1.13 CHARACTERISATION OF SMC DIFFERENTIATION OF CRISPR-EDITED MARFAN IPSCs.....	41
FIGURE 3.1 FBN1 MUTATION IN EXON 30 IN MFC1242Y PATIENT CELL-LINE.....	74
FIGURE 3.2 MF <sup>C1242Y</sup> IS A DISEASE-CAUSING MUTATION IN A CALCIUM-BINDING EGF DOMAIN.....	75
FIGURE 3.3 SCHEMATIC DIAGRAM OF ANTISENSE OLIGONUCLEOTIDE-MEDIATED EXON- SKIPPING. ....	76
FIGURE 3.4 ESE-RICH REGIONS IN EXON 30. ....	79
FIGURE 3.5 IN SILICO PREDICTIONS OF MOST EFFECTIVE AONs FOR EXON-SKIPPING BASED ON PRE-mRNA FOLDING .....	80
FIGURE 3.6 BINDING ENERGY CALCULATIONS TO VALIDATE AON EFFICACY. ....	82

FIGURE 3.7 TRANSFECTION OPTIMISATION USING A GFP-LABELLED AON.....	84
FIGURE 3.8 GFP-LABELLED AON IS TIME-DEPENDENT IN WT-SMCs .....	85
FIGURE 3.9 A COCKTAIL OF AONs CAUSES EXON SKIPPING IN MF <sup>C1242Y</sup> SMCs. ....	87
FIGURE 3.10 SEQUENCING ANALYSIS OF EXON 30 NON-SKIPPED AND SKIPPED TRANSCRIPTS. .....	89
FIGURE 3.11 AONE30 COCKTAIL REMAINS STABLE IN THE CELLS OVER A PERIOD OF 6 DAYS. .....	91
FIGURE 3.12 MULTIPLE TRANSFECTIONS DOES NOT AFFECT THE SKIPPING EFFICIENCY IN MF <sup>C12427</sup> NC-SMCs.....	92
FIGURE 3.13 CO-TRANSFECTING A SCRAMBLE GFP-LABELLED AON WITH AN EXON- SKIPPING AON COCKTAIL INCREASES SKIPPING EFFICIENCY IN MF <sup>C12427</sup> NC-SMCs .....	94
FIGURE 3.14 A COCKTAIL OF AONs CAUSES EXON SKIPPING IN CRISPR-TARGETED MF <sup>C12427</sup> NC-SMCs.....	96
FIGURE 3.15 EXON SKIPPING HAS A MODEST EFFECT ON RESTORING THE PROLIFERATION CAPACITY OF MF <sup>C1242Y</sup> NC-SMC.....	98
FIGURE 3.16 EXON SKIPPING IS ABLE TO REDUCE MATRIX DEGRADATION IN MF <sup>C1242Y</sup> NC- SMC .....	100
FIGURE 3.17 AONE30 REDUCES APOPTOSIS IN MF <sup>C1242Y</sup> NC-SMC.....	102
FIGURE 3.18 AONE30 CAUSES A MODERATE EFFECT ON SMC MORPHOLOGY. ....	104
FIGURE 3.19 MRNA LEVELS OF DOWNSTREAM TARGETS FROM <i>FBNI</i> MUTATION IN SKIPPED AND UNSKIPPED NC-SMCs.....	105
FIGURE 3.20 CRISPR-MEDIATED EXON 30 REMOVAL IN MF <sup>C1242Y</sup> hiPSC.....	107
FIGURE 3.21 MF <sup>C1242Y</sup> hiPSC TARGETED WITH CRISPR-MEDIATED EXON 30 REMOVAL RETAIN THEIR PLURIPOTENCY PROFILE.....	109
FIGURE 3.22 MF <sup>C1242Y</sup> hiPSC TARGETED WITH CRISPR-MEDIATED EXON 30 REMOVAL ARE UNABLE TO DIFFERENTIATE INTO NC. ....	110
FIGURE 4.1 CRISPR-CORRECTED EXPRESS LESS MMPs COMPARED TO MARFAN- UNCORRECTED NC-SMCs AT EARLY AND LATE DIFFERENTIATION STAGES OF SMCs. .....	117

FIGURE 4.2 CRISPR-CORRECTED NC-SMCs ARE LESS APOPTOTIC THAN MARFAN-UNCORRECTED NC-SMCs. ....	118
FIGURE 4.3 MARFAN NC-SMCs EXHIBIT A SPECTRUM OF DISEASE CHARACTERISTICS OVER TIME <i>IN VITRO</i> .....	120
FIGURE 4.4 BOTH EARLY AND LATE CRISPR-CORRECTED AND MARFAN-UNCORRECTED NC-SMCs ARE COLLECTED FOR RNA-SEQUENCING. ....	122
FIGURE 4.5 QUALITY CONTROL OF TOTAL RNA FOR SAMPLES INTENDED FOR RNA-SEQUENCING. ....	123
FIGURE 4.6 SCATTERPLOTS OF RNA SEQUENCING DATA. ....	125
FIGURE 4.7 HEAT-MAP SAMPLE-TO-SAMPLE DISTANCE DISTRIBUTION.....	126
FIGURE 4.8 PCA OF CRISPR-CORRECTED AND MARFAN-UNCORRECTED NC-SMC AT EARLY AND LATE DIFFERENTIATION STAGES. ....	127
FIGURE 4.9 VOLCANO PLOTS DIFFERENTIALLY EXPRESSED GENE DISTRIBUTION OF CRISPR-CORRECTED AND MARFAN-UNCORRECTED NC-SMC AT EARLY AND LATE DIFFERENTIATION STAGES. ....	128
FIGURE 4.10 HEAT-MAPS AND CORRESPONDING VENN DIAGRAM OF DIFFERENTIALLY EXPRESSED GENES OF CRISPR-CORRECTED AND MARFAN-UNCORRECTED NC-SMC AT EARLY AND LATE DIFFERENTIATION STAGES. ....	130
FIGURE 4.11 KEGG PATHWAY ANALYSIS FROM SIGNIFICANTLY DE GENES ENRICHMENT. ....	132
FIGURE 4.12 IPA PATHWAY ANALYSIS FROM SIGNIFICANTLY DE GENES ENRICHMENT. ....	134
FIGURE 4.13 INTERACTION NETWORK OF PREDICATED CANONICAL PATHWAYS BASED ON THE EARLY DE GENE DATASET.....	136
FIGURE 4.14 PROTEIN INTERACTOME OF LARGEST CONNECTED COMPONENT. ....	137
FIGURE 5.1 MF <sup>C1242Y</sup> NC-SMC PROLIFERATE IN RESPONSE TO TREATMENT WITH LOSARTAN AND SB203580. ....	142
FIGURE 5.2 MF <sup>C1242Y</sup> NC-SMCs TREATED WITH LOSARTAN OR SB203580 SHOW REDUCED PROTEOLYSIS. ....	144
FIGURE 5.3 MF <sup>C1242Y</sup> NC-SMCs TREATED WITH LOSARTAN SHOW REDUCED mRNA MMP EXPRESSION COMPARED TO DMSO TREATMENT.....	146

FIGURE 5.4 MF <sup>C1242Y</sup> NC-SMCs TREATED WITH LOSARTAN SHOW REDUCED MMP ACTIVITY.....	147
FIGURE 5.5 Z'-FACTOR CALCULATION FOR THE MMP ACTIVITY LOW-THROUGHPUT SCREEN.....	148
FIGURE 5.6 A 96-WELL FORMAT DID NOT DISPLAY DIFFERENCES IN MMP ACTIVITY LEVELS BETWEEN CONTROL AND LOSARTAN-TREATED MF <sup>C1242Y</sup> NC-SMCs. ....	149
FIGURE 5.7 SCHEMATIC FLOW-CHART OF PILOT 100-COMPOUND SCREEN TO MEASURE THE EFFECT ON MMP ACTIVITY. ....	151
FIGURE 5.8 REPRESENTATIVE PERCENTAGE OF NUMBER OF GENES AND THEIR ASSOCIATED GENE-TARGET AND RESPECTIVE PATHWAY.....	152
FIGURE 5.9 A SUBSET OF NON-CYTOTOXIC AZ COMPOUNDS REPRODUCIBLY REDUCES MMP ACTIVITY IN MF <sup>C1242Y</sup> NC-SMC COMPARED TO DMSO-TREATED CONTROLS. ....	153
FIGURE 5.10 MMP ACTIVITY IS REDUCED IN CRISPR-CORRECTED LINEAGES AND ELEVATED IN MARFAN-UNCORRECTED LINEAGES. ....	155
FIGURE 5.11 AZ COMPOUNDS SELECTED BASED ON TOXICITY, MMP ACTIVITY REDUCTION POTENTIAL AND PROLIFERATION. ....	157
FIGURE 5.12 CANONICAL WNT PATHWAY.....	161
FIGURE 5.13 MARFAN-UNCORRECTED EXPRESS ELEVATED mRNA LEVELS OF GSK3B .	163
FIGURE 5.14 MARFAN-UNCORRECTED NC-SMCs EXPRESS REDUCED LEVELS OF GSK3B .....	164
FIGURE 5.15 GSK3B INHIBITION REDUCES MMP ACTIVITY IN MARFAN-UNCORRECTED NC-SMCs AT 24H AND 96H TREATMENTS. ....	166
FIGURE 5.16 GSK3B INHIBITOR 1 REDUCES TUNEL-POSITIVE CELLS IN MARFAN-UNCORRECTED NC-SMCs AT 96 HOURS POST-TREATMENT. ....	168
FIGURE 5.17 MARFAN-UNCORRECTED NC-SMCs EXHIBIT LOW LEVELS OF TOTAL B-CATENIN IN BOTH CELLULAR COMPARTMENTS. ....	170
FIGURE 5.18 B-CATENIN ACTIVITY MEASURED BY LUCIFERASE ACTIVITY AT 4H AND 24H POST-TRANSFECTION. ....	171
FIGURE 5.19 GSK3B DYSREGULATION WORKING MODEL IN MFS.....	173
FIGURE 5.20 MFS DISEASE MODEL DOWNSTREAM OF PATHOGENIC FBN1 MUTATION...	174

## LIST OF ABBREVIATIONS AND ACRONYMS

AMPA:  $\alpha$ -Amino-3-hydroxy-5-Methyl-4-Isoxazolepropionic Acid

AngII: Angiotensin II

AT1R: Angiotensin II Type 1 Receptor

AON: Antisense Oligonucleotide

BMP: Bone Morphogenic Protein

BSA: Bovine Serum Albumin

CCB: Calcium-Channel Blocker

CRISPR: Clustered Regularly Interspaced Short Palindromic Repeats

DEG : Differentially Expressed Genes

DN: Dominant-Negative

ECM: Extracellular Matrix

EDS: Ehlers-Danlos Syndrome

EGF: Epidermal Growth Factor-like

FBS: Foetal Bovine Serum

FDA: Food and Drug Administration

FITC-gelatine: Fluorescein Isothiocyanate-gelatine

HI: Haploinsufficiency

IPA: Ingenuity Pathway Analysis

iPSC: Induced Pluripotent Stem Cells

KSR: Knockout Serum Replacer

LAP: Latency-Associated Peptide

LARII: Luciferase Assay Substrate

LDS: Loeys-Dietz

LLC: Large Latent Complex

LTBPs: Latent Transforming Growth Factor- $\beta$  binding Proteins

MMP: Matrix Metalloproteinase

nMFS: Neonatal Marfan syndrome

P : Pennicillin

PCA: Principal Component Analysis

PE: Propidium Iodide

PFA: Paraformaldehyde

PI3-K: Phosphoinositide 3-Kinase

PLB: Passive Lysis Buffer

PS : Phosphorothioate

PVA : Polyvinyl Acetate

RFU: Relative Fluorescent Units

S: Streptomycin

SLC: Small Latent Complex

SMC: Smooth Muscle Cells

TB: Transforming Growth Factor  $\beta$ -binding Protein-like

## LIST OF APPENDICES

APPENDIX 8.1 TABLE OF SIGNIFICANTLY DIFFERENTIALLY EXPRESSED GENES COMPARING MARFAN-UNCORRECTED AND CRISPR-CORRECTED NC-SMCs AT BOTH EARLY AND LATE STAGES OF DIFFERENTIATION RESPECTIVELY .....	213
APPENDIX 8.2 DIFFERENTIAL EXPRESSION OF SMC GENES COMPARING EARLY AND LATE DIFFERENTIATION STAGES FOR BOTH MARFAN-UNCORRECTED AND CRISPR-CORRECTED NC-SMCs RESPECTIVELY .....	214
APPENDIX 8.3 PERCENTAGE OF GENE TARGETS IN SELECTION OF PATHWAYS FOR 100-COMPOUND PILOT SCREEN.....	215
APPENDIX 8.4 RAW MMP ACTIVITY VALUES (RFU) FOR 1000 COMPOUNDS DRUG SCREEN .....	216

# 1 INTRODUCTION

## 1.1 Overview of the Introduction Chapter

Marfan Syndrome (MFS) is a pleiotropic connective tissue disorder that exhibits abnormalities in the ocular, skeletal and cardiovascular systems. This multisystemic disease can result in vascular complications and lead to the development of potentially lethal aortic aneurysms. Currently there is no cure for MFS and the available medical treatments focus on either surgically removing the aneurysm or helping to delay the onset of further complications by lowering blood pressure using  $\beta$ -blockers. Therefore, there is a need for novel therapeutic approaches and this thesis will attempt to address different strategies that could potentially be developed into treatments for the clinic.

I will begin the introduction chapter to this thesis with an overview of early developmental events that lead to the formation of blood vessels as it is increasingly apparent that developmental origins impact on vascular disease development. As the aim of this thesis is to identify innovative treatment strategies for MFS, I will further focus on the known pathological signatures that characterise the pathology. MFS is caused by a range of documented mutations in fibrillin-1, an extracellular matrix component (ECM) encoded by the gene *FBNI*. Although the genetic root-cause has been identified for this condition, it remains unclear how the structural and bio-regulatory abnormalities of fibrillin-1 lead to the pleiotropic manifestations seen in MFS patients.

Defective fibrillin-1 has been suggested to cause the loss of TGF- $\beta$  binding, which may provoke excessive release of TGF- $\beta$  in the extracellular matrix and drive disease progression. Therefore, after outlining the promising pre-clinical results of TGF- $\beta$  inhibition in MFS murine models, this section will discuss the controversies surrounding the TGF- $\beta$  hypothesis as a disease driver. Indeed, the translation of TGF- $\beta$  inhibition to the clinical as a therapeutic approach proved challenging and there is an increasing need for improved pre-clinical models for MFS. Recent advances in human induced pluripotent stem cell (iPSC)-derived technology is providing reliable platforms to study complex disease. Here, I will describe our robust *in vitro* system recently developed by our lab to model MFS using patient-derived iPSCs, which harbour distinct pathological *FBNI* mutations and recapitulate the complexity of patient abnormalities. Finally, I will elaborate the proposed therapeutic strategies using our human *in vitro* disease platform to interfere at the level of the mutation and using an unbiased drug screen to capture all signalling pathways, which potentially participate in the pathology.

## 1.2 Early Embryogenesis

In order to understand how the vasculature can contribute to disease progression, it is important to first consider how the vasculature arises from the developing embryo. Immediately after fertilisation, the zygote will journey through a series of cleavages starting with a two-celled organism and developing into a blastocyst of about 32 cells. Following blastulation, the embryo engages in a series of development stages whereby it self-organises to form the inner cell mass (ICM), which will give rise to the definitive structures of the embryo. The ICM further polarises and separates into the epiblast and the hypoblast, from which originate the ectoderm and the extraembryonic endoderm, respectively. The epiblast cells will burrow along the midline of the embryo to form the primitive streak. The hypoblast will progressively be replaced to form the definitive endoderm and the remaining cells will migrate to allow the generation of the intraembryonic mesoderm, which sits between the ectoderm and endoderm<sup>1</sup> (Figure 1.1A).

As a result, the next stage of early embryogenesis, gastrulation, generates the three germ layers of the embryo: ectoderm, mesoderm and endoderm. Each layer undergoes a tightly controlled process of specialisation destined to differentiate into different sets of tissues and organs. The intraembryonic mesoderm differentiates into three mesodermal structures, which include the paraxial mesoderm, the intermediate mesoderm and the later-plate mesoderm (Figure 1.1B). Located centrally within the mesoderm, the notochord signals to the ectodermal layer to initiate the process of neuralisation and form the neural plate. This structure, which will further differentiate into the neuroectoderm and non-neuroectoderm, gives rise to the central nervous system and epidermis, respectively. A subset of cells from the neural plate will migrate into the mesoderm and form a ring structure known as the neural tube. During this process, a selection of cells known as neural crest (NC) cells will delaminate from the neural tube and migrate through the embryo to produce a variety of neural and non-neural cell types. As the embryo continues to develop and increase in size, it can no longer solely rely on diffusion for oxygen and nutrients. To enable the embryo to access the additional required energy for its development, a primitive vascular network starts to develop during the second week post-fertilisation.

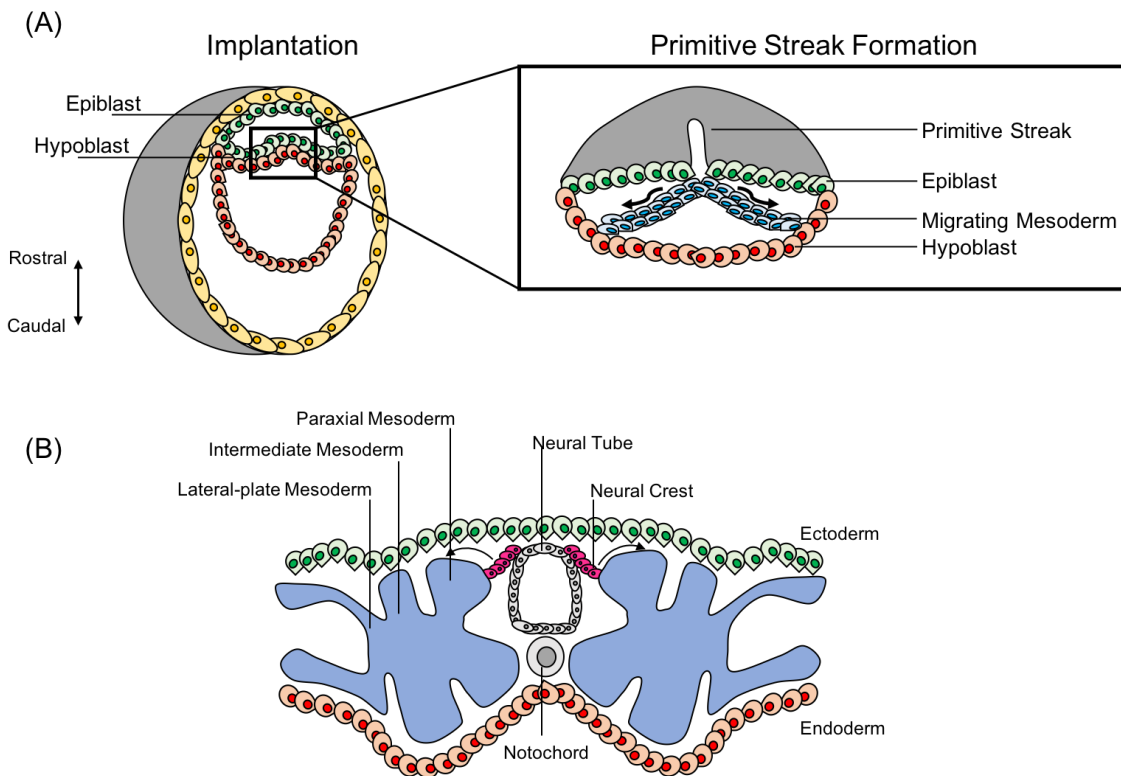


**Figure 1.1 Primitive Streak Formation and Gastrulation**

(A) The primitive streak originates from the epiblast and forms during the early stages of embryonic development towards the caudal end of the embryo. The epiblast migrates and displaces the hypoblast, triggering the formation of the definitive endoderm and a newly-formed intraembryonic mesoderm layer between the ectoderm and endoderm. (B) The mesoderm progenitors, denoted as paraxial, intermediate, and later-plate, arise from the intraembryonic mesoderm and the neural crest population delaminate from the developing neural tube.

## 1.3 Development of the vasculature

### 1.3.1 Pharyngeal aortic arches

One of the first systems to develop in the embryo is the cardiovascular system, which enables the early embryo to supply oxygen to all its developing tissues to facilitate proper development. The primitive vascular network stems from the early arrangement of six aortic arches (I-VI) and their derivatives, known as the pharyngeal aortic arches (PAA). The three germ layers participate in the formation of each arch and all six arches undergo extensive remodelling to eventually give rise to the major vessels of the embryo, such as the pulmonary arteries and dorsal aorta, as well as a honeycomb-like plexus that connects these vessels (Figure 1.2).

The first three arches are adapted to supply the cervical and cranial regions and form the internal carotid artery, responsible for supplying blood to the brain. As the heart is an asymmetrical structure, the fourth PAA develops asymmetrically whereby the dorsal segment becomes the mature aortic arch and the ventral segment forms the right subclavian artery. Unlike other organisms, humans do not develop a fifth PAA and, finally, the sixth aortic arch gives rise to the pulmonary arteries responsible for the vascularisation of the lungs. This dynamic remodelling of the primary vessel blue-print will eventually generate the mature vascular anatomy, which is comprised of differentiated arteries, veins and small vessels<sup>2</sup>. In order to generate these specialised vessels, endothelial cells (ECs) integrate tightly with supporting mural cells, including smooth muscle cells (SMCs) and pericytes, allowing the nascent vessels to undergo maturation.

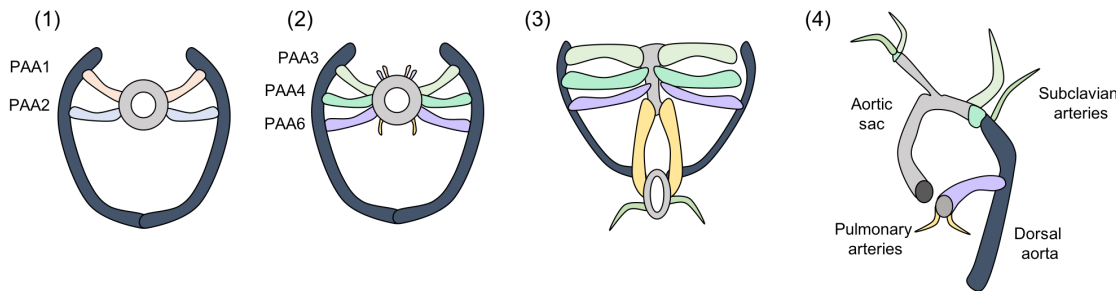


**Figure 1.2 Vascular network development from the pharyngeal arches**

The pharyngeal arches 1-6 (PAA) contribute the dynamic remodelling of the arterial circulation during embryogenesis. Arches 1 and 2 (PPA1, PPA2) regress early in development, PPA3 forms the carotid system, PPA4 forms the aortic arch and the subclavian arteries, whilst PPA5 disappears and PPA6 gives rise to the pulmonary trunk and arteries. (1) Carnegie Stage 10, (2) Carnegie Stage 12, (3) Carnegie Stage 13, and (4) Carnegie Stage 20.

### 1.3.2 Structure and maturation of blood vessels

Mural cells endow the vessel walls with viscoelastic and vasomotor properties to provide structural integrity and maturation aid to the developing vessel. Mural cells are subdivided into two sub-types of cells: vascular smooth muscle cells (SMCs) and pericytes. The mural cell composition of a vessel will depend on its wall density and its anatomical location. Generally, blood vessels are composed of three layers known as the tunica intima, the tunica media and the tunica adventitia (Figure 1.3). The tunica intima, closest to the lumen, consists of a single layer of ECs and elastic tissue known as the internal elastic lamella. Similar to the other components of the tunica intima, the internal elastic lamellae provide vascular integrity whilst allowing the vessel to expand in response to changes in blood flow. The tunica media, or the muscular layer, regulates vascular tone and will vary in thickness depending on the vessel type. Larger vessels, such as the aorta, contain multiple layers of SMCs and extracellular matrix (ECM)

components, which contribute to the elastic recoil of the vessel by regulating vasoconstriction and -dilation. In contrast, the composition of the tunica media in smaller vessel, such as capillaries, is majoritarily composed of a thinly distributed layer of pericytes. Finally, the outermost layer of the vessel, the tunic adventitia, is loosely assembled of ECM, fibroblasts, innervation points and smaller arteries called vasa vasorum, which supply nutrients to the outer-layers of the larger arteries<sup>3,4</sup>.

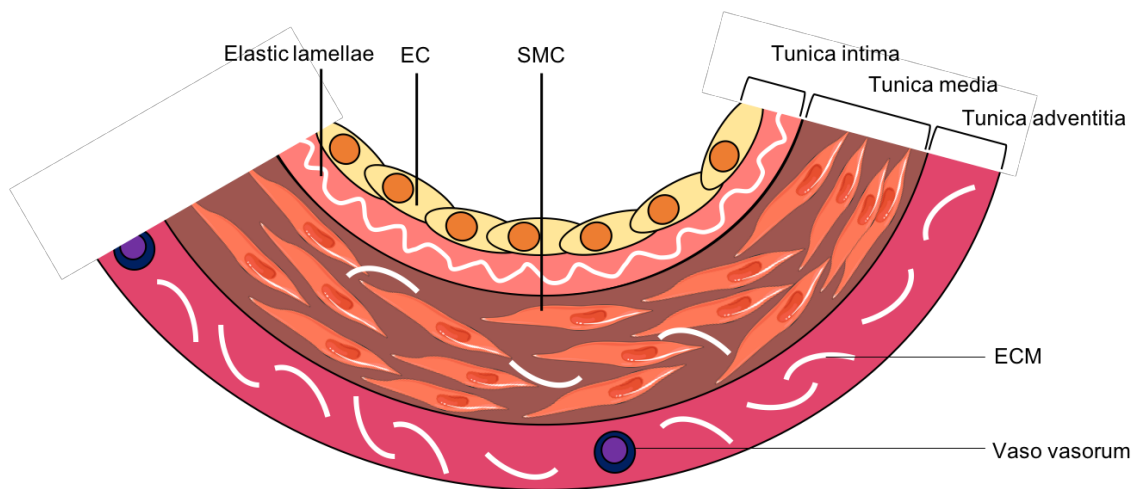


**Figure 1.3 Structure of the vessel wall**

The arterial wall is composed of three layers: tunica intima (endothelial cells and internal elastic membrane), tunica media (vascular smooth muscle cells and external elastic membrane (ECM)), and tunica adventitia (ECM and vasa vasorum). SMC, smooth muscle cells; ECM, extracellular matrix; EC, endothelial cell.

## **Development of novel therapies for Marfan Syndrome using a human iPSC-derived disease model**

Vessel stabilisation and maturation is regulated by a number of signalling mediators during vascular development. In the vessel wall, ECs secrete Platelet Derived Growth Factor (PDGF)-BB, a chemoattractant for SMCs, in response to Vascular Endothelial Growth Factor (VEGF), which synergistically drives mural cell accumulation<sup>5</sup>. The Tie receptor family, Tie1 and Tie2, and respective ligands Angiopoietin-1 (Ang-1) and Ang-2 produced by mural cells stabilise vascular networks initiated by VEGF<sup>6-8</sup>. It has been reported that Tie2 receptor dysfunction induces loss of SMCs and vascular malformation<sup>9</sup>. SMCs distinctly play a role in protecting new vessel formation from rupture and regression, illustrating the importance of these cells in the proper development and maturation of the vasculature.

## 1.4 Origins of vascular smooth muscle cells

### 1.4.1 SMC lineage diversity

SMCs express a panel of contractile and cytoskeletal proteins, which include Calponin-1 (CNN1), Smooth Muscle  $\alpha$ -Actin (SM $\alpha$ A), Smooth Muscle Protein 22- $\alpha$  (SM22- $\alpha$ ), Smooth Muscle Myosin Heavy Chain (SMMHC), and Smoothelin Isoform B (SMTN-B)<sup>10</sup>. SMCs are also characterised by pronounced structural properties including large cytoskeletal features and focal adhesions, which mediate the contractile response between the SMC and ECM<sup>11</sup>. All mural cells have similar functions, which is to regulate the proper development of the vasculature, maintain vessel wall integrity, and regulate vascular tone. Whilst the physiological role of mural cells is largely similar, the developmental origins of these cells remain diverse.

Initially, the concept of SMC heterogeneity originated from studies of cytoskeletal and contractile protein expression in vascular development and disease. Here, the common finding highlights a striking plasticity in SMCs whereby a panel of SMC specific marker genes is coordinately upregulated as SMCs differentiate and acquire contractile capabilities. In contrast, proliferating SMCs in the context of primary tissue culture or disease exhibit high rates of proliferation and migration and downregulate levels of SMC markers; an expression profile known as phenotypic switching<sup>12,13</sup>. However, these results were unable to discern whether the heterogenous response of SMCs to various stimuli was characteristic of a developmentally distinct sub-population of SMCs or due to a stochastic process of the resident cells.

Fate-mapping studies in chick-quail transplants, later confirmed in mice, provided early evidence that SMCs originate from different sources<sup>14,15</sup>. NC progenitors give rise to SMCs that populate the ascending aorta, aortic arch and its derivatives, and the ductus arteriosus<sup>16</sup>. Interestingly, this model does not label the base of the aortic root and descending thoracic and abdominal aorta, suggesting that these aortic regions arise from different embryonic origins. Further tissue-marking studies pursued the SMC fate enigma in mouse and chick models, where results showed that the lateral-plate mesoderm generates prospective SMCs in the aortic root and, additionally, that labelled paraxial mesoderm gives rise to SMCs of the descending aorta<sup>17-19</sup>. Therefore, vascular smooth muscle tissue that was initially defined as seamless and continuous is now known to be

## Development of novel therapies for Marfan Syndrome using a human iPSC-derived disease model

produced from a mosaic of SMCs that originate from at least seven unique and non-overlapping regions of the embryo<sup>20</sup>. (Figure 1.4).

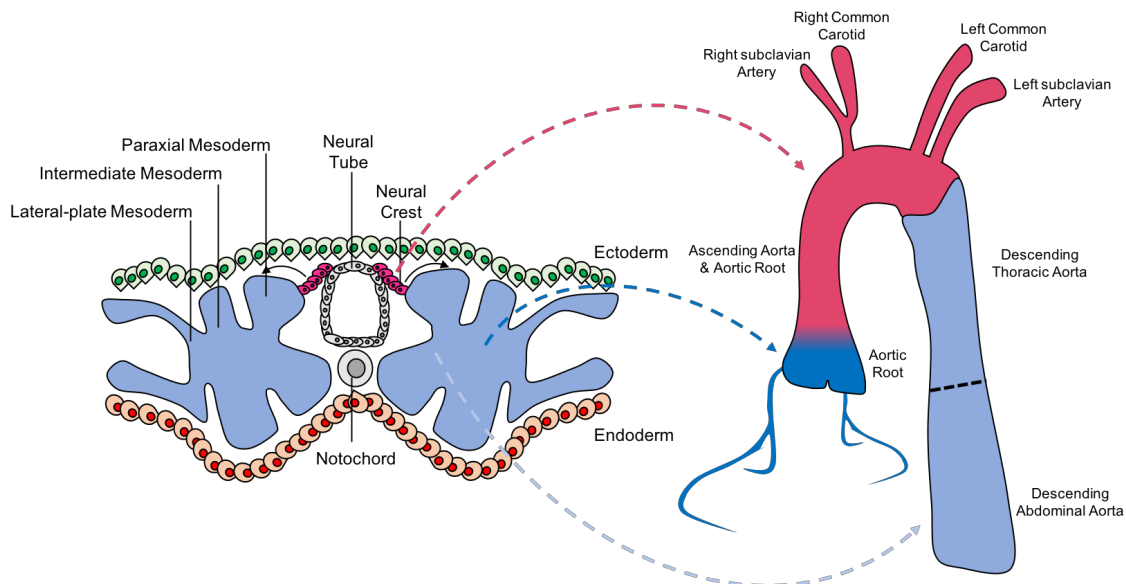


**Figure 1.4 Embryonic Origins of SMCs and Their Distribution in the Vasculature**

The aorta illustrates the heterogeneity of smooth muscle cells (SMC) origin *in vivo*. The paraxial mesoderm provides SMCs of the descending thoracic and abdominal aortas (light blue), the neural-crest gives rise to SMCs of the ascending aorta, aortic arch and its derivatives (pink), and the lateral-plate mesoderm generates SMCs of the aortic root (dark blue).

### 1.4.2 Relation of SMC diversity to vascular disease

Since the discovery that SMC populations arise from distinct sources of progenitors, it has been proposed that the vascular tree responds heterogeneously to pathologic stimuli due to the diversity of SMCs. Aortic homograft transplantations in dogs investigated the response of different aortic segments subjected to an atherogenic diet<sup>21</sup>. Here, Haimovici showed that relocating atherosclerosis-prone sections of the aorta (abdominal aorta) to atherosclerosis-resistant areas (thoracic aorta) did not prevent

disease development. These findings suggest that embryological origin influences disease susceptibility of a particular vascular bed.

An aortopathy that displays a region-dependent characteristic is aortic aneurysm and dissection<sup>22</sup>. An aortic aneurysm is defined by a dilation of the aorta, which can occur as a result of environmental factors, trauma or genetic abnormalities in the connective tissue, the latter being a characteristic of cardiovascular syndromes that include Marfan Syndrome (MFS), Loeys-Dietz (LDS) and Ehlers-Danlos (EDS). These three diseases are common examples of heritable connective tissue disorders and share a degree of phenotypic overlap. Fibrillin-1 mutations were identified as the genetic cause of MFS in 1991<sup>23</sup> whilst LDS is provoked by mutated components of the TGF- $\beta$  signalling pathway, whereby loss-of-function mutations paradoxically provoke an increase in TGF- $\beta$  activity<sup>24</sup>. Finally, EDS results from collagen structural modifications that can be caused by abnormal structure, processing, folding and deposition of fibrillar collagens within the ECM<sup>25</sup>. Aortic dilation is frequently caused by maladaptive ECM remodelling, which weakens the tissue and predisposes the aortic wall to tear. Subsequently, blood infiltrates between the tunica intima and media, causing the layers to separate and dissect. These types of pathologies are life-threatening and twenty-percent of patients with Marfan Syndrome are known to undergo surgical removal of aortic aneurysms<sup>26</sup>.

Animal and clinical observations demonstrated the impact of embryonic origin also on SMC mineralisation. NC-derived SMCs, which colonise the aortic arch and ascending aorta, are more prone to calcification than the mesoderm SMC subpopulations that compose the descending regions of the aorta<sup>27</sup>. Furthermore, our lab designed a recent *in vitro* disease model for Marfan Syndrome derived from patient cells that exhibits a correlation between SMC subpopulation and disease severity. Here, NC-derived SMCs, harbouring mutations typically associated with aneurysm formation in the ascending aorta and derivatives, display more severe disease characteristics than SMCs generated from the other mesoderm sources<sup>28</sup>. Altogether, these *in vitro* and *in vivo* studies support a correlation between SMC embryonic origin and regional disease predisposition.

## 1.5 Vascular ECM and arterial mechanics in vascular disease

In addition to SMC origin, difference in vascular wall structure has been suggested to contribute to regional-dependent disease susceptibility. A major function of SMCs is to produce and organise ECM, which governs the mechanical properties of the vessel wall. SMCs produce a battery of ECM molecules depending on the function of the particular vessel, termed lamellar units, which provides a unique mechanical signature. The number of lamellar units varies according to the aortic region, whereas the thoracic aorta contains 55-60 units, the abdominal aorta contains between 28-32 units<sup>29</sup>. Wagenseil and colleagues performed a large-scale gene expression analysis on different sections of the aorta to identify the types of matrix proteins required to generate a functional ECM network<sup>4</sup>. Results showed that elastic fibres and fibrillar collagens consist the major structural matrix proteins of the vessel wall. Elastin, deposited during foetal and early neonatal life, imparts elasticity to the connective tissue. The family of fibrillin proteins, fibrillin 1-3, provide a scaffold for elastin fibre assembly and play a bioregulatory role for a range of growth factors. Collagen accounts for vascular stiffness and strength, which allows vessels to support the pressure of the pulsatile blood flow. As a result, the vessel structure adjusts according to the regional pressure demands, which depends on the ability of SMCs to transduce mechanical signals and provide optimal vascular mechanical behaviour.

Abnormalities in these structural proteins lead to aortic wall weakness and compromise the function of the ECM network. Therefore, the variable local mechanical properties will not only predispose to site-specific differences in strength but also in vascular disease development. Aneurysm formation, which is the result of degradative structural medial integrity and loss of SMCs, more commonly occurs in the abdominal aorta but is also found in the thoracic aorta<sup>30</sup>. Pathophysiological studies have identified disparities in vessel mechanics and matrix remodelling enzymes that may drive aneurysm formation in a regional-dependent manner<sup>31-33</sup>.

As previously described, the abdominal aorta is composed of fewer lamella units, which may predispose this aortic zone to elastin fragmentation and SMC death, and therefore increase the risk of abdominal aortic aneurysm (AAA) formation. Indeed, AAAs are correlated with advanced age and a collection of environmental risk factors, making them far more common than thoracic aortic aneurysm (TAAs), which display

high heritability often due to mutations in components of the ECM, cytoskeleton and TGF- $\beta$  signalling cascade. Interestingly, dissecting lesions commonly arise at the following aortic junctions: (i) the overlapping region of later-plate mesoderm- and NC-derived SMCs, which populate the base of the aortic root and ascending aorta respectively and (ii) the intersection of NC- and paraxial mesoderm-derived SMCs, where the ascending arch becomes the descending aorta. Therefore, regional SMC heterogeneity and the produced ECM within the tissue dictates a unique set of functional properties and potentially predisposes the individual aortic zones to disease susceptibility in a region-specific manner. Patients suffering from Marfan Syndrome, a genetic connective tissue disorder, preferentially display aneurysm progression in the ascending aorta. Thus, this particular aortic zone, and its respective origin-specific SMCs are an interesting set of targets for therapeutic intervention.

## 1.6 Marfan Syndrome: a disease with multiple facets

Marfan Syndrome (MFS) is an autosomal dominant disorder of connective tissue with an estimated incident of 1 in 5,000-10,000 individuals<sup>34</sup>. MFS displays variable pleiotropic manifestations, including ocular defects, bone overgrowth and cardiovascular abnormalities. Phenotypic variability is high in MFS and diagnosis is established according to clinical criteria (revised Ghent nosology)<sup>35,36</sup>. Marfan patients harbour mutations in *FBN1*, which encodes fibrillin-1, a principal glycoprotein of the ECM. This large molecule is the bed-rock for microfibril assembly and provides structural support in the aorta through association with elastic fibres. This highly-organised network conveys mechanical stability to the dynamic connective tissue and helps direct load bearing<sup>37</sup>. Defective fibrillin-1 causes a plethora of pathophysiological down-stream effects, which ultimately lead to aneurysm development.

Current available treatments are limited to surgical intervention in order to remove life-threatening aortic aneurysms and  $\beta$ -blocker administration, which is thought to help limit blood pressure and haemodynamic stresses on the aortic wall. The treatments available in the clinic focus on minimising aortic wall stress, but no specific therapy exists to cure or inhibit the underlying disease process in MFS. Rather, the following standards are employed to improve certain aspects of the disease and prevent premature death: (i) moderate restriction of physical activity, (ii) serial imaging of the aorta, (iii)  $\beta$ -blocker medication for aortic protection and (iv) surgical removal of aortic dilatation and aneurysm<sup>38</sup>. To manage aortic dissection, MFS patients undergo surgical replacement of the aortic root with a composite graft. Unfortunately, early surgical intervention represents only a limited therapy, as aneurysms are subject to a 30-70% recurrence in patients<sup>39</sup>. Additionally, a medical approach by blocking  $\beta$ -adrenergic receptors was suggested in 1971 to reduce the risk of developing aortic complications<sup>40</sup>. Although, a single trial on just 70 patients demonstrated the effectiveness of  $\beta$ -blockers for aortic protection, the study was non-blinded and primitive imaging modalities were used to monitor aortic size<sup>41</sup>. A secondary uncontrolled trial of only 25 patients showed that low doses of propranolol, a  $\beta$ -blocker representative of b-adrenergic blocking agents widely used in patients with MFS, do not yield overt benefits<sup>42</sup>. Taken together, these studies indicate a heterogeneous and inconclusive response to  $\beta$ -blocker treatment in patients and little evidence suggest that  $\beta$ -blockers affects the underlying pathological mechanisms.

Therefore, efforts in developing alternative treatments for MFS remain valuable and I will explore the virtues of losartan treatment as a medical therapy for MFS further along in this chapter.

## 1.7 Fibrillin-1

### 1.7.1 Molecular structure and function of fibrillin-1

As previously described, Marfan Syndrome (MFS) is caused by mutations in fibrillin-1, a connective tissue ECM protein that was first discovered in 1986. Lynne Sakai and colleagues isolated the protein from fibroblasts and demonstrated it to have widespread deposition throughout the extracellular matrix<sup>43</sup>. Fibrillin-1 is a large extracellular glycoprotein (350kDa), which has a highly modular organisation. The protein is constituted of 47 motifs called epidermal growth factor-like (EGF) domains, which are dominated by 43 calcium binding epidermal growth factor-like (cbEGF) domains arranged in several long tandem repeats. Each cbEGF module contains six cysteine residues, which will disulphide bond and crucially participate in the final protein conformation<sup>44</sup>. cbEGF domains function to sequester extracellular calcium, increase fibrillin-1 monomer interaction with other cellular structural components and stabilise the structure of the protein. Loss of calcium binding affects the structural integrity of the cbEGF domains and leads to fibrillin-1 proteolysis. Additionally, each set of cbEGF tandem repeats is interspersed with 8-cystein containing transforming growth factor  $\beta$ -binding protein-like (TB) modules, which are also found in the homologous family of latent transforming growth factor- $\beta$  binding proteins (LTBPs)<sup>45-47</sup> (Figure 1.5). Once secreted, fibrillin-1 monomers assemble to form microfibrils of 10-12nm in diameter, which deposit in the ECM of connective tissue and play a role in elastin fibre homeostasis. Strong evidence supports a model of parallel head-to-tail organisation of aligned fibrillin monomers, which strengthens connective tissue through their association with elastic fibres<sup>37</sup>. Thus, it was initially hypothesised that mutant fibrillin-1 within the aorta would result in weakening the aortic wall through disruption of the microfibril network<sup>48</sup>.

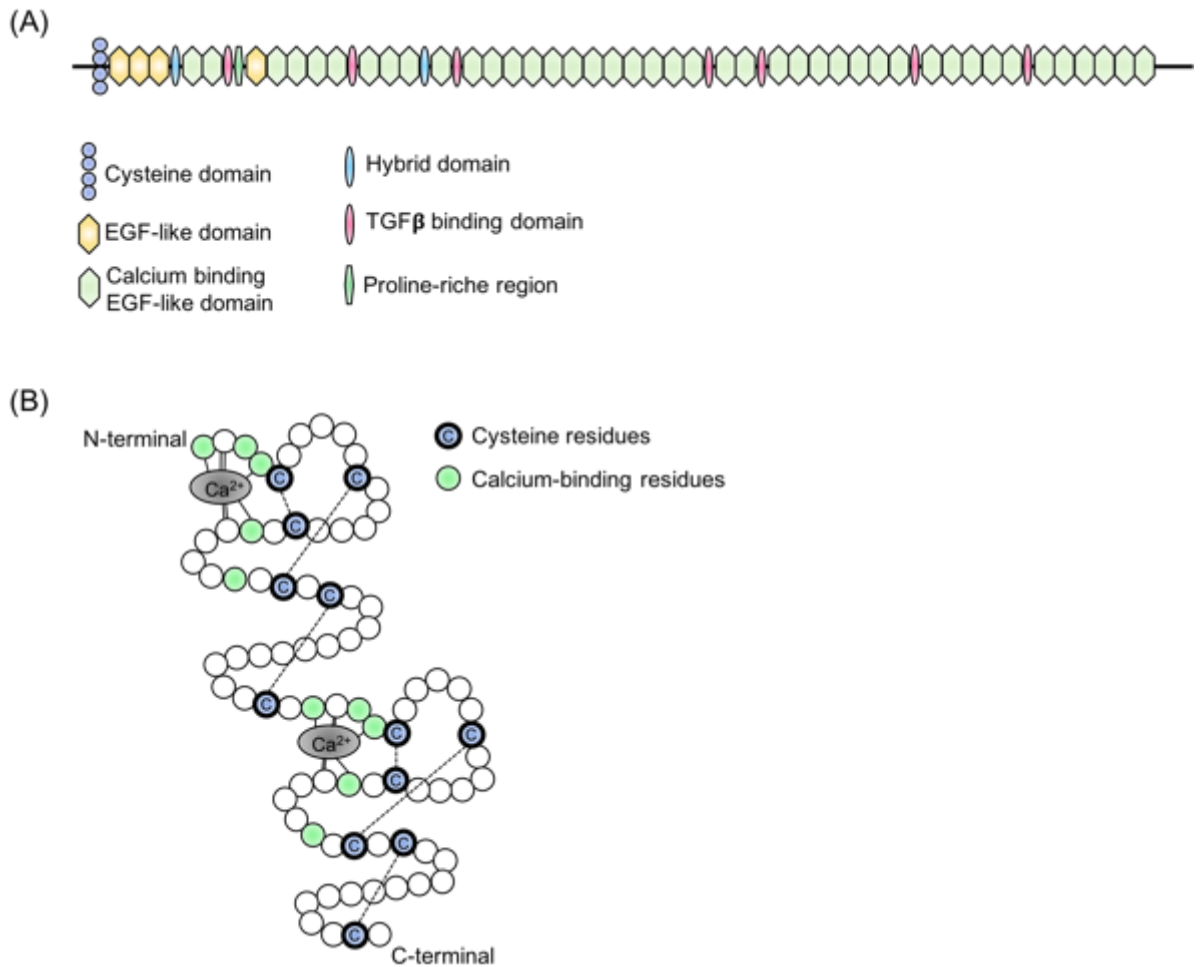


**Figure 1.5 Structure of fibrillin-1 and assembly of microfibrils.**

(A) Schematic representation of the primary structure of a pro-typical fibrillin molecule from which is assembled fibrillin-rich microfibrils and elastic fibres. Fibrillin monomers self-assemble into microfibrils that incorporate or are decorated by additional proteins, in addition to associating with elastin in the elastic fibres. (B) Schematic organisation of two adjacent calcium-binding EGF domains where the conserved cysteine residues are shown in blue. In green are shown the calcium binding consensus residues with the predicted ligand arrangement for calcium indicated (grey). Disulphide bonds are indicated by a dashed line. Diagrams adapted from Handford et al, 2000<sup>44</sup>

### 1.7.2 The bi-functionality of fibrillin-1

In addition to providing structural integrity to connective tissue, fibrillin-1 is capable of binding a range of binding partners, including LTBPs. As a result, fibrillin-1 controls the bioavailability of TGF- $\beta$ , a well-annotated mediator of vascular remodelling, by sequestering latent TGF- $\beta$ . TGF- $\beta$  is synthesised as a pre-propolypeptide, which is cleaved in a post-Golgi compartment to yield a mature version of the growth-factor. Here, TGF- $\beta$  is non-covalently bonded to the latency-associated peptide (LAP) to form a biologically inactive complex called the small latent complex (SLC). Finally, the SLC binds to LTBPs by the formation of disulphide bonds and the final complex, the large latent complex (LLC), is secreted to direct LTBPs to ECM components, specifically fibrillin-1 microfibrils (Figure 1.6). Therefore, TGF- $\beta$  is dually sequestered by the LAP rendering the growth factor inactive and by the interaction between the LLC and the microfibril network, which localises and concentrates the latent form of TGF- $\beta$  to specific focal areas of the ECM<sup>49-51</sup>. Dietz et al were the first to identify multiple mutations in *FBNI* and correlate them with MFS pathophysiology, which led them to hypothesise that abnormalities in fibrillin-1 may impair sequestration of latent TGF- $\beta$  complexes and increase TGF- $\beta$  signalling<sup>52,53</sup>.



## Development of novel therapies for Marfan Syndrome using a human iPSC-derived disease model

over 3000 unique mutations in *FBNI* have been identified and are systematically recorded in the UMD-FBN1 computerised database. Mutations have been found in all 65 exons of *FBNI*, showing no predilection for a specific region of the gene<sup>52</sup>. *FBNI* mutations are typically partitioned into three major categories: (i) missense mutations including cysteine substitutions, (ii) nonsense mutations and out-of-frame deletions causing premature termination of translation and will commonly lead to the most severe form of MFS, neonatal MFS and (iii) mutations causing exon skipping or genomic exon deletions that maintain the reading frame. Interestingly, exon skipping mutations affecting the splicing hotspots are relatively common (13%)<sup>34</sup>.

Thus far, a clear genotype-phenotype correlation has been slow to emerge except for a cluster of mutations spanning exon 24-32, which have a greater correlation with severe forms of MFS (neonatal (nMFS) and severe classic MFS)<sup>56</sup> and mutations located in the exonic region 59-63, which lead to a milder phenotype with less aortic involvement<sup>57</sup>. A number of mutations predicted to cause skipping of a single exon have been reported and the majority of these patients had the classic MFS form. Only a minority of cases linked exon-skipping mutations to nMFS. In this report, we discuss the feasibility of skipping one mutated exon of *FBNI* (exon 30) in order to restore proper function of fibrillin-1. Although it is thought that in-frame exon skipping mutations cause a disruption in the alignment of fibrillin monomers, which radically affects microfibril formation and ECM structure<sup>58</sup>, there have been no reported cases of mutations causing the skip of exon 30 within the exon itself. Only a single nMFS patient case harbouring an intronic mutation causing the skip of exon 30 has been recorded<sup>59</sup>. Thus far, no one has shown whether removing an exon when it already carries a missense cysteine mutation, which causes a severe form of MFS, is able to reduce or further harm MFS pathogenesis. Therefore, the precise mechanism by which the pleiotropic phenotype is produced by fibrillin-1 mutations remains unclear. This raised the need for appropriate *in vivo* models for MFS to help underpin the pathogenic events downstream of the mutation.

## 1.8 Mouse models of Marfan Syndrome

Following the previously mentioned studies, Aoyama et al argued that heterozygous mutations in fibrillin-1 may adversely impact the proper deposition and assembly of wild-type molecules<sup>60</sup>. Subsequent investigations in mouse models refined this theory by proposing a dominant-negative (DN) effect to explain MFS pathogenesis; where disease onset is dependent on threshold levels of mutant fibrillin-1 monomers incorporated within the matrix, which potentially triggers secondary pathogenic cellular events<sup>48,61,62</sup>. Subsequent efforts by Pereira et al achieved the generation of MFS mouse models using homologous gene targeting. The first murine (mg $\Delta$ ) line lacked exons 19-24 in *FBNI* and was generated to replicate the DN pathogenic model of MFS. Here, mutant fibrillin-1 was shown to assemble into microfibrils and incorporate in the ECM. However, mg $\Delta$  alleles produced a 90-95% reduction of the normal amount of fibrillin-1, which made it difficult to conclude whether or not mutant fibrillin-1 exerts a DN effect in heterozygous mg $\Delta$  animals. Their second model (mgR) to emerge contains a targeting cassette that disrupts the production of fibrillin-1 by reducing the product amount to 15-20% and weakening its expression compared to the wild-type allele. Again, mgR/+ are normal but mgR/mgR gradually display severe skeletal abnormalities leading to early adulthood death due to vascular abnormalities that recapitulate a MFS-like phenotype. The mgR mouse data further refined our understanding of pathogenicity and additionally contested the DN hypothesis.

As some MFS aspects seemed difficult to reconcile with the proposed DN model such as skeletal overgrowth and alterations in muscle growth, these observations prompted further investigation to understand the mechanisms behind the pleiotropic features of MFS. Judge et al disputed the DN model and argued a haploinsufficiency (HI) model to be the more relevant explanation for MFS pathogenesis, where insufficient wild-type fibrillin-1 production rather than the presence of a mutant protein is the root cause for abnormal microfibril assembly. Here, a human mutated *FBNI* form carrying a cysteine substitution (C1663R) was overexpressed in mice. Despite overexpression of mutant protein and direct evidence of its incorporation into the endogenous murine microfibril network, C1663R mice do not display any clinical abnormalities<sup>63</sup>. Additionally, Judge and colleagues showed that overexpression of wild-type human *FBNI* transgene in a missense MFS mouse model (C1039G), replicating the less common

### **Development of novel therapies for Marfan Syndrome using a human iPSC-derived disease model**

form of mild MFS, rescues the defective aortic phenotype. The C1039G murine model contains a cysteine substitution in an EGF domain and displays excess free TGF- $\beta$  in their vascular tissues, further recapitulating the patient phenotype. In this model, TGF- $\beta$  antagonism through intraperitoneal injections of TGF- $\beta$ -neutralising antibodies reduced mitral valve thickness and highlighted a causal relationship between TGF- $\beta$  dysregulation and MFS progression<sup>64</sup>. Taken together, these data suggest that the loss of products of one allele is an important component of disease progression and hyperactive TGF- $\beta$  may play a role in driving the pathogenesis. Despite experimental limitations, these studies underline that the molecular pathogenesis of MFS remains to be fully understood.

## 1.9 Hyperactive TGF- $\beta$ signalling in MFS

### 1.9.1 TGF- $\beta$ as a driver of MFS

In order to understand the disease mechanism of MFS, the structural role of fibrillin-1 as primary cause for the weakened microfibril network was revisited. As described previously, fibrillin-1 interacts with a plethora of binding partners including LTBPs, which controls the reservoir of available TGF- $\beta$ . Therefore, structurally defective fibrillin-1 levels may lead to aberrant TGF- $\beta$  signalling, which can drive aneurysm progression in MFS<sup>65</sup>. In light of this hypothesis, additional mouse work showed that *mg $\Delta$*  mice displayed lung abnormalities related to excessive TGF- $\beta$  activation and signalling<sup>66</sup>. TGF- $\beta$  is involved in stimulating multiple signalling cascades and it remains unclear which is primarily responsible for driving aortic disease. In canonical signalling, the TGF- $\beta$  receptors I and II (T $\beta$ RI/II) form a complex, which phosphorylates receptor-activated Smad2 and/or Smad3 (pSmad2 and pSmad3 respectively). The latter partners recruit Smad4 and induce its nuclear translocation where Smad-dependent genes are activated for transcription<sup>67</sup>. Recent work shed light on noncanonical TGF- $\beta$  signalling involving RhoA and mitogen-activated protein kinase (MAPK) pathways. Extracellular signal-regulated kinase (ERK), Jun N-terminal kinase (JNK) and p38 are all mediators of the MAPK signalling pathway<sup>68</sup>. This realisation of alternative TGF- $\beta$  signalling pathways shifted the focus away from aberrant Smad signalling being the exclusive cause for MFS pathogenesis. Therefore, TGF- $\beta$  canonical and noncanonical signalling show promise for therapy development in attempts to reduce the lethal development of aneurysms in MFS patients.

### 1.9.2 Controversy over role of TGF- $\beta$ in aneurysm development

Despite the initially prevalent belief that TGF- $\beta$  hyperactivity is the main driver of aneurysm progression in MFS, paradoxical findings have questioned our understanding of the precise role of TGF- $\beta$  in disease development. Initial evidence stating that blocking TGF- $\beta$  dysregulation led to no further aortic dilatation and reduced elastin fragmentation in the aortic wall was based on a MFS mouse model that seldom

## Development of novel therapies for Marfan Syndrome using a human iPSC-derived disease model

manifests the lethal complications of the disease<sup>69</sup>. Lynn Sakai's group tested whether deletion of a hybrid domain in fibrillin-1 responsible for binding the LTBP complex would perturb microfibril assembly in vivo. Results showed that absence of the TGF- $\beta$  sequestering domain did not interfere with matrix deposition patterns<sup>70</sup>. Jason R. Cook et al further challenged the initial findings showing a dimorphic effect of TGF- $\beta$  neutralisation. Here, blocking promiscuous TGF- $\beta$  either exacerbated or mitigated aneurysm formation depending on the time of treatment. Blocking TGF- $\beta$  postnatally before aneurysm formation provoked a dramatic acceleration in disease progression whereas neutralisation at the later stages led to aneurysm regression and preservation of aortic integrity; suggesting an early protective role for TGF- $\beta$ <sup>71</sup>.

Concomitantly, TGF- $\beta$  signalling inactivation markedly enhanced angiotensin II (Ang II)-induced aneurysm rupture in both thoracic and abdominal regions when initiated before pathogenesis<sup>72,73</sup>. Further studies showed that perturbing SMC-specific TGF- $\beta$  signalling by genetically removing TGF- $\beta$  receptor II in MFS mice did not prevent aneurysm development<sup>74,75</sup>. Therefore, there is accumulating evidence that TGF- $\beta$  signalling may not be the sole factor or indeed primarily responsible for driving aneurysm formation.

### 1.9.3 Losartan: an alternative therapy

The TGF- $\beta$  activation hypothesis prompted inhibitory studies to directly block this growth factor for therapeutic purposes. Ng et al demonstrated that treating C1039G mice with TGF- $\beta$  neutralising antibody reversed aortic defects in the animals<sup>64</sup>. However, the accumulating body of evidence disputing TGF- $\beta$  inhibition as a therapeutic goal to reverse aneurysm progression has urged the targeting of alternative signalling routes. Early studies focusing on hypertension treatment-development identified the renin-angiotensin aldosterone system (RAAS) as a dysregulated modality in the context of renal and cardiovascular disease<sup>76</sup>. In homeostatic conditions, the hormonal cascade RAAS plays a critical role in regulating vascular pressure. RAAS is initiated by the controlled secretion of renin, the rate-limiting enzyme that hydrolyses angiotensinogen into angiotensin (AngI). The angiotensin-converting enzyme (ACE) subsequently catalyses the hydrolysis of Ang I into AngII, a potent vasoconstrictor and the primary active compound of the RAAS pathway. A large body of work has focused on understanding

the dysregulations of RAAS in cardiovascular disease in order to develop a class of RASS-blockade drugs.

Human vascular SMCs express at their surface the angiotensin II type 1 receptor (AT<sub>1</sub>R), which is the target receptor for AngII. Furthermore, increased levels of AngII are known to drive MMP-2 expression, through AT<sub>1</sub>R activation, and participate in thoracic aortic aneurysm pathology<sup>77,78</sup>. In *in vitro* culture conditions, SMCs derived from patients with aortic disease show increased AT<sub>1</sub>R activity, which may be caused by several reasons: (i) the active ligand AngII, is present in the serum of SMC-differentiation protocols, (ii) SMCs may present basal levels of AT<sub>1</sub>R activity regardless of ligand-based stimulation, (iii) cell-to-cell contact may trigger AT<sub>1</sub>R signalling via mechanotransduction in a ligand-independent manner. Losartan, a selective inhibitor of AT<sub>1</sub>R, has achieved a similar rescue by blocking a selective inhibitor of AT<sub>1</sub>R activity and also acts to blunt TGF- $\beta$  signalling<sup>69,79</sup>. Additionally, Holm TM et al showed that selective inhibition of the ERK 1/2 pathway significantly reduced aortic root growth. Thus, noncanonical TGF- $\beta$  signalling presents a potential therapeutic target for reversing aneurysm formation in MFS.

As lifelong weekly injections of TGF- $\beta$  neutralising antibody infusions did not present a feasible or safe treatment, losartan was considered the promising alternative to bring forward into clinical trials. Losartan, a clinically-approved drug to treat high-blood pressure and kidney damage caused by diabetes, is interesting not only for its blood pressure lowering qualities but also because it leads to TGF- $\beta$  antagonism through lowering of indicators of TGF- $\beta$  signalling, such as pSmad2. A clinical trial was conducted to compare the efficacy of losartan to that of atenolol to slow down the rate of aortic growth. Lacro RV et al analysed treated children and young adults with MFS who were randomly assigned losartan or atenolol, a commonly used  $\beta$ -blocker, treatment and found no significant difference in aortic dilatation rate between both treatment groups<sup>80</sup>. More recently, a placebo-controlled trial reported similar findings whereby losartan treatment was compared to placebo in 303 patients. Here, losartan showed no additional benefit in limiting aortic dilation in patients receiving  $\beta$ -blocker background treatment<sup>81</sup>.

A retrospective analysis of the Lacro trial further interpreted the data and suggested that losartan may constitute a beneficial therapy depending on the type of *FBNI* mutation harboured by the patient<sup>82</sup>. Here, results suggest that losartan may be effective in reducing aortic root dilatation in HI patients but not in DN patients, showing a mutation-specific response to losartan treatment. Thus, it is hypothesised that losartan

## **Development of novel therapies for Marfan Syndrome using a human iPSC-derived disease model**

may still be valuable for HI patients as a single or combinatorial treatment. Furthermore, our lab has shown that losartan treatment *in vitro* restores fibrillin-1 deposition and certain aspects of the disease phenotype, which will be described further along in the introduction. Nevertheless, this subgroup analysis stems from a retrospective study and should be interpreted cautiously, which supports the enduring need to develop alternative strategies to treat patients with both types of mutations, DN and HI.

To date, most knowledge of MFS has been obtained from studies in FBN1 deficient mice. The great disparity of losartan's impact on the disease progression between mice and humans supports the notion that the ability of mouse models to predict the efficacy of novel drugs for MFS treatment remains limited. The emergence of human induced pluripotent stem cells (iPSCs) has given research a new tool to study both early development and disease pathology. MFS patient-derived iPSCs give us the unique opportunity to examine key pathophysiological features of MFS on a human genetic background. Here, we suggest using a human *in vitro* MFS disease platform based on patient-derived iPSCs, which phenocopies reliably the observed human MFS phenotype of aortic SMCs.

## **1.10 hIPSCs as a research tool to study disease pathology**

### **1.10.1 Human Pluripotent Stem Cells**

Murine studies have informed the scientific community on which signalling pathways govern mammalian development. However, differences in reproductive physiology between early mouse and human embryonic stem cells may explain the limitations of directly translating therapeutic mouse studies to the human clinic<sup>83,84</sup>. Recently, maintaining human blastocysts up to 13 days *in vitro* is possible and this provides a platform to investigate the mechanisms of human development<sup>1,85</sup>. Nevertheless, the 14-day culture limit, respected by the research community, on embryo experimentation highlights the need for new models to be developed to allow further exploration of human development<sup>86</sup>.

In 1998, human embryonic stem cells (ESC) were isolated from the ICM and cultured onto a mitotically inactivated layer of fibroblasts<sup>87</sup>. ESCs are defined by their derivation source (i.e. the preimplantation embryo), their ability to self-renew and remain undifferentiated indefinitely, and their pluripotent potential to form all three embryonic germ layers under well-defined culture conditions. These cells now provide a reliable platform to dissect out the molecular signatures underpinning human embryology and prove useful for drug discovery and regenerative medicine.

### **1.10.2 Generation of Induced Pluripotent Stem Cells**

Since the derivation of ESC as the golden standard of pluripotency, additional studies have shown the possibility of reprogramming somatic cells to a state of pluripotency and generate what is known as induced pluripotent stem cells (iPSC). Yamanka reported the first technique for reprogramming adult cells by introducing four transcription factors: OCT4, SOX2, KLF4 and c-MYC in to human fibroblasts using retroviral transduction. This study demonstrated a successful reprogramming method to allow the generation of patient-specific stem cells, which retain their pluripotent characteristic and disease background<sup>88</sup>. Since, a variety of well-defined culture conditions have been established to optimally maintain human reprogrammed stem cells without the reliance of mitotically inactivated fibroblasts. As a result, Fibroblast Growth

## Development of novel therapies for Marfan Syndrome using a human iPSC-derived disease model

Factor (FGF) and Activin/Nodal signalling have been shown to play a key role in maintaining pluripotency in human iPSC<sup>89-92</sup>.

### 1.10.3 Differentiation of Human Pluripotent Stem Cells for Disease Modelling

With the discovery of induced pluripotent stem cells, it is now possible to convert iPSC into a wide variety of different cell fates. Directed and controlled differentiation of human iPSC is made possible by chemically-defined culture protocols, which allow us to replicate the developmental stages that occur during embryonic lineage commitment. Removing the Yamanka factors combined with inhibition of the Activin/Nodal signalling cascade results in the loss of pluripotency and initiates differentiation towards the neurectoderm lineage. Mesoendodermal induction is activated by the combination of Activin/Nodal stimulation with FGF2, Bone Morphogenic Protein (BMP)-4 and LY294002 (LY) treatment, a phosphoinositide 3-kinase (PI3-K) inhibitor<sup>93</sup>. Mesoderm induction is based on the signalling gradients, which govern the formation of the primitive streak. Co-treatment with LY, FGF2 and BMP4 rapidly induces the expression of BRACHURY, a common transcription factor expressed by mesoderm progenitors<sup>94</sup>. Subsequently, from this progenitor population, modulating the concentration of BMP4 to mimic the embryological gradient observed along the primitive streak will yield mesoderm specification. Lateral-plate mesoderm is generated by the removal of LY and increased BMP4, whilst the removal of BMP4 and maintaining LY and FGF2 produces paraxial mesoderm<sup>95</sup>.

Humans iPSCs have not only enhanced our understanding of the signalling cascades that orchestrate embryonic development, these cells also provide a platform to study disease manifestation and serve as a tool for drug discovery. This potential technique proves useful for complex disease where the causative genes are known but the underlying mechanisms remain unclear. Patient-specific human iPSC can be differentiated to all three embryonic lineages, giving access to all cell-types of the body, and can be used for developing phenotypic drug screens. Additionally, the emerging iPSC technology is providing the previously unanticipated possibility of developing a precise prediction tool for individual patients' responses to different drugs. However, it has been cautioned that iPSC lines derived from patients with different mutations may exhibit variations in biological properties. Several studies have generated and characterised

multiple donor lines in the aim of determining variability at two levels: (i) variability in lines from different donors and (ii) variability in cell lines from the same donor. One group observed reprogramming instability amongst cells lines issued from different donors and amongst multiple clones from the same donor. This suggests that certain lines may be less adequate for differentiation into disease-relevant cell-types and representing the pathogenic features of the patient *in vitro*<sup>96</sup>. This is particularly relevant for late onset diseases, where the slow progression of pathophysiological changes may only manifest itself subtly in a culture-based environment<sup>97</sup>.

Although iPSCs coaxed out of their embryonic state are more akin to early embryonic or foetal cells than adult cells, some aspects of early and late-onset diseases can still be reliably modelled using immature cell types<sup>98</sup>. Various cardiovascular pathologies are characterised by abnormal vascular networks and maturation failures of vascular mural cells. As a result, there is an incentive to use human iPSC-derived SMCs to model complex and pleiotropic vascular disorders, such as Marfan Syndrome. In this work, I used a well-characterised MFS patient fibroblast line that harbours a point mutation and exhibits the key disease features with limited variability in culture across multiple differentiations of the same iPSC clone<sup>28</sup>. Additional patient lines harbouring different MFS mutations are available within our lab but their phenotypic panel of disease characteristics remain to be fully characterised. It is important to highlight that SMCs are the main producers of fibrillin-1 and their *in vitro* study may help further clarify the pathogenic sequence of events that occur downstream of the fibrillin-1 mutation. Furthermore, the recent discovery of CRISPR/Cas9 provides a powerful gene-editing tool to correct disease-causing mutations in patient-specific iPSCs and enables the rescue of the pathological characteristics exhibited *in vitro* by the disease cell types<sup>99</sup>. In the following work, we describe how to capitalise iPSC technology by developing a “disease-in-a-dish” model for Marfan Syndrome using patient-derived iPSCs.

## 1.11 Generation of a human iPSC derived model of MFS

### 1.11.1 Characterisation of MFS-specific hiPSC

Previously, Dr Alessandra Granata and colleagues in our lab established a patient-derived human iPSC model for Marfan Syndrome (MFS)<sup>28</sup>. Patient fibroblasts harbouring a point mutation in *FBNI*, the gene coding for fibrillin-1, were used to generate hiPSC. This cell line, MF<sup>C1242Y</sup>, carries a missense mutation in exon 30 where a guanine in position 3725 is replaced by an adenine (3725G>A)<sup>100</sup>. This point mutation affects the sixteenth cbEGF domain in fibrillin-1. Sequencing analyses of the genomic DNA confirmed the specific *FBNI* mutation (Figure 1.7A) and human pluripotency-associated gene expression was confirmed by immunocytochemistry. (Figure 1.7B).

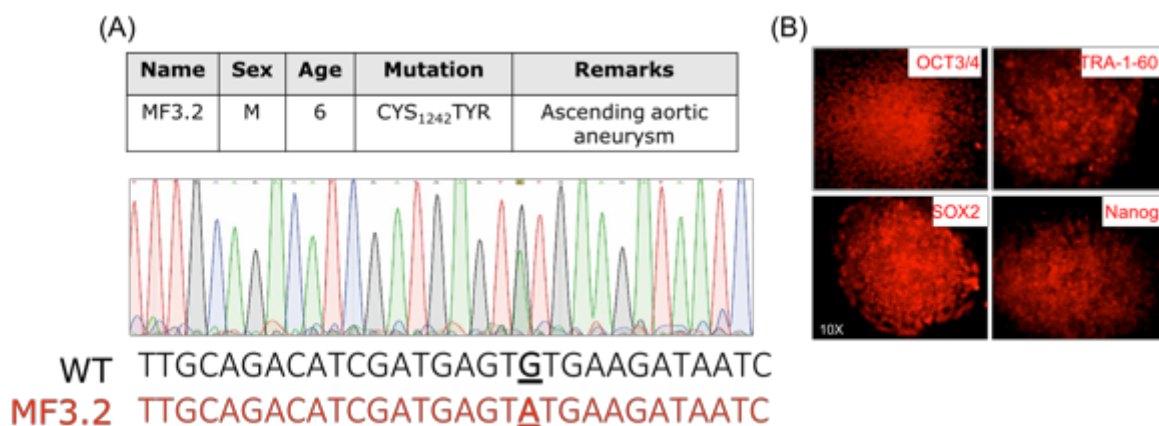


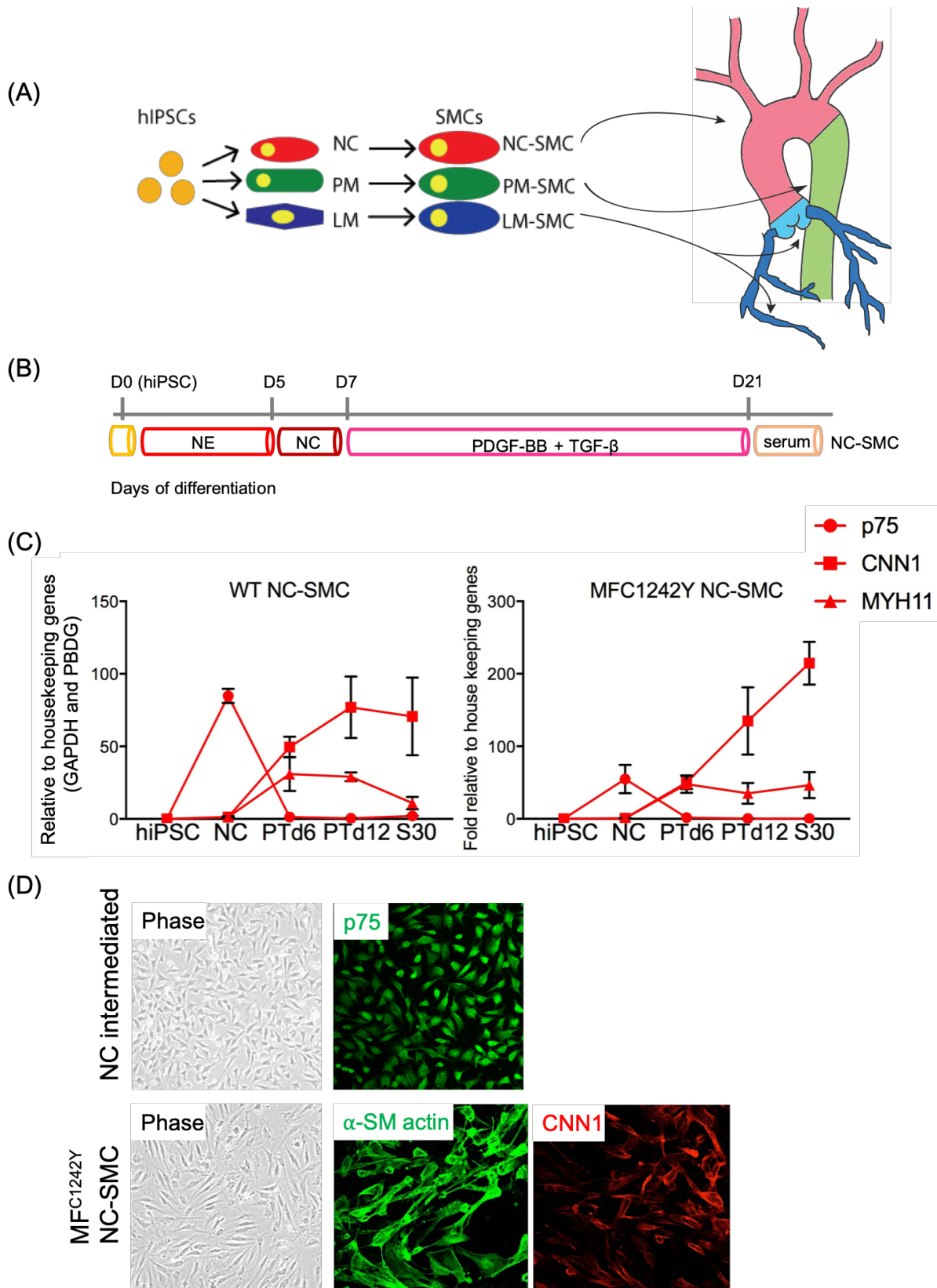
**Figure 1.7 Characterisation of human induced pluripotent stem cell Marfan model.**

A) DNA Sequencing analysis of Marfan humane induced pluripotent stem cells (hiPSC) showing 3725G>A mutation in *FBNI* in exon 30. B) Immunofluorescent staining of MF1242Y hiPSC colonies for the pluripotency markers, OCT3/4, TRA-1-60, SOX2 and Nanog. Magnification 10X. Adapted from Granata A, *Nat Gen*, 2017.

### 1.11.2 Differentiation of MFS hiPSC in SMC intermediate and mature populations

The MFS hiPSC line was differentiated into all three embryonic germ layers to assess pluripotency. Next, hiPSC were differentiated into the three embryonic origin-specific SMC lineages using protocols previously established in our lab<sup>101</sup> (Figure 1.8A). In this study, we focus on the neuroectoderm (NE) and neural crest (NC) populations, which provide a SMC population more sensitive to the pathogenic effects of the MFS mutation. The NE population of cells was trypsinised to single cells and passaged up to 8 times to generate neural crest-like cells (Serrano F et al, 2018, in submission). NC cells were differentiated to SMC using PDGF-BB and TGF- $\beta$ 1, multifunctional cytokines that promote SMC maturation and are known to regulate vascular remodelling in early angiogenesis<sup>102</sup>, treatment for 12 days (PT) and allowed to mature in serum-containing medium (Figure 1.8B). In response to PT treatment, the expression of intermediate NC population markers, such as *p75*, were downregulated while the expression levels of specific SMC markers such as *CNN1* and *MYH11* increased as shown by quantitative RT-PCR and immunocytochemistry (Figure 1.8C and 1.8D). Although *CNN1* is considered a relatively immature SMC marker, the RNA expression data for *MYH11* supports the fact that our lab's protocol is generating mature SMCS *in vitro* akin to human aortic SMCs. In addition, it was challenging to detect *MYH11* in culture as the quality of the antibodies is quite poor and immunostainings for this marker were, as a result, not included in this body of work. Furthermore, previous studies have shown that the expression of multiple SMC markers increase over time with PT treatment. The upregulation of early SMC markers (*ACTA2*, *TAGLN* and *CNN1*) precede the later markers (*SMTH-B*, *MYH11*), where *SMTH-B* represents a vascular isoform and clearly identifies these differentiated populations as uniquely vascular<sup>95</sup>. The figure legend for Figure 1.8 is found on the overleaf (page 32).

Development of novel therapies for Marfan Syndrome using a human iPSC-derived disease model



Adapted from A Granta et al, *Nat Gen* 2017

**Figure 1.8 Differentiation of hiPSC into NC-derived SMC.**

(A) Schematic of hiPSC differentiation into intermediate populations (NC, PM, and LM), followed by further maturation into SMC derived populations (NC-SMC, PM-SMC, and LM-SMC). (B) Differentiation protocol stages: MF<sup>C1242Y</sup> hiPSC, at intermediate NC population stage, at early SMC differentiation stage (PTd6), end of differentiation protocol (PTd12) and at mature stage (serum). (C) Intermediate NC markers (*p75*) and expression of SMC markers (*CNN1* and *MYH11*) during differentiation. Results are presented as SD of n=3. (D) Immunostaining shows NC intermediate marker (*p75*), MF<sup>C1242Y</sup> NC-SMC SMC markers ( $\alpha$ -SMC actin and CNN1) after 12 days of PT treatment (scale bar=50mm). Results presented as means SD of three independent biological experiments (n=3). Abbreviations:  $\alpha$ -SM actin, alpha smooth muscle actin; CNN1, calponin-1; LM, lateral mesoderm; MYH11, myosin heavy chain 11; NC, neural crest; NE, neuroectoderm; PM, paraxial mesoderm; PPDGF-BB, platelet derived growth factor-BB; SMC, smooth muscle cell; TGF- $\beta$ , transforming growth factor beta. Adapted from Granata A *Nat Gen* (2017).

**1.11.3 MF<sup>C1242Y</sup> NC-SMC recapitulate the human MFS aortic phenotype**

This hiPSC-derived SMC model allows us to observe changes in NC-SMC phenotype in response to MFS mutations, which may reflect the aortic aneurysm pathogenesis and progression that occurs in MFS patients. In the first instance, extracellular fibrillin-1 deposition, analysed by immunocytochemistry, was irregular and drastically less abundant in MF<sup>C1242Y</sup> SMC compared to WT SMC subtypes (Figure 1.9A). Remarkably, loss of fibrillin-1 was quantifiably more severe in MF<sup>C1242Y</sup> NC derived SMC compared to that of other subtypes (Figure 1.9B). This is largely consistent with the clinical distribution of aneurysms, which occur preferentially in the region of the aortic root, ascending aorta and arch; areas predominantly populated by NC-derived SMC<sup>95</sup>.

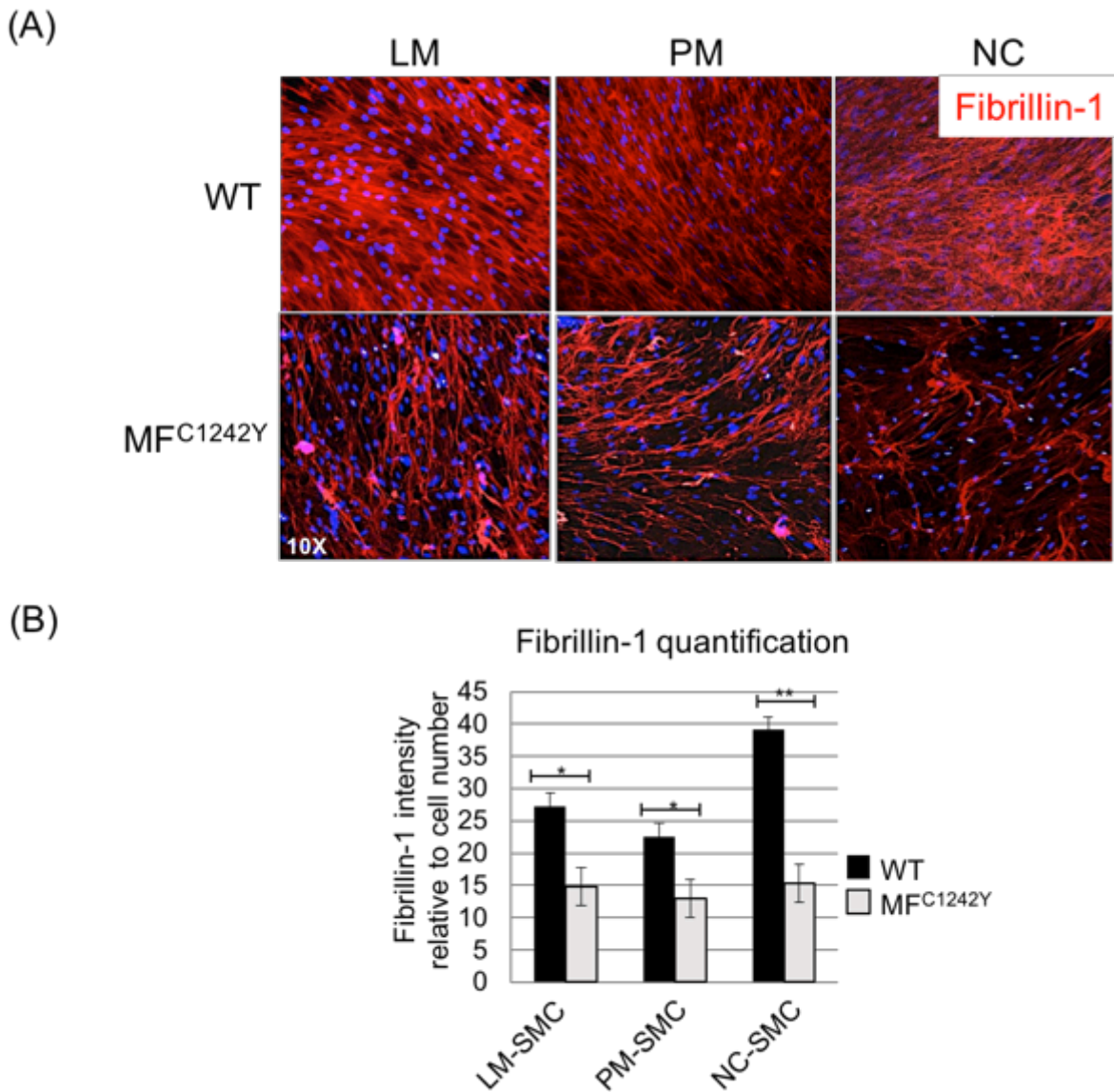


**Figure 1.9 Fibrillin-1 phenotype in MF<sup>C1242Y</sup> SMC.**

(A) Immunostaining analysis of extracellular fibrillin-1 in MF<sup>C1242Y</sup> and WT SMC embryonic subtypes (LM, PM and NC) after 30 days of maturation in serum-containing serum. (B) Quantification of fibrillin-1 by measuring fluorescence staining intensity relative to cell number in WT and MF<sup>C1242Y</sup> SMC derived from all embryonic lineages. The relative mRNA level of each sample was normalized to its *GAPDH* and *PBGD* content. The results are presented as means  $\pm$  SD of three independent biological experiments. The asterisks indicate statistically significant differences; \*  $p < 0.05$ ; \*\*  $p < 0.01$ . Adapted from Granata A *Nat Gen* (2017)<sup>28</sup>.

Previous work on mouse models assessed the involvement of TGF- $\beta$  in MFS pathogenesis. According to these models, abnormal fibrillin-1 deposition causes excessive release of TGF- $\beta$ , which leads to a series of unwanted effects. Our disease model shows increased total protein levels of TGF- $\beta$  in all MFS SMC populations compared to the WT and this increase is greater in the NC-derived population (Figure 1.10A and 1.10B). These results indicate an over-activation of TGF- $\beta$  pathway activity. Indeed, both canonical and noncanonical elements of the TGF- $\beta$  pathway, such as SMAD2, ERK1/2 and p38 showed increased phosphorylation in MF<sup>C1242Y</sup> NC-MSC (Figure 1.10C). Furthermore, mRNA levels of a range of matrix metalloproteinases (MMPs) were increased in MF<sup>C1242Y</sup> NC-SMC relative to WT NC-SMC (Figure 1.10D). In addition, WT and MF<sup>C1242Y</sup> NC-SMC were plated onto a fluorescently-labelled gelatine (FITC-gelatine) to monitor their respective proteolytic activity. MF<sup>C1242Y</sup> NC-SMC showed extensive matrix degradation, which could be observed by dark patches within the green matrix, in comparison to WT NC-SMC, which further suggests that MMPs are increasingly more active in MF<sup>C1242Y</sup> NC-SMC compared to their wild-type counterparts (Figure 1.10E).

## Development of novel therapies for Marfan Syndrome using a human iPSC-derived disease model

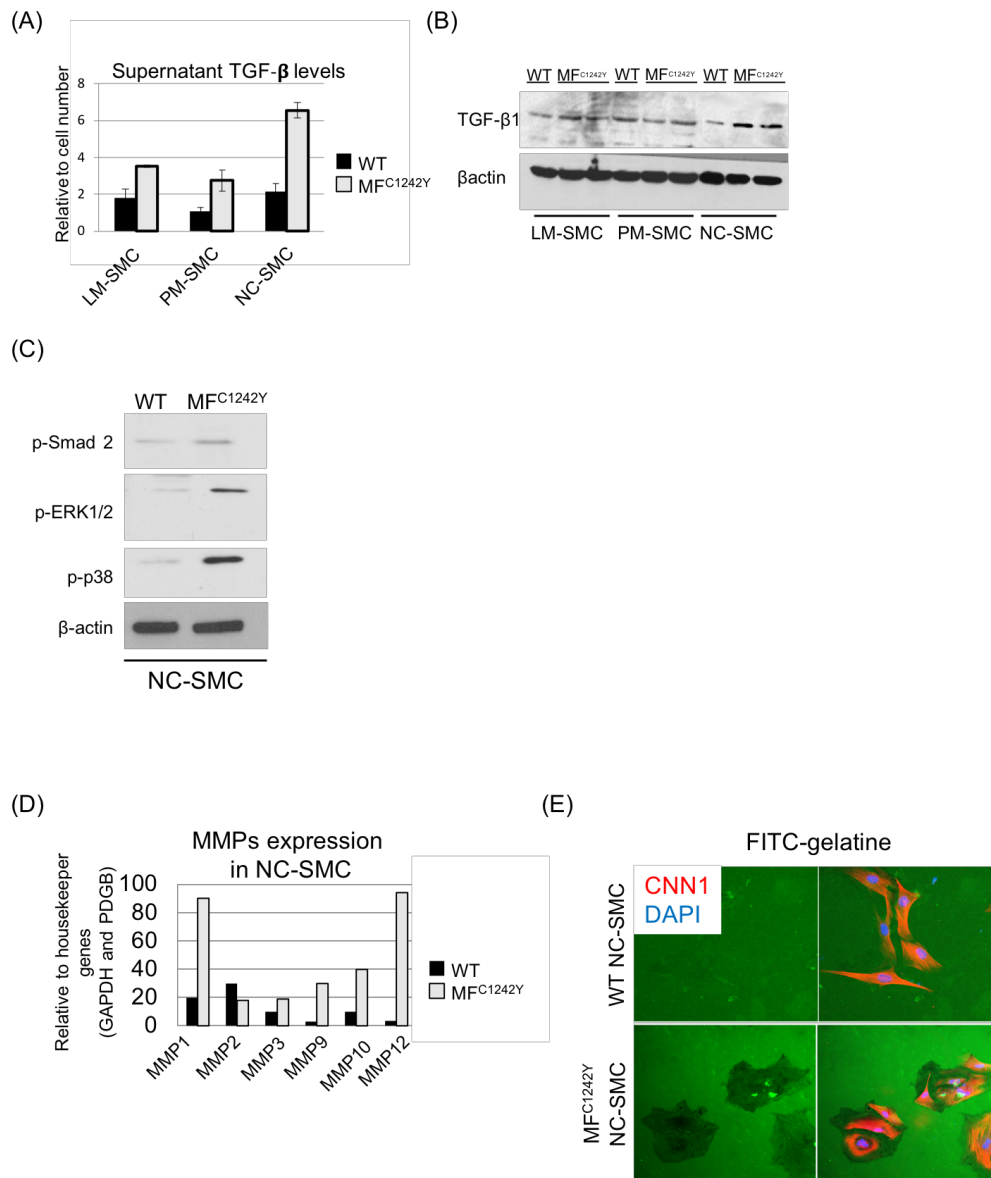


**Figure 1.10 Increased TGF- $\beta$  signalling correlates with MMP expression and matrix degradation in MF<sup>C1242Y</sup> NC-SMC.**

(A) ELISA quantification of TGF- $\beta$  in supernatant of WT and MF<sup>C1242Y</sup> SMC from all embryonic lineages. (B) Protein quantification of TGF- $\beta$  by western blot in all embryonic-derived WT and MF<sup>C1242Y</sup> SMC lineages. (C) Quantification of downstream targets of TGF- $\beta$  signalling pathways (p-Smad2, p-ERK1/2, and p-p38) in WT and MF<sup>C1242Y</sup> NC-SMC. (D) Quantitative RT-PCR expression profile of a selection of matrix metalloproteinases (MMPs) in WT and MF<sup>C1242Y</sup> NC-SMC. (E) FITC-gelatin degradation assay performed with WT and MF<sup>C1242Y</sup> S30 NC-SMC over 48h. Cells were then fixed and stained for the SMC marker, CNN1 (red), DAPI (blue). Adapted from Granata A *Nat Gen* (2017).

Changes in phenotype consistent with those observed in MFS patients were also observed in our disease model. The pathophysiological features included impaired proliferative capacity in MF<sup>C1242Y</sup> NC-SMC compared with WT NC-SMC (Figure 1.11A). Concurrently, MF<sup>C1242Y</sup> NC-SMC display a higher incidence of apoptosis, which is consistent with SMC death observed in MFS aortic dilatation (Figure 1.11B). In addition to the poor proliferative and increased apoptotic profile, MF<sup>C1242Y</sup> NC-SMC appear to be less able to contract in response to carbachol, a cholinergic agent (Figure 1.11C). This may suggest that the cytoskeleton and calcium release response is compromised in MF<sup>C1242Y</sup> NC-SMC; a hypothesis supported by Fluo4-AM assay performed to monitor intracellular calcium release in response to carbachol stimulation. Results show that MF<sup>C1242Y</sup> NC-SMC fail to propagate cyclic calcium waves after calcium release whilst their WT counterparts display regular calcium waves shown by single cell trace (Figure 1.11D). In conclusion, these observations indicate that our disease model display phenotypic changes typical of those observed in patient aortas, suggesting a reliable disease platform for observing MFS pathogenesis.

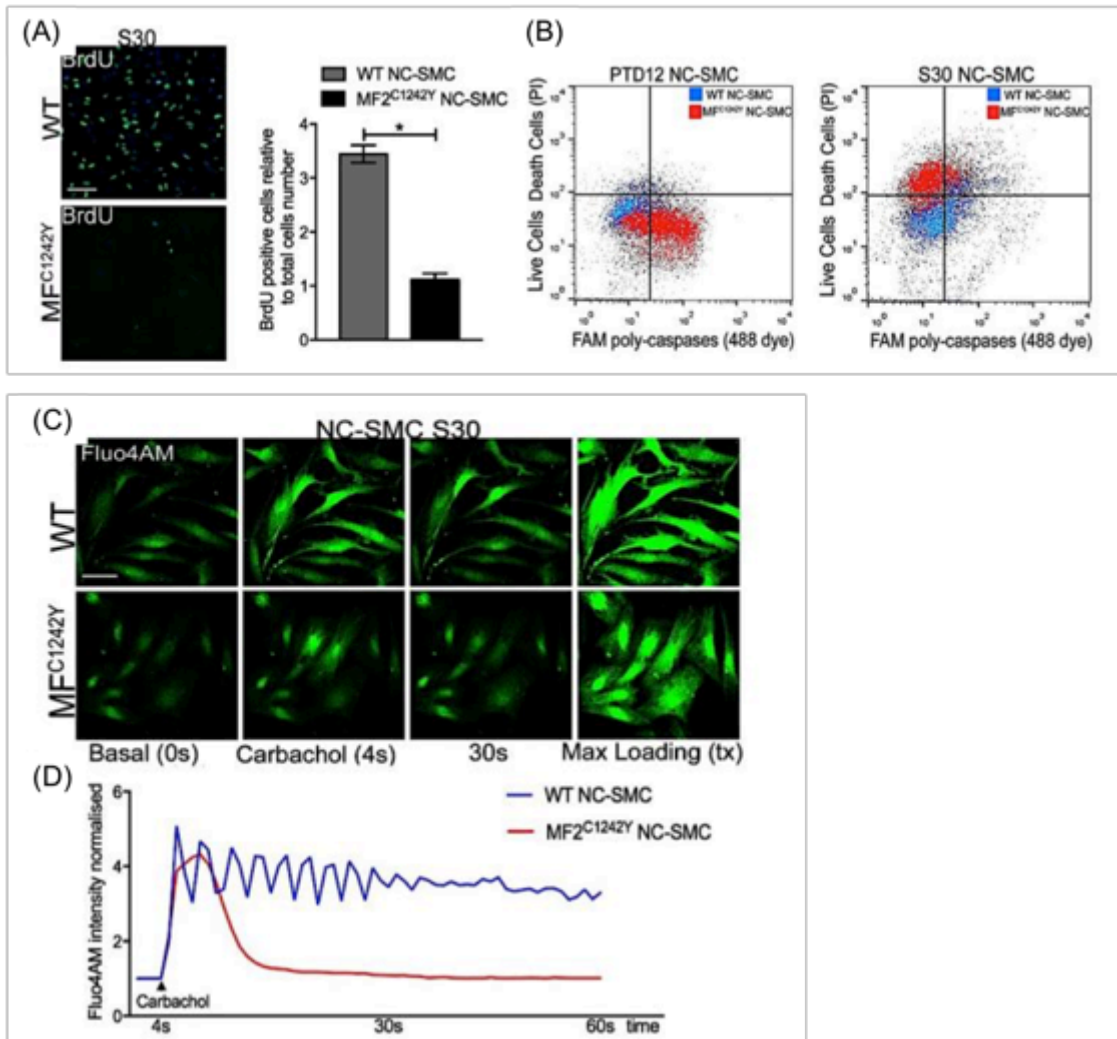


**Figure 1.11  $MF^{C1242Y}$  NC-SMC exhibit functional abnormalities consistent with the human disease phenotype.**

(A) BrdU staining (SMC matured 30 days in serum, S30). Percentage of BrdU positive cells is expressed relative to the total number of nuclei-DAPI staining cells. (B) Flow cytometric analysis of apoptotic pathway activation measured by FAM poly-caspase assay in  $MF^{C1242Y}$  and WT NC-SMC at early PTD12 and late S30 stages. (C) Ca<sup>2+</sup> flux measured by Fluo-4AM loading and intensity of WT and  $MF^{C1242Y}$  NC-SMC at basal (0s), stimulation with carbachol (4s), after 30s stimulation and total loading after triton (tx) treatment. (D) Graph representing single cell fluorescence tracing of WT and  $MF^{C1242Y}$  NC-SMC before and after carbachol stimulation (4s), relative to basal level and total Fluo-4AM loading. All results are representative of n=3; means  $\pm$  SD). The asterisk indicates statistically significant difference (\* p< 0.05). Adapted from Granata *A Nat Gen* (2017).

## 1.12 CRISPR-correction of MF<sup>C1242Y</sup> iPSC

It is important to note that the patient background is a contributing factor to disease development. Therefore, it was necessary to generate an isogenic cell-line, which harbours the patient background and is simultaneously corrected for the specific Marfan Syndrome mutation of this study. The correction experiments were designed and performed by Dr Felipe Serrano using the gene-editing tool, CRISPR/Cas9. Briefly, a pair of guide-RNAs (gRNAs) was designed to specifically direct the donor plasmid containing the wild-type nucleotide and introduce the change in the mutant allele. Briefly, the correction strategy used a set of primers to PCR out a portion 1,063 bp upstream and 970 bp downstream of exon 30 from wild type genomic DNA. Two restriction sites were created into the intronic sequence upstream of exon 30 (KpnI and BcII) and the construct *piggyBac* transposon containing a selectable puromycin marker (*puroR*) was inserted to generate the final donor plasmid (Figure 1.12).

Following homologous recombination after Cas9 genomic DNA cutting of *FBNI* exon 30 in the MF allele, the correction strategy was verified by sequencing. Partial sequencing of *FBNI* exon 30 showed that the point mutation (A to G) in exon 30 was successfully corrected by CRISPR/Cas9. Further along in the text, these targeted lines will be referred to as the following: the targeted and successfully corrected iPSC line is termed ‘CRISPR-corrected’ and the targeted but uncorrected disease iPSC line, which still carries the point mutation in the mutant allele, is termed ‘Marfan-uncorrected’ (Figure 1.13A). Proper SMC differentiation of the CRISPR-targeted hiPSC lines was confirmed by immunostaining (pluripotency, OCT3/4; NC intermediates, p75 and NC-SMC, CNN1) (Figure 1.13B). Finally, fibrillin-1 deposition was monitored by immunocytochemistry, which confirmed that CRISPR-mediated repair of the disease mutation restores fibrillin-1 deposition in the matrix. As expected, Marfan-uncorrected NC-SMCs showed low levels of fibrillin-1 staining similar to untargeted MF<sup>C1242Y</sup> NC-SMCs (Figure 1.13C). To ensure that the genome-editing strategy was free of any off-target effects, a list of off-target sites was generated *in silico*. The top five off-target sequences were amplified by PCR and revealed no genomic alterations. Finally, the PGK-Puro cassette, which had been inserted intronically between exons 30 and 31 of *FBNI* and used for the selection of positively-targeted clones, was removed. The genomic DNA spanning exons 29 to 31 was sequenced and confirmed a scar-less gene-editing strategy (data not shown).

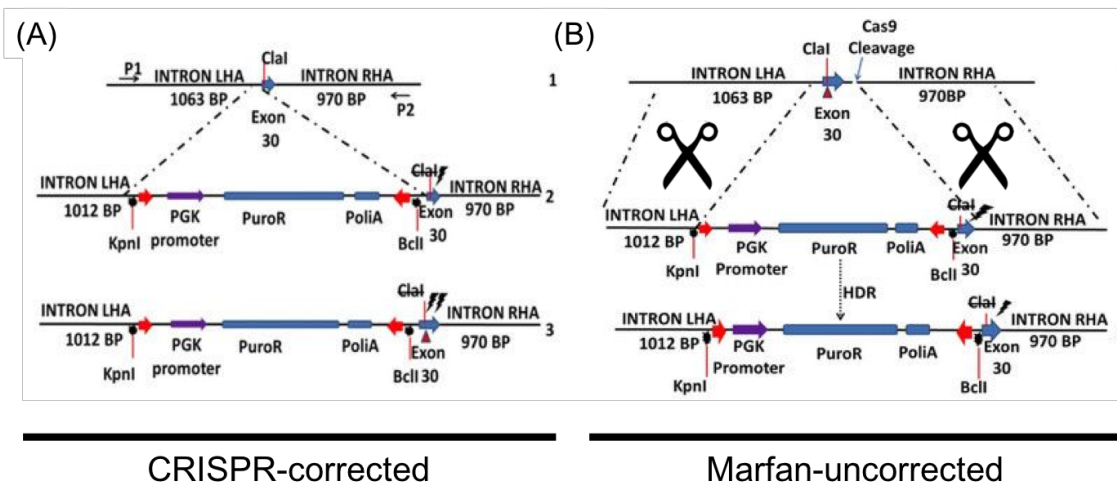


**Figure 1.12 Correction strategy for *FBN1* mutation C1242Y using CRISPR/Cas9 technology.**

(A1) *FBN1* exon 30 wild-type genomic location (MF C1242Y mutation is shown as a red triangle). (A2-3) Primers (red arrows) were used to PCR out 1,063 bp upstream and 970 bp downstream of exon 30 from wild type genomic DNA. Two restriction sites were created into the intron sequence upstream of exon 30 (KpnI and BclI) and the construct *piggyBac* transposon with the selectable marker puroR was inserted to generate the final donor plasmid. Clal restriction site in exon 30 was removed by direct-mutagenesis to generate a silent point mutation in the donor plasmid to facilitate posterior screening. (B1) *FBN1* exon 30 following Cas9 cleavage (scissors). (B2) Final donor plasmid with intronic homology arms surrounding *FBN1* exon 30 (LHA and RHA) for specific homology direct repair (HDR) with genomic DNA. (B3) Insertion of the donor plasmid following homologous recombination after cas9 genomic DNA cutting. Figure generated by Dr Felipe Serrano.

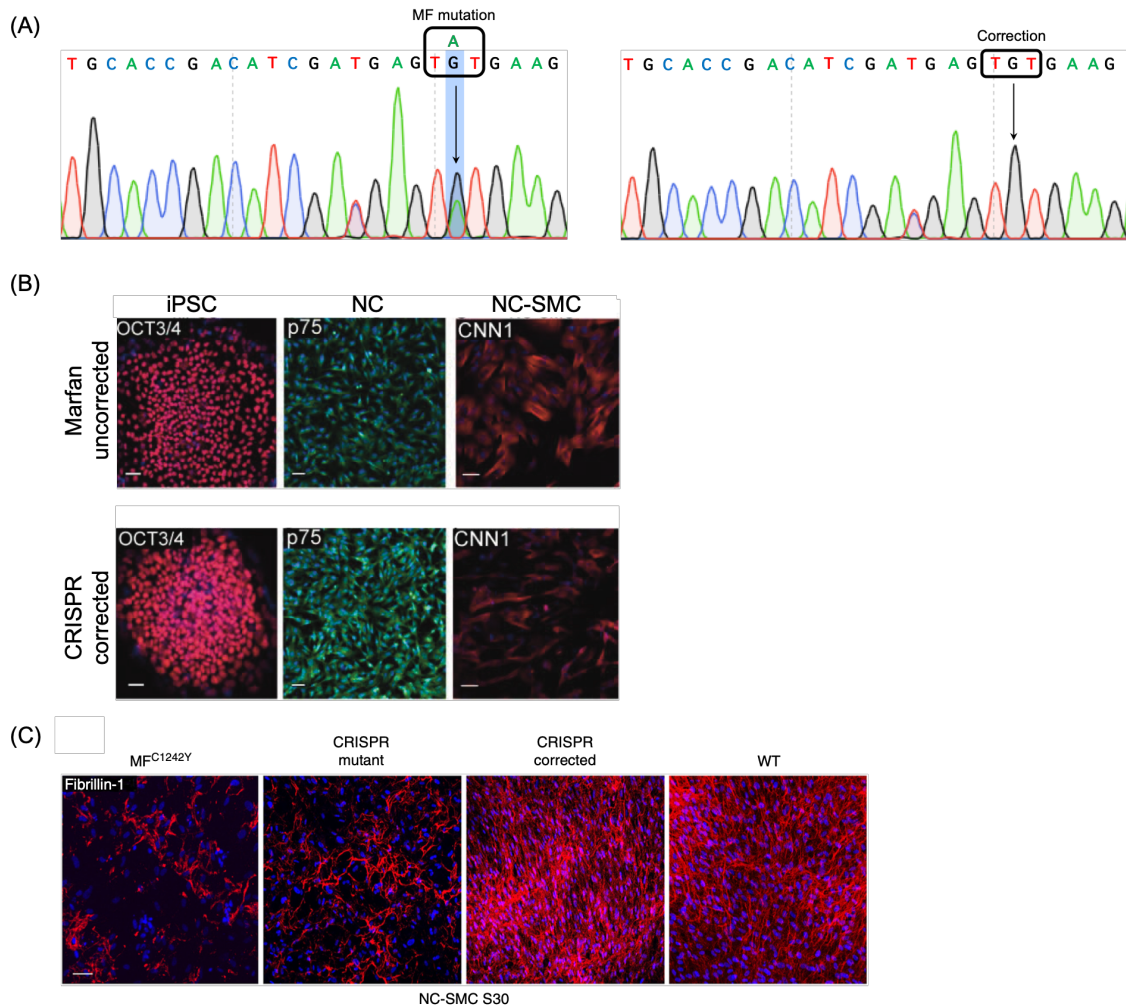


**Figure 1.13 Characterisation of SMC differentiation of CRISPR-edited Marfan iPSCs.**

(A) Partial sequences of *FBNI* exon 30 for MF CRISPR/cas9 mutant allele (Marfan-uncorrected, left panel) and MF CRISPR/cas9 corrected allele (CRISPR-corrected right panel). (B) Characterisation of Marfan-uncorrected (top panel) and CRISPR-corrected (bottom panel) by immunostaining for hiPSC pluripotency (OCT3/4), NC differentiation (p75) and NC-SMC differentiation (CNN1). Scale bars, 50  $\mu\text{m}$  (C) Immunostaining for fibrillin-1 in S30 NC-SMCs derived from MF<sup>C1242Y</sup> human iPSCs, Marfan-uncorrected (CRISPR mutant), CRISPR-corrected and WT NC-SMCs. Scale bars, 100  $\mu\text{m}$ .

## 1.13 Potential of MFS disease model to develop novel therapeutic strategies

### 1.13.1 AON-mediated exon-skipping to target and correct genetic diseases

As previously described, we possess various MFS cell lines that harbour different mutations in the *FBN1* transcript. One example is MF<sup>C1242Y</sup>, which displays a point mutation in exon 30 whereby a cysteine is replaced by a tyrosine in amino acid position 1242. Removing the mutation-containing exon 30 may offer therapeutic potential, whereby a shorter but mutation-free fibrillin-1 protein is synthesised, and proper function is restored. We hypothesise that modulating the splicing machinery in order to omit exon 30 in *FBN1* mRNA transcript will enable the restoration of a functional fibrillin-1 protein. Previous work employed a similar study to restore dystrophin expression levels in patients with Duchenne's, a muscular dystrophy disease<sup>103</sup>. Furthermore, Drisapersen, an anti-sense oligonucleotide exon-skipping drug that allows synthesis of a partially functional dystrophin in DMD patients, showed an encouraging outcome in a small patient study of 12 individuals<sup>104</sup>. More recently, Eric Olson's group performed CRISPR/Cas9 gene-editing to correct a mutational hotspot for DMD in canines and dystrophin levels were restored up to 92% of normal<sup>105</sup>.

In this report, we develop a strategy to selectively remove exon 30 in the *FBN1* pre-mRNA transcript using antisense oligonucleotide nucleotide (AON)-mediated exon skipping, an approach pioneered by our collaborator, Dr Aartma-Rus<sup>106</sup>. AONs have the ability to hybridise to a region of the pre-mRNA and hide the targeted exon from splicing modulation. Effectively, the exon of interest is skipped, and the open reading frame is maintained. Fibrillin-1 assembly results in the formation of stable microfibrils and previous work has shown that fibrillin-1 molecules are not required to be in perfect register for the microfibril network to be functional<sup>107</sup>. As a result, we hypothesise that the amended translation leads to a shorter but presupposed functional fibrillin-1 protein.

### 1.13.2 Complementary unbiased strategies to identify novel disease-causing pathways

Due to species differences, animal models cannot adequately represent human pathophysiology. The lack of robust and physiologically relevant cell-based assays represents a major hurdle for drug discovery in the context of cardiovascular disease. Therefore, there is an urgent need for *in vitro* systems capable of recapitulating complex diseases, which can provide preclinical models for drug screening. Novel protocols have achieved efficient differentiation of human iPSCs for a variety of complex disease for high-throughput applications, such as muscular dystrophy<sup>108</sup>, cardiac hypertrophy<sup>109,110</sup> and restenosis, a recurring event after vascular corrective surgery<sup>111</sup>. Here, the phenotypic assays enable the profiling of compound sets, which offers the potential to dissect out disease-causing pathways and identifying next-generation therapeutics. Our *in vitro* MFS disease model faithfully mimics the complexities of the disease observed in patients and offers a resourceful platform for drug testing.

Here, we suggest developing a medium-throughput drug screening assay based on correcting elevated MMP activity, a phenotypic feature displayed by patients and recapitulated in MFS murine models as well as our *in vitro* MFS disease platform. As a complementary technique to identify disease-causing pathways driving MFS pathogenesis, we have adopted RNA-sequencing technology to highlight the transcriptomic differences between healthy and MFS SMCs. Here, we propose to identify novel gene signatures for MFS and overlap the differentially expressed transcriptomic datasets to the putative hits capable of reversing MFS disease features in our phenotypic drug screen.

## 1.14 Hypothesis and Objectives of This Thesis

### 1.14.1 Hypothesis

I hypothesise that interfering with MFS pathogenesis either directly at the level of the *FBNI* transcript or by identifying and targeting novel disease-causing pathways downstream of fibrillin-1 offer promising and complementary approaches to reverse the disease phenotype in our *in vitro* human iPSC-derived model of MFS.

### 1.14.2 Current Challenges and Objectives

The availability of multiple MFS mouse models has greatly improved our knowledge of the disease. However, there remains a need for a complimentary human *in vitro* disease model to further understand the pathological mechanisms that can be used for drug screening. This work is based on the development of a human *in vitro* induced pluripotent stem cell (iPSC) disease model, which recapitulates most of the pathological characteristic featured in MFS patients. Despite convincing mouse model data, the development of effective drugs, such as losartan, have failed in clinical settings. Here, I will explore two alternative potential therapeutic approaches to reduce or reverse the panel of disease elements displayed by our *in vitro* human iPSC MFS model.

1. Firstly, I will attempt to remove the mutation-containing exon using an antisense-oligonucleotide-based technology. I hypothesise that modulating the splicing machinery in order to omit exon 30 in the final translated protein will restore a shorter but more functional fibrillin-1 protein in SMC.
2. Secondly, I will design a phenotypic assay based on matrix-degradation properties using our human iPSC model. A low- to medium-throughput drug screen will be further developed for high-throughput screening conditions in order to identify putative hits. These potential therapeutic compounds will be further tested in-house using a panel of phenotypic assays that characterise our MFS disease model.

# 2 MATERIALS AND METHODS

## 2.1 Cell Culture

### 2.1.1 Patient human iPSC Derivation and Culture Conditions

MF<sup>C1242Y</sup> fibroblasts were purchased from Coriell cell bank (GM21943). Fibroblasts were cultured in DMEM (Sigma) with 10% FBS (Sigma), 50 U ml<sup>-1</sup> penicillin (P) and 50 U ml<sup>-1</sup> streptomycin (S). To generate hiPSC, MF fibroblasts harbouring FBN1 mutations were transfected using a commercially available mono-cistronic iPSC reprogramming kit (Vectalys), consisting of four vectors encoding: OCT4, SOX2, KLF4, v-MYC; retroviral transduction was performed on 100 000 cells per on well of 6-well plate in mitotically inactive mouse embryonic fibroblasts (MEF) media without P/S per patient line. Five days post-transduction, the cells were resuspended in trypsin, and 1X10<sup>5</sup> cells were seeded onto 10-cm dishes pre-plated with irradiated MEF feeders (CF-1 MEF IRR). Colonies appeared between day 12 and 32 after transfection. Colonies with hESC-like morphology were manually picked and transferred to 12-well plates pre-plated with inactivated MEF feeders containing 10 µM p160ROCK (Rho-Associated coiled-coil containing Protein Kinase 1) inhibitor (Y-27632, Tocris). Two independent colonies were picked and expanded from the MF line. All hiPSC were maintained on irradiated mouse feeders in typical DMEM/F12 medium, supplemented with 20% Knockout Serum Replacement (Gibco), 2 mM L-glutamine, 0.1 mM non-essential amino acids, 0.1 mM β-mercaptoethanol, and 4 ng/ml FGF-2 (R&D Systems). Medium was changed every day. Cells were routinely passaged using 1 mg/ml type IV collagenase (Invitrogen). Human WT hiPSC were obtained from the Cambridge Biomedical Research Centre iPS Core Facility. Marfan patient specific hiPS and control hiPS cells are referred to MF hiPSC and WT hiPSC respectively. Media used to maintain hPSCs are detailed in Table 2.1.

Medium	Components	Concentration	Supplier
CDM BSA	IMDM:F12 (1:1)	-	ThermoFisher Scientific
	Chemically defined concentrated lipids	1%	ThermoFisher Scientific
	1-thioglycerol	450nM	Sigma-Aldric
	Insulin	7 $\mu$ g/mL	Roche
	Transferin	15 $\mu$ g/mL	Roche
	Penicillin/Streptomycin	1%	ThermoFisher Scientific
	Bovine Serum Albumin (BSA)	5mg/mL	Europa Bio Product
	Polyvinal Alcohol	1mg/mL	Sigma Aldrich
E8 Medium	IMDM:F12 (1:1)	-	ThermoFisher Scientific
	Insulin-Transfferin-Selenium	2%	ThermoFisher Scientific
	Sodium Bicarbonate	0.05%	ThermoFisher Scientific
	L-Ascrobic acid 2-Phosphate	1%	Sigma-Aldrich
KSR Medium	Advanced DMEM/F12	400mL	ThermoFisher Scientific
	Knockout Serum Replacer (KSR)	100mL (20%)	ThermoFisher Scientific
	L-Glutamine	1%	ThermoFisher Scientific
	$\beta$ -mercaptoethanol	100 $\mu$ M	Sigma Aldrich

**Development of novel therapies for Marfan Syndrome using a human iPSC-derived disease model**

	Penicillin-Streptomycin	1%	ThermoFisher Scientific
MEF Medium	Advanced DMEM/F12	-	ThermoFisher Scientific
	Foetal Bovine Serum (FBS)	10%	Biosera
	L-Glutamine	1%	ThermoFisher Scientific
	$\beta$ -mercaptoethanol	100 $\mu$ M	Sigma Aldrich
	Penicillin-Streptomycin	1%	ThermoFisher Scientific
Gelatine	Embryo transfer water	-	ThermoFisher Scientific
	Gelatine from porcine skin	0.1%	Sigma Aldrich
Collagenase	Advanced DMEM/F12	-	ThermoFisher Scientific
	Knockout Serum Replacer (KSR)	20%	ThermoFisher Scientific
	L-Glutamine	1%	ThermoFisher Scientific
	Collagenase IV	1mg/mL	ThermoFisher Scientific

**Table 2.1 Composition of Media Used for Maintaining human iPSCs**

## 2.1.2 Humans iPSC Differentiation Protocols

### 2.1.2.1 Neural crest differentiation

Differentiation assays were performed as previously described<sup>95</sup>. For differentiation into embryonic lineages, hiPSC were cultured in chemically defined medium (CDM) with 10 ng/mL Activin A (R&D Systems) and 12 ng/mL FGF-2 (R&D Systems) on 0.1% gelatine-coated plates as described previously<sup>92</sup>. CDM-BSA comprised Iscove's modified Dulbecco's medium (Gibco) plus Ham's F12 NUT-MIX (Gibco) medium in a 1:1 ratio, supplemented with Glutamax-1, chemically defined lipid concentrate (Life Technologies), transferrin (15 µg/ml, Roche Diagnostics), insulin (7 µg/ml, Roche Diagnostics) and monothioglycerol (450 µM, Sigma). hiPSC were induced to differentiate into neural crest progenitors.

### 2.1.2.2 NC-SMC lineage differentiation

The neural crest (NC) population was derived using fibroblast growth factor (FGF-2, 12 ng/ml) and the activin/nodal inhibitor SB431542 (10 µM) and passaged first at day 4 and then repeatedly in FGF-2 and SB431542 (unpublished work). After obtaining the intermediate population, cells were trypsinised and cultured in SMC differentiation medium CDM-PVA containing PDGF-BB (10 ng/ml, Peprotech) and TGF-β1 (2 ng/ml, Peprotech) for 12 days (PT). For long-term cultures, SMCs were grown in DMEM/F12 medium (Sigma M5650) containing 10% foetal bovine serum (Sigma F7524) up to 10 passages. The intermediate population was tested for the expression of specific genes (p75) by RT-PCR and immunostaining.

## 2.2 AON-Mediated Exon-Skipping

### 2.2.1 AON Design

The antisense oligonucleotides (AON) sequences used in this study were designed according to the guidelines published in “Overview on AON Design” by Annemieke Aartsma-Rus (2012). Briefly, the secondary structure of the target exon, exon 30 of the human FBN1 gene, was predicted using m-fold software (<http://unafold.rna.abl.vanderbilt.edu/?q=mfold>), including 50 nucleotides upstream and downstream. The most energetically stable structure was chosen to select regions qualified as partially closed and partially accessible to AON binding. In parallel, exon 30 was analysed using the human splicing finder software (<http://www.umd.be/HSF3/>) to identify the presence of exonic splicing enhancer (ESE) sites. 20 nucleotide-long regions combining data from both the above software were selected (TABLE). Additional criteria such as optimal GC percentage and a melting temperature ( $T_m$ ) higher than 48°C were used to increase the likelihood of AON effectiveness. The reverse complements of the target sequences were generated to obtain the AON sequences. Next, the free energy of the AON and AON-AON complexes were calculated using the RNA structure software (<http://rna.urmc.rochester.edu/>). The energy should be greater than -4 and greater than -15 free energy units for AON and AON-AON complexes respectively. Finally, the binding energy of each AON to its target sequence was calculated and fell optimally between 21 and 28 free energy units. AON sequences were blasted against the human genome to confer their uniqueness.

### 2.2.2 AON Transfection

#### 2.2.2.1 AON solution preparation

The AONs were chemically modified to 2'-O-methyl RNA phosphorothioate (2'OMePS) and obtained from TriLink. The 2'OMe modification increases stability and improve target sequence affinity and the phosphorothioate (PS) modification improves

stability and enhances uptake over the cell membrane. All AONs were resuspended in H<sub>2</sub>O to achieve a stock concentration of 1 mM and subsequently diluted to a working concentration of 100  $\mu$ M. AON sequences are listed in Table 2.2.

<b>AON ID</b>	<b>Backbone</b>	<b>Purification</b>	<b>Supplier</b>	<b>Sequence (5'-3')</b>
AON1	PO 2'OMe RNA	AX-HPLC	Trilink	CAC UGA CCA CCA UCA CAG AU
AON3	PO 2'OMe RNA	AX-HPLC	Trilink	CAG AUG CCA UGA AUC CAU CA
AON4	PO 2'OMe RNA	AX-HPLC	Trilink	GUC UUC AUG UCU UCA GAU GC
Scr AON	PO 2'OMe RNA	AX-HPLC	Trilink	CUG ACA CUA AUC CAG CCA AC

**Table 2.2 AONs Used Throughout This Study**

#### 2.2.2.2 AON lipofection

MF<sup>C1242Y</sup> and wildtype (WT) SMCs previously cultured in serum for 1 month were plated at  $2 \times 10^4$  cells/well in 12-well plates 24 hours prior transfection. Cells at 80% confluence were transfected with 2'OMePS AONs (100 nmol/L Scrambled AON coupled to GFP, 250 nmol/L AON-1 and 50 nmol/L AON-3) in Opti-MEM (Gibco) using the transfection agent Lipofectamine 2000 (1  $\mu$ L per transfection) (Thermo Fisher Scientific). After 24 hours incubation, the transfection medium was replaced by fresh culture medium for another 24 hours before collection.

## 2.3 CRISPR/Cas9-mediated Exon 30 Skipping

The CRISPR/cas9 targeting experiments were designed with the help of Dr Felipe Serrano.

### 2.3.1 Construction and Cloning Strategy of CRISPR guide RNA/Cas9 plasmid

The cas9 and single guide RNA (sgRNA) plasmid pspCas9(BB)-2A-Puro (PX459) was obtained from Addgene (plasmid 48141). The sgRNAs targeting the exon 30 of FBN1 gene were designed according to the rule of 5'-GN<sub>20</sub>NGG-3'. One sgRNA (CR7) annealed to an intronic sequence 17 bp upstream of exon 30 and the other (CR2) annealed to an intronic sequence 183 bp downstream of exon 30. Upstream CR7: ccaatatcaacaacctgtggtt. Downstream CR2: ctctgtcagatatgttatgagg

### 2.3.2 Exon 30 Targeting in MF<sup>C1242Y</sup> human iPSC using CRISPR/Cas9

For exon targeting, 1X10<sup>6</sup> MF hiPSCs were electroporated with 2 µg of C2 and 1.3 µg of C7 sgRNA plasmid (Addgene) in 82 µl P3 media (Lonza) + 18 µL supplement 1 (Lonza) using 4D-nucleofector system (Amaxa). Transfected cells were plated onto DR4 irradiated feeders (Jackson Laboratory) and cultured in KSR supplemented with FGF-2 (4 ng/ml) and Y-27632 (10µM). 48 hours post-transfection, puromycin selection (1 µg/ml) was applied and the surviving colonies were picked and expanded for PCR screening verification. Forward primer: accaaggataaccaatgggct; reverse primer: ttcacctctaaaagttcgacttgggtatt

## 2.4 RNA extraction, RT cDNA synthesis and Quantitative PCR Analysis

### 2.4.1 RNA Extraction and Reverse Transcriptase cDNA Synthesis

Total RNA was extracted using the RNeasy Mini Kit (Qiagen) according to the manufacturer's protocol. Concentration and purity of total RNA was assessed using the Nanodrop-8000 spectrophotometer (Thermo Fisher Scientific) before storage at -80°C. First-stranded cDNA synthesis was performed from 200ng of total RNA extracted using Superscript® III Reverse Transcriptase kit (Thermo Fisher Scientific) with oligo(dT) primers according to the manufacturer's instructions. First-stranded cDNA synthesis was also performed from 200ng of total RNA extracted using Maxima First Strand cDNA synthesis kit (enzyme to buffer, 1:2) with random hexamers (RH) (Fermentas). All samples were stored at -20°C. Reverse transcription reactions were performed as follows (Tables 2.2-2.6):

<b>Component</b>	<b>Master Mix per 10uL Reaction</b>
Maxima Enzyme Mix	1µL
Reaction Mix, 5X	2µL
RNA	200ng minimum
Nuclease Free H <sub>2</sub> O	To 10µL

**Table 2.3 mRNA cDNA Synthesis Maxima Master Mix Composition**

First Step Components	Master Mix per 10uL Reaction
Forward Primer, 10 $\mu$ M	1 $\mu$ L
Reverse Primer, 10 $\mu$ M	1 $\mu$ L
RNA	200ng minimum
Nuclease Free H <sub>2</sub> O	To 10 $\mu$ L
Second Step Components	Master Mix per 10uL Reaction
RT Buffer, 10X	2 $\mu$ L
MgCl <sub>2</sub> , 25mM	4 $\mu$ L
DTT, 0.1M	2 $\mu$ L
RNaseOUT™	1 $\mu$ L
SuperScript™ III RT	1 $\mu$ L

**Table 2.4 mRNA cDNA Synthesis SuperScript III Master Mix Composition**

Temperature	Time
25°C	10 minutes
50°C	15 minutes
85°C	5 minutes
4°C	$\infty$

**Table 2.5 mRNA cDNA Synthesis Thermocycling Conditions for Maxima Kit**

Temperature	Time	Components
65°C	5 minutes	RNA + Primers +dNTPs
4°C	1 minute	RNA + Primers +dNTPs
25°C	10 minutes	Add cDNA Synthesis Mix
50°C	50 minutes	
85°C	5 minutes	
4°C	$\infty$	

**Table 2.6 mRNA cDNA Synthesis Thermocycling Conditions for SuperScript III Kit****2.4.2 Polymerase Chain Reaction and Agarose Gel Run**

To validate the exon skipping strategy, cDNA samples generated by oligo(dT)s were amplified by polymerase chain reaction (PCR) using the FastStart DNA Taq Polymerase kit (Roche). cDNA amplification was performed according to the reactions detailed in Table 2.7 Primers were designed using the DNASTAR software available at <http://www.dnastar.com>. The specificity of the primer pairs to PCR template sequences was checked against the NCBI database using the Primer-BLAST software (<http://www.ncbi.nlm.nih.gov/tools/primer-blast>). Primer sequences were as follows: FBN1Exon30 forward, 5'-atcagctgtccccaacac-3' and FBN1Exon30 reverse, 5'gcccatatcacagtggcaga-3'. The wildtype and skipped transcripts were amplified as 500 bp and 377 bp respectively. Samples were loaded onto a 1.1% agarose gel and fragments were separated by electrophoresis at 100V for 40 min. A 100 bp DNA ladder (Thermo Fisher Scientific) was used to analyse fragment sizes.

<b>Components</b>	<b>Master Mix per 25uL Reaction</b>
Buffer, 10X	2.5µL
MgCl <sub>2</sub> , 25mM	1µL
dNTPs	0.25µL
Forward Primer, 10µM	1µL
Reverse Primer, 10µM	1µL
Nuclease Free H <sub>2</sub> O	15µL
cDNA	4µL

**Table 2.7 cDNA Amplification FastStart Master Mix Composition**

### 2.4.3 Quantitative RT PCR Analysis

To measure the level of gene expression, cDNAs generated by random hexamers (1:30 dilution in nuclease-free water) were subjected to quantitative real-time PCR (qRT PCR) amplification using SYBR Green PCR Master Mix (Applied Biosystem) on a 7500 Fast Real-Time PCR System under the following conditions: Taq polymerase activation and initial denaturation at 95 °C for 5 minutes, followed by 50 cycles for 20 seconds at 95 °C, and 1 minute at 65 °C. The specificity of amplification products was determined from melting curve analysis performed at the end of each run using a cycle at 95 °C for 15 seconds, 65 °C for 15 seconds, and 95 °C for 15 seconds. Relative mRNA levels in each sample were normalised to housekeeping genes, GAPDH and PDGB using  $\Delta$ CT method. qRT-PCR reactions were prepared as follows (Table 2.8 and 2.9) and gene specific primers are detailed in Table 2.10

<b>Component</b>	<b>Per Reaction</b>
Fast SYBR Green Master Mix, 2X	7.50 $\mu$ L
Forward Primer, 10 $\mu$ M	0.15 $\mu$ L
Reverse Primer, 10 $\mu$ M	0.15 $\mu$ L
cDNA Template, 1:30	3 $\mu$ L
Nuclease Free H <sub>2</sub> O	4.20 $\mu$ L

**Table 2.8 mRNA qRT-PCR Master Mix Composition**

<b>Temperature</b>	<b>Time</b>	<b>Number of Cycles</b>
95°C	5 minutes	1
95°C	20 seconds	50
65°C	1 minute	

**Table 2.9 mRNA qRT-PCR Thermocycling Conditions**

<b>Gene</b>	<b>Direction</b>	<b>Sequence (5'-3')</b>
AKT1	Forward	TACGAGAAGAAGCTCAGCCC
	Reverse	GTCAGGTGGTGTGATGGTGAT
AKT2	Forward	GCCTCTTCGAGCTCATCCTC
	Reverse	TCCTTCTTAAGCAGCCCAGC
AKT3	Forward	TAATGGGGGCGAGCTGTTTT
	Reverse	ACCATAGAAACGTGTGCGGT
ACTA2	Forward	CACTGTCAGGAATCCTGTGA
	Reverse	CAAAGCCGGCCTTACAGA
CNN1	Forward	GTCCACCCTCCTGGCTTT
	Reverse	AAACTTGTTGGTGCCCATCT
FBN1	Forward	GGTGAATGTACAAACACAGTCAGCA
	Reverse	ATAGGAACAGAGCACAGCTTGTTGA
KLF4	Forward	CACCTGGCGATCTGACAT
	Reverse	GTCGCTTCATGTGGGAGAG
GAPDH	Forward	AACAGCCTCAAGATCATCAGC
	Reverse	GGATGATGTTCTGGAGAGCC
GSK3 $\alpha$	Forward	ACACCAACCCGGGAACAAAT
	Reverse	CCTCTAGTGGGGAGAGCCTT
GSK3 $\beta$	Forward	CGAGACACACCTGCACTCTT
	Reverse	TTAGCATCTGACGCTGCTGT
MMP1	Forward	CTGGCCACAACCTGCCAAATG
	Reverse	CTGTCCCTGAACAGCCCAGTACTTA
MMP2	Forward	TTCCTGACATTGACCTTGGC
	Reverse	CAAGGTGCTGGCTGAGTAGATC
MMP9	Forward	GCTTTTCTTCTTCTCTGGGCGCC

**Development of novel therapies for Marfan Syndrome using a human iPSC-derived disease model**

	Reverse	CGGTCCTGGCAGAAATAGGCTTT
MMP10	Forward	ACTCTTTTGATGGCCCAGGA
	Reverse	GAGTGGCCAAGTTCATGAGC
PBGD	Forward	GGAGCCATGTCTGGTAACGG
	Reverse	CCACGCGAATCACTCTCATCT
PLC $\beta$ 1	Forward	AGGCTAGAAGAAGCGCAAA
	Reverse	CAGAGGGATCCTCATGGCAA
TGF $\beta$	Forward	TCCTGCTTCTCATGGCCA
	Reverse	CCTCAGCTGCACTTGTAG

**Table 2.10 List of Primer Sequences used for qRT-PCR**

## 2.5 Western Blotting Analysis

Samples were lysed in ice-cold RIPA buffer (10 mM Tris-Cl (pH 8.0), 1 mM EDTA, 0.5 mM EGTA, 1% Triton X-100, 0.1% sodium deoxycholate, 0.1% SDS, 140 mM NaCl) with added protease and phosphatase inhibitors (Life Technologies). Protein concentration was determined by Bicinchoninic Acid (BCA) protein assay (Pierce). 30  $\mu$ g of whole-cell lysate was resolved by 10-12% Tris-HCl precast sodium dodecyl sulphate (SDS)-polyacrylamide gel (Bio-Rad), then transferred to polyvinylidene difluoride membranes (PVDF; Merck Millipore). After blocking with 5% milk in Tris-buffered saline and 0.05% TWEEN 20 (TBS-T, Sigma) for 1 h at room temperature, membranes were probed with specific primary antibody overnight at 4°C followed by horseradish peroxidase-conjugated secondary antibodies for 1h at RT (1:2000; Cell Signaling Technology). Immunoblotted proteins were visualized by enhanced chemiluminescence (Amersham Biosciences). To assess for the total amount of the endogenous proteins and to control for equal loading and transfer of the samples, the membranes were reprobbed with anti- $\beta$ -actin (Sigma Aldrich) antibody or GAPDH (Sigma Aldrich). Densitometry analysis of electrophoretic bands was performed using the ImageJ software program (National Institutes of Health). The density of the bands was normalized to the loading controls ( $\beta$ -actin) and presented as percentage increase. The results are the mean  $\pm$  SD of three independent experiments. Buffers and antibodies used for Western Blotting are detailed in Table 2.11 and 2.12 respectively.

**Development of novel therapies for Marfan Syndrome using a human iPSC-derived disease model**

<b>Buffer</b>	<b>Component</b>	<b>Supplier (Cat#)</b>	<b>Concentration</b>
RIPA	NaCl	VWR (27810)	150mM
	NP-40	Sigma (I3021)	1%
	SodiumDeoxycholate	Sigma (D6750)	0.5%
	SDS	Sigma (L4390)	0.1%
	Tris, pH 8.0	Sigma (T6066)	50mM
Towins	Tris	Sigma (T6066)	25mM
ElectroTransfer	Glycine	Biorad (1610781)	192mM
Buffer	Methanol	Sigma (32213)	20%
TBS-t	Tris	Sigma (T6066)	20mM
	NaCl	VWR (27810)	150mM
	Tween-20	Sigma(P7949)	0.1%
	pH	-	7.6

**Table 2.11 Buffers Used for Western Blotting**

<b>Target</b>	<b>Manufacturer</b>	<b>Species</b>	<b>Dilution</b>
AKT	Cell Signalling Technologies	Rabbit	1:1000
Phospho-AKT	Cell Signalling Technologies	Rabbit	1:1000
GSK3 $\beta$	Cell Signalling Technologies	Rabbit	1:1000
Phospho-GSK3 $\beta$	Cell Signalling Technologies	Rabbit	1:1000
$\beta$ -catenin	R&D Systems	Goat	1:1000
Phospho- $\beta$ -catenin (Ser33/37/Thr41)	Cell Signalling Technologies	Rabbit	1:1000
U2AF65	Sigma Aldrich	Mouse	1:1000
GAPDH	Sigma Aldrich	Rabbit	1:10,000
$\beta$ -actin	Sigma Aldrich	Mouse	1:20,000

**Table 2.12 List of Antibodies Used for Western Blotting**

## 2.6 Cell Fractionation

Media was removed, and cells were washed once with PBS. Samples were incubated with TripleE for 10 min at 37°C and collected to be transferred into a falcon tube containing 4°C 1%BSA in PBS. Samples were then centrifuged at 1200rpm for 3 min at 4°C and supernatant is discarded. Samples were immediately placed on ice to initiate the lysis of the cytoplasmic compartment. Based on the pellet size, 6x the packed cell volume of Isotonic Lysis Buffer was added to the pellet, resuspended gently and incubated for 12 min on ice to allow the cells to swell. 0.3% Triton-X100 in H<sub>2</sub>O is added to the samples and incubated on ice for 3 min. Following centrifugation at 18000 rpm for 5 min at 4°C, the supernatant collected is termed the cytoplasmic fraction and is removed into a clean tube and stored at -20°C. The remaining nuclear pellet is washed in a volume 10x the packed cell volume with Isotonic Lysis Buffer without Triton X-100 and centrifuged at 4128 rpm at 4°C for 3 min. The supernatant is discarded, and the remaining nuclear pellet is resuspended in 2x packed cell volume of Nuclear Lysis Buffer. This volume is transferred to Eppendorf tubes and pestles (KIMBLE Sigma Aldrich, Z359947-100EA) are used for homogenisation. Samples are incubated for 30 min on ice to lyse the nuclear membrane. Benzose nucleases (Sigma Aldrich, E1014) are added at 125 units per mL of lysate to digest the nucleic acids and left to incubate at RT for 45 min. The final lysate is the nuclear fraction. Both cytoplasmic and nuclear fractions are quantified for protein concentration and processes according to the western blotting protocol above. Protease and phosphatase inhibitors (Halt™ Protease Inhibitor Cocktail (100X), ThermoFisher Scientific 87786) are diluted fresh into the buffers used for fractionation and the recipes are detailed in the table below (Table 2.13).

<b>Buffer</b>	<b>Component</b>	<b>Concentration</b>
Isotonic Lysis Buffer	Tris-HCl pH 7.5, 1M	10mM
	CaCl <sub>2</sub> , 1M	3mM
	MgCl <sub>2</sub> , 1M	2mM
	Sucrose	2mM
	H <sub>2</sub> O	Make up to 50mL
Nuclear Lysis Buffer	Tris-HCl pH 7.5, 1M	50mM
	NaCl, 5M	100mM
	KCl <sub>2</sub> , 2.5M	50mM
	MgCl <sub>2</sub> , 1M	2mM
	EDTA, 0.5M	1mM
	Glycerol	10%
	Triton-X100	0.3%

**Table 2.13 Buffers used for Cell Fractionation**

## 2.7 Immunocytochemistry

Adherent cells were fixed with 4% paraformaldehyde (PFA, Affymetrix), in PBS for 20 min at 4°C. Fixed cells are then washed with PBS twice and permeabilised with a blocking solution for one hour at RT in 3% BSA (Sigma)/ 0.1% Triton-X100 (Sigma) in PBS. Samples are incubated with primary antibody overnight at 4°C in 3% BSA/0.1% Triton-X100 in PBS. After 24 hours, the samples are washed three times in 0.1% Triton X-100 in PBS and incubated with Alexa Fluor-tagged secondary antibody (1:800, Molecular Probes Invitrogen) in in 3% BSA/0.1 Triton-X100 in PBS for one hour at RT. Samples are then washed three time in 0.1% Triton X-100 in PBS and stained with 4'-6-diamidino-2-phenylindole (DAPI, ThermoFisher Scientific) in PBS for 10 min at RT. Images were acquired using a LSM 700 confocal microscope (Leica) or an EVOS Cell Imaging System (ThermoFisher Scientific). The complete list of antibodies used for immunofluorescence are detailed in Table 2.14.

Name	Manufacturer	Species	Dilution
OCT3/4	Santa Cruz sc-5279	Mouse	1:100
SOX2	R&D AF2018	Goat	1:100
TRA-1-60	Santa Cruz sc-21705	Mouse	1:100
P75	Abcam ab8874	Rabbit	1:500
CNN1 (Calponin 1)	Sigma C-2687	Mouse	1:10,000
SM22 $\alpha$	Abcam	Rabbit	1:1000
SM $\alpha$ A-FITC	Dako M0851	Mouse	1:400

**Table 2.14 List of Antibodies Used for Immunocytochemistry**

## 2.8 Luciferase Activity Assay

$2 \times 10^5$  CRISPR-corrected and Marfan-uncorrected NC-SMCs were plated in 2 ml of media (Advanced DMEMF12 supplemented with 10% FBS with penicillin/streptomycin) per well of a 12-well plate, respectively. Each well was transfected with 1  $\mu$ g of TopFlash-Firefly Luciferase reporter (Addgene) and 20ng of CMV-Renilla Luciferase reporter (Addgene). The DNA mixture was transfected into the cells using 0.3  $\mu$ L of lipofectamine transfection reagent (Invitrogen). Cells were re-fed 24h later and, as a positive control, CRISPR-corrected NC-SMCs were treated with Chiron for 4 additional hours. Media was removed, and cells were washed with PBS for 5 min. Cells were lysed using 250  $\mu$ L of 1x Passive Lysis Buffer (PLB) and gentle rocked for 15 min at RT. The lysate was transferred to a 96-well plate (20  $\mu$ L per well) and treated according to the manufacturer's protocol detailed in the Dual-Luciferase® Reporter Assay Kit (Promega). Briefly, Luciferase Assay Substrate (LARII) was resuspended in Luciferase Assay Buffer II to dispense 100  $\mu$ L per well of the 96-well plate. Firefly Luciferase activity was measured using a GloMax® 96 Microplate Luminometer (Promega). 100  $\mu$ L of Stop & Glo® reagent was dispensed per well and, similarly, Renilla luciferase activity was recorded in relative fluorescent units (RFU).

## 2.9 Phenotypic Assays

### 2.9.1 Cell Proliferation Assay

For BrdU labelling, cells were treated with BrdU (10 $\mu$ M, BD Bioscience) overnight before collection. Cells were fixed with PFA 4% (Affymetrix) and blocked with 3 % BSA/0.5% Triton-X100 in PBS for 20 min at room temperature (RT). Cells were then treated with 1.5M HCl for 30 min at RT and stained with an anti-BrdU antibody (1:50, Becton Dickinson) overnight at 4°C. The following day, the cells were incubated with a secondary Alexa FITC-tagged secondary antibody (1:500, Molecular Probes Invitrogen) and DAPI (10  $\mu$ g/ml, Vector Laboratories) for 1h at RT. The numbers of BrdU-positive cells and total cells were counted in a blinded manner and divided by the total number of cells (DAPI stained nuclei).

### 2.9.2 Apoptosis and Cell Death Assays

#### 2.9.2.1 Annexin V Staining

For AnnexinV staining, 1x10<sup>6</sup> cells/ml were harvested and resuspended in 1X annexin-binding buffer and incubated with 5 $\mu$ L of AnnexinV-488 (Alexa Fluor® 488) or 1  $\mu$ l of Propidium Iodide (Annexin V/Dead Cell Apoptosis Kit; Life technologies) for 15 minutes at RT. Cells were then resuspended in PBS and data collected was measured with a Beckman Coulter Cyan<sub>ADP</sub> cell analyser. Flow cytometric data was further analysed with FlowJo v10.1 software.

#### 2.9.2.2 TUNEL staining

For TUNEL staining, cells were fixed with 4% PFA 4% (Affymetrix), washed twice in PBS for 5 min each time, and blocked with 3 % BSA/0.5% Triton-X100 in PBS for 20 min at room temperature (RT). After permeabilization, cells were treated following the manufacturer's instruction from the DeadEnd<sup>TM</sup> Fluorometric TUNEL System kit (Promega). Cells were washed twice in PBS for 5 min each time and 100 $\mu$ L of

Equilibration Buffer and left to equilibrate for 10 min at RT. 50  $\mu$ L of TdT reaction mix was added to the surface area of each well, taking care to not let anything dry out, and left to incubate for 60 min at 37°C in a humidified chamber; avoiding exposure to light. Cells were immersed in 2X SSC for 15 min and then washed with PBS three times for 5 min each time. Cells were stained using DAPI (10  $\mu$ g/ml, Vector Laboratories) for 10 min at RT and then washed three times for 5 min each time with PBS before imaging following. 5 images were taken for each well of each of the three independent experiments done for each condition. The results are presented as means  $\pm$  SD of three independent experiments.

### 2.9.3 Matrix Degradation Assay

FITC-gelatine (gelatine from pig skin, fluorescein conjugate, Molecular Probes) was dissolved in 5 mL of distilled water (dH<sub>2</sub>O) (1 mg/ml) and stored at 4°C. 200 $\mu$ L of FITC-gelatine was used to coat chambers of a  $\mu$ -slide 8 well (Ibidi) and air dried. The gelatine was rehydrated with dH<sub>2</sub>O for 15 min.  $2 \times 10^3$  cells were seeded per chamber for 48 hours at 37°C in 250 $\mu$ L of DMEM/F12 +10% FBS. Cells were fixed with PFA 4% and stained using the relevant immunofluorescence protocol

## 2.10 Cyclic Stretching of MF<sup>C1242Y</sup> NC-SMC

WT and MF<sup>C1242Y</sup> SMC were plated on silicone elastomer-bottomed culture Collagen I, precoated plates and grown for 2 up to 7 days and subjected to cyclic strain with a Cyclic Stress Unit (FX5000 Tension System, Flexcell International Corporation). Cyclic sine wave deformation (60 cycles/min) and 10% elongation were applied for 24h previous to cells harvesting for RNA analysis.

## 2.11 RNA Sequencing

RNA-sequencing (RNA-seq) was carried out on total RNA purified from Marfan-uncorrected and CRISPR-corrected NC-SMCs from time-points PTd12 and serum 2 weeks (n = 2 per group). Total RNA was extracted using the RNeasy Mini Kit (Qiagen) according to the manufacturer's protocol using DNase treatment. Concentration and purity of total RNA was assessed using the Nanodrop-8000 spectrophotometer (Thermo Fisher Scientific) before storage at -80°C. The total RNA underwent a RiboZero depletion (MRZH11124, Illumina) and included ERCC-spike-ins (4456740, Life Technologies). All samples had an RNA integrity score above 9 and were used to generate a cDNA library using a standard direction RNA-sequencing protocol from Bio Scientific (NOVA-5138-08, Newmarket Scientific). All libraries were pooled and sequenced on a HiSeq4000 with paired-end 150bp reads. Sequencing reads were aligned to the homo sapiens reference genome 'hsa' using SeqMonk v11 and Ingenuity Pathway Analysis software. Differentially expressed genes (DEGs) were identified based on a FDR of 10% and a minimum fold change calculated using  $\log_2\left(\frac{[\text{FPKMcondition1} + 1]}{[\text{FPKMcondition2} + 1]}\right) \geq \pm \log_2(1.3)$ , where FPKM is fragments per kilobase of transcript per million mapped reads. Values for genes of interest were extracted from the RNA-seq data for the present study.

## 2.12 Drug Screen

### 2.12.1 Drug-Screen Format and Cell-Density

NC-SMC were seeded into a 24-well format at a density of 20,000 cells per well. SMC were left to attach overnight and treated the next day with a library of compounds from a phenotypically-annotated library (AstraZeneca). Cells were treated for 48h and media was changed with fresh compound for another 48h. On day 4, media was collected to assay for MMP activity.

### 2.12.2 MMP-Activity Detection Assay

MF<sup>C1242Y</sup> SMCs previously cultured in serum for 1 month were plated at  $1 \times 10^4$  cells/well and  $5 \times 10^3$  cell/well in 12-well plates and 24-well plates respectively. Once cells had attached, cells were treated with losartan (1:1000), SB203580 (1:1000 or 1:5000) or DMSO (0.1%) for 7 days. Details of small molecule inhibitors used positive control for drug screen are listed below in Table 2.15. After treatment, the supernatant was collected to measure MMP activity using the SensoLyte® 520 Generic MMP Assay Kit Fluorometric (Anaspec) according to the manufacturer's instructions for protocol B. Samples were incubated with 1mM AMPA for 3 hours at 37°C and then distributed into a 96-well plate (50 µl per well). 50 µl MMP substrate solution (1:100) was added to the samples and reagents were incubated for 60 min at RT. 50 µl of stop solution was added to end the reaction. Fluorescence intensity was measured at Ex/Em = 490nm/520nm. A substrate control containing buffer was included.

Name	Specificity	Supplier	Working concentration
Losartan	Block ATR1	TOCRIS	1µM
SB203580	P38 MAPK inhibitor	Cell Signalling Technologies	1µM

**Table 2.15 List of Inhibitors used as Positive Controls for Drug Screen**

## 2.13 Statistics

Statistical analysis between groups was performed using the following parametric statistical techniques: (i) paired two-tail Student's t-test for the comparison of two groups and (ii) a one-way ANOVA test for the comparison of means from more than two conditions using Excel Microsoft Software and Prism Software, respectively. All statistical analysis reported in this thesis uses a one-way ANOVA other than the following experiments, which is performed using a paired two-tail t-test comparison test: (i) fibrillin-1 quantification in figure 1.9, (ii) exon-skipping induced matrix degradation in figure 3.16 and MMP activity measurements in losartan-treated MF<sup>C1242Y</sup> NC-SMCs in (iii) figure 5.3 and (iv) figure 5.4.

P-values inferior to 0.05 were considered statistically significant and individual P-values for experiments are detailed in the respective figure legends. Results are presented as the mean of  $\pm$  SEM of a minimum of three biological replicates unless otherwise stated in the text. All multiple comparisons were adjusted using the Tukey multiple comparison post-hoc test in Prism Software. The Tukey test is a single-step multiple comparison test that compares the means of every condition to the means of every other condition and, therefore, applies simultaneously to the set of all pairwise comparisons.

# 3 REMOVING THE DISEASE- CAUSING MUTATION IN MFS SMC USING AON- MEDIATED EXON-SKIPPING

### 3.1 Objectives of this Chapter

As previously described, disease-causing mutations span the entire *FBNI* transcript, which codes for the extracellular-matrix fibrillin-1. MF<sup>C1242Y</sup> is a patient fibroblast line that harbours a heterozygous point mutation in exon 30, where a tyrosine substitutes a highly-conserved cysteine residue in amino acid position 1242 (Figure 3.1). The cysteine substitution is thought to negatively affect the tertiary folding of the final protein and result in loss of structural integrity of the cbEGF domain and therefore, we hypothesise, loss of microfibril architecture. Calcium-binding mutations are expected to impact the stable rod-like conformation cbEGF domain pair in fibrillin-1, which restricts flexibility and increases proteolytic susceptibility<sup>112</sup> (Figure 3.2).

This chapter aims to determine the therapeutic benefits of removing the mutation-containing exon 30 in fibrillin-1. One of the most advanced mutation-specific genetic approaches is based on the use of antisense oligonucleotides (AON), which induced skipping of a target exon and restore or maintain the reading frame of the protein of interest. Although the list of diseases for this technology is growing, most efforts in this field have focused on the development of exon-skipping based therapeutic strategies for Duchenne Muscular Dystrophy (DMD). In the context of DMD, exon-skipping strategies induce the deletion of a string of consecutive mutation-containing exons, which restores the reading frame of the faulty dystrophin protein and results in a milder form of the disease, Becker's Muscular Dystrophy<sup>113,114</sup>.

Here, the hypothesis suggests that modulating the pre-mRNA splicing machinery in order to omit exon 30 in the transcribed *FBNI* mRNA transcript will enable the restoration of a functional fibrillin-1 protein. In this report, we develop a strategy to selectively remove exon 30 in the *FBNI* pre-mRNA transcript using AON-mediated exon skipping, an approach coined by our collaborator, Dr Aartma-Rus<sup>115</sup>. AONs have the ability to hybridise to a region of the pre-mRNA and hide the targeted exon from splicing modulation. Effectively, the exon of interest is skipped, and the open reading frame is maintained. As a result, the amended translation leads to a shorter but presupposed functional fibrillin-1 protein (Figure 3.3).

## Development of novel therapies for Marfan Syndrome using a human iPSC-derived disease model

(A)

Mutation C1242Y (MFC<sup>1242Y</sup>)

WT: TTGCAGACATCGATGAGTGTGAAGATAATCCCAATATCTGT  
MF: TTGCAGACATCGATGAGTATGAAGATAATCCCAATATCTGT

(B)

Exon 27:

ATATTGATGAGTGTGAGAGAGATCCTCTCCTATGCCGAGGTGGTGTGGCCATAACACAGAG  
GGAAGTTACCGCTGTGAATGCCCGCCTGGCCATCAGCTGTCCCCAACATCTCCGCGTGTATC  
G

Exon 28:

ACATCAATGAATGTGAGCTGAGTGCACACCTGTGCCCAATGGCCGTTGCGTGAACCTCATA  
GGGAAGTATCAGTGTGCCTGCAACCCTGGCTACCATTCAACTCCCGATAGGCTATTTTGTGTT  
G

Exon 29:

ACATTGATGAATGCAGCATAATGAATGGTGGTTGTGAAACCTTCTGCACAACTCTGAAGGC  
AGCTATGAATGTAGCTGTCAGCCGGATTTGCACTAATGCCTGACCAGAGATCATGCACCG

Exon 30:

ACATCGATGAGTGTGAAGATAATCCCAATATCTGTGATGGTGGTCAGTGCACAAATATCCCT  
GGAGAGTACAGGTGCTTGTGTTATGATGGATTATGGCATCTGAAGACATGAAGACTTGTGT  
AG

Exon 31:

ATGTCAATGAGTGTGACCTGAATCCAAATATCTGCCTAAGTGGGACCTGTGAAAACACGAAA  
GGCTCATTTATCTGCCACTGTGATATGGGCTACTCCGGCAAAAAAGGAAAAACTGGCTGTAC  
AG

### Figure 3.1 FBN1 mutation in exon 30 in MFC1242Y patient cell-line

(A) The gene encoding fibrillin-1 (FBN1) is situated on chromosome 15 at 15q15-q21.1. The gene is very large (over 200kb) and is highly fragmented into 65 exons. The gene is transcribed into a 10kb mRNA that encodes a 2871 amino acid protein. Marfan patients MFC<sup>1242Y</sup> harbour a mutation in their exon 30, which is responsible for encoding a cbEGF domain. Here, the point mutation replaces a cysteine (C) residue with a tyrosine (Y) at the amino acid position 1242. The point mutation is highlighted in red on the Marfan allele (MF). Below: The complete exon is described, and the point mutation position is highlighted in red. The total length of exon 30 is 226 nucleotides. The annealing sequences of the forward and reverse primers used to sequence region of interest containing the mutation are highlighted in green.

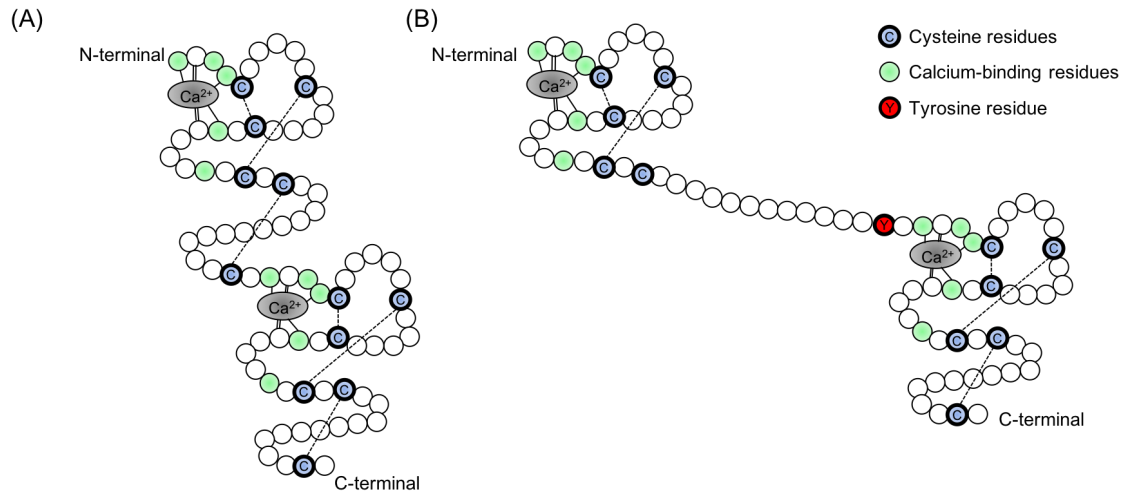


**Figure 3.2 MF<sup>C1242Y</sup> is a disease-causing mutation in a calcium-binding EGF domain**

(A) In wild-type conditions, fibrillin-1 are produced and folded into tertiary structures to allow the proper assembly of microfibrils and binding of calcium ions (shaded in grey). (B) A calcium-binding mutation substitutes a highly conserved cysteine (blue, C) residue with a tyrosine (red, Y) residue in amino acid position 1424. This is predicted to affect the protein-folding and negatively impact deposition and assembly of fibrillin-1 molecules. The calcium-binding residues are indicated in green and the disulphide bonds are labelled as dashed lines. Diagrams adapted from Handford et al, 2000<sup>44</sup>.

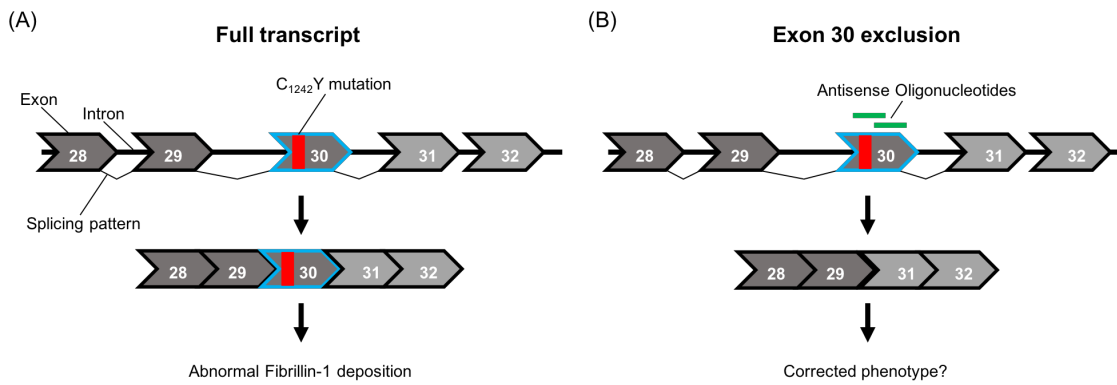


**Figure 3.3 Schematic diagram of antisense oligonucleotide-mediated exon-skipping.**

Schematic diagram of antisense oligonucleotide (AON)-mediated exon skipping of exon 30 in *FBNI*. (A) Marfan *FBNI* pre-mRNA is reassembled by the splicing machinery to yield an mRNA with the mutation-containing exon 30. (B) – AONs anneal to exon 30, causing its removal by the splicing machinery along with the introns. The resulting mRNA product is devoid of exon 30. Exon 30 (lined in blue), mutation C1242Y (red band), antisense oligonucleotides (green lines).

## 3.2 AON-mediated removal of exon 30 in *FBNI*

### 3.2.1 In-silico design of AONs with exon-skipping potential

#### 3.2.1.1 Exon 30 regions containing enhancer motif sites

Antisense oligonucleotides (AON) were designed to target exonic regions of the exon 30 *FBNI*, which contain active splicing sites. Here, the designed AONs were predicted *in silico* to yield a high skipping efficiency by blocking exonic splicing enhancer (ESE) sites. ESE sites are responsible for directing accurate splicing of pre-mRNA to mRNA and are involved with exon recognition. The presence of ESE sites was analysed using the *in-silico* tool Human Splicing Finder (<http://www.umd.be/HSF3/>). This platform studies exon and intronic regions and determines the associated pre-mRNA splicing patterns by calculating the splice-site potential of a particular region. Each splice site is given a consensus value between 1 and 100, where a value closest to 100 predicts a highly-potent ESE sites.

In addition to designing AONs that target ESE sites, it is generally assumed that disrupting the binding of serine arginine-rich (SR) proteins, which are involved in exon recognition or in the prevention of splicing complexes assembly at acceptor splice sites, can affect the splicing machinery recognition capacity. Therefore, SR sites were included in the analysis in the aim of designing AONs capable of executing a high skipping efficiency (<https://doi.org/10.1038/sj.mt.6300095>). Four enhancer motifs within exon 30 were identified according to these criteria and chosen for further analysis (Table 3.1 and Figure 3.4). A series of enhancer motifs (ESE) were identified along multiple nucleotide positions in exon 30. ESEs are responsible for directing the splicing machinery. ESEs were selected based on their association with a SR protein. SR proteins are constituted of a domain with long repeats of serine (S) and arginine (R) amino acid residues and are involved in exon recognition. Four ESEs with a value close to 100 and with non-overlapping sequences were selected for further analysis (green).

**Development of novel therapies for Marfan Syndrome using a human iPSC-derived disease model**

Sequence Position	Linked SR gene	Linked SR protein	ESE sites	Value 0-100
42	SRFS2	SC35	GGTCAGTG	88.01
44	SRSF5	SRp40	TCAGTGC	83.11
56	SRFS2	SC35	TATCCCTG	81.68
58	SRSF5	SRp40	TCCCTGG	84.13
59	SFRS1	SF2/ASF (IgMBRCA1)	CCCTGGA	78.15
64	SFRS1	SF2/ASF	GAGAGTA	73.44
68	SRSF5	SRp40	GTACAGG	83.17
69	SFRS1	SF2/ASF (IgMBRCA1)	TACAGGT	70.54
69	SFRS1	SF2/ASF	TACAGGT	77.23
75	SRSF2	SC35	TGCTTGTG	75.72
91	SRSF2	SC35	GATTCATG	85.06
98	SRSF6	SRp55	GGCATC	74.24
98	SRSF2	SC35	GGCATCTG	78.8
102	SRSF5	SRp40	TCTGAAG	80
103	SRSF1	SF2/ASF (IgMBRCA1)	CTGAAGA	76.85
103	SRSF1	SF2/ASF	CTGAAGA	77.34
108	SRSF1	SF2/ASF	GACATGA	76.12
116	SRSF2	SC35	GACTTGTG	86.11
120	SRSF6	SRp55	TGTGTA	83.78

**Table 3.1 Identification of ESE-rich regions in exon 30 for splicing machinery disruption**

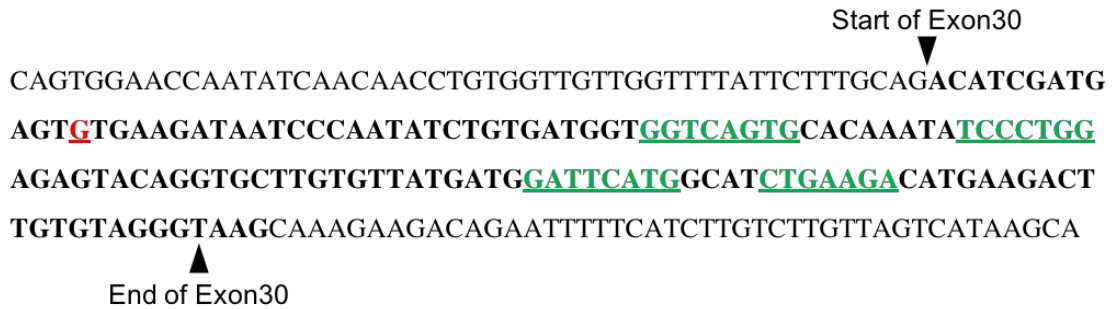


**Figure 3.4 ESE-rich regions in exon 30.**

The ESE motifs selected for further analysis are highlighted in exon 30 (green) as is the mutation (red) and the start and end of exon 30 within the cDNA (arrows).

#### 3.2.1.2 Exon 30 accessibility to AONs

Next, we evaluated the accessibility of the target site to our AONs of interest. Post-transcription, pre-mRNAs form secondary structures by which certain regions are complexed to each other whilst others present relatively more accessible loops where strict nucleotide-nucleotide binding is reduced<sup>106</sup>. Although these structures are dynamic, previous work has shown that effective AONs more often bind open (accessible) structures than closed (entirely closed) regions<sup>116,117</sup>. Energetically most stable RNA secondary structure and folding was evaluated using sequence alignment tools (e.g. using mFold, <http://unafold.rna.albany.edu/?q=mfold/RNA-Folding-Form>). The mFold software also generated an ss-count, which calculates the number of times any given nucleotide is single stranded (unbound) in all energetically likely structures. It is therefore important to select target regions with an ss-count corresponding to structures that are both partially open and partially closed in order to avoid AONs binding without any effect or AONs not binding at all. The mFold software (mFold software version X) generated a gradient of most energetically stable RNA structures and my results confirmed the four AONs bound partially-open regions of the predicted folded RNA (Figure 3.5).

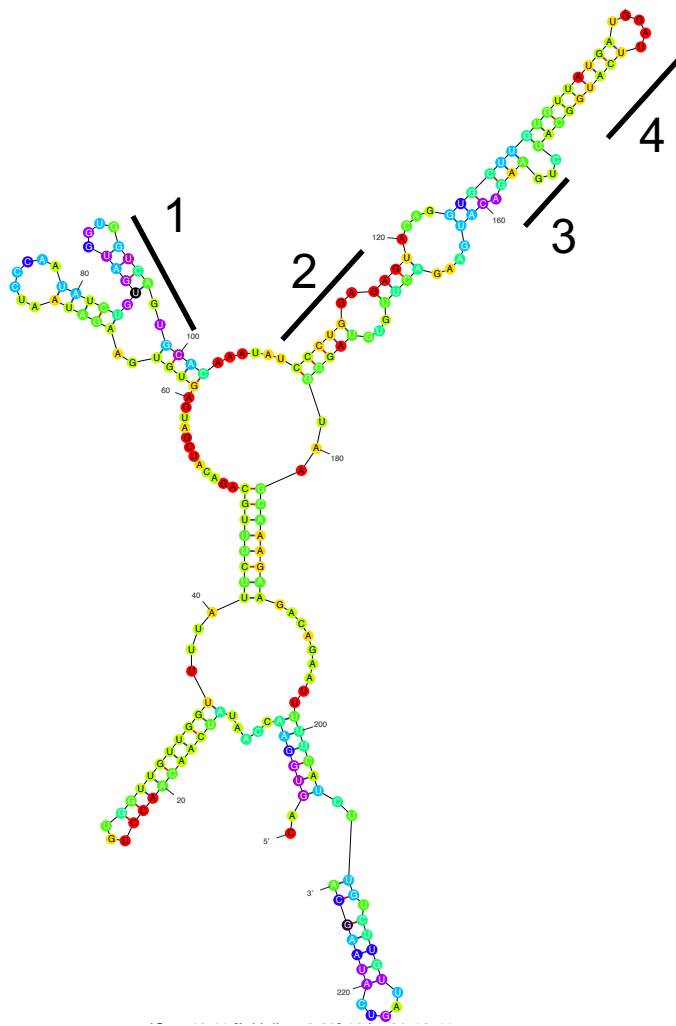


**Figure 3.5 In silico predictions of most effective AONs for exon-skipping based on pre-mRNA folding**

The most energetically stable predicted mRNA structure with binding sequences highlighted 1-4. The selected AONs are predicted to bind regions that are partially open based on an ss-count.

In order to improve the predicted skipping potential of the designed AONs, additional parameters previously established by Aartsma-Rus were included in the final design of the AONs. The parameters included 1) Optimal GC percentage of 40-50%, 2) A T<sub>m</sub> of >48°C measured by BioTools software developed by North Western University (<http://biotools.nubic.northwestern.edu/OligoCalc.html>) and 3) The reverse complement sequence to the binding sequence on the exon was generated to yield the AON sequence (Table 3.2).

Nam e	Binding Sequence on Exon	Reverse Complement (AON sequence)	T <sub>m</sub> (°C)	GC (%)
AON 1	ATCTGTGATGGT <u>GGTCA</u> <u>GTG</u>	CACTGACCACCATCACA GAT	51. 8	50
AON 2	AGTGCACAAATATCCCT GGA	TCCAGGGATATTTGTGC ACT	49. 7	45
AON 3	TGATGGATTCATGGCAT CTG	CAGATGCCATGAATCCA TCA	49. 7	45
AON 4	GCATCTGAAGACATGAA GAC	GTCTTCATGTCTTCA GATGC	49. 7	45

**Table 3.2 AON parameters showing the binding sequence of the AON, the sequence of the AON (reverse complement), the annealing temperature (T<sub>m</sub>) and the guanine and cysteine percentage in each binding sequence (GC%).**

As AONs 1 and 2 overlapped, we decided to proceed with our AON design process using only AONs 1, 3 and 4. Finally, to assess the efficacy of the AONs, the free energy of the AON and AON-to-AON complexes was calculated using the RNAstructure software (RNAstructure, version 6.0.1) (Figure 3.6A). AONs of 20 base pairs should yield an energy of > -4 kcal/mol and AON-to-AON complexes should yield an energy of > -15 kcal/mol. Lastly, the binding energy of the AON was calculated based on its

## Development of novel therapies for Marfan Syndrome using a human iPSC-derived disease model

equation (Figure 3.6B and Table 3.3). All AONs were confirmed in their unique binding ability by BLAST analysis.

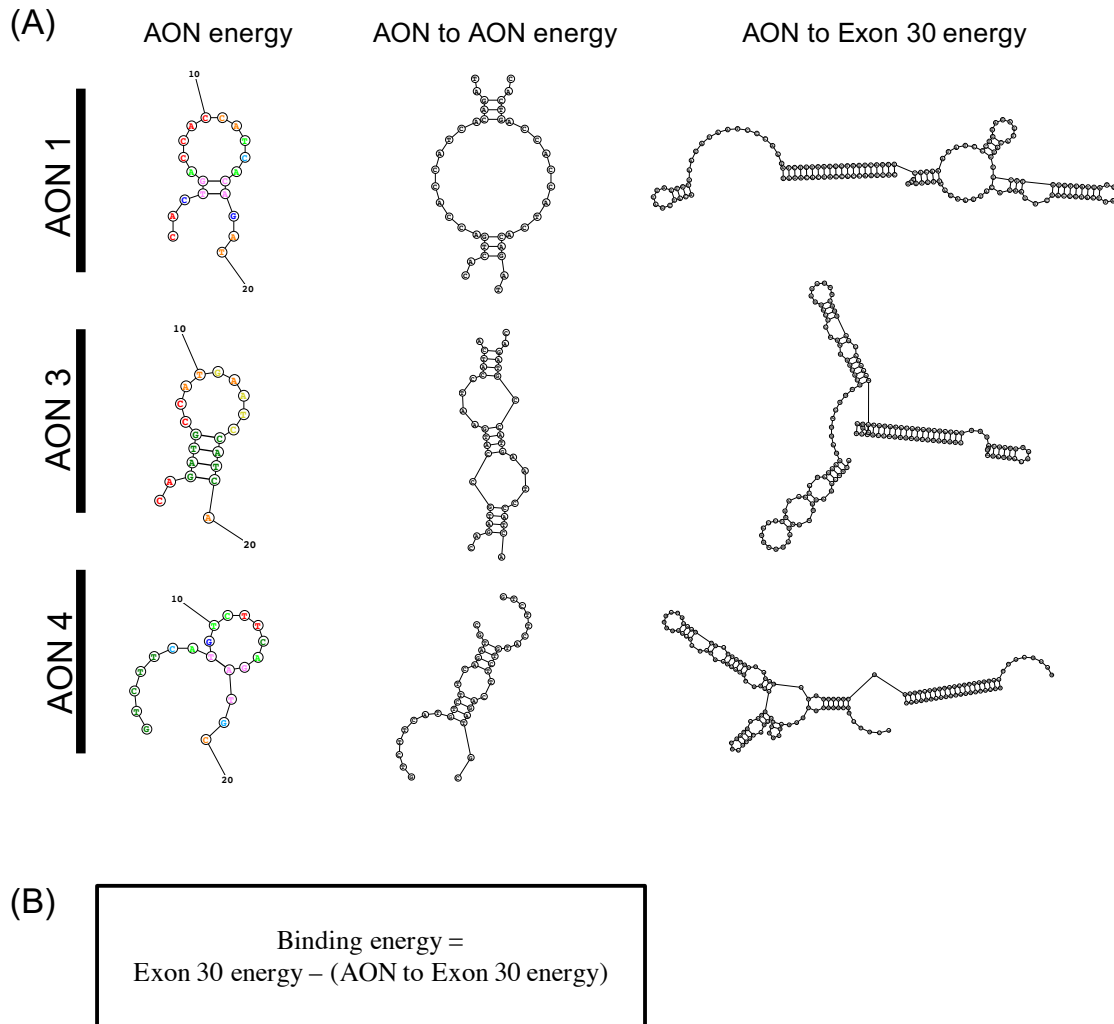


**Figure 3.6 Binding energy calculations to validate AON efficacy.**

(A) Schematic diagrams of stable structures of AON folding, AON to AON binding and AON to Exon 30 binding for AON1, AON3 and AON4. (B) Binding energy equation.

AON	AON energy	AON to AON energy	AON to Exon 30 energy	Exon 30 energy	Binding energy
1	1.5	-3.2	-57.6	-29.4	28.2
3	1.6	-8.2	-53.6	-29.4	24.4
4	1.4	-5.5	81.68	-29.4	27.6

**Table 3.3** Steric energy values (kcal/mol) for each structure type as well as exon 30 alone with associated binding energy (RNAStructure version 6.0.1).

### 3.2.2 AON-mediated exon skipping leads to exon 30 exclusion in FBNI

#### 3.2.2.1 Comparing and optimising single and dual AON transfection protocol

##### 3.2.2.1.1 *AONs designed for exon 30 targeting*

Two antisense oligonucleotides (AON1 and AON3) were designed and identified as optimal for targeting exonic regions of exon 30 in *FBNI* (Figure 3.2). These AONs were predicted *in silico* to have a high skipping efficiency by blocking exonic splicing sites, which are responsible for directing accurate splicing of pre-RNA sequences. The predicted thermodynamic properties and free energy binding parameters certified AON1 and AON3 to be suitable to cause efficient skipping of exon 30 in *FBNI*.

##### 3.2.2.1.2 *Transfection efficiency evaluated by a scramble AON-GFP*

Wild-type neural-crest derived smooth muscle cells (WT NC-SMCs) were initially used to obtain the optimal transfection ratios of AONs and transfection reagent.

## Development of novel therapies for Marfan Syndrome using a human iPSC-derived disease model

As previously described, NC-SMCs are SMCs which arise from the NC embryonic origin, which populate the aortic arch, the ascending aorta and its derivatives (Figure 1.8). Here WT NC-SMCs were transfected with different concentrations of a scrambled GFP-linked AON to monitor the transfection efficiency. By fluorescent microscopy, the GFP-labelled AONs primarily targeted the nuclei as most cells were GFP-labelled when collected and quantified using flow cytometry. Results showed a positive correlation between AON-GFP concentration and number of GFP-labelled cells, where 400nM of GFP-labelled AON was sufficient to successfully and significantly target 75% of WT NC-SMCs (Figure 3.7). In a relaxed state, smooth muscles can span from 20 to 600  $\mu\text{m}$  in length. Furthermore, WT NC-SMCs were seeded at two different densities in 12-well format and results showed that AONs were stable in the cells for at least 72 hours. Again, GFP-positive cells were quantified by flow cytometry over a period of 72 hours and samples were collected every 24 hours. Results showed that the number of GFP-positive cells decreased over time, potentially explained by the proliferation of cells diluting out the stable and constant amount of GFP-AON within the cells (Figure 3.8).

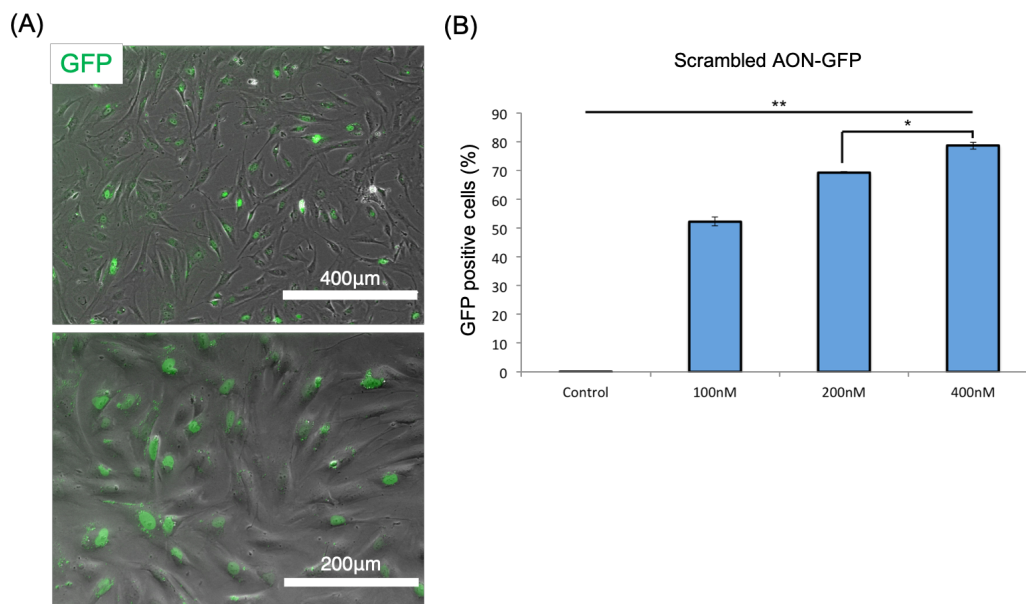


**Figure 3.7 Transfection optimisation using a GFP-labelled AON**

(A) WT-SMCs transfected with a GFP-labelled AON show that the AONs target the nuclei of the cells, where their primary actions lay. (B) Quantification of GFP-positive cells transfected with a spectrum of GFP-AON concentrations (100nM, 200nM and 400nM). All results are representative of  $n=3$ ; means  $\pm$  SEM. The asterisk indicates statistically significant difference (\*  $p < 0.05$  and \*\* $p > 0.001$ ).

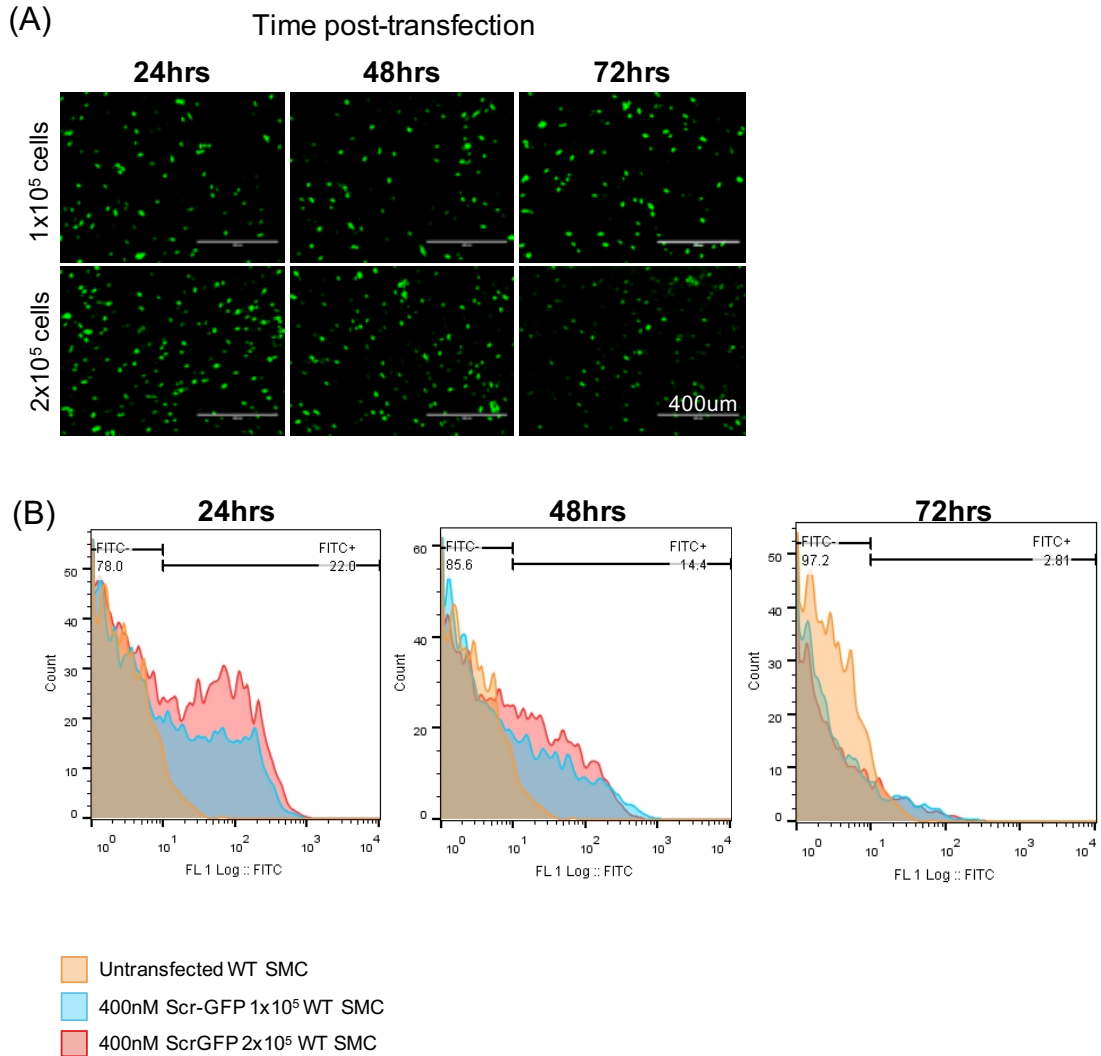


**Figure 3.8 GFP-labelled AON is time-dependent in WT-SMCs**

(A) WT-SMCs transfected at different densities (1x10<sup>5</sup> or 2x10<sup>5</sup> per 12-well) with 400nM of a scramble GFP-labelled AON (Scr-GFP) and GFP signal is monitored over three time points, 24 hours, 48 hours and 72 hours post-transfection and observed by fluorescent microscopy. (B) Flow cytometry quantification of GFP-positive cells over three time-points, 24 hours, 48 hours and 72 hours post-transfection of 400nM of scramble GFP-labelled AON.

3.2.2.1.3 *Exon-skipping efficiency using single or a combinatory AON transfection conditions*

The extent of exon 30 skipping, under a range of conditions, was measured by PCR amplification and gel electrophoresis for detection of a shorter skipped cDNA transcript relative to the full-length transcript. As described earlier, a pair of primers was designed to anneal upstream and downstream of exon 30 to detect the percentage of successfully skipped transcript and, therefore, monitor for the removal of the mutation-containing exon 30 in FBN1. In the scenario of exon skipping, a shorter cDNA transcript (amplicon length 377bp) compared to the full transcript (amplicon length 500bp) is expected to be transcribed. Here, WT NC-SMCs and MF<sup>C1242Y</sup> NC-SMCs were matured in serum for 2 weeks (S15) to 1 month (S30) and were used for transfection studies. Both cell types were transfected with either a single AON designed for skipping (AON1 or AON3) or in combination at different ratios (AONe30). In addition, cells were transfected with the scramble GFP-labelled AON as control. Following transfection, samples were collected to assess for the percentage of skipped transcript by PCR amplification and gel electrophoresis analysis.

Surprisingly, exon skipping was achieved using the combination of AONs (AONe30) rather than with a single AON (AON1 or AON3 individually). Furthermore, the skipping efficiency of AONe30 cocktail was evaluated using different ratios of AON1 and AON3, where a higher percentage of AON1 relative to AON3 yielded increased skipping efficiency of 45%. Skipping efficiency quantifications showed that the optimal AON transfection conditions lead to 39% and 43% skipping of exon 30 in all transcripts in WT and MF<sup>C1242Y</sup> NC-SMC respectively (Figure 3.9 and Table 3.4). Sequencing analyses confirmed that all short transcripts were devoid of the mutation-containing exon 30 in MF<sup>C1242Y</sup> (Figure 3.10).

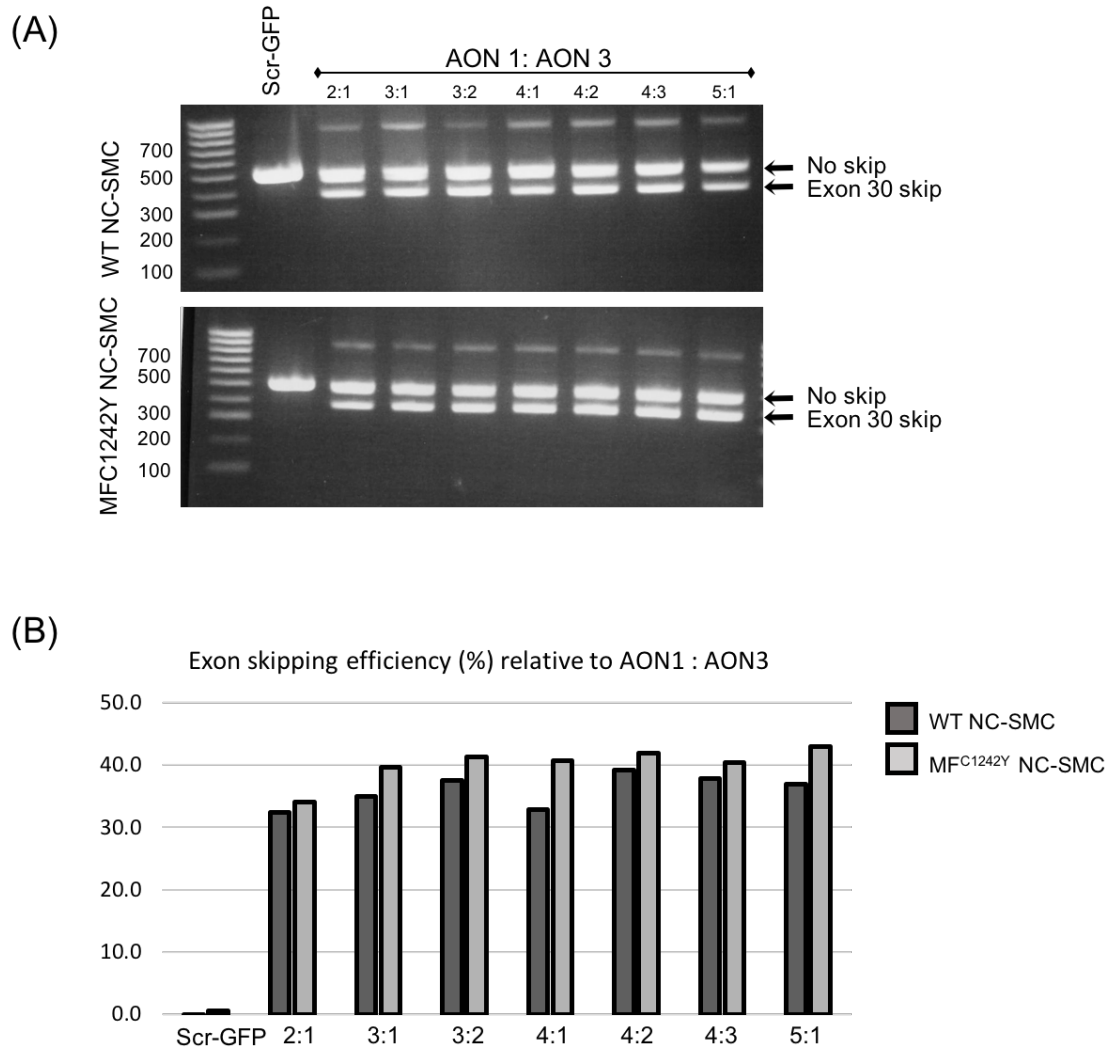


**Figure 3.9 A cocktail of AONs causes exon skipping in MF<sup>C1242Y</sup> SMCs.**

(A) PCR detection of exon 30 skipping on 1% agarose gel where the top band (500bp) corresponds to the full transcript with exon 30 and the bottom band (377bp) is the transcript without exon 30 in WT and MF<sup>C1242Y</sup> NC-SMC matured in serum for 30 days (S30). A scrambled AON (Scr AON-GFP) is used as negative control. AON1 and AON3 are AONs are predicted *in silico* to skip exon 30. (B) Quantification of skipping efficiency where the quantity of the bottom transcript is measured relative to the total amount of transcript in WT and MF<sup>C1242Y</sup> NC-SMC transfected with AONs. Data is shown n=1.

Development of novel therapies for Marfan Syndrome using a human iPSC-derived disease model

Sample	AON 1 to AON 3 ratio	Exon skipping (%)
WT NC-SMC	Scr-GFP	0
	2:1	32
	3:1	35
	3:2	38
	4:1	33
	4:2	39
	4:3	38
	5:1	37
MF <sup>C1242Y</sup> NC-SMC	Scr-GFP	0
	2:1	34
	3:1	40
	3:2	41
	4:1	41
	4:2	42
	4:3	40
	5:1	43

**Table 3.4 Exon-skipping percentage**

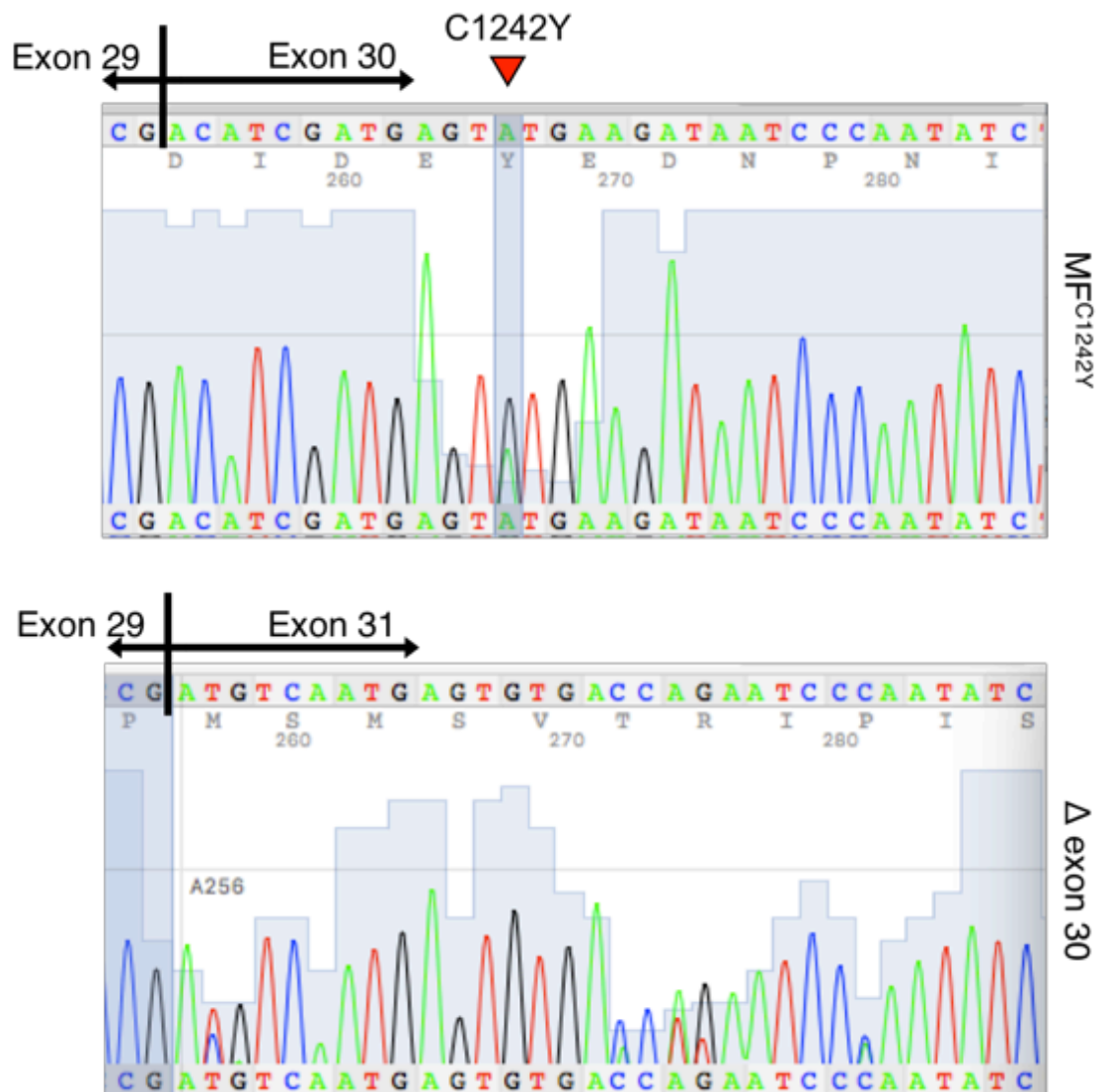


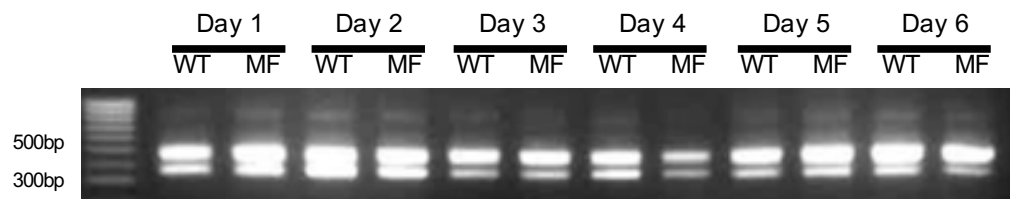
**Figure 3.10 Sequencing analysis of exon 30 non-skipped and skipped transcripts.**

The different samples were purified, and Sanger sequence analysed. In the unskipped situation, exon 30 was present (MF<sup>C1242Y</sup>), where in the properly targeted SMCs, exon 30 was absent. This confirmed the deletion of exon 30 at the level of the RNA ( $\Delta$  exon 30). The double peak, indicated by a red triangle, G (black) and A (green) in the full transcript indicates the nucleotide-causing mutation substitution in both WT and MF alleles respectively.

### **Development of novel therapies for Marfan Syndrome using a human iPSC-derived disease model**

Skipping efficiency was also evaluated over time by collecting samples over a period of 6 days. Here, the skipping percentage was on average 42% and 37% for WT NC-SMC and MF<sup>C12427</sup> NC-SMC respectively over the 6 days. The skipping efficiency showed a slight increase at day 3 post-transfection in WT NC-SMC whereas the percentage of skipped transcript in MF<sup>C1242Y</sup> NC-SMC remained relatively constant over the period of interest. These results confirmed that AONs are stable in the cells for at least a period of 6 days. (Figure 3.11). In the attempt to increase exon skipping efficiency, MF<sup>C1242Y</sup> NC-SMCs were transfected repeatedly with AONe30 skipping cocktail. However, recurrent transfections had no effect on elevating the amount of skipped transcript detected (Figure 3.12).

(A)



(B)

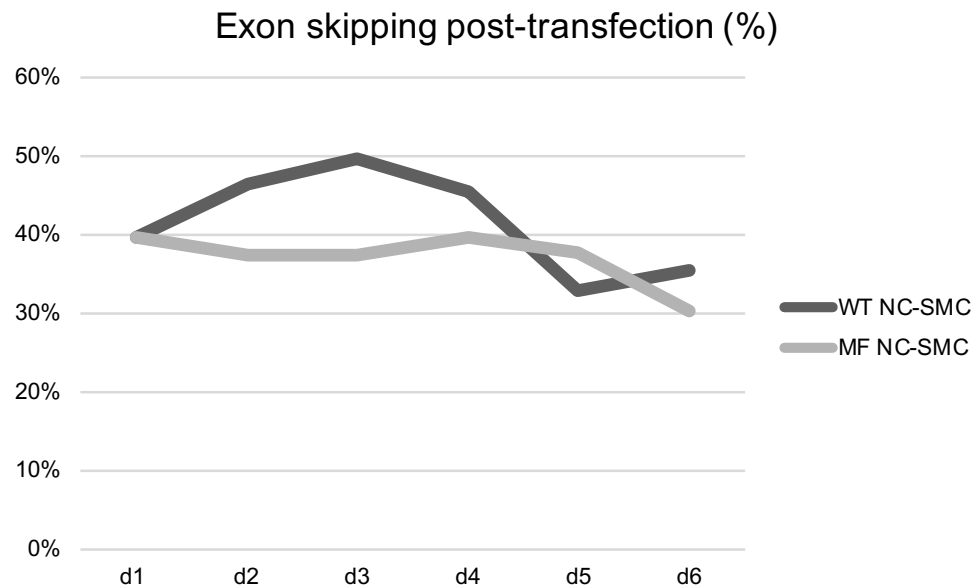


**Figure 3.11 AONe30 cocktail remains stable in the cells over a period of 6 days.**

(A) PCR detection of exon 30 skipping on 1% agarose gel where the top band (500bp) corresponds to the full transcript with exon 30 and the bottom band (377bp) is the transcript without exon 30 in WT and MF<sup>C1242Y</sup> NC-SMC matured in serum for 30 days (S30). The transfection cocktail AONe30 caused skipping of exon 30 in both WT and MF<sup>C1242Y</sup> NC-SMC and was stable over 6 days post-transfection. (B) Quantification of skipping efficiency where the quantity of the bottom transcript is measured relative to the total amount of transcript in WT and MF<sup>C1242Y</sup> NC-SMC.

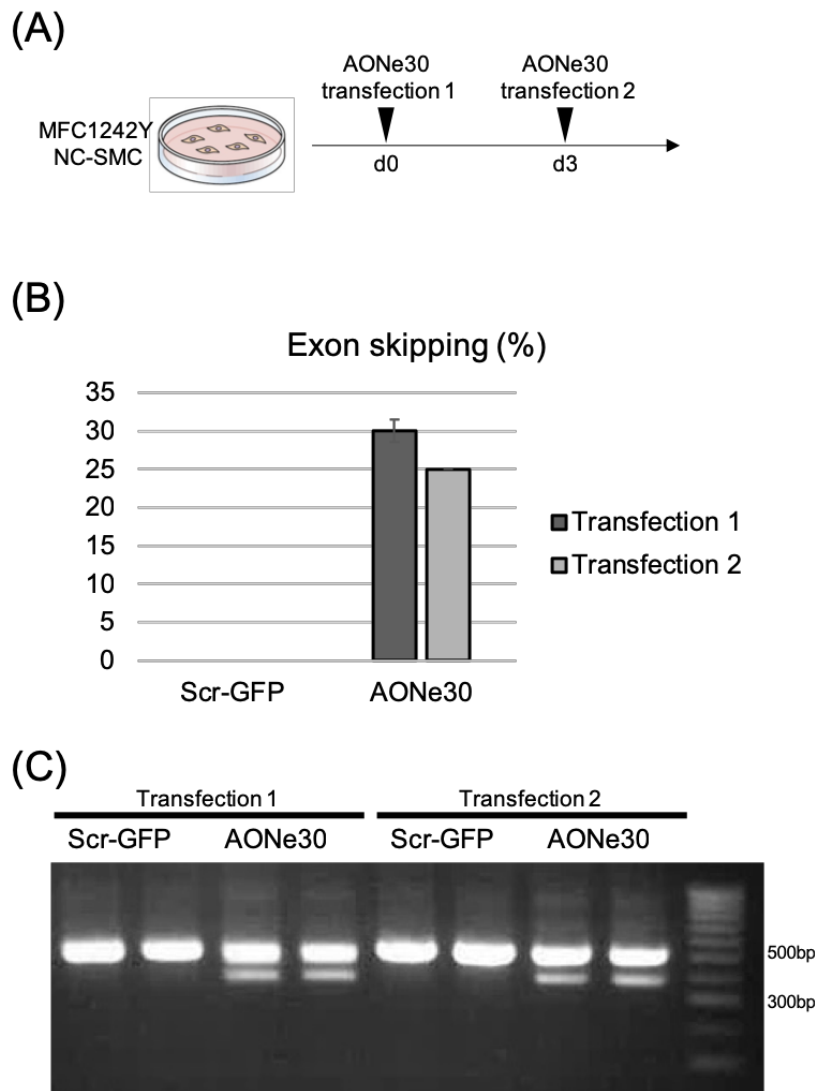


**Figure 3.12 Multiple transfections does not affect the skipping efficiency in MF<sup>C1242Y</sup> NC-SMCs**

(A) Schematic diagram of transfection time-line where the first transfection (AONe30 transfection 1) was performed at day 0 and samples collected at day 3 and the second transfection (AONe30 transfection 2) was performed at day 3 and samples collected at day 6 post-transfection. (B) Quantification of skipping efficiency where the quantity of the bottom transcript is measured relative to the total amount of transcript in MF<sup>C1242Y</sup> NC-SMC transfected multiple times with AONe30. Data shown is the mean  $\pm$  SEM of 3 technical replicates (n=1). (C) PCR detection of exon 30 skipping on 1% agarose gel where the top band (500bp) corresponds to the full transcript with exon 30 and the bottom band (377bp) is the transcript without exon 30 in MF<sup>C1242Y</sup> NC-SMC matured in serum for 30 days (S30).

### 3.2.2.2 Exon-skipping efficiency using AONe30 and Scr-GFP

The targeting AONs were designed to be coupled directly to a GFP protein. However, we had difficulty obtaining positive transfection results as no green cells were observed post-transfection. In order to enhance AON nuclear delivery, the scrambled AON coupled to a GFP (Scr-GFP) molecule was co-transfected with the AON cocktail (AONe30) previously shown to yield 43% skipping in MF<sup>C1242Y</sup> NC-SMCs. Results showed that the addition of Scr-GFP greatly increased the skipping percentage of the targeted transcript. Although skipping levels were variable between experiments, the skipping percentage varied between 70% to 90%. The skipping percentage was also dependent on the concentrations of AONe30 and of Scr-GFP. We found that the least cytotoxic and highest skipping inducing concentration combination was that of AONe30 at 400nM and Scr-GFP at 50nM (Figure 3.13). The element responsible for the enhanced skipping levels provoked by the additive effect of co-transfecting Scr-GFP with AONe30 remains to be elucidated.

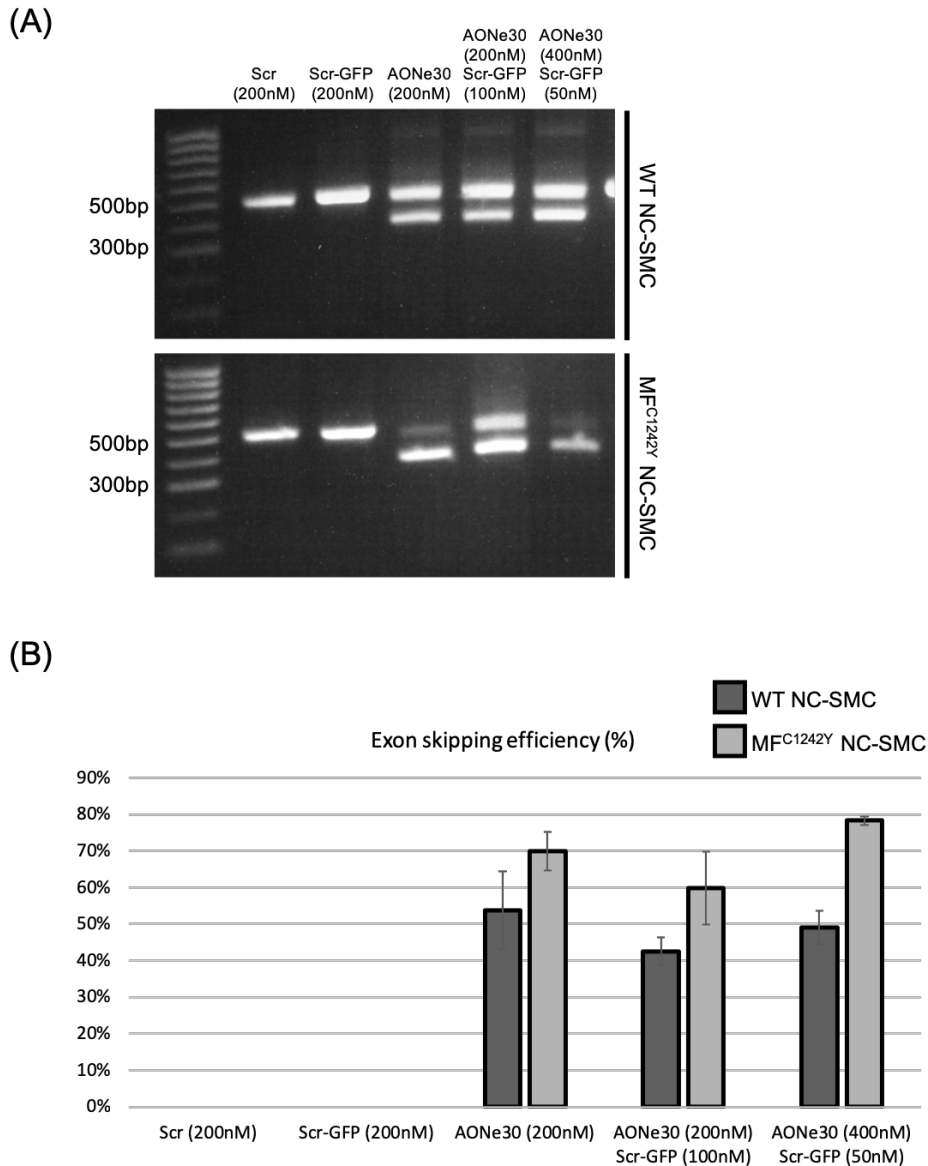


**Figure 3.13 Co-transfecting a scramble GFP-labelled AON with an exon-skipping AON cocktail increases skipping efficiency in MF<sup>C1242Y</sup> NC-SMCs**

(A) PCR detection of exon 30 skipping on 1% agarose gel where the top band (500bp) corresponds to the full transcript with exon 30 and the bottom band (377bp) is the transcript without exon 30 in WT and MF<sup>C1242Y</sup> NC-SMC matured in serum for 30 days (S30). A scrambled AON coupled to a GFP molecule (Scr-GFP) is used as negative control. As detected by PCR amplification, the transfection cocktail AON1 and AON3 (AONe30) co-transfected with Scr-GFP was able to cause skipping of exon 30 in both WT and MF<sup>C1242Y</sup> NC-SMC. (B) Quantification of skipping efficiency where the quantity

of the bottom transcript is measured relative to the total amount of transcript in WT and MF<sup>C1242Y</sup> NC-SMC. Data shown is the mean  $\pm$  SEM of 3 technical replicates (n=1).

Skipping was also evaluated in CRISPR-corrected NC-SMCs and Marfan-uncorrected NC-SMCs using the optimal AONe30 cocktail. Results showed that the AONe30 cocktail induced high skipping efficiency in untreated MF<sup>C12427</sup> NC-SMCs compared to SMCs differentiated from CRISPR-targeted iPSC patient lines harbouring the same mutation. In this particular experiment, MF<sup>C1242Y</sup> NC-SMCs revealed nearly 70% skipping whilst the Marfan-uncorrected line yielded 25% skipping (Figure 3.14). In parallel, we attempted to separate the population of GFP-positive cells using fluorescence activated cell sorting (FACS) technology. Unfortunately, the consecutive procedures of transfection followed by sorting may have been too harsh on the cell populations and we were unable to recuperate sufficient cells for subsequent analysis.

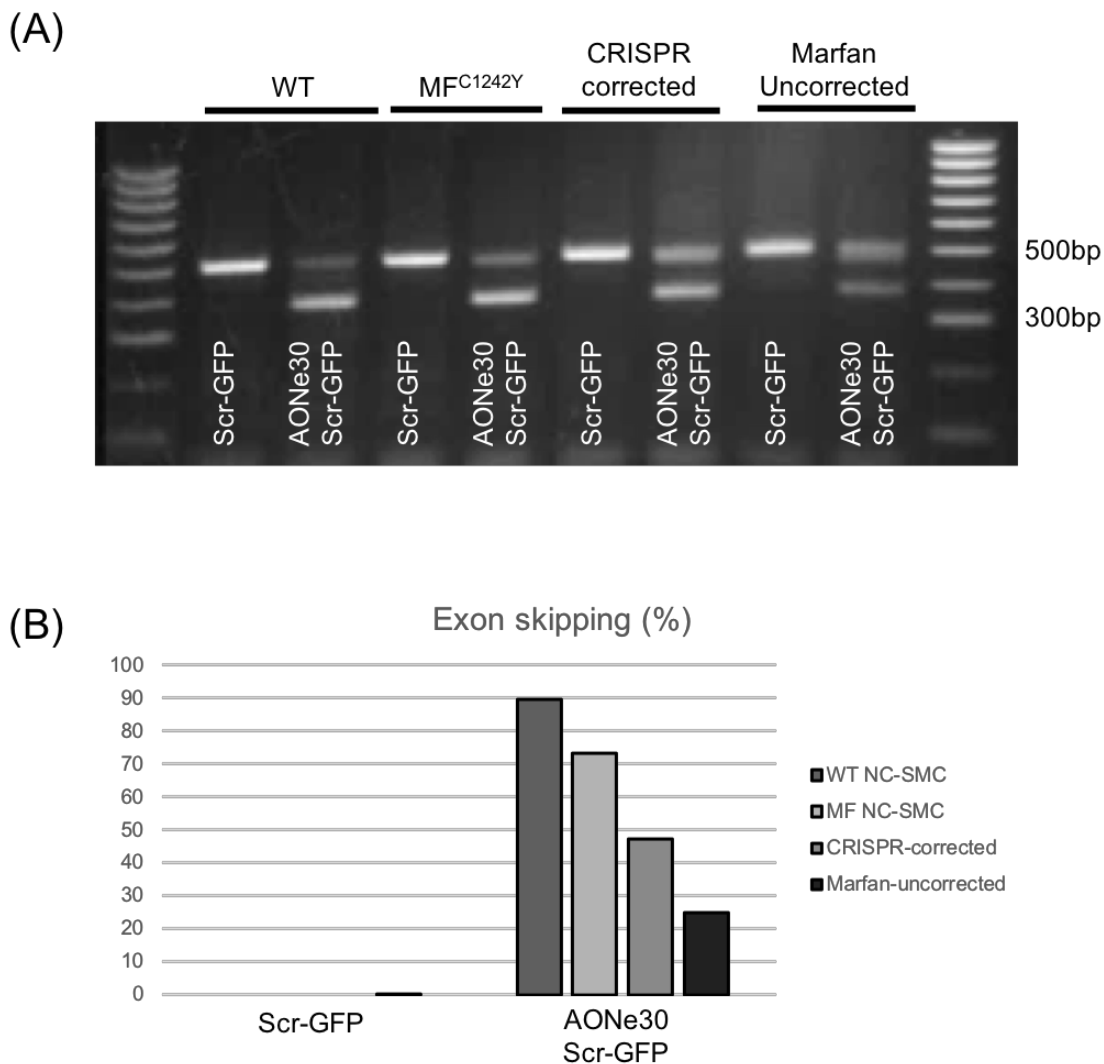


**Figure 3.14 A cocktail of AONs causes exon skipping in CRISPR-targeted MF<sup>C12427</sup> NC-SMCs.**

(A) PCR detection of exon 30 skipping on 1% agarose gel where the top band (500bp) corresponds to the full transcript with exon 30 and the bottom band (377bp) is the transcript without exon 30 in WT and MF<sup>C1242Y</sup> NC-SMC matured in serum for 30 days (S30). A scrambled AON coupled to a GFP molecule (Scr-GFP) is used as negative control. As detected by PCR amplification, the transfection cocktail AON1 and AON3 (AONe30) co-transfected with Scr-GFP was able to cause skipping of exon 30 in all four cell types: WT, MF<sup>C1242Y</sup>, CRISPR-corrected isogenic and Marfan-uncorrected NC-SMCs. (B) Quantification of skipping efficiency where the quantity of the bottom transcript is measured relative to the total amount of transcript in WT, MF<sup>C1242Y</sup>, CRISPR-corrected isogenic and Marfan-uncorrected NC-SMCs transfected with the AONe30 cocktail with or without Scr-GFP. Data shown is based on n=1.

### **3.3 Phenotypic evaluation of removal of mutation-containing exon 30 in FBN1**

#### **3.3.1 Evaluation of AONe30 transfection on SMC proliferation rates**

In order to evaluate the effect of removing the mutation-harboring exon, a battery of phenotypic assays was performed on the exon-skipped NC-SMC cell populations. MF<sup>C12427</sup> NC-SMCs have previously been shown to display reduced proliferative properties and increased cell-death characteristics<sup>28</sup>. Here, MF<sup>C12427</sup> and WT NC-SMCs were transfected with the previously determined combination of AONs that yielded the highest amount of skipped transcript (AONe30 400nM, Scr-GFP 50nM). Proliferation capacity was evaluated by BrdU incorporation, whereby BrdU was added to the transfected cell populations 48h after transfection. Following fixation and permeabilisation, samples were incubated in presence of an anti-BrdU antibody capable of recognising proliferating cells. Results, although variable, showed that AONe30-mediated exon skipping induced a moderate effect in restoring the proliferative capacity of MF<sup>C12427</sup> NC-SMCs. As expected, WT NC-SMCs were unaffected by the AONe30 transfection cocktail and maintained high levels BrdU-labelled cells, which is indicative of high proliferation rates (Figure 3.15).

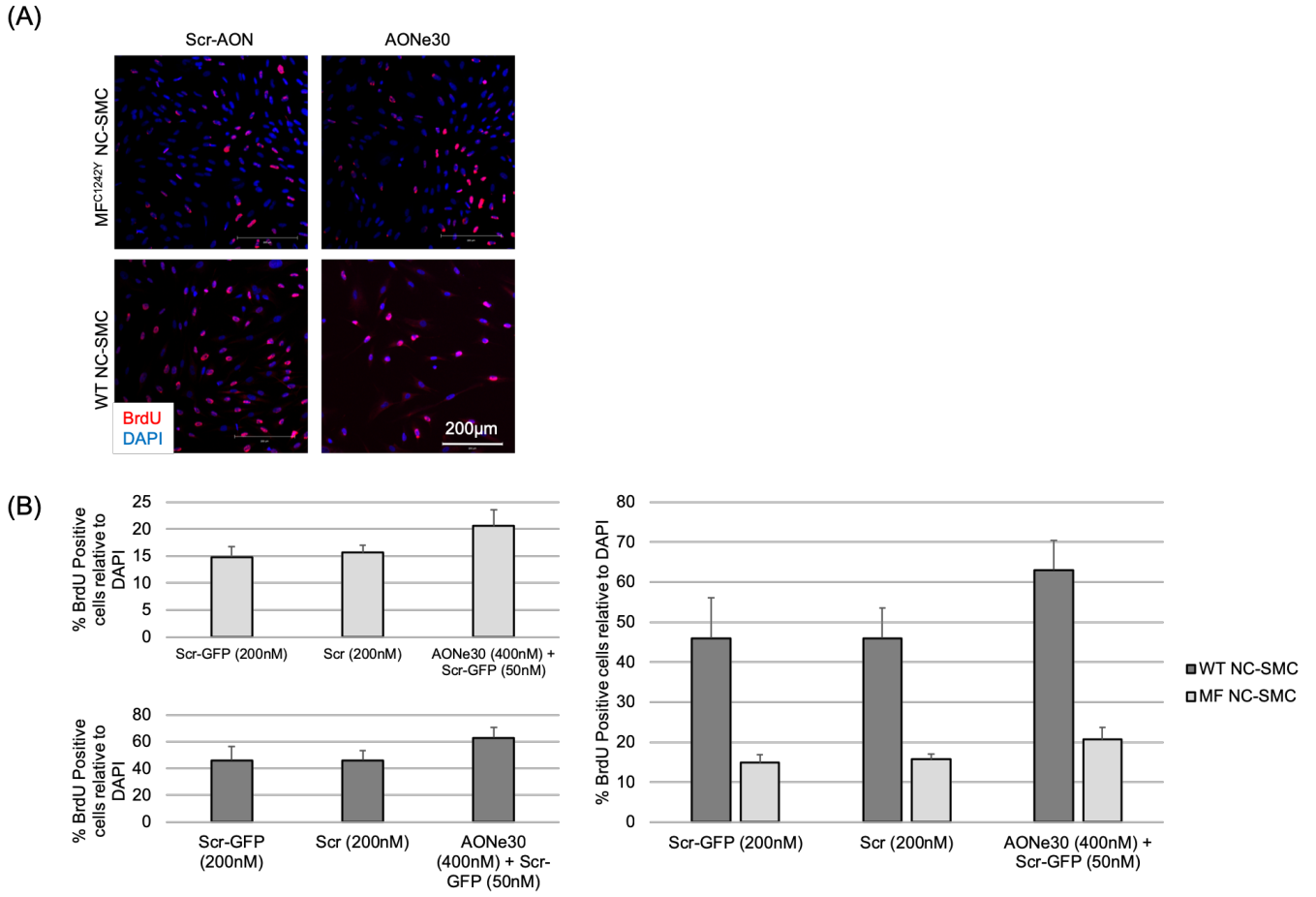


**Figure 3.15 Exon skipping has a modest effect on restoring the proliferation capacity of MF<sup>C1242Y</sup> NC-SMC.**

(A) Immunocytochemistry labelling of BrdU (red) in WT NC-SMC and MF<sup>C1242Y</sup> NC-SMC cultured for one month serum and transfected with a scramble (Scr-AON) or exon-skipping cocktail of AONs (AONe30). Nuclei were counted and stained using the nuclear dye DAPI (blue). (B) Quantification of BrdU positive cells relative to total DAPI-stained cells. Data shown is the mean  $\pm$  SEM of 5 technical replicates (n=1).

### 3.3.2 AONe30 cocktail restores abnormal matrix degradation properties

The effect of AONe30 was evaluated on the proteolytic properties of MF<sup>C12427</sup> NC-SMCs. Here, I showed that AONe30 transfection can restore the severe matrix degradation features displayed by MF<sup>C12427</sup> NC-SMCs. Previous work has shown that MF<sup>C12427</sup> NC-SMCs express elevated levels of extracellular matrix (ECM) degrading enzymes, such as the family of matrix metalloproteinases (MMPs). As a result, the abnormal proteolytic profile results in highly degraded ECM, which can be observed using a fluorescently-labelled gelatine (FITC-gelatine). Briefly, MF<sup>C12427</sup> NC-SMCs are seeded on FITC-gelatine for 24hrs and degrade their environment, leaving prominent dark patches within the green-labelled matrix. Here, matrix degradation was measured based on pixel intensity. Each image was converted to a binary version and pixel intensity was calculated, where high pixel intensity corresponded to high levels of FITC-gel and therefore low degradation and low pixel intensity translated to low levels of FITC-gel and thus elevated degradation. MF<sup>C12427</sup> NC-SMCs treated with a scramble AON (Scr-AON) showed lower pixel intensity and therefore high proteolytic levels, as was confirmed by staining, compared to their Scr-AON treated WT NC-SMCs counterparts. Surprisingly, AONe30-transfected MF<sup>C12427</sup> NC-SMCs seemingly restored the degradation profile to similar levels observed in WT NC-SMCs (Figure 3.16). Here, results show that 40% skipping of exon 30 in MF<sup>C12427</sup> NC-SMCs is potentially sufficient to reduce the proteolytic properties displayed by the Marfan SMCs.

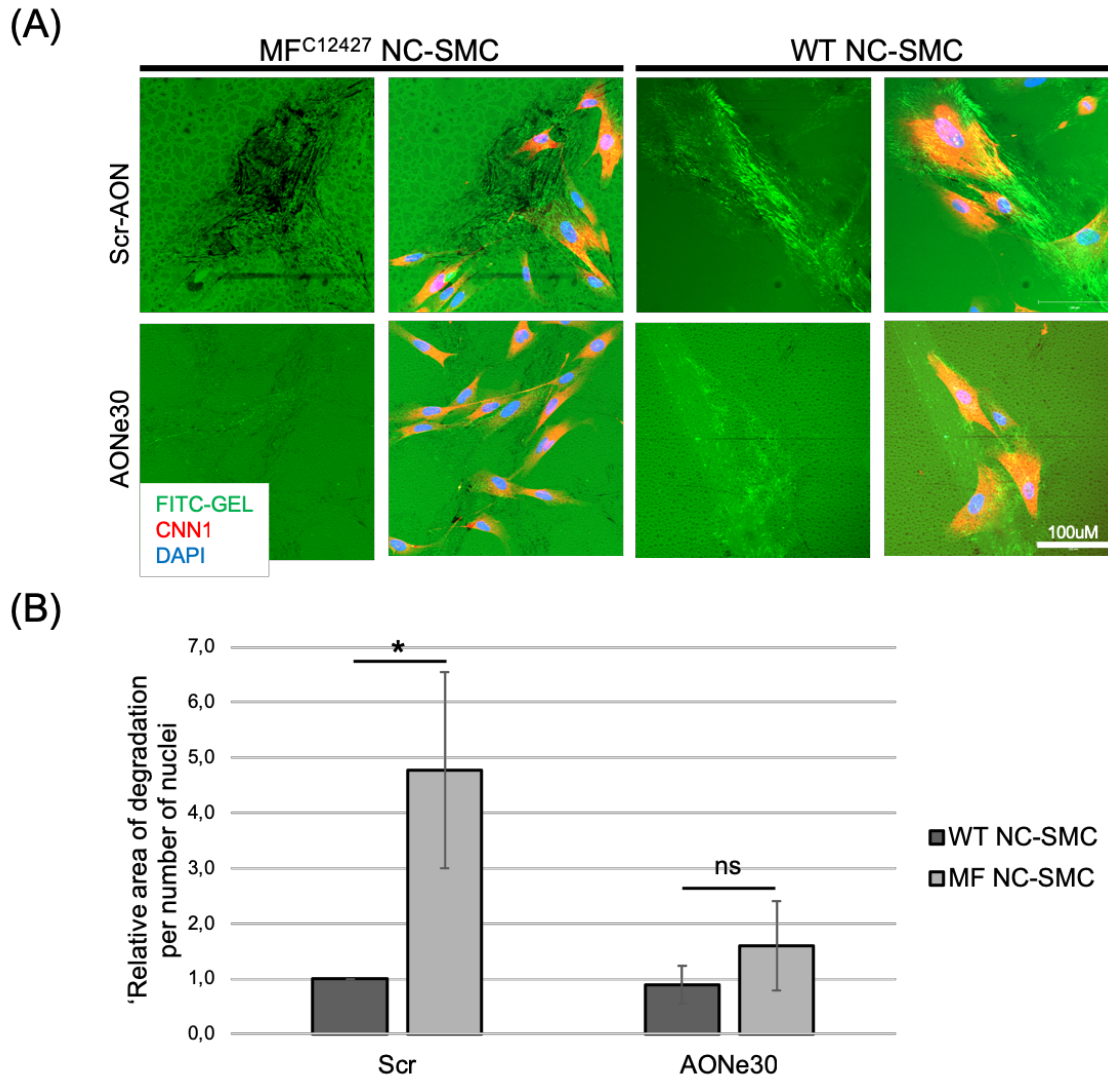


**Figure 3.16 Exon skipping is able to reduce matrix degradation in MF<sup>C1242Y</sup> NC-SMC**

(A) Immunocytochemistry labelling of FITC-gelatine (green), SMC marker calponin-1 (CNN1) and DAPI (blue) in WT NC-SMC and MF<sup>C1242Y</sup> NC-SMC cultured for one month in serum and transfected with a scramble (Scr-AON) or exon-skipping cocktail of AONs (AONe30). (B) Matrix degradation quantification was measured by green pixel intensity relative to number of cells (DAPI-positive). All results are representative of n=3; means ± SEM. The asterisk indicates statistically significant difference (\* p< 0.05 and ns, non-significant).

### 3.3.2.1 AONe30 transfection potentially reverses severe apoptosis in SMCs

In culture, MF<sup>C12427</sup> NC-SMC at both early and late differentiation stages become highly apoptotic and are prone to high rates of cell death. In order to determine if AONe30 is able to reduce apoptosis, WT and MF<sup>C1242Y</sup> NC-SMCs were transfected according to the usual exon-skipping protocol. Three days post-transfection, both cell types were collected and labelled for Annexin-V, a marker of early apoptosis that is displayed on the cell surface when the cell's viability becomes compromised. AONe30 transfection conditions were able to reduce the high apoptotic levels in MF<sup>C124Y</sup> NC-SMCs. As expected, WT NC-SMCs displayed low levels of apoptotic features in both control and AONe30 transfection conditions. Unfortunately, levels of apoptosis were also drastically reduced in control MF<sup>C1242Y</sup> NC-SMCs transfected with a scramble AON. Low apoptotic levels in the control conditions for both WT and MF<sup>C1242Y</sup> NC-SMCs could be due to the scramble sequence targeting pro-apoptotic genes and, as an off-target effect, interfering with the transcription of these sequences (Figure 3.17 and Table 3.5). Additionally, apoptotic levels were evaluated in NC-SMCs solely transfected with lipofectamine and, here, Annexin-V positive levels remained unchanged compared to unstained samples (data not included).

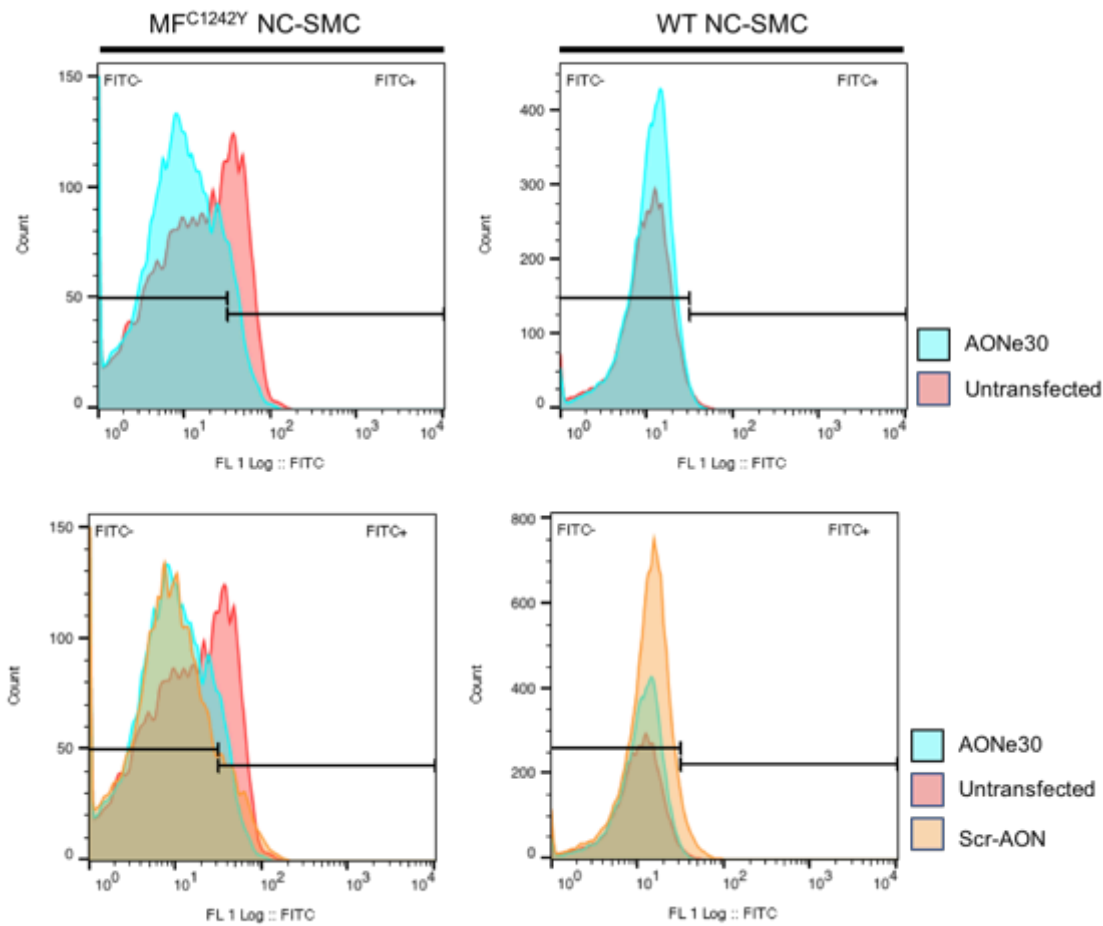


**Figure 3.17 AONe30 reduces apoptosis in MF<sup>C1242Y</sup> NC-SMC.**

Apoptotic profile measured by AnnexinV and propidium iodide (PE) staining in WT and MF<sup>C1242Y</sup> NC-SMC untreated (untransfected), treated with a scramble AON (Scr-AON), and treated with cocktail of AONs targeting exon 30 (AONe30). SMCs were cultured for 2 weeks in serum and collected for annexin-V staining three days post-transfection of AONs.

Condition	MF NC-SMC	WT NC-SMC
AONe30	10.8	0.99
Untransfected	26.8	1.77
Scr-AON	12.7	5.08

**Table 3.5 Apoptotic percentages measured by FITC<sup>+</sup> positive cells**

### 3.3.3 AONe30 potentially restores elongated SMC morphology

MF<sup>C12427</sup> NC-SMCs are often observed to display abnormal cytoskeletal features and abnormal NC-SMC marker expression profiles in comparison to the elongated spindle-shape morphology shown by WT NC-SMCs. An exon-skipping mediated restored fibrillin-1 profile could potentially affect the morphology of NC-SMCs and we attempted to check if AONe30 treatment would have an impact on morphology. Here, the NC-SMCs were transfected in absence of the AON Scr-GFP, as the green fluorescence would have interfered with the immunohistochemistry analysis. NC-SMCs were stained for markers such as  $\alpha$ -smooth muscle cell actin ( $\alpha$ -SMA, green) and calponin (CNN1, red). MF<sup>C12427</sup> NC-SMCs transfected with the AONe30 cocktail displayed signs of elongation that resembled the spindle-like shape of WT NC-SMCs (Figure 3.18). However, this encompassed only a small portion of the culture in its totality and it remains difficult to conclude the effect of exon-skipping on morphology.

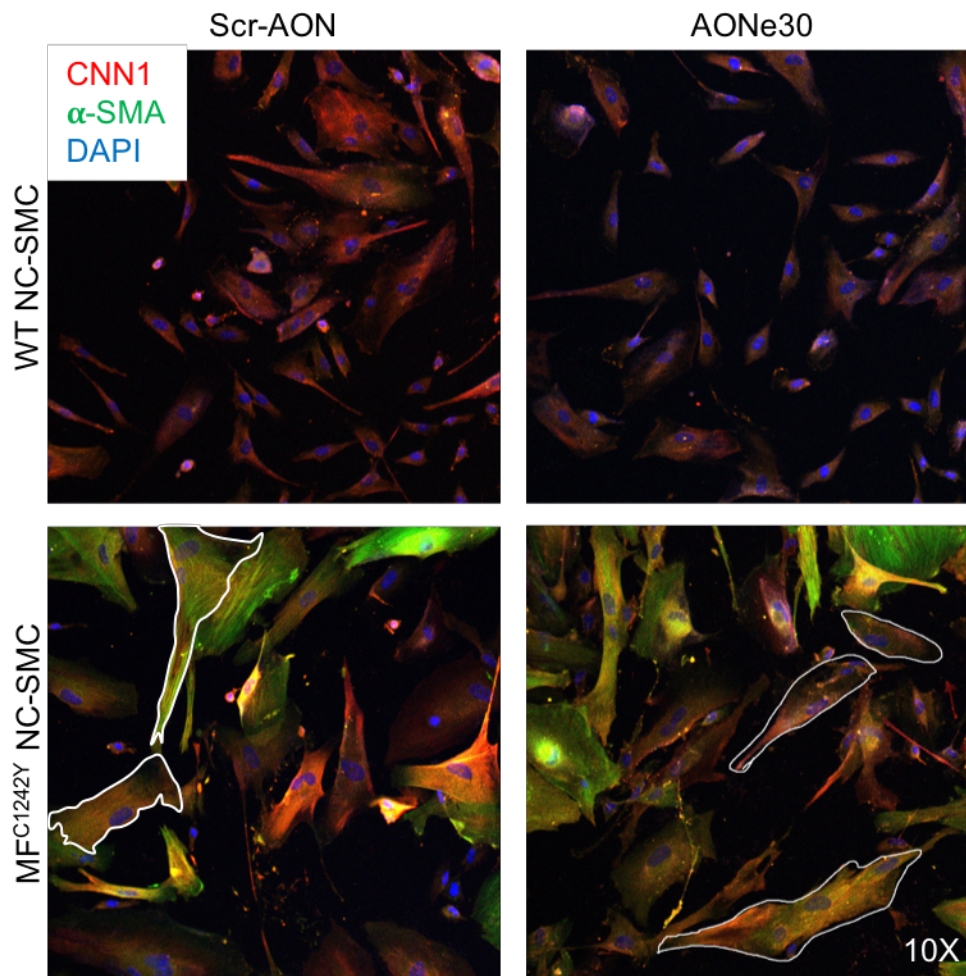


**Figure 3.18 AONe30 causes a moderate effect on SMC morphology.**

Cell morphology assessed using SMC-markers, calponin (CNN1, red) and alpha-smooth muscle actin ( $\alpha$ -SMA, green). Nuclei are labelled using DAPI (blue). Elongation is semi-qualitatively indicated by a white outline.

### 3.3.4 Transcription evaluation of targets downstream of the FBN1 mutation

Finally, we evaluated the mRNA expression profile by RT-qPCR of a panel of phenotypic markers such as MMPs and downstream targets, which we previously suggested may be involved in the pathology such as KLF4. As expected, control (Scr-GFP) MF<sup>C12427</sup> NC-SMCs showed elevated levels of MMPs (MMP1 and MMP10) and KL4 compared to WT NC-SMCs. However, AONe30 treatment had no significant impact on the expression of these markers in MF<sup>C12427</sup> NC-SMCs. These results denote a difficulty in interpreting phenotypic results due to variable transfection efficiencies (Figure 3.19).

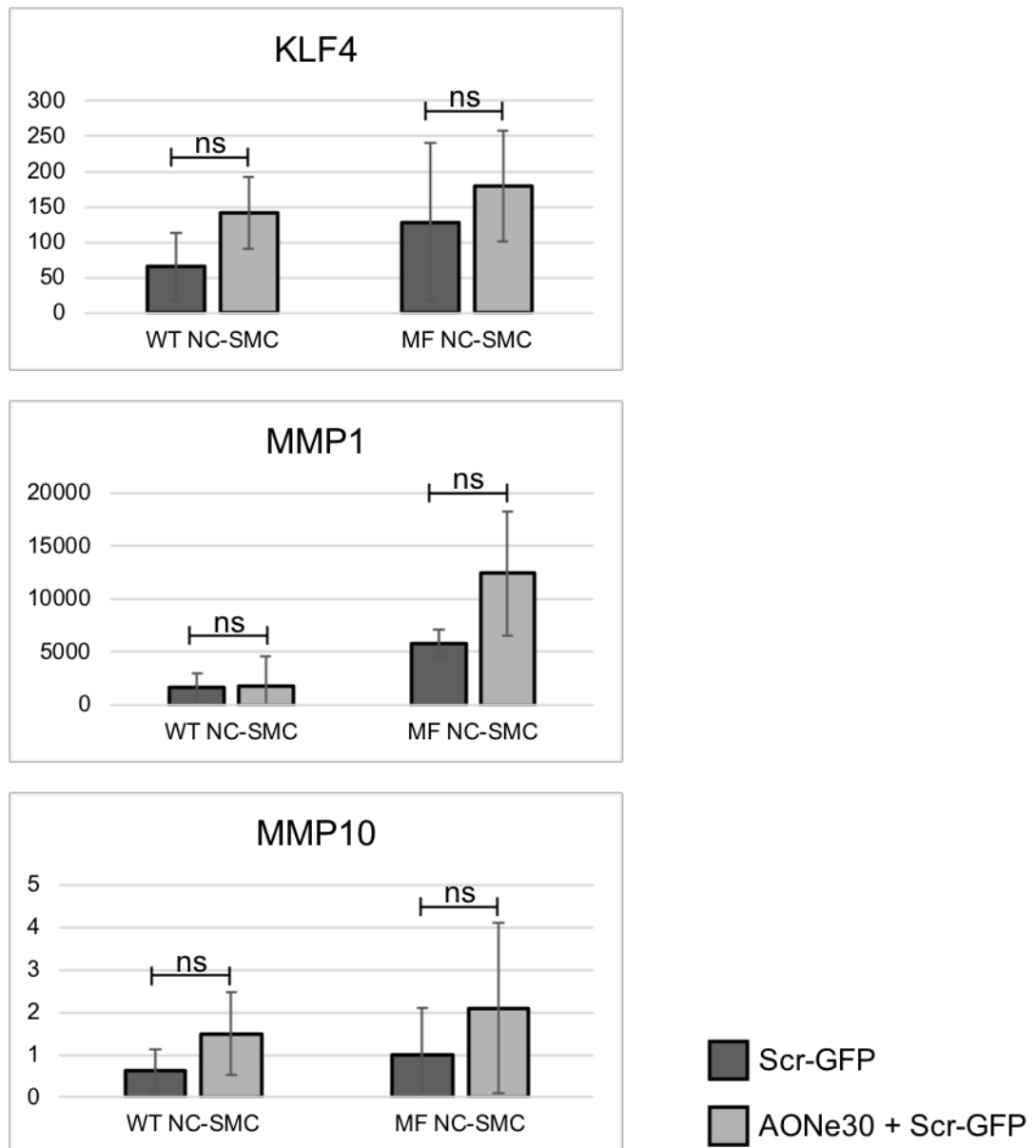


**Figure 3.19 mRNA levels of downstream targets from *FBN1* mutation in skipped and unskipped NC-SMCs**

*KLF4*, *MMP1* and *MMP10* mRNA levels in WT and MF<sup>C1242Y</sup> NC-SMCs measured by RT-qPCR. The relative mRNA level was normalized to a housekeeping gene (*GAPDH*) content. All results are representative of 3 biological replicates; means ± SEM (ns, non-significant).

### 3.4 CRISPR/Cas9-mediated deletion of exon 30 in MF<sup>C1242Y</sup> NC-SMCs

#### 3.4.1 CRISPR/Cas9 strategy to remove exon 30

The previous work showed that AON-mediated exon-skipping is a strategy that presents itself with limitations, such as obtaining 100% skipping efficiency and therefore accurately determining the effect of exon-skipping on the disease phenotype. In order to obtain 100% skipping efficiency, CRISPR/Cas9 was used as an alternative approach to remove the mutation-harboring exon in *FBNI*. Using the gene-editing tool of CRISPR/cas9, I proposed to target the genome directly and delete exon 30 entirely. Briefly, Dr Felipe Serrano in our lab designed two guide RNAs (gRNA) to anneal intronically upstream and downstream of exon 30, labelled as CR2 and CR7 respectively. The gRNAs are designed to allow the Cas9 enzyme to cut at the designated sites and remove exon 30 entirely from the genome. The gRNAs were nucleofected into the MF<sup>C1242Y</sup> iPSC line and fifty clones were selected for genotyping. Results revealed that exon 30 was absent from both alleles in one clone (homozygous skipped), absent from one allele from another clone (heterozygous skipped) and, finally, one clone was untargeted (homozygous un-skipped) (Figure 3.20).

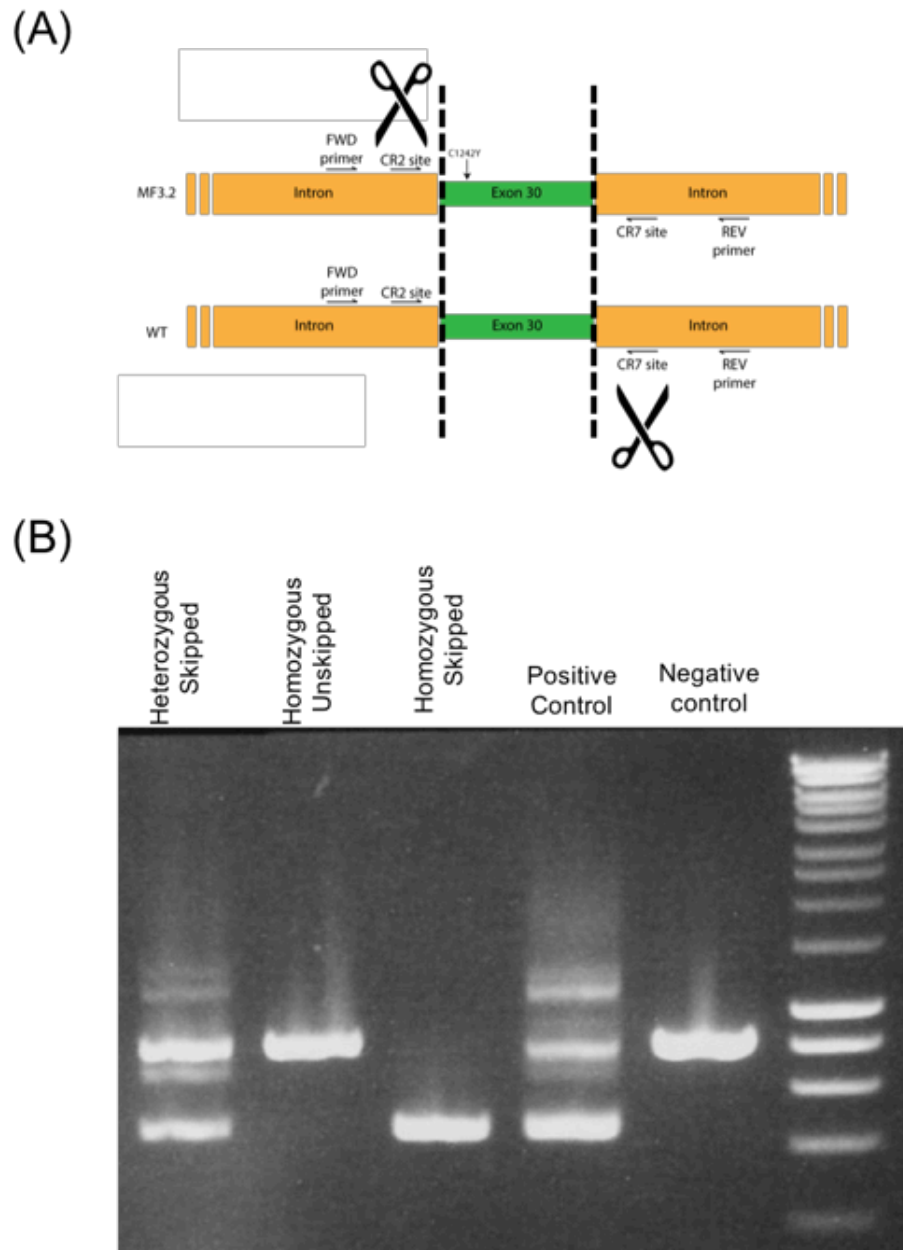


**Figure 3.20 CRISPR-mediated exon 30 removal in MF<sup>C1242Y</sup> hiPSC.**

(A) Schematic diagram of CRISPR/Cas9 mediated removal of exon 30 in *FBNI* using two guide RNAs (CR2, CR7) in MF<sup>C1242Y</sup> hiPSC. The diagram represents the targeted sites in both the WT and MF<sup>C1242Y</sup> alleles. Forward (FWD) and reverse (REV) primer sets are depicted in the intronic areas upstream and downstream of exon 30. (B) PCR detection on 1% agarose gel of non-skipped full transcripts (top band, 400bp) and exon 30 skipped transcripts (bottom band, 200bp) in heterozygous skipped, homozygous unskipped and homozygous skipped targeted MF<sup>C1242Y</sup> hiPSC. A positive (pool of CRISPR/Cas9 targeted hiPSC) and negative (H9) were included.

### 3.4.2 Characterisation of exon-skipped MF<sup>C1242Y</sup> iPSC lines

After the MF<sup>C12427</sup> iPSC lines were nucleofected with the gRNAs and the Cas9 enzyme, multiple iPSC clones were picked to screen for absence or presence of exon 30. Twenty clones were genotyped and three clones with distinct genotypes were selected: heterozygous skipped, heterozygous unskipped (control) or homozygous skipped profile. To verify the pluripotency profile of the iPSC lines post-nucleofection, the iPSC colonies were stained for pluripotency factors, SOX2 and TRA-1. Results showed that all iPSC lines retained their pluripotent character (Figure 3.21). In order to assess if complete removal of exon 30 had an effect on MF<sup>C12427</sup> NC-SMCs, the three previously described clones were differentiated into the NC progenitor stage, the first step to SMC differentiation. However, the cells proved unable to expand and overcome the first passaging procedure from NCp1 to NCp2 (Figure 3.22). All genetic conditions were highly apoptotic compared to their un-transfected MF<sup>C12427</sup> NC counterparts. It is worth noting that MF<sup>C12427</sup> at the NC stage do not display a high cell-death profile. Elevated apoptotic levels in Marfan lines are solely a feature associated with SMC maturation.

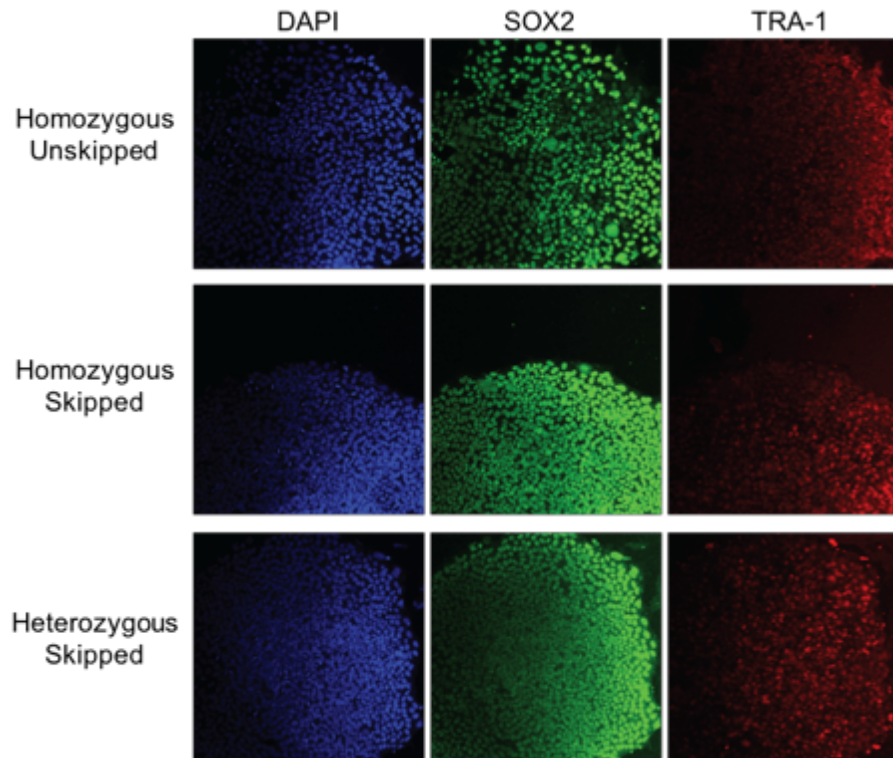


**Figure 3.21**  $MF^{C1242Y}$  hiPSC targeted with CRISPR-mediated exon 30 removal retain their pluripotency profile.

Pluripotency markers, SOX2 and TRA-1-60, immunostaining in homozygous heterozygous skipped  $MF^{C1242Y}$  hiPSC. Images are at 10X magnification.

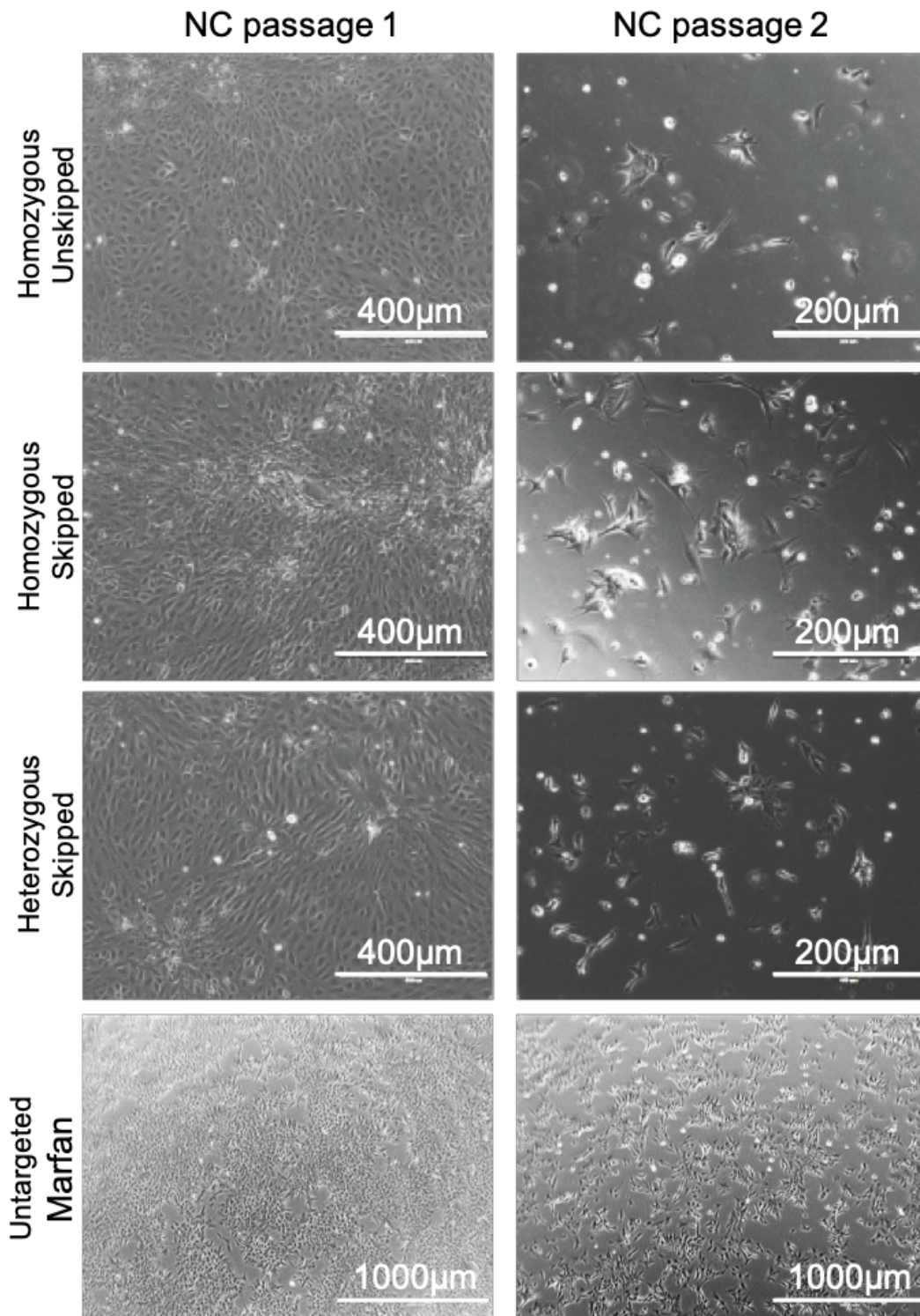


**Figure 3.22 MF<sup>C1242Y</sup> hiPSC targeted with CRISPR-mediated exon 30 removal are unable to differentiate into NC.**

Phase images of differences between neural crest passage 1 (NC passage 1) and neural crest passage 2 (NC passage 2) in CRISPR-targeted MF<sup>C1242Y</sup> hiPSC differentiated into NCs compared to untargeted MF<sup>C1242Y</sup> hiPSCs.

### 3.4.3 Off-target activity in exon-skipped hiPSC clones

Due to the poor NC potential of the control homozygous unskipped iPSC, which still harboured the Marfan mutation, it was hypothesised that the detrimental effect on SMC maturation could possibly be explained by gRNA off-target activity. The gRNAs were screened for off-target effects using the software CRISPR Design (<http://crispr.mit.edu/>), which lists off-target sequences associated to each gRNA of interest. The *in-silico* analysis identified potential off-target sequences and the top five for each gRNA were selected for further analysis. It is worth noting that each potential off-target sequence possessed a minimal mismatch of four base-pairs compared to the gRNA sequences. This elevated percentage of mismatch (20% mismatch) is thought to prevent potential effects of off-target activity. Primer pairs were designed upstream and downstream of the genes located in the top five off-target sequences to amplify the off-target regions. PCR amplification did not reveal any major base-pair rearrangements in all CRISPR-targeted clones (data not shown) but off-target activity remains to be more thoroughly investigated by Sanger-sequencing in each amplified transcript to identify minor base-pair modifications potentially provoked by CRISPR/Cas9 editing. Here, results show the possibility of using CRISPR-cas9 to remove a targeted exon, but it remains to be further investigated whether an alternative gRNA strategy may be more appropriate for successful differentiation from the iPSC to the NC-SMC stages.

### 3.5 Conclusions

In this chapter, I have discussed the possibility of targeting the removal of a mutation-containing exon in fibrillin-1 using AON-mediated exons-skipping to restore a shorter and potentially functional protein. As previously discussed, AONs have become a versatile tool to harness the splicing machinery and exclude portions of transcripts that, untouched, may lead to disease manifestation. Skipping exon 30, which contains a missense mutation in our MF<sup>C1242Y</sup> patient-derived iPSC line, is a suggested approach to correct the pathogenic characteristics recapitulated in our disease model.

Removal of the faulty exon, which codes for a single cbEGF domain, is hypothesised to restore the translation of a shorter yet functional fibrillin-1 protein. AON-mediated exon skipping of multiple exons in the gene that encodes dystrophin proved successful to restore functional protein levels of dystrophin in animal models for Duchenne's muscular dystrophy (DMD) <sup>118</sup>. Our data shows that skipping of this particular exon is possible using a cocktail of antisense oligonucleotides (AON) and the skipping efficiency is augmented when in presence of a scramble fluorescently-labelled AON. However, the variable level of skipping efficiency is potentially insufficient to reverse or reduce the key aspects of MFS pathology.

In attempt to increase the skipping efficiency of the target exon, we employed CRISPR/Cas9-mediated technology to remove the mutated exon 30 in both alleles of the MF<sup>C1242Y</sup> hiPSC line. The CRISPR/Cas9 system allows precise modification of the genome and represents a potential tool to correct disease-causing mutations. Despite the positively-edited hiPSC showing major difficulties in differentiating towards NC-SMC, CRISPR/Cas9 technology holds promise for correcting the disease-causing exon in our model of MFS and could potentially reverse or reduce the phenotypic abnormalities displayed *in vitro* by mature SMC. Further optimisation of gRNAs and gene-editing strategy will allow to potentially determine the impact of exon-skipping as a beneficial therapeutic approach MFS.

However, germline editing is not feasible in humans and Long C and colleagues have developed an alternative approach to correct targeted genes in postnatal tissues. Their results demonstrated effective delivery of adeno-associated-virus-9 (AAV9) containing gene-editing components to skip mutant dystrophin exons in mdx mice, a model of DMD <sup>119</sup>. Therefore, it may be important to consider AAV delivery of exon-skipping components as a realistic therapeutic tool to correct the vascular pathology

displayed *in vivo* in a MFS mouse model. These alternative therapeutic strategies will be further discussed in Chapter 6.

# 4 RNA-SEQUENCING IDENTIFIES POTENTIAL DISEASE-CAUSING PATHWAYS IN MFS

## 4.1 Objectives of this Chapter

In this chapter, the power of genome engineering combined with human patient iPSCs is harnessed to explore the genetic signatures exhibited by MFS SMCs in our *in vitro* model compared to their isogenic control. Here, the Marfan Syndrome patient iPSC line, harbouring the point mutation C1242Y (MF<sup>C1242Y</sup>), was targeted using the gene-editing tool, CRISPR-cas9, to correct the mutation in the MFS allele (work performed by Dr Felipe Serrano). This technology enables the analysis of isogenic iPSC pairs that differ from a single genetic change whilst maintaining the patient genetic background. As a result, this comparison allows a thorough assessment of the molecular, cellular and phenotypic abnormalities that result directly from the disease mutation.

Thus far, the complete series of signalling events that are triggered by the mutation in fibrillin-1 remain unknown. Previous work suggested that the deconstructed protein product loses its ability to bind TGF- $\beta$ , which leads to increased TGF- $\beta$  levels in the tissue and damaging consequences to the aortic wall integrity. However, recent evidence has questioned the pivotal role of TGF- $\beta$  in driving aneurysm progression in MFS mouse models and patients. Molecular pathways that are TGF- $\beta$ -independent or rely on mechanosensing have been proposed as alternative or complementary disease-drivers. Therefore, there may be other signalling pathways, which are potentially responsible for partially or entirely causing the disease features exhibited by MFS patients. As previously described, our *in vitro* disease model replicates all the key features of the disease and offers a promising platform for exploring the different genetic signatures between MFS and healthy SMCs.

In this work, the transcriptomes of healthy (CRISPR-corrected) and MFS (Marfan-uncorrected) SMCs are analysed using RNA-sequencing to identify gene targets, which are potentially involved in pathogenic pathways. Both CRISPR-corrected and Marfan-uncorrected targeted human iPSC lines were differentiated according to the well-defined SMC protocols towards two maturation stages: early SMC (PTd12) and late SMC (serum 2 weeks) (Figure 1.8)<sup>95</sup>. Finally, the differential gene expression profile was compared between corrected and uncorrected SMCs, at both time-points respectively to identify disease-driving pathways and potentially druggable gene targets.

## **4.2 Characterisation of CRISPR-targeted MF<sup>C1242Y</sup> hiPSC-derived NC-SMCs at different maturation stages**

Previously, both the CRISPR-corrected and Marfan-uncorrected hiPSC lines were successfully characterised by immunostaining for hiPSC pluripotency<sup>28</sup>. I performed additional characterisation on differentiated CRISPR-corrected and Marfan-uncorrected NC-SMCs at both early (PTd12) and late (serum 2 weeks) differentiation stages to assess the functionality of the NC-SMCs. As expected, results showed that at both PTd12 and serum 2 weeks, the mutant Marfan-uncorrected NC-SMCs that still harbour the deleterious mutation, expressed higher mRNA levels of members of the proteolytic family of enzymes called matrix metalloproteinases (MMPs) compared to CRISPR-corrected NC-SMCs. Results showed that mRNA levels of MMP1 and MMP10 and MMP1 and MMP2 were more elevated in Marfan-uncorrected NC-SMCs at PTd12 and serum 2 weeks respectively compared to their corrected counterparts (Figure 4.1).

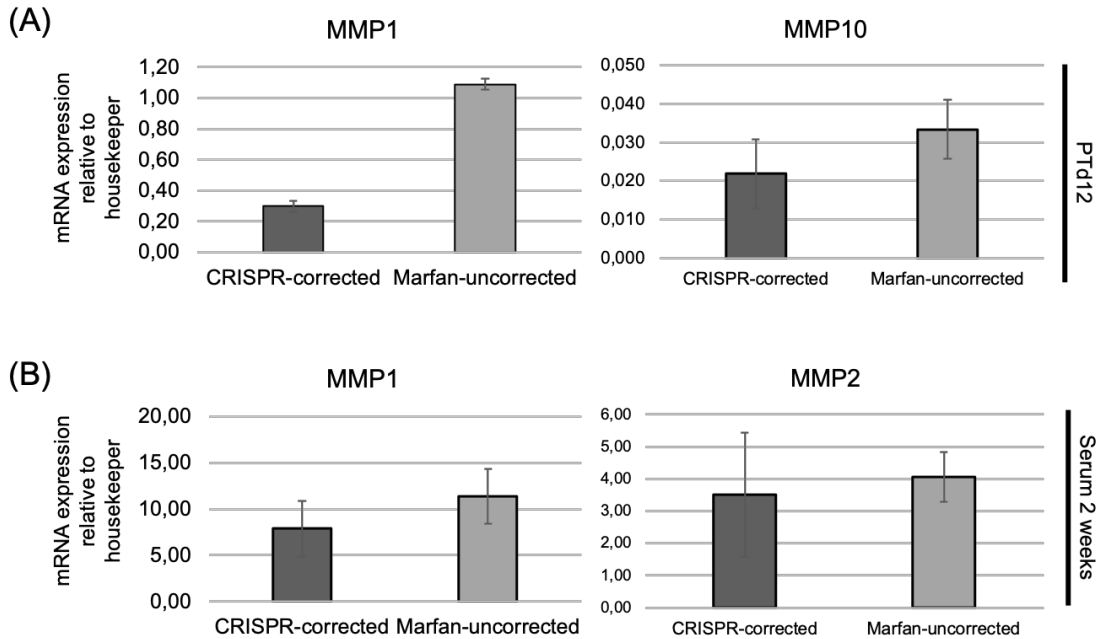


**Figure 4.1 CRISPR-corrected express less MMPs compared to Marfan-uncorrected NC-SMCs at early and late differentiation stages of SMCs.**

(A) RT-qPCR of MMP1 and MMP10 expression at PTd12 (early) for CRISPR-corrected and Marfan-uncorrected NC-SMCs. (B) RT-qPCR of MMP1 and MMP2 expression at serum 2 weeks (late) for CRISPR-corrected and Marfan-uncorrected NC-SMCs. Data shown is the mean  $\pm$  SEM of 3 technical replicates (n=1).

Furthermore, the cell-death profile of both cell-lines was evaluated by Annexin-V staining, which labels cells entering apoptosis. Marfan-uncorrected NC-SMCs (19.1%) showed a stronger apoptotic profile, similar to untargeted MF<sup>C1242Y</sup> NC-SMCs (32.2%). As expected, levels of apoptosis were significantly lower in the CRISPR-corrected NC-SMCs (8.32%) (Figure 4.2). It is important to state that no PI staining was performed as the instrument used to perform the Annexin V-staining is unable to separate both 480nm and 569nm wavelengths. Nevertheless, the functional assays allowed us to confidently state that CRISPR-targeting reversed the abnormal proteolytic and apoptotic phenotypes and that the corrected lines behaved similar to the wild-type. Thus, we proceeded to collect cells from both targeted lines from early (PTd12) and late (serum 2 weeks) differentiation stages for RNA-sequencing transcriptomics.

Development of novel therapies for Marfan Syndrome using a human iPSC-derived disease model

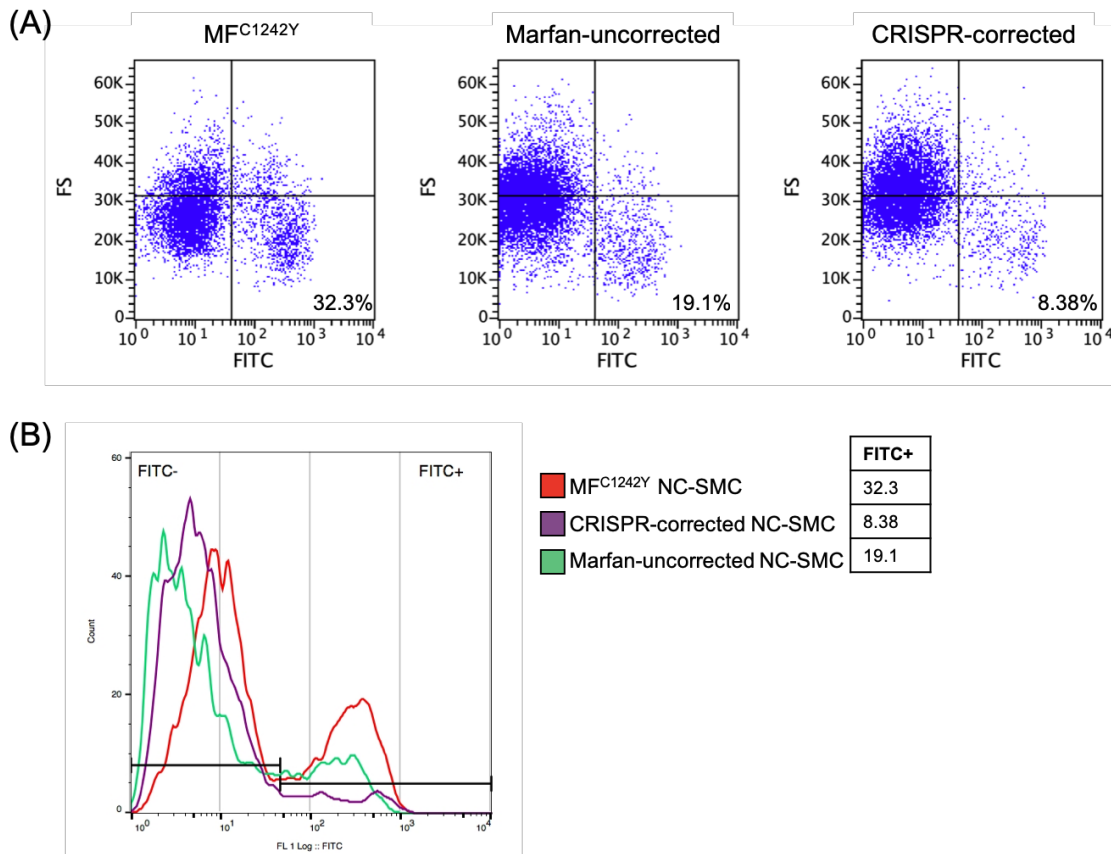


**Figure 4.2 CRISPR-corrected NC-SMCs are less apoptotic than Marfan-uncorrected NC-SMCs.**

Annexin-V staining of CRISPR-corrected, Marfan-uncorrected and MF<sup>C1242Y</sup> NC-SMCs to measure percentage of apoptotic-positive cells (i.e. FITC+). 10,000 events per sample were measured. Events are detected as a dot plot (A) or as a FL1 histogram (B) for FITC-positive cells.

### 4.3 RNA-Sequencing

As previously described, our group has established well-defined protocols to differentiate iPSC into SMCs from different embryonic origins. Here, we use SMCs derived from the neural crest (NC) origin because they express the most severe disease phenotype *in vitro*. In order to explore the differential gene expression profiles between healthy and Marfan SMCs, I differentiated iPSCs towards NC progenitors and induced SMC differentiation using media supplemented with PDGF-BB and TGF- $\beta$ 1 for twelve days (PTd12). At day twelve, early MF<sup>C1242Y</sup> NC-SMCs begin to express high mRNA levels of species of the MMP family. Further SMC maturation increased the severity of the disease profile expressed by MF<sup>C1242Y</sup> NC-SMCs *in vitro* compared to SMCs harbouring the healthy nucleotide in both alleles. Mature MF<sup>C1242Y</sup> NC-SMCs displayed elevated levels of cell-death and were highly proteolytic, which was evidenced by abnormal and excessive matrix degradation (Figure 4.3).

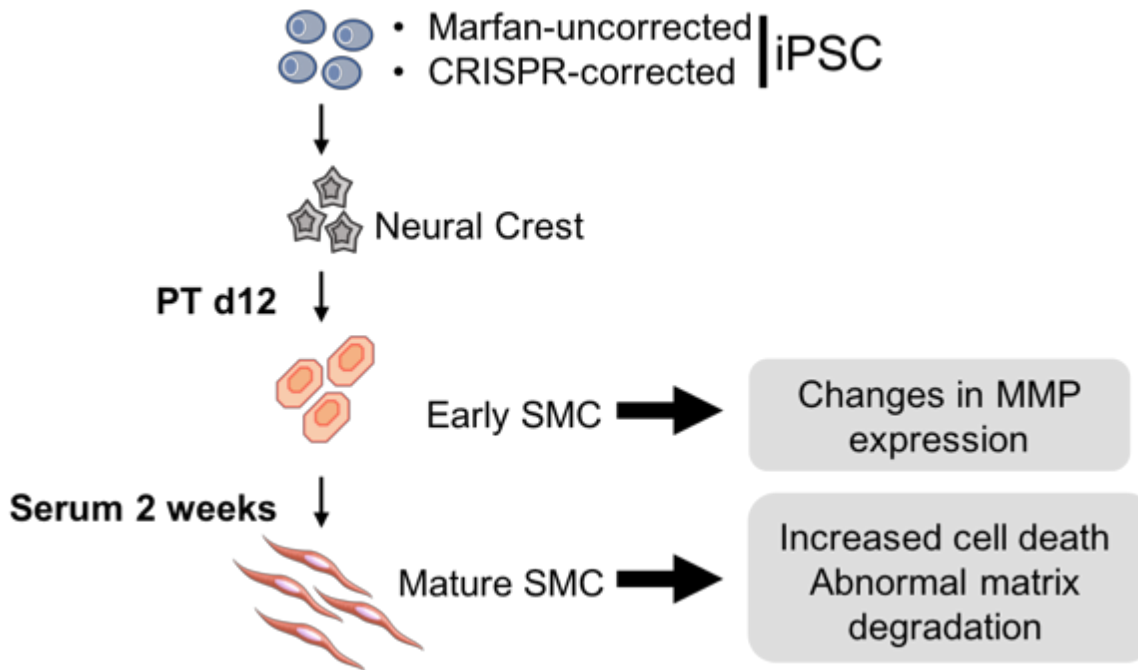


**Figure 4.3 Marfan NC-SMCs exhibit a spectrum of disease characteristics over time *in vitro***

Schematic diagram of NC-SMC differentiation from patient-derived iPSC (blue cells). Marfan NC-SMCs display elevated MMP expression levels as early as after 12 days in PDGF-BB and TGF- $\beta$  treatment (PTd12). Increased levels of cell-death and abnormal matrix degradation become more severe after serum treatment with 10% foetal bovine serum for two weeks (Serum 2 weeks).

#### 4.3.1 Quality control of total RNA samples

In order to coin the differences in gene expression profiles between healthy and Marfan NC-SMCs, CRISPR-corrected isogenic NC-SMCs were generated for transcriptomic comparisons with Marfan-uncorrected NC-SMCs. As the disease severity increases over the course of maturation stages *in vitro*, it was important to identify disease pathways that are communal and unique to the distinct differentiation time-points. Therefore, RNA samples from PTd12 and serum 2-week were collected from CRISPR-corrected and Marfan-uncorrected NC-SMCs for bulk RNA-sequencing (Figure 4.4). To assess the RNA integrity and quality, an initial assessment by electrophoresis of total RNA followed by staining with ethidium bromide was performed. Although mRNA and

long-noncoding RNA only compromise a minor portion (1-3%) of total RNA samples, it is not readily detectable by the most sensitive methods. Therefore, we assessed ribosomal RNA, which makes up >80% of total RNA samples and is considered as the benchmark for intact RNA. rRNA is comprised by the 28S and 18S rRNA species of the ribosomal unit and these were visualised on an agarose gel. Results depicted correct band sizes for the 28S (5kb) and 18S (2kb) species as well as an approximate band ratio of 2:1, indicating that that our RNA samples were intact and usable for RNA-sequencing (Figure 4.5A). Further quality control on the total RNA samples was performed using an improved analytical tool called the Agilent Bioanalyzer. Here, smaller inputs are needed to evaluate both RNA concentration and integrity, where integrity is assigned an RNA integrity number (RIN) that ranges from 1 to 10, with 10 being the least degraded. The total RNA ratio is more accurately calculated by taking the ratio of the area under the 18S and 28S rRNA peaks to the total area under the graph. Our results revealed that all RNA samples were intact with an assigned a RIN ranging between 9.50 to 10.0 (Figure 4.5B). Therefore, our samples were validated for cDNA library generation and RNA sequencing.

## Development of novel therapies for Marfan Syndrome using a human iPSC-derived disease model

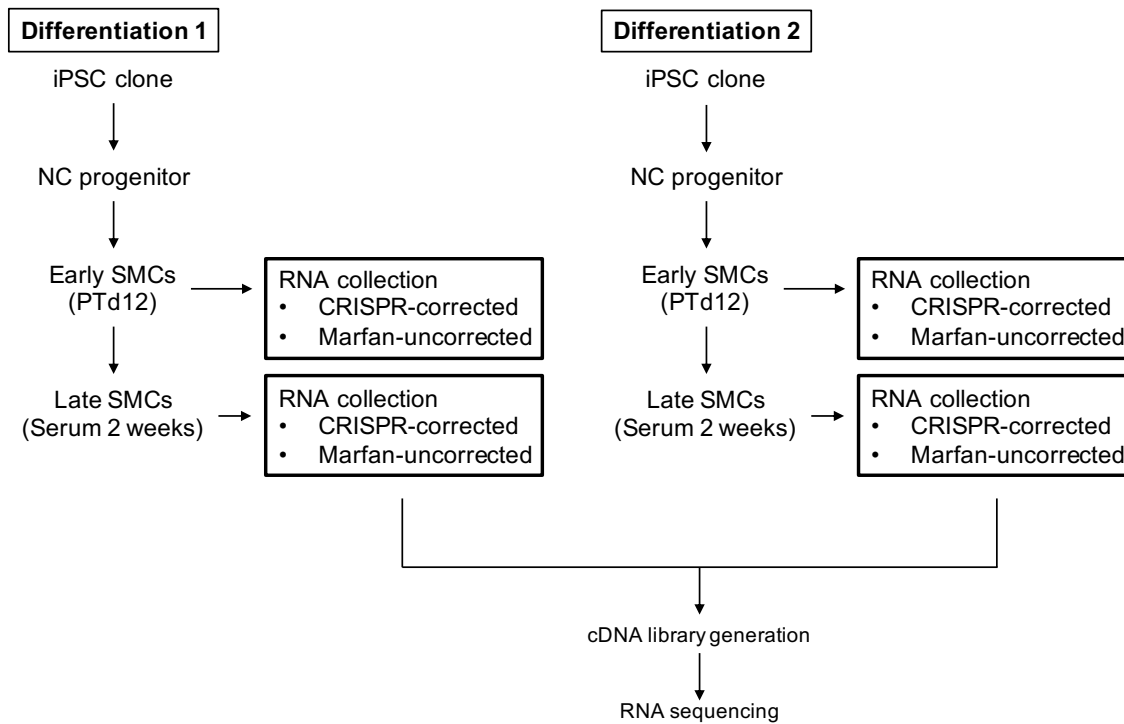


**Figure 4.4 Both early and late CRISPR-corrected and Marfan-uncorrected NC-SMCs are collected for RNA-sequencing.**

Schematic diagram of NC-SMC differentiation starting from two separate iPSC clones. Each iPSC clone was differentiated into early (PTd12) and late (serum 2 weeks) NC-SMCs for both CRISPR-corrected and Marfan-uncorrected cells respectively. RNA was collected at both early and late stages (RNA collection) for both cell lines for further cDNA library generation and transcriptomic sequencing.

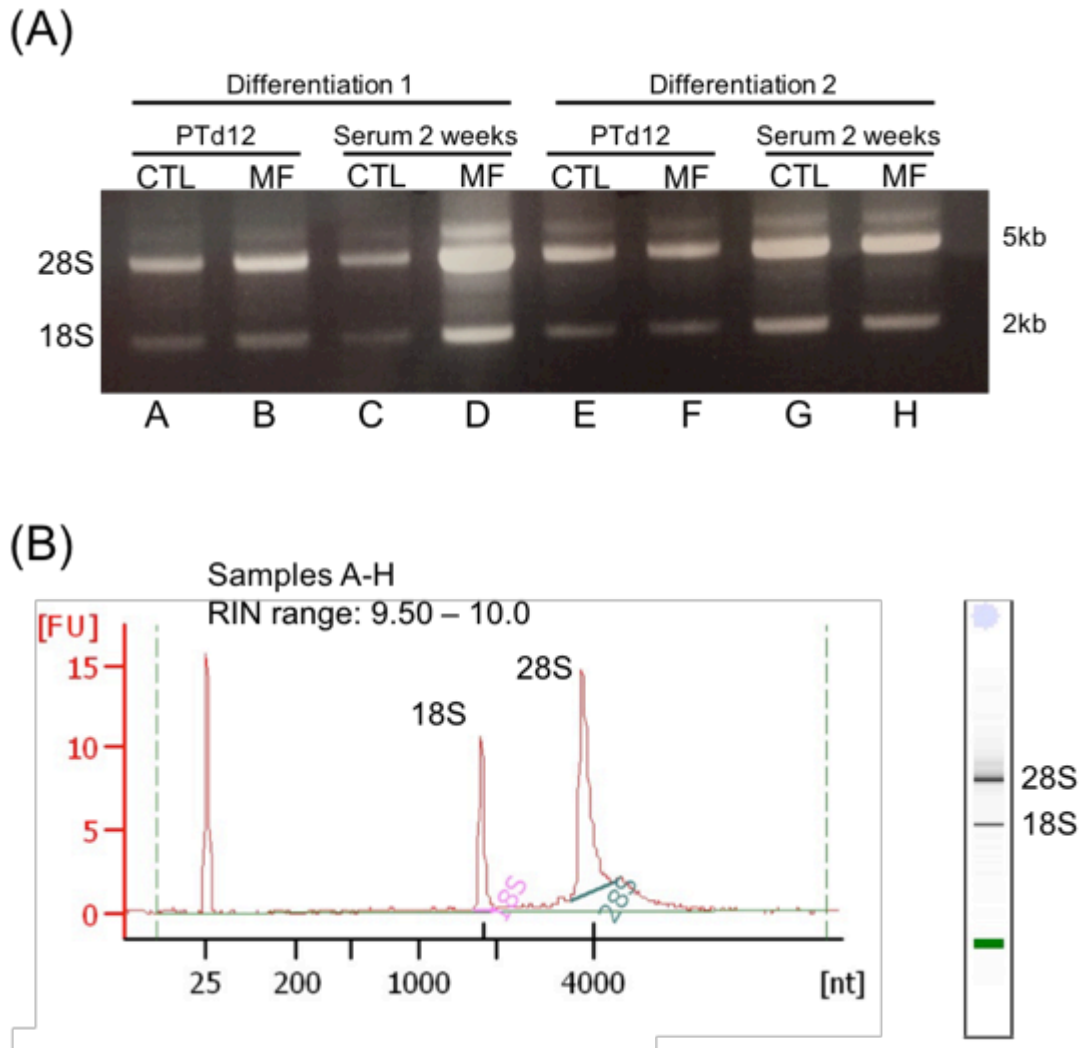


**Figure 4.5 Quality control of total RNA for samples intended for RNA-sequencing.**

(A) Gel electrophoresis of total RNA to assess ribosomal RNA (rRNA) integrity and detection of rRNA species 28S and 18S at 5kb and 2kb band-size respectively. The ratio of 28S:18S is approximately 2:1 for all samples A-H. CRISPR-corrected (CTL; A, C, E and G) and Marfan-uncorrected (MF; B, D, F and H) NC-SMCs at PTd12 (A-B and E-F) and Serum 2 weeks (C-D and G-H) for two distinct iPSC-derived NC-SMC differentiations (Differentiation 1 and Differentiation 2). (B) Bioanalyser profiles of total RNA isolated from CRISPR-corrected (CTL; A, C, E and G) and Marfan-uncorrected (MF; B, D, F and H) NC-SMCs at PTd12 (A-B and E-F) and Serum 2 weeks (C-D and G-H) with 28S:18S rRNA ratios. The area below both the 18S rRNA and 28S rRNA fragments remains constant in all samples A-H, which indicates that the RNA is intact and shows signs of limited degradation.

#### 4.3.2 DESeq2 statistical analysis of RNA-sequencing data

Each sequencing experiment was paired-end and used to generate a set of FASTQ files, which contain the bases for each read and their quality score. Reads were then aligned to the human reference transcriptome and the number of reads were counted and unambiguously assigned to genomic features. Raw counts were then used as the input for the DESeq2 package, which was used as the main statistical model to analyse our RNA-seq data. To minimise differences between samples for reads with small counts, the raw count data was transformed to the log<sub>2</sub> scale, which normalised counts to the library size. The log transformation is applied to produce a robust variance stabilising effect. The bioinformatics analysis was performed in part with the help of Dr Pierro Richiuto (AstraZeneca).

In order to visually compare the differences between samples, raw number of reads from the RNA seq data has to be transformed into usable values. In RNA-seq data, variance grows with the mean, which means that the logarithm (log<sub>2</sub>) of the normalised count values are needed to perform common statistical methods, such as principal-component analysis (PCA) and heat-maps. However, in the case of log<sub>2</sub> transformation, the resulting values create a bias, whereby the genes with low counts will tend to dominate and skew the results due to the Poisson noise inherent to small-count values. To avoid this bias, we used the DESeq2 regularised-logarithm transformation package (rlog). Here, rlog transformation shrinks the low-count values towards genes' averages across all samples making the rlog-transformed data approximately homoscedastic. Homoscedastic data means that the variance of the observed quantity is no longer dependent on the mean and that all genes have approximately an equal contribution; thus, making the data usable to directly assess similarities between samples.

Here, my data was visually displayed according to the log<sub>2</sub> transformation and compared it to the rlog transformation methods. The low counts on the bottom left-hand corner of the graph are excessively variable on the ordinary log<sub>2</sub> scale whilst the rlog transformation compresses the differences for the low-count genes for which the data would be unable to provide reliable information regardless (Figure 4.6).

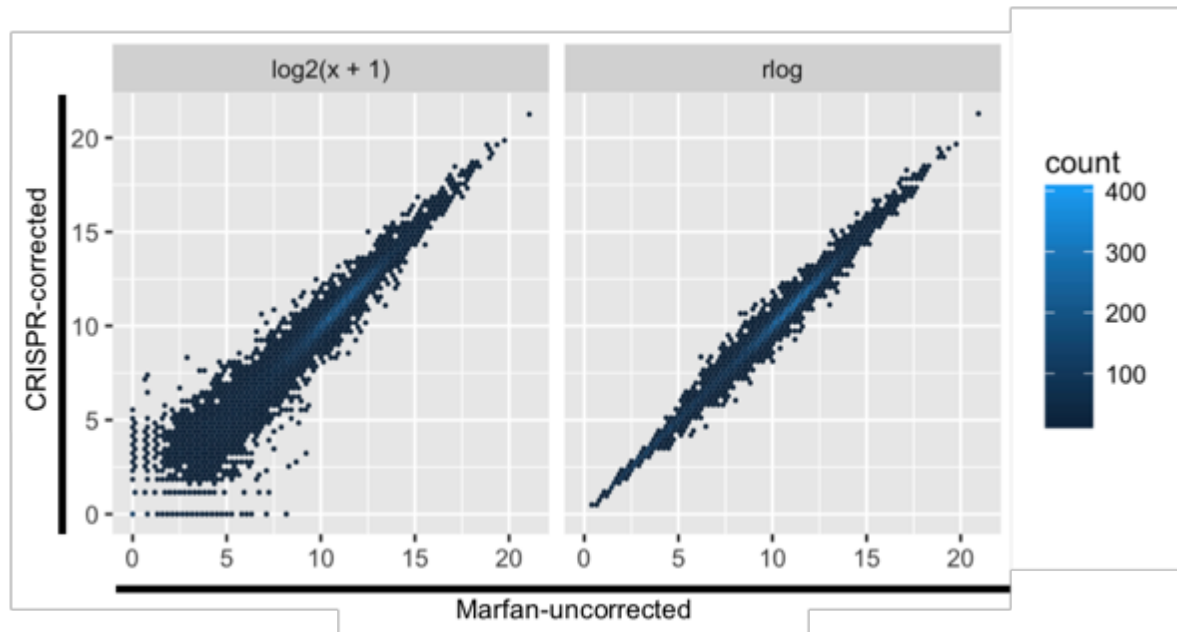


**Figure 4.6 Scatterplots of RNA sequencing data.**

Genes with low counts (bottom-left corner) are excessively variable on the ordinary logarithmic  $\log_2$  scale, whereas  $rlog$  transformation compresses the differences for these same low-count genes.

### 4.3.3 Identification of differentially expressed genes at early and late SMC differentiation stages

In order to visualise sample clustering, a heatmap of sample-to-sample distances was generated using the  $rlog$  transformed values. Results showed that samples clustered primarily according to presence or absence of the pathological nucleotide. CRISPR-corrected samples segregated clearly from the Marfan-uncorrected samples. Although, CRISPR-corrected samples clustered further according to early and late differentiation stage, this time-dependent segregation was not as clear in the Marfan-uncorrected samples (Figure 4.7). Additionally, a principal component (PCA) plot was generated to optimally project the data points (i.e. our samples) onto a 2D plane. From our data, the x-axis is the direction, which most separates the data points. Therefore, we can conclude that the majority of differences (PC1) is explained by the presence or absence of the pathological nucleotide (i.e. CRISPR-corrected vs Marfan-uncorrected). The next separation is shown on the y-axis (PC2), which is explained by the stage of differentiation stage (i.e. early vs late). The percentage of total variance of each particular PC is noted

## Development of novel therapies for Marfan Syndrome using a human iPSC-derived disease model

on the axis label (i.e. PC1 54% and PC2 22%). Hence, 54% of the variance is explained by the pathological mutation and 22% of the differences are explained by the time-point at which the NC-SMCs were collected (Figure 4.8). It is important to note that these two percentages do not add to 100% because additional dimensions exist to explain the remaining smaller variances.

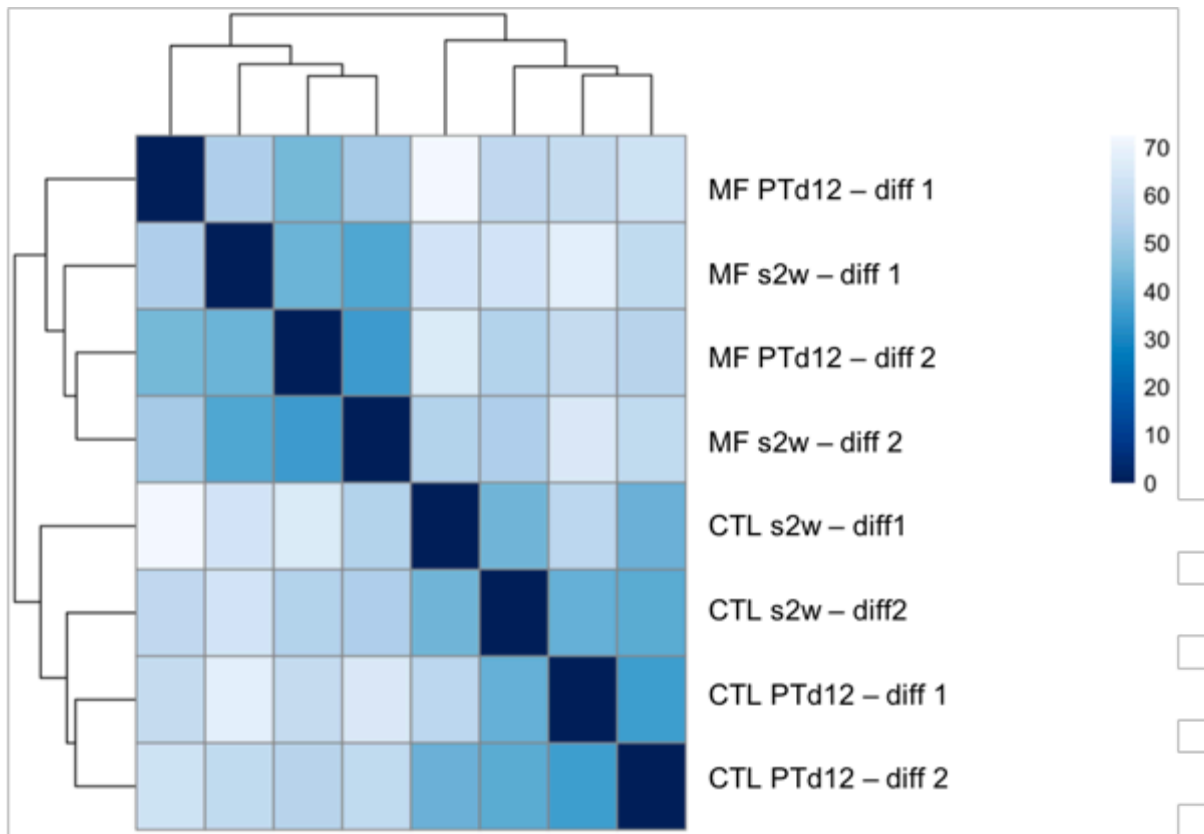


**Figure 4.7 Heat-map sample-to-sample distance distribution.**

CRISPR-corrected (CTL) from both distinct differentiations (diff1 and diff2) segregate clearly from the respective Marfan-uncorrected (MF) samples. Differentiation time-point segregation is evident in CTL samples where early (PTd12) and late (s2W, serum 2 weeks) samples cluster accordingly. However, MF samples cluster less clearly based on differentiation time-point.

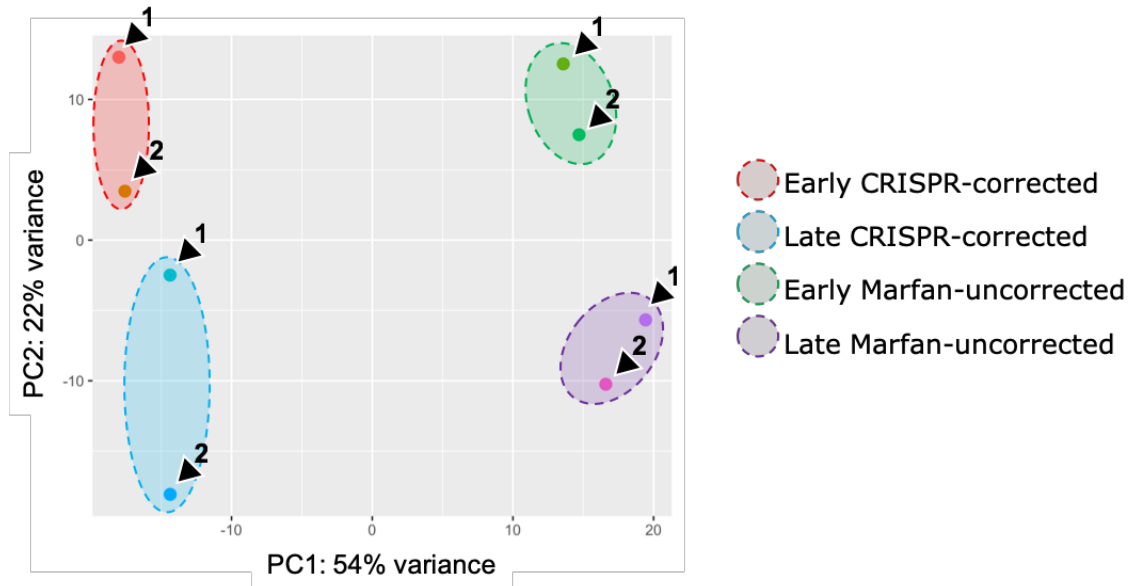


**Figure 4.8 PCA of CRISPR-corrected and Marfan-uncorrected NC-SMC at early and late differentiation stages.**

CRISPR-corrected (red and blue) and Marfan-uncorrected (green and purple) segregate clearly. The presence or absence of the disease-causing nucleotide in the MF allele explains 54% of the variance (PC1). The differentiation time-point explains 22% of the variance amongst samples (PC2). Two individual differentiations were initiated from the MF<sup>C1242Y</sup> patient iPSC line and the identity of the differentiated population is labelled by a 1 and 2 (black triangles), respectively.

In order to identify the genes significantly differentially expressed, a cut-off was set to identify genes that had an average fold-change (avgFC) higher or equal to 2.5 and a p adjusted value (Adj pval) less than or equal to 0.05. Volcano plots were generated to measure the statistical significance ( $-\log_{10}(\text{Adj pval})$ ) against the avgFC between Marfan-uncorrected NC-SMCs and CRISPR-corrected NC-SMCs at both early and late differentiation stages. Results demonstrated that genes that are farther to the left (upregulated in CRISPR-corrected NC-SMCs) and right (upregulated in Marfan-uncorrected NC-SMCs) sides of the plots are highly dysregulated, whilst the highly significant changes appear higher up on the plot DE genes with an avgFC of 2.5 and an adj pval of 0.05 are represented as green dots (Figure 4.9).

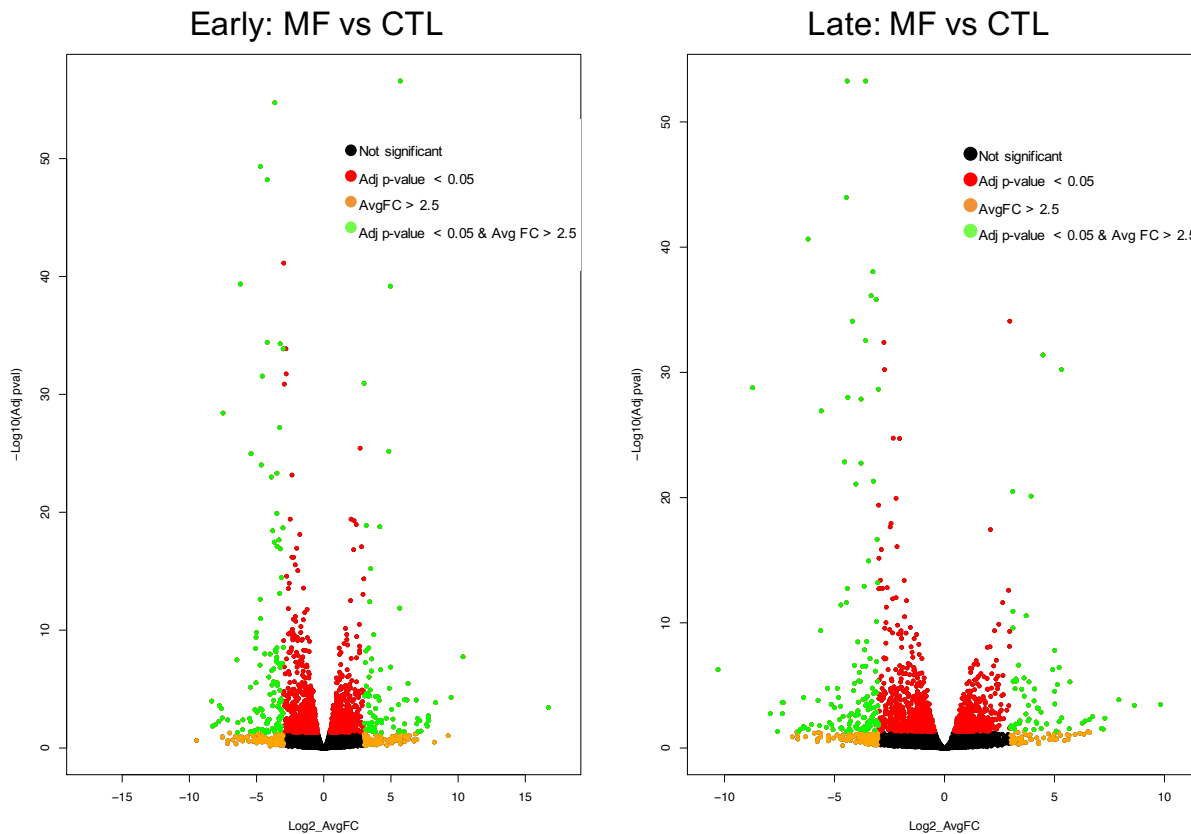


**Figure 4.9** Volcano plots differentially expressed gene distribution of CRISPR-corrected and Marfan-uncorrected NC-SMC at early and late differentiation stages.

Marfan-uncorrected (MF) and CRISPR-corrected NC-SMCs (CTL) differentially expressed genes are visually displayed in a volcano plot for both early (right plot) and late (left plot) stages respectively. Genes that are significantly upregulated in MF and downregulated in CTL feature to the right of the volcano plot. Conversely, genes that are significantly downregulated in MF and upregulated in CTL feature to the left of the volcano plot. Fold-change (FC) is calculated for all rlog transformed gene count and plotted against the logarithmic 10 adjusted p-value ( $-\log_{10} \text{Adj p-value}$ ). Genes with a fold change greater than 2.5 ( $\log_2 \text{avgFC} > 2.5$ ) are labelled orange, genes with an Adj p-value  $< 0.05$  are labelled red, genes that intersect both  $\log_2 \text{avgFC} > 2.5$  and Adj p-value  $< 0.05$  criteria are labelled green, and non-significant genes are labelled black.

To better visualise the significant DE genes, I generated heat-maps to highlight the differences between Marfan-uncorrected and CRISPR-corrected NC-SMCs at early and late differentiation stages of the most highly variable genes. As expected, *KLF4* and *MMP1* were significantly upregulated in Marfan-uncorrected NC-SMCs at the early stage of PTd12. Consistent with upregulated MMP expression levels, Marfan-uncorrected NC-SMCs displayed downregulation of members of the ADAMT metallopeptidase with thrombospondin family (*ADAMTS16* and *ADAMTSL2*), which are known to be dysregulated in models of aneurysm<sup>120</sup>. In addition, several members of collagen protein family (*COL9A3* and *COL8A2*) were downregulated, which suggests an abnormality in the production of extracellular matrix proteins that is consistent with the Marfan phenotype exhibited *in vitro*. Furthermore, various ion-channel subunits, such as *KCNQ5* and *KCNH2* showed a dysregulated expression profile relative to CRISPR-corrected NC-SMCs at both differentiation stages. This potentially suggests that Marfan-uncorrected NC-SMCs respond abnormally to mechano-sensing information due to a dysregulation at the level of their expressed ion channels.

To explore the Wnt cascade and its potential role in aortic aneurysm, a sub-set of Wnt signalling pathway partners were identified as differentially expressed at both early and late stages of differentiation. From the list of DEGs for both early (38 genes) and late (34 genes) differentiation stages, 7 genes were common to both groups and dysregulated in both conditions (*FZD1*, *GNAI4*, *ITGA8*, *MMP8*, *PI3KAP1*, *PIK3IP1* and *WISPI*). One example included *WISPI*, a downstream target of the Wnt pathway, which is shown as significantly downregulated at both PTd12 and serum 2 weeks in Marfan-uncorrected NC-SMCs in comparison to their isogenic counterparts (Figure 4.10 A and B). *GSK3B* is a promising target for reducing MMP-activity in our disease model and is also a well-documented modulator of the Wnt signalling pathway, which will be further discussed in our Drug-Screen and Target Validation chapter. Therefore, Marfan-uncorrected NC-SMCs display differences in the Wnt pathway at both the level of transcriptomics and downstream targets. All significant differentially expressed genes are listed in the Appendix 8.1

To assess the maturation of these cell types, differentially expressed genes associated with the acquisition of a vascular SMC phenotype were compared at both early and late stages of differentiation for CRISPR-corrected and Marfan-uncorrected NC-SMCs respectively. The SMC gene panel included *CNN1*, *ACTA2*, *MYH11* and *TAGLN* and all showed a negative Log<sub>2</sub>-fold change (Log<sub>2</sub>FC) in the early condition compared

## Development of novel therapies for Marfan Syndrome using a human iPSC-derived disease model

to the later differentiation stage, suggesting that the mature SMC genetic signature is progressively acquired (Appendix 8.2). This expression dynamic was observed in both Marfan-uncorrected and CRISPR-corrected NC-SMCs. However, all Log2FC were not associated with a significant p-adj value (i.e.  $p\text{-adj} > 0.05$ ), which suggests a need to RNA-sequence additional biological replicates in order to statistically reflect the biological SMC profile displayed by our iPSC-derived Marfan disease model (Figure 1.8)

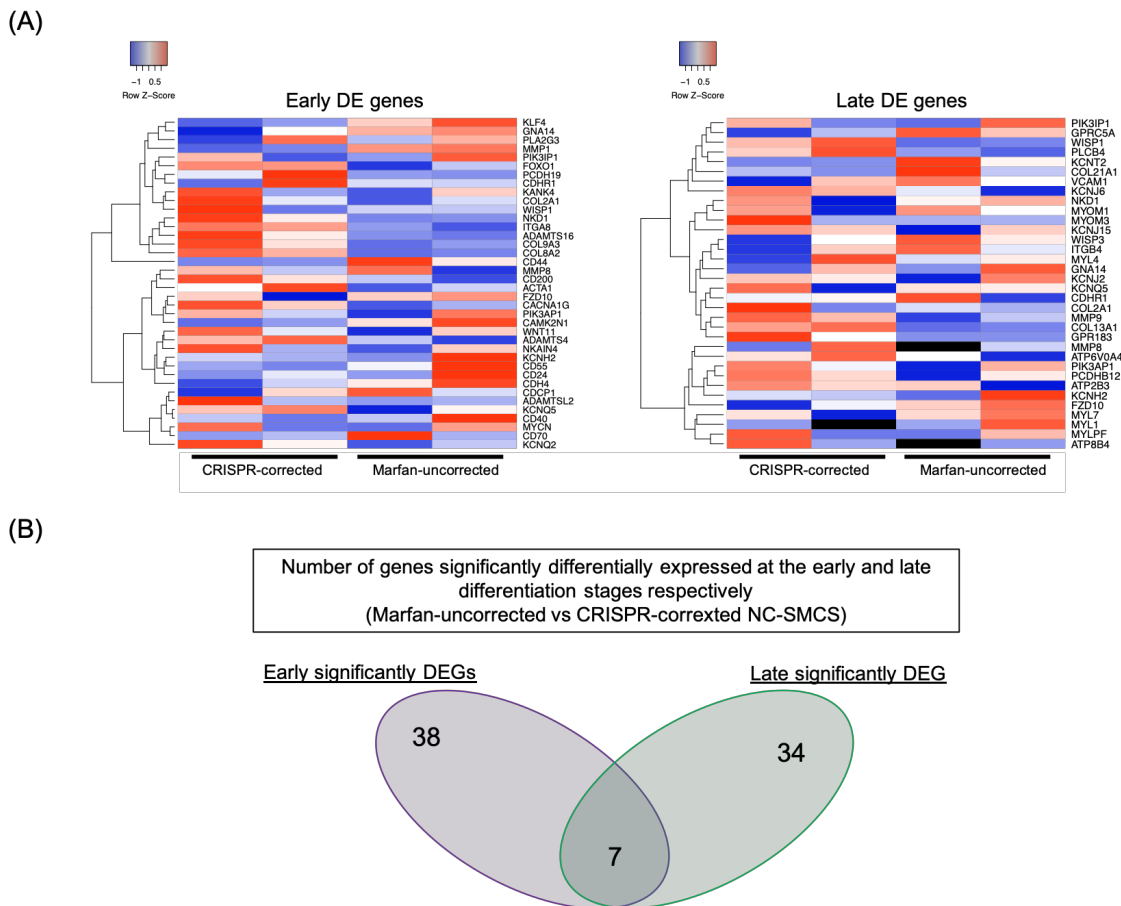


**Figure 4.10 Heat-maps and corresponding Venn diagram of differentially expressed genes of CRISPR-corrected and Marfan-uncorrected NC-SMC at early and late differentiation stages.**

(A) Heat-map of a sub-set of differentially expressed genes in CRISPR-corrected and Marfan-uncorrected NC-SMCs at early (right heat-map) and late (left heat-map) differentiation stages. Rlog transformed data for each gene of interest was normalised to z-score by colour key and density plot, namely, the from-blue-to-red colour represents the value of gene expression low to high. Rows were clustered based on Euclidean distance. DE genes are selected on log fold-change  $> 2.5$  and Adj p-value  $< 0.05$ . (B) Out of the 38 and 34 DEGs for early and late conditions respectively, 7 genes were commonly dysregulated in differentiation stages.

#### 4.3.4 Identification of potential disease-causing pathways based on DE gene panel

In order to identify novel disease-causing pathways, a gene ontology (GO) term enrichment analysis was performed whereby each DE gene dataset at both early and late stages respectively were assigned to a set of predesigned pathways depending on their functional characteristics. Initially, we mapped each dataset to the publicly-available Kegg pathway dataset as an initial enrichment analysis. The top GO terms included pathways such as the Wnt signalling and PI3K-Akt signalling at both early and late stages (Figure 4.11). We were primarily interested in these pathways as GSK3 $\beta$  is a modulator of both signalling pathways and both pathways are known to be involved in the regulation and maintenance of apoptosis and proliferation levels<sup>121,122</sup>.

## Development of novel therapies for Marfan Syndrome using a human iPSC-derived disease model

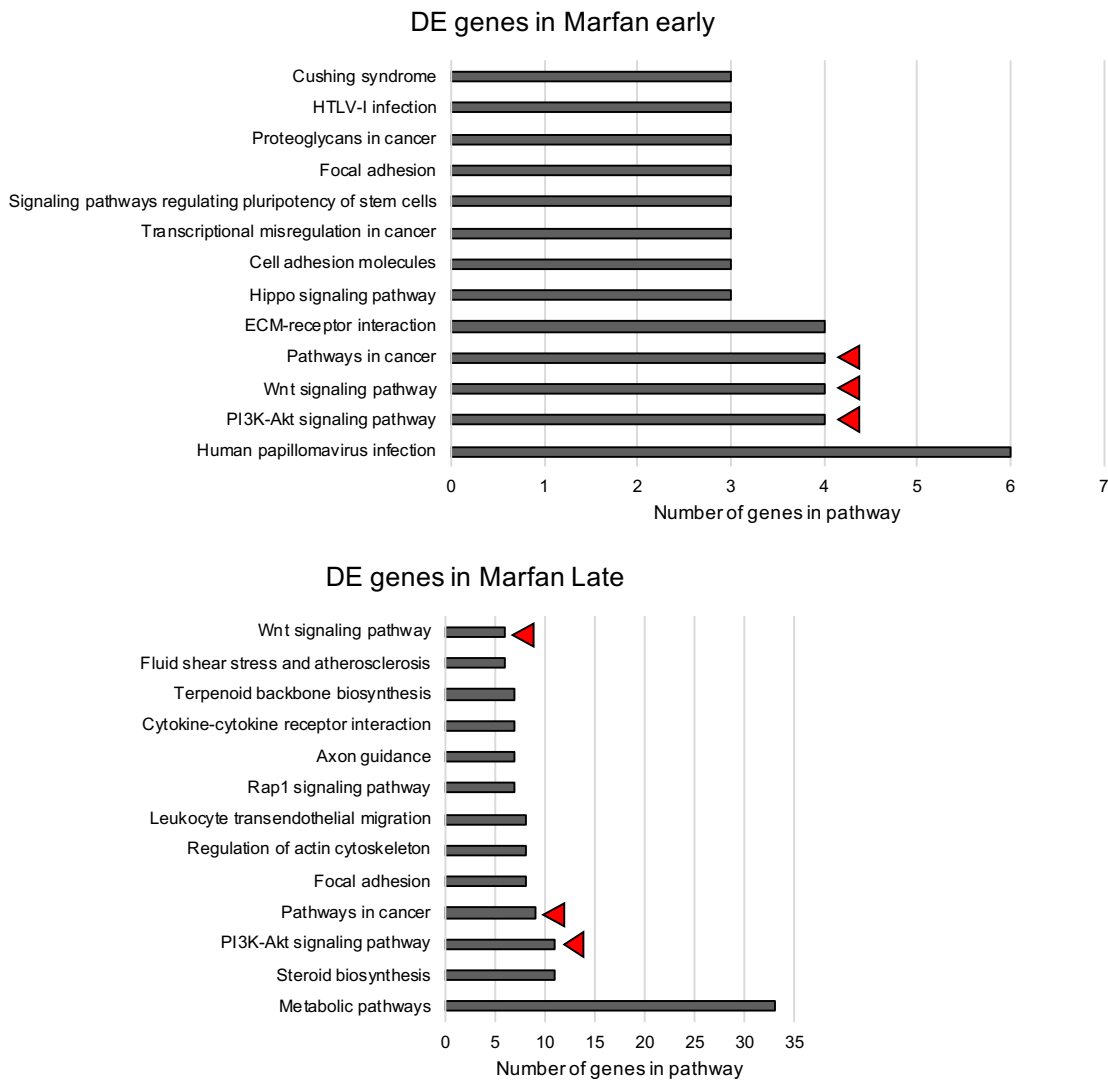


**Figure 4.11 Kegg pathway analysis from significantly DE genes enrichment.**

A list of top 13 pathways, generated from the Kegg database, significantly associated to the significantly DE genes (i.e.  $\log FC > 2.5$  and  $\text{Adj } p\text{-value} < 0.05$ ) from both early and late differentiation datasets. Pathways in cancer, Wnt signalling pathway and PI3K-Akt signalling pathway are present in both early and late lists (red triangle).

In order to statistically analyse the GO terms, the more thorough enrichment analysis tool, ingenuity pathway analysis (IPA), was used to score the top pathways associated to the DE genes based on p-value, ratio and z-score at both early and late stages. The IPA platform incorporates three statistical values to generate a list of pathways predicted to be associated with each respective significant DE gene list, which include the p-value, the ratio and the z-score. The p-value represents the probability of a gene being present in the list of total genes annotated to a particular GO term. The higher the  $\log_{10}$  value, the more significant the particular GO term associated with the group of genes of interest and the less likely the observed annotation to the group of genes occurs by chance. The ratio indicates the ratio of genes from the dataset, which successfully map to the associated pathway divided by the total number of annotated genes that map to the same pathway. Finally, the z-score indicates whether a particular pathway represents genes with increased mRNA expression (green) or decreased mRNA expression (red) (Figure 4.12).

## Development of novel therapies for Marfan Syndrome using a human iPSC-derived disease model

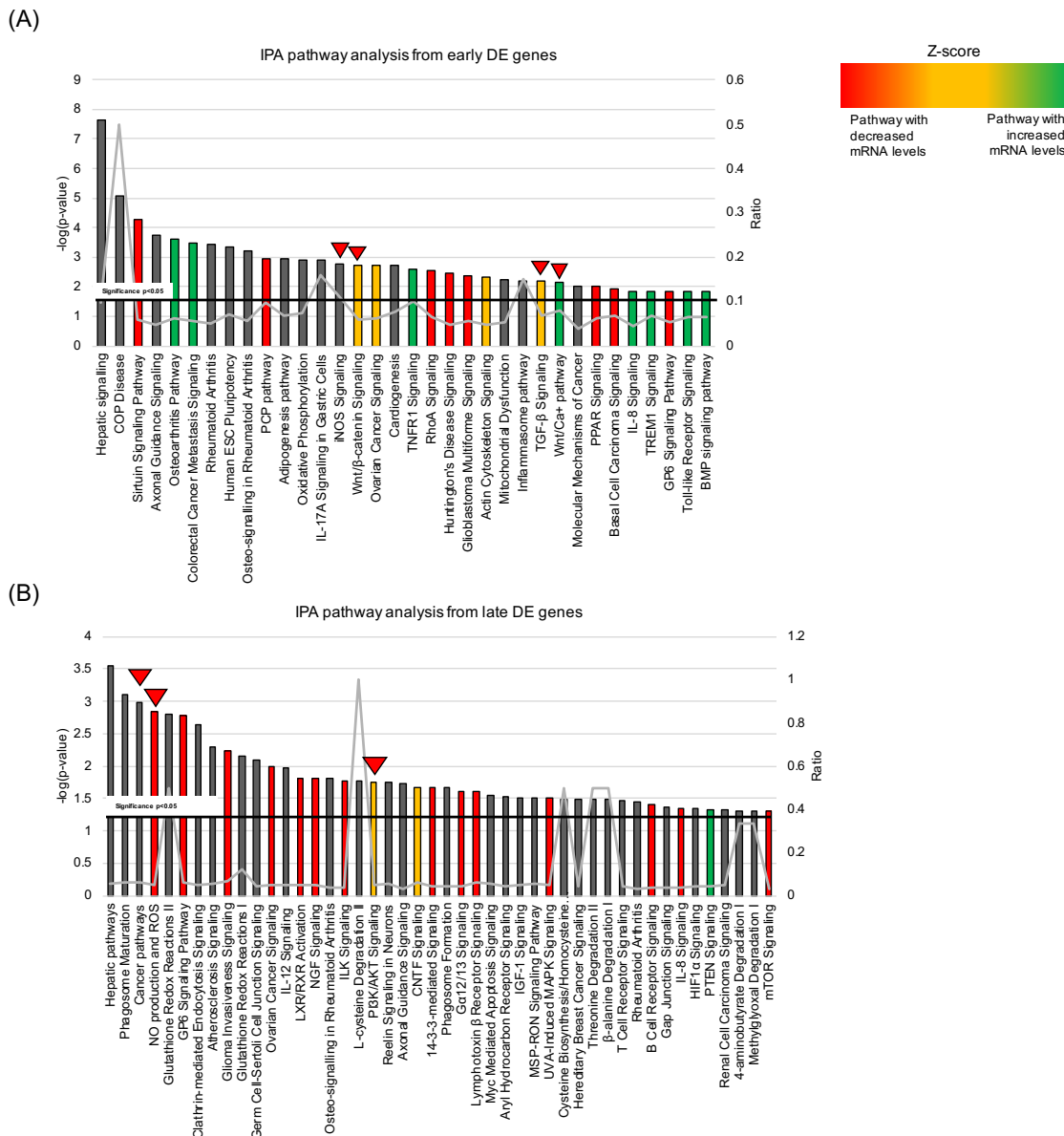


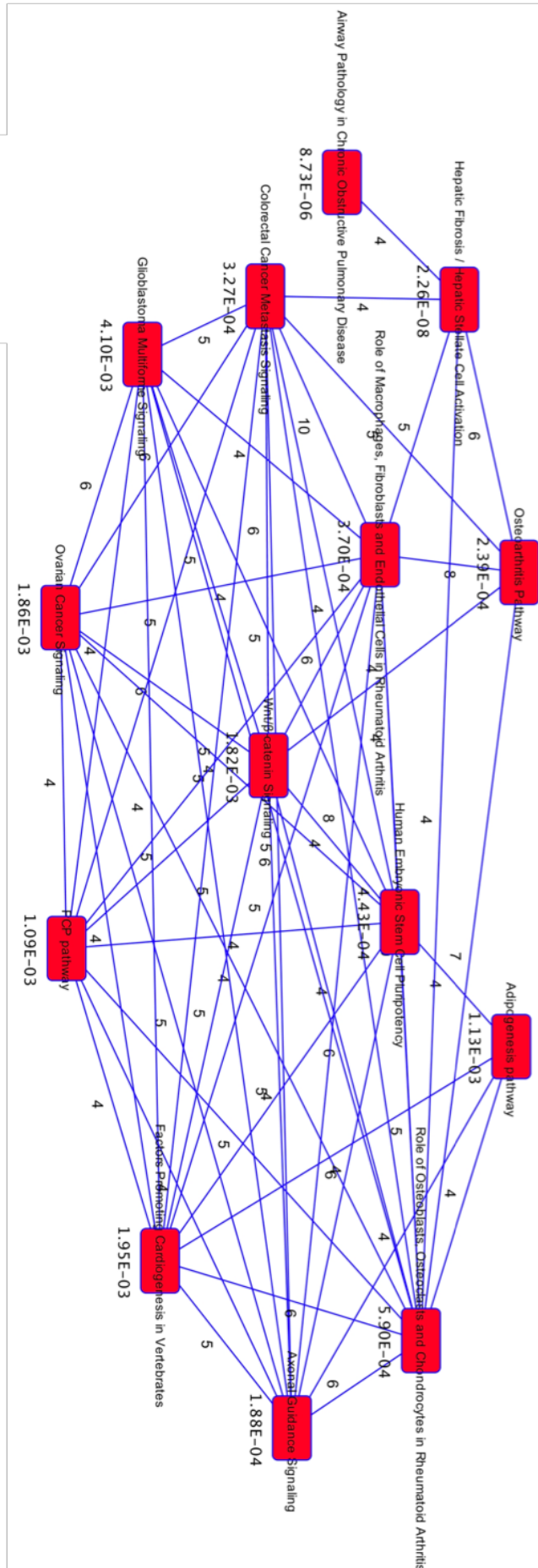
**Figure 4.12 IPA pathway analysis from significantly DE genes enrichment.**

Top pathways were identified based on Adj p-value, ratio and z-score for significantly DE genes at early (A) and late (B) stages. The p-value ( $p < 0.05$ ) represents the probability of a gene being present in the list of total genes annotated to a particular GO term. The ratio indicates the ratio of genes from the dataset, which successfully map to the associated pathway divided by the total number of annotated genes that map to the same pathway. The z-score indicates whether a particular pathway represents genes with increased mRNA expression (green) or decreased mRNA expression (red). Pathways that are grey didn't have a calculated z-score. Pathways of interest are labelled with a red-triangle.

Here, our results indicate that the early DE genes set are associated to a set of pathways, which include Wnt/ $\beta$ -catenin signalling and the TGF- $\beta$  pathway. Similarly, the respective DE genes at the late differentiation stage are significantly associated with the PI3K/Akt pathway and mTOR pathway, which both encapsulate the Wnt/ $\beta$ -catenin signalling pathway. A network was generated to visually represent the most interconnected pathways predictably associated to the combination of early and late DE genes datasets. Again, the Wnt pathway was identified as significantly most-interconnected (Figure 4.13). Finally, to identify key gene regulatory networks, an interactome was generated, whereby communities of highly connected genes and protein form interconnected clusters. The largest connected component (LCC) is composed of the most connected nodes. Unsurprisingly, my results show that MMP2, a primary connected node, is part of the LCC that links genes and proteins that include FBN1. However, the same interconnected network included collagen family members (COL12A1, COL4A2, COL5A1 and COL2A1) and a mechano-sensing channel identified as PIEZO1, which suggests a link between SMC stiffness, matrix-degradation abnormalities and mechano-sensitivity in Marfan SMCs (Figure 4.14).

**Figure 4.13 Interaction network of predicated canonical pathways based on the early DE gene dataset.**

A network of interconnect pathways for which the p-value indicates how significantly the genes in the DE list populate this particular pathway. Amongst the list of pathways, the Wnt/b-catenin signalling pathway (Adj p-value 1.82E-03) is significantly associated to the genes that are differentially expressed at the early differentiation stage between Marfan-uncorrected and CRISPR-corrected NC-SMCs.



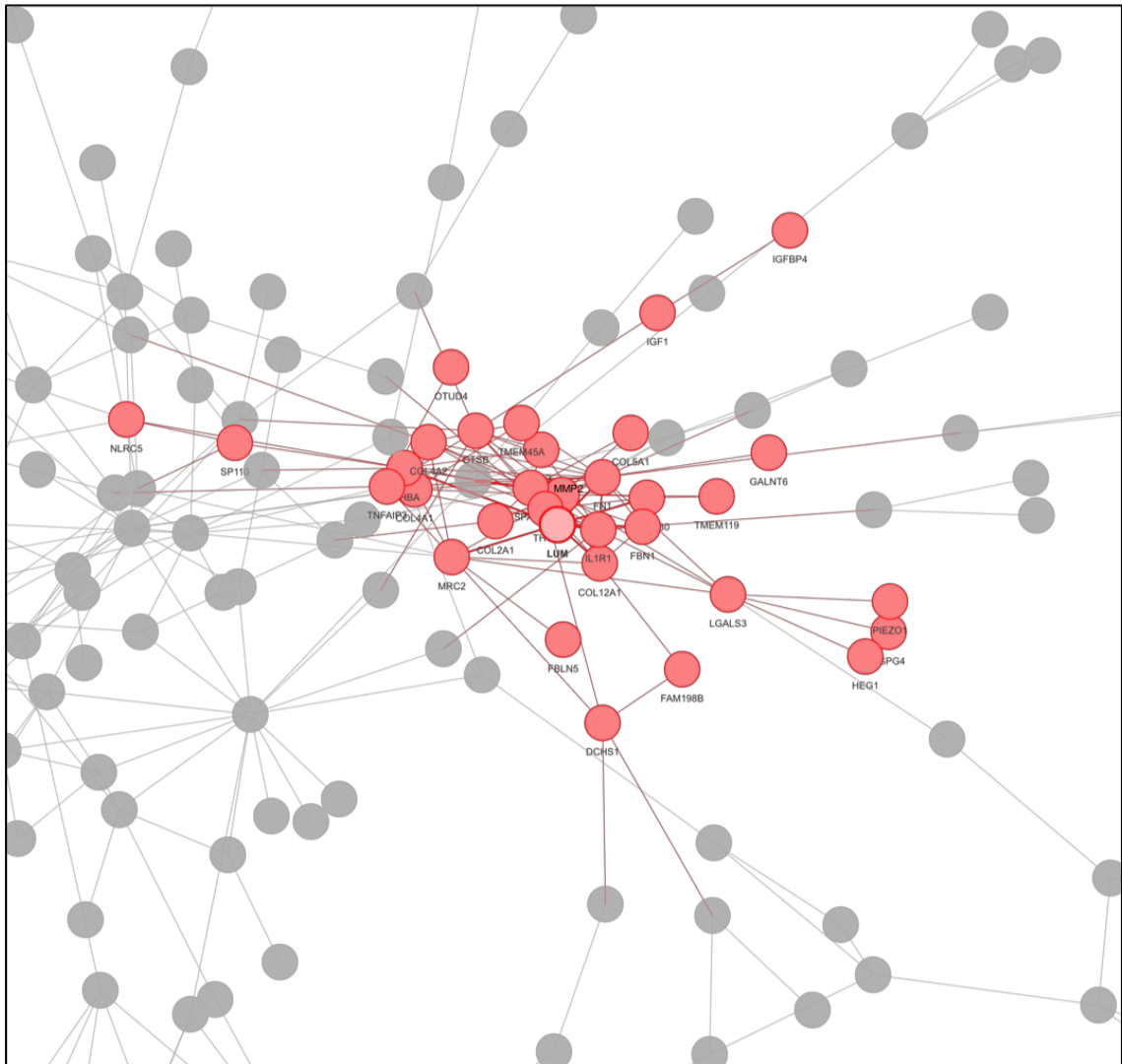


**Figure 4.14 Protein interactome of largest connected component.**

A protein interactome predicted from the early DE dataset identifies multiple clusters of predicted interacting proteins and gene targets. The largest interacting cluster of proteins, the largest connect component (LCC), highlighted in red shows the predicted interaction of MMP2, collagen family members (e.g. COL12A1) and mechano-sensing channels (e.g. PIEZO1).

## 4.4 Conclusions

In this chapter, the transcriptomic profiles of early and late patient-derived NC-SMCs, harbouring the Marfan mutation C1242Y in exon 30 of *FBNI*, were compared to the respective CRISPR-corrected NC-SMCs profiles. Therefore, the work presented in this chapter aimed to identify transcriptomic signatures and novel disease-causing pathways that are responsible for the phenotypic abnormalities displayed by our *in vitro* MFS disease model.

To obtain an overview of gene expression changes, a heat-map and PCA plots were generated, which demonstrated that uncorrected MFS NC-SMCs derived from two individual iPSCs-based differentiations clustered together, whilst isogenic controls clustered separately. The clustering analysis showed that the presence or absence of the pathological mutation is the first component, which provokes the segregation of the RNA-sequencing samples. Samples then further clustered according to the differentiation time-point, suggesting an impact of *in vitro* SMC maturation on the transcriptomic landscape. Taken together, these results suggest that isogenic controls have reverted to a healthy gene expression profile after repair of the C1242Y point-mutation in exon 30. Similar approaches have been used to understand the underlying molecular pathology of neurodegenerative disease<sup>123</sup>, diabetes<sup>124</sup> and cardiac hypertrophy<sup>125</sup> using adequate human iPSC-based complex disease modelling systems.

Differential gene expression analysis revealed a list of significantly associated pathways, which included the Wnt/ $\beta$ -catenin pathway as a promising pathway for further investigation. Aberrant activation of Wnt signalling and upregulation of Wnt target genes have previously been detected in the arterial intima and media of human and murine tissue sections during ageing, which is an important risk factor for abdominal aneurysm and atherosclerosis progression<sup>126</sup>. Additional growing evidence promotes a role for Wnt signalling in pathological hypertrophy after myocardial infarction<sup>127</sup> and this pathway may be an interesting target to pursue for aneurysm treatment, whereby tightening of leaky vessels and tissue remodelling are desirable<sup>128</sup>. Therefore, the Wnt transduction pathway and its respective mediators may be interesting for therapeutic intervention in cardiovascular pathology and these strategies will be further discussed in Chapter 6. Furthermore, any detected dysfunction in biological pathways can be further validated using our battery of phenotypic assays that characterise our MFS *in vitro* system.

# 5 PHENOTYPIC DRUG SCREEN TO IDENTIFY PUTATIVE NOVEL DISEASE DRIVERS IN MFS

## 5.1 Objectives of this Chapter

In this chapter, I aimed to develop a phenotypic assay capable of reliably identifying small molecule inhibitors (SMI) with the potential of restoring a healthy phenotype in our MFS disease model. I chose to investigate the severe disease characteristics exhibited by our *in vitro* system, which are important properties observed in tissue sections of patients with MFS. As previously described, MF<sup>C1242Y</sup> NC-SMCs are highly proteolytic and apoptotic. The complexity of the signalling pathways that drive both disease features is exhibited in our *in vitro* disease model whereby ERK1/2 regulates matrix degradation and p38 MAPK governs cell-death in addition to proteolysis, since p38 MAPK inhibitors were shown to restore fibrillin-1 deposition and reduce abnormal apoptosis in MF<sup>C1242Y</sup> NC-SMCs

For the purpose of developing a medium-throughput drug screen, I chose to investigate matrix degradation as a read-out for the drug-screen because it is an easier feature to measure in large numbers in comparison to cell-death. MF<sup>C1242Y</sup> NC-SMCs exhibit a powerful ability to degrade extracellular matrix and, in combination, release a panel of proteolytic enzymes that include MMPs. Therefore, abnormal MMP expression levels were selected as the initial screening feature and a selection of SMIs were monitored for their ability to reduce MMP activity.

Furthermore, our *in vitro* model enables to observe the disease progression of NC-derived SMCs from an early developmental stage (PTd12) to a more mature stage (serum 2 weeks), which may mimic disease progression in MFS patients<sup>28</sup>. MF<sup>C1242Y</sup> NC-SMCs begin to display abnormal matrix remodelling when cultured in serum for further maturation. Thus, MF<sup>C1242Y</sup> NC-SMCs were matured in serum for two weeks and then subjected to an unbiased medium-throughput drug-screen to potentially capture the majority of pathways involved in driving the matrix abnormalities displayed by the pathology. In my assay, the panel of MMP-reducing SMIs preferentially targeted GSK3 $\beta$ . Here, we further explore the potential dysregulation of GSK3 $\beta$  in our MFS model at the molecular level. I further investigate the role of GSK3 $\beta$  in other the phenotypic properties by focusing on the impact of GSK3 $\beta$  inhibition on cell-death. I also examine additional targets linked to GSK3 $\beta$  and if their dysregulation sheds light on the abnormal pathways governing Marfan Syndrome. Finally, I attempt to suggest a model by which GSK3 $\beta$  inhibition could therapeutically benefit our disease model for Marfan Syndrome.

## 5.2 Optimisation of phenotypic assay based on MF<sup>C1242Y</sup> NC-SMCs proteolytic properties

In an attempt to first miniaturise the assay, MF<sup>C1242Y</sup> NC-SMCs were seeded in a 24-well format and cultured for 48h before any treatment was applied. Following cell attachment, MF<sup>C1242Y</sup> SMC were subjected to treatment with either a highly selective angiotensin II type 1 receptor antagonist (losartan), or a p38 MAP kinase inhibitor (SB203580). The concentration required to displace 50% of endogenous ligand binding (IC<sub>50</sub>) is 10.5nM and 0.3-0.5  $\mu$ M for losartan and SB203580, respectively. *In vivo*, these compounds have shown promising results in reversing or reducing aortic aneurysm formation in mouse models of MFS<sup>69</sup> and unpublished work by Felipe Serrano. Although losartan has not been shown to be clinically effective compared to atenolol (a  $\beta$ -blocker)<sup>80</sup>, it is important to highlight that losartan was administered at doses fifty-fold less than those used *in vivo* to reverse aneurysm progression in MFS mice models. The limited effect of losartan evaluated in clinical trials could stem from the compound being administered at too low of a dosage. Furthermore, losartan is converted by the liver into an active compound that is 10- to 40-fold higher potency than its parent compound. Prior to metabolism, losartan is still known to possess an inhibitory effect on AT<sub>1</sub>R despite it having less pharmacological activity than its resulting active metabolite<sup>129</sup>. Several studies have demonstrated that losartan and its active metabolite both have an AT<sub>1</sub>R-blockade effect<sup>130,131</sup>, suggesting that losartan is targeting AT<sub>1</sub>R in the *in vitro* SMC system used in this work.

In these experiments, MF<sup>C1242Y</sup> SMC treated with dimethyl sulfoxide (DMSO) vehicle were used as a control. Here, MF<sup>C1242Y</sup> SMC were treated for two days with losartan and SB203580 at the determined concentrations, 1 $\mu$ M and 5 $\mu$ M, respectively. On the second day, the media was refreshed with a new dose of compound for an additional two days and cells were imaged on the fifth day post-treatment. As expected, losartan and SB203580 restored the proliferation properties of MF<sup>C1242Y</sup> SMCs compared to the control group solely treated with DMSO (0.1% and 0.5%). Losartan has a more beneficial effect at 1 $\mu$ M whilst SB203580 treatment was effective at restoring proliferation both at 1 $\mu$ M and 5 $\mu$ M (Figure 5.1).

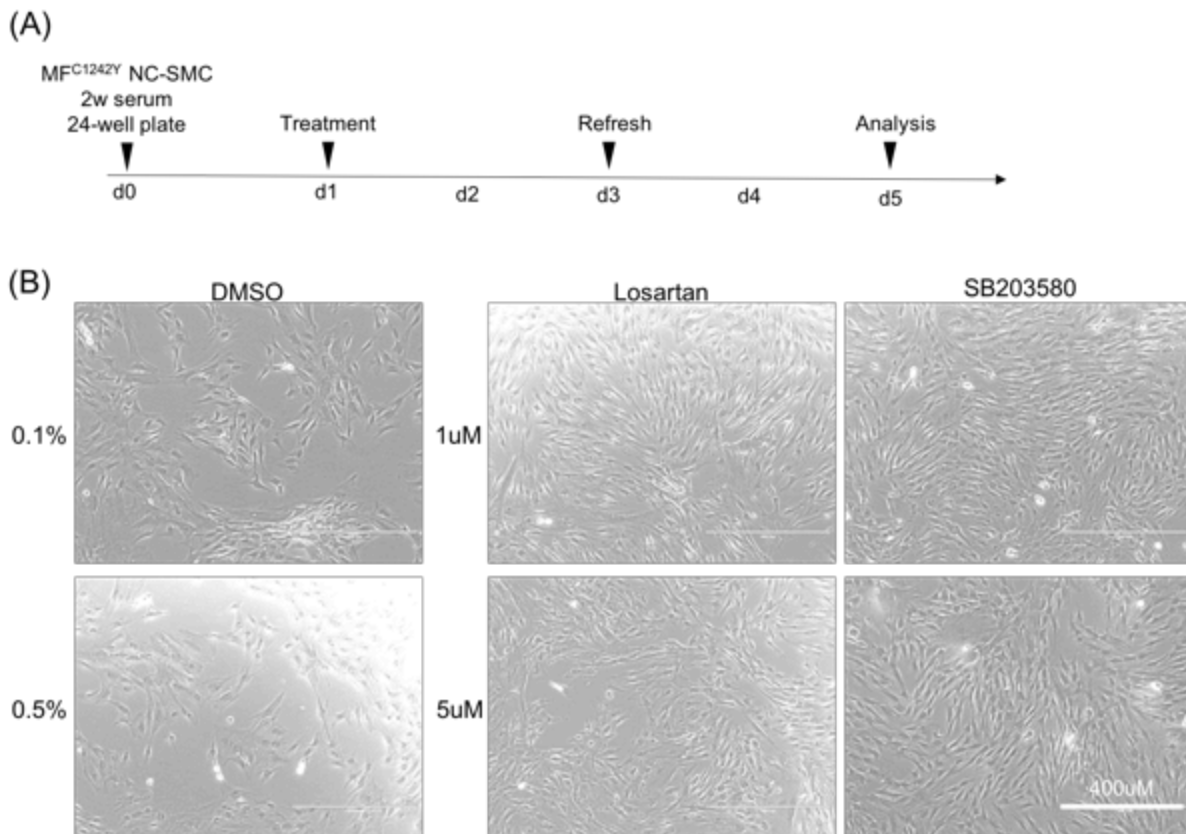


**Figure 5.1 MF<sup>C1242Y</sup> NC-SMC proliferate in response to treatment with losartan and SB203580.**

(A) Diagram of treatment protocol over a period of five days. SMCs are plated in a 24-well format on day 0 (d0) and are treated 24h later on day 1 (d1) with either losartan or SB203580 at two concentrations of 1μM or 5μM. On day 3 (d3), the media is refreshed with a new dose of compound and cells were imaged by phase microscopy on day 5 (d5) to monitor for proliferation. SMCs were treated with DMSO at 0.1% or 0.5% as a control. (B) Phase microscopic images of MF<sup>C1242Y</sup> SMCs on day 5 post-treatment treated with DMSO (0.1% or 0.5%), losartan (1μM or 5μM) or SB202580 (1μM or 5μM) respectively.

Initially, to assess the proteolytic ability of MF<sup>C1242Y</sup> SMCs, a fluorescent-based system was set-up to measure matrix degradation. MF<sup>C1242Y</sup> SMCs were seeded as previously described into a 24-well plate and treated according to the treatment protocol previously described with DMSO, losartan, or SB203580. On the fifth day post-treatment, 2000 cells per condition were seeded onto FITC-labelled gelatine-coated wells and left to attach and re-express the phenotype for 48 hours. Here, matrix degradation is visualised

by proteolysis of the gelatine labelled with a green fluorochrome, which appears as dark non-fluorescent patches within the matrix. This approach allowed me to combine matrix degradation visualisation by immunofluorescence with a semi-quantitative proliferation method. Here, I used a simple scoring technique to approximate proliferation based on the estimated number of DAPI-positive cells co-stained with calponin, a SMC-specific marker. High-degradation and/or high-proliferation were attributed “+++” whereas reduced degradation or stunted proliferation received a single “+” or “-” respectively.

As expected, losartan (1 $\mu$ M) and SB203580 (1 $\mu$ M and 5 $\mu$ M) reversed the excessive degradation properties of MF<sup>C1242Y</sup> SMCs compared to their counterparts treated with DMSO. Losartan at a higher concentration proved to be cytotoxic, which may explain the increased degradation observed in the cells treated with 5 $\mu$ M of losartan. Consistently, both losartan at 1 $\mu$ M dose and SB at 1 $\mu$ M and 5 $\mu$ M increased proliferation of MF<sup>C1242Y</sup> SMCs and these results were recorded using my semi-quantitative scoring system (Figure 5.2). These results strengthened the notion that the cells are able to display the expected disease phenotype in a 24-well format as well as respond accordingly to different SMI treatments. However, in the context of a low-throughput drug screen, reliably quantifying matrix degradation based on the level of fluorescently-labelled gelatine proved challenging. Levels of basal fluorescence remained variable as the dispensation of FITC-labelled gelatine in the ibidi imaging slides, used for the assay, was often unequal across the well. Therefore, an alternative approach to measure proteolytic properties was opted for using MMP activity as a read-out.

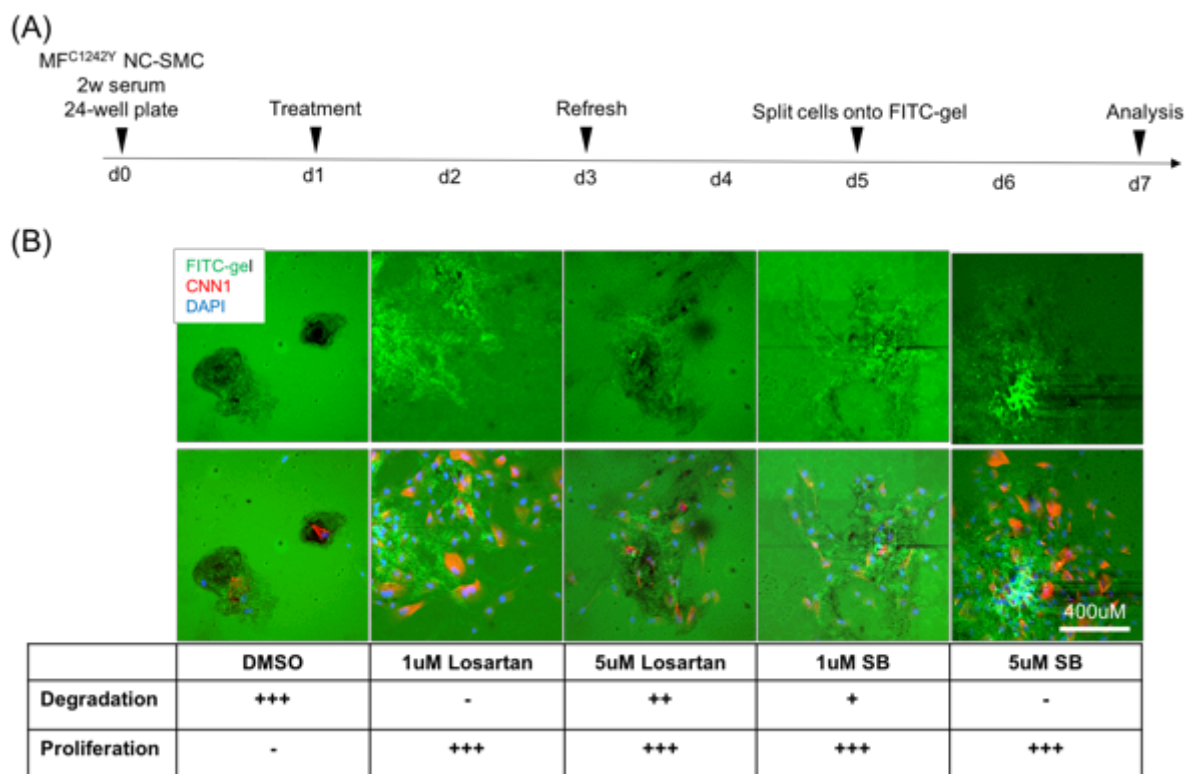


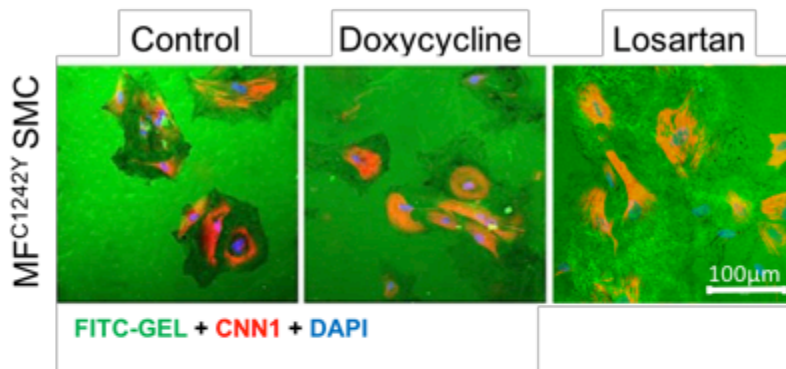
**Figure 5.2 MF<sup>C1242Y</sup> NC-SMCs treated with losartan or SB203580 show reduced proteolysis.**

(A) Diagram of the five-day drug treatment protocol followed by a two-day period (d5-d7) whereby SMCs are seeded onto a fluorescently-labelled gelatine (FITC-gel, green) to assess for matrix degradation. (B) SMCs in the different treatment groups were stained for a SMC marker, calponin (CNN1, red) and a nuclear marker, DAPI (blue). The dark patches in the FITC-gel represent matrix degradation by the SMCs. The table below displays a semi-quantitative scoring method for degradation and proliferation, which is represented from – (absence of degradation and/or proliferation), + to +++ (increasing presence of degradation and/or proliferation).

### **5.3 Designing a drug screen based on the proteolytic properties of MF<sup>C1242Y</sup> NC-SMCs**

As previously described, MF<sup>C1242Y</sup> SMC expressed elevated mRNA expression levels of MMPs relative to their WT counterparts, which correlated with increased matrix degradation (Figure 5.3). MF<sup>C1242Y</sup> SMC matured between 2 weeks to 1 month in serum were cultured in a 24-well plate and treated, according to the previously-described protocol, with the control compounds of DMSO, losartan or SB203580. To facilitate quantification analysis, MMP activity was selected as a read-out for identifying novel small molecule inhibitors (SMI) capable of reversing the pathological proteolytic phenotype in our *in vitro* MFS system. Supernatant from control and compound-treated MF<sup>C1242Y</sup> SMCs was collected for MMP activity analysis using a fluorometric kit. Briefly,  $\alpha$ -amino-3-hydroxy-5-methyl-4-isoxazolepropionic acid (AMPA) is added to the supernatant to activate MMPs present in the collected supernatant. The MMP-specific substrate is added, which upon MMP-driven cleavage releases a fluorescent signal capable of being detected and measured by a fluorescence plate-reader. Results indicated that losartan-treated MF<sup>C1242Y</sup> SMCs show a 50% decrease in MMP activity compared to DMSO-treated control MF<sup>C1242Y</sup> SMCs (Figure 5.4).

(A)



(B)

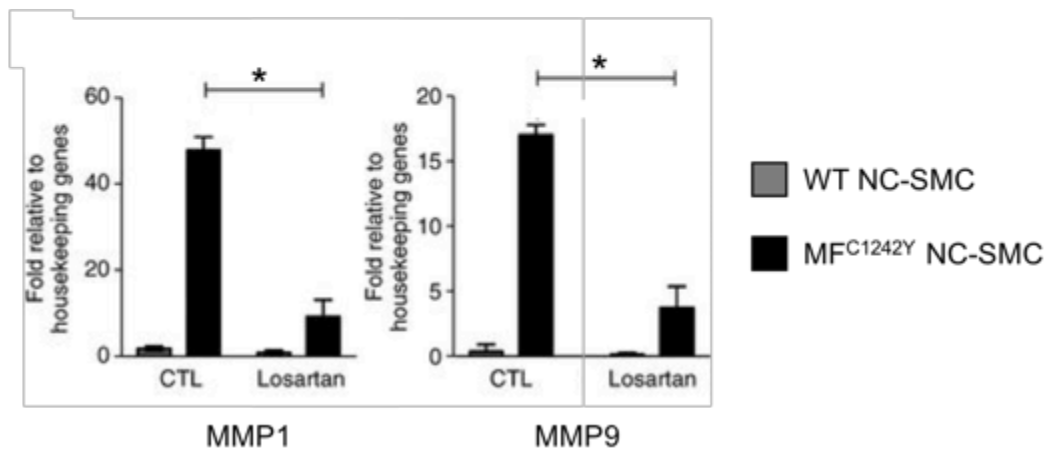


**Figure 5.3 MF<sup>C1242Y</sup> NC-SMCs treated with losartan show reduced mRNA MMP expression compared to DMSO treatment.**

(A) MF<sup>C1242Y</sup> NC-SMCs treated with doxycycline, a non-specific MMP inhibitor, and losartan and then seeded onto FITC-labelled gelatine to assess visually for matrix degradation. FITC-gel (green), calponin (CNN1, red) and DAPI (blue). (B) mRNA expression levels of members of the matrix metalloproteinase (MMP) enzyme family measured by RT-qPCR. MMP1 and MMP9 are highly expression in MF<sup>C1242Y</sup> NC-SMC relative to their WT NC-SMC counterparts. All results are representative of n=3; means ± SEM; \*p ≤ 0.05.

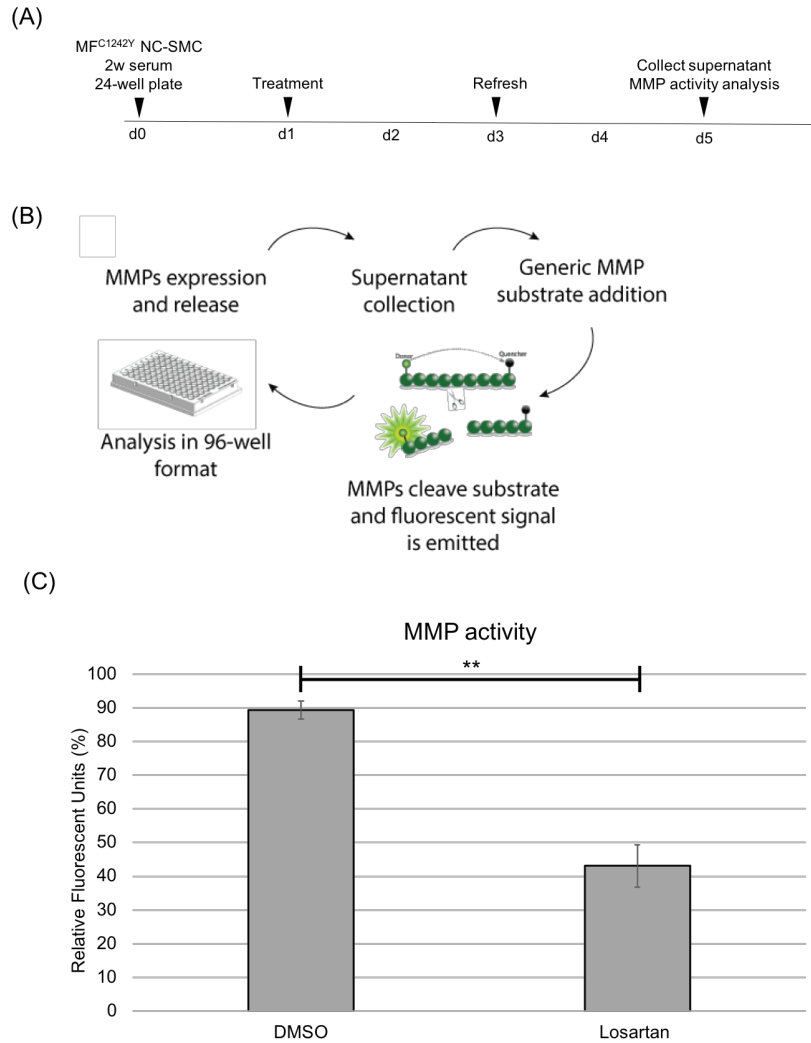


**Figure 5.4 MF<sup>C1242Y</sup> NC-SMCs treated with losartan show reduced MMP activity.**

(A) Diagram of five-day treatment protocol where MF<sup>C1242Y</sup> NC-SMCs are treated with DMSO or losartan. On the fifth day post-treatment (d5), supernatant from each treatment condition is collected to assess for MMP activity. (B) Schematic of MMP activity assay. MF<sup>C1242Y</sup> NC-SMCs express MMPs and release the enzymes into the supernatant. The supernatant of treated and control cells is collected and incubated with a MMP substrate. The MMP substrate, upon cleavage, releases a fluorescent signal that is subsequently measured by a fluorescent plate-reader. (C) MMP activity recorded in percentage of relative fluorescent units (RFU%). MF<sup>C1242Y</sup> NC-SMCs treated with losartan for 4 days show significant reduction in MMP activity compared to DMSO-treated MF<sup>C1242Y</sup> NC-SMCs. All results are representative of n=3; means ± SEM; \*\* p ≤ 0.01.

A preliminary  $Z'$ -factor, which is a value that determines the signal-to-noise ratio between positive and negative samples suitable for a high throughput assay, equal to 0.3 was calculated. Although this  $Z'$ -factor is only marginally reliable for high-throughput conditions, this value is sufficient for my low- to medium-throughput screen, which will identify putative hits for MMP-reduction that will be further validated using secondary phenotypic assays (Figure 4.5 and Table 5.1).

$$Z' \text{ factor} = 1 - \frac{3 \times (\sigma_p + \sigma_n)}{|\mu_p - \mu_n|} \quad Z' = 0.3$$

**Figure 5.5  $Z'$ -factor calculation for the MMP activity low-throughput screen.**

The  $Z'$ -factor is the widely used statistic that represents a measure of assay quality. It is based on the separation between the distributions of the positive and negative controls of a particular assay of interest. The  $Z'$ -factor, based on the signal-to-noise ratio between positive and negative samples, indicates the probability of false positive and negatives. In our MMP activity assay, the  $Z'$ -factor is equal to 0.3, which corresponds to a value marginally reliable for developing a high-throughput screen. “ $\sigma$ ”<sub>p</sub> is the standard deviation of the positive control, “ $\sigma$ ”<sub>n</sub> is the standard deviation of the negative controls, “ $\mu$ ”<sub>p</sub> is the mean of the positive control, and “ $\mu$ ”<sub>n</sub> is the mean of the negative control.

<b><math>Z'</math>-factor</b>	<b>Interpretation</b>
1	Ideal. $Z'$ -factors can never exceed 1.
0.5 – 1.0	An excellent assay.
0 - 0.5	A marginal assay.
<0	There is too much overlap between the positive and negative controls for the assay to be reliable for HTS.

**Table 5.1 Description of the range of  $Z'$ -factor values likely to be usable in a high-throughput context.**

In further attempts to miniaturise the assay, the same treatment protocol was applied to MF<sup>C1242Y</sup> SMCs seeded into a 96-well format. However, levels of MMP activity remained unchanged between DMSO-treated and losartan-treated conditions and no difference in MMP activity was detected. In order to optimise miniaturisation, additional studies adjusting cell density would need to be performed to identify the correct conditions for adequate MMP activity measurements in 96-well (Figure 5.6).

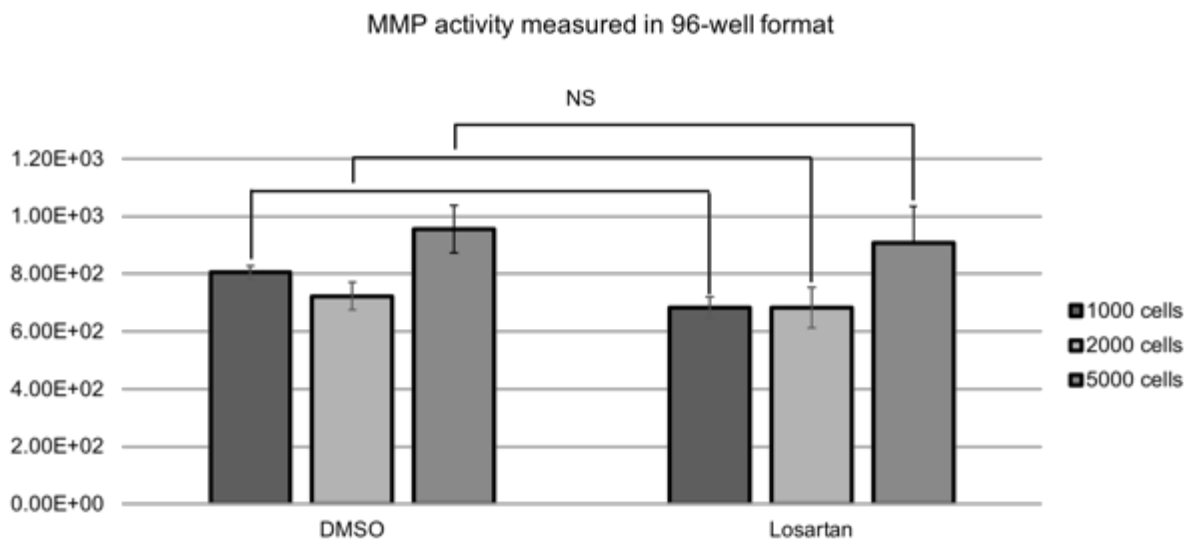


**Figure 5.6 A 96-well format did not display differences in MMP activity levels between control and losartan-treated MF<sup>C1242Y</sup> NC-SMCs.**

MF<sup>C1242Y</sup> NC-SMCs were seeded at different densities in 96-wells (1000, 2000 and 5000 cells/well respectively). SMCs were treated with losartan according to the five-day treatment protocol and DMSO was used as a control. MMP activity was normalised to cell number per cm<sup>2</sup>. All error bars are representative of n=8; means  $\pm$  SEM; ns, non-significant.

## 5.4 Pilot screen of 100 compounds from phenotypic drug library

In order to validate our phenotypic assay at a low-throughput level, a phenotypic drug library was provided by AstraZeneca Cambridge through a collaboration with the company's Pharmaceutical Target Open Innovation platform and the guidance of Dr David Smith (AstraZeneca). This library is composed of 14,000 annotated molecules, which have a well-documented list of primary and secondary targets. This is interesting for my assay's purpose as I am interested in selecting novel SMIs that are able to reverse MMP activity and subsequently identify their target to identify novel disease-driving signalling pathways.

Initially, a small pilot study was conducted using a subset of 100 compounds issued from the library. The 100-compound subset was generated using the Protein Analysis Through Evolutionary Relationships (Panther) database. This software tool allows the analysis of gene lists obtained from large-scale datasets and can filter a gene-list of interest to generate a respective pathway classification. Here, compounds were selected based on their ability to target genes implicated in known disease-driving pathways, such as the TGF- $\beta$  signalling pathway and the p38 MAP kinase pathway. In order to investigate alternative and novel mechanisms, compounds were also selected to target pathways that have not been robustly recorded in the literature to participate in the MFS pathophysiology, such as notch signalling and oxidase stress response (Figure 5.7) and (Figure 5.8 and Appendix 8.3).

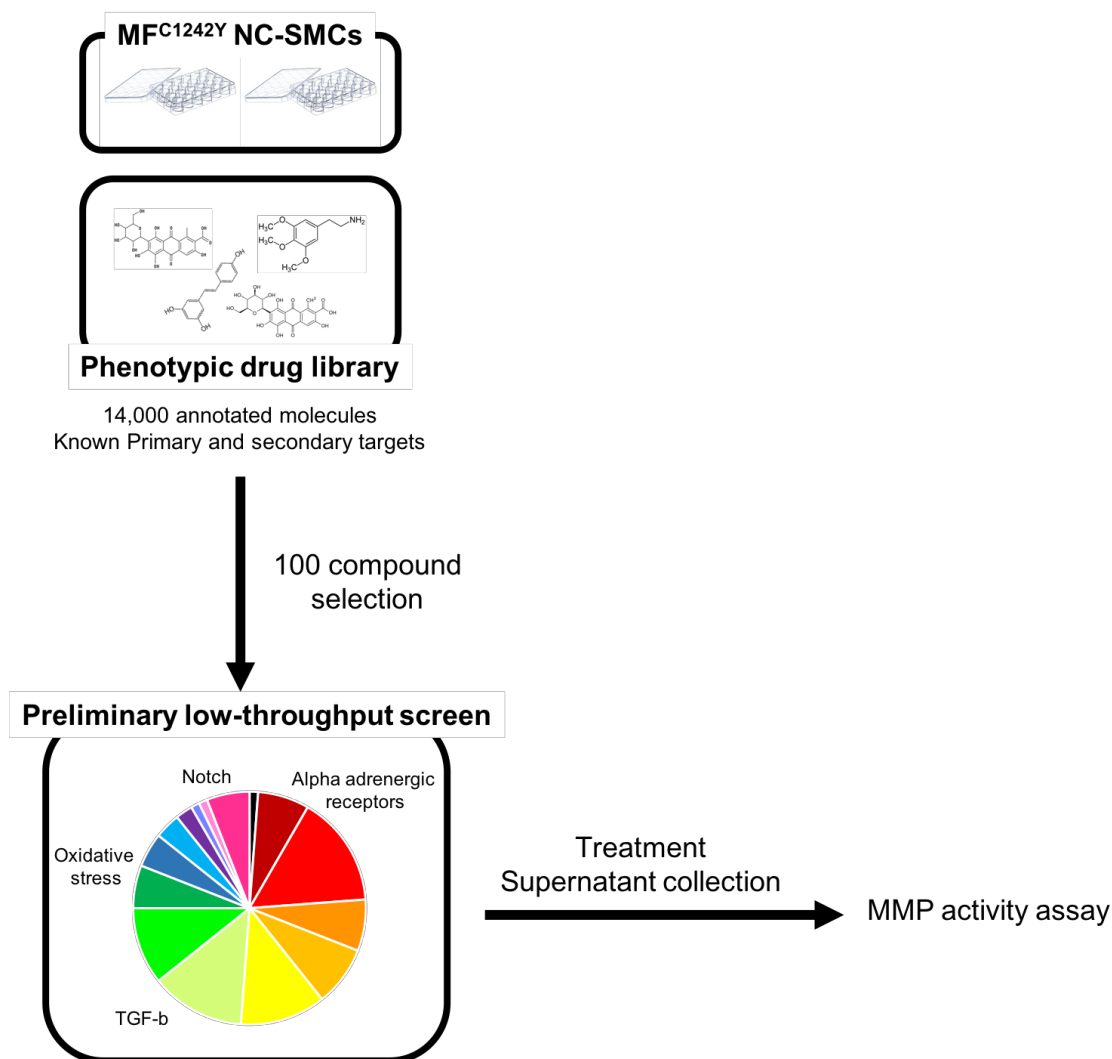


**Figure 5.7 Schematic flow-chart of pilot 100-compound screen to measure the effect on MMP activity.**

MF<sup>C1242Y</sup> NC-SMCs are seeded in 24-wells and treated with a cohort of 100 compounds selected from a larger phenotypic drug library of 14,000 compounds provided by AstraZeneca UK. The compound selection targets different pathways, which fall into previously-described pathogenic pathways involved in Marfan Syndrome but also pathways having no documented role in driving the disease. Following the previously described treatment protocol, supernatant from each treatment condition is collected and assayed for MMP activity.

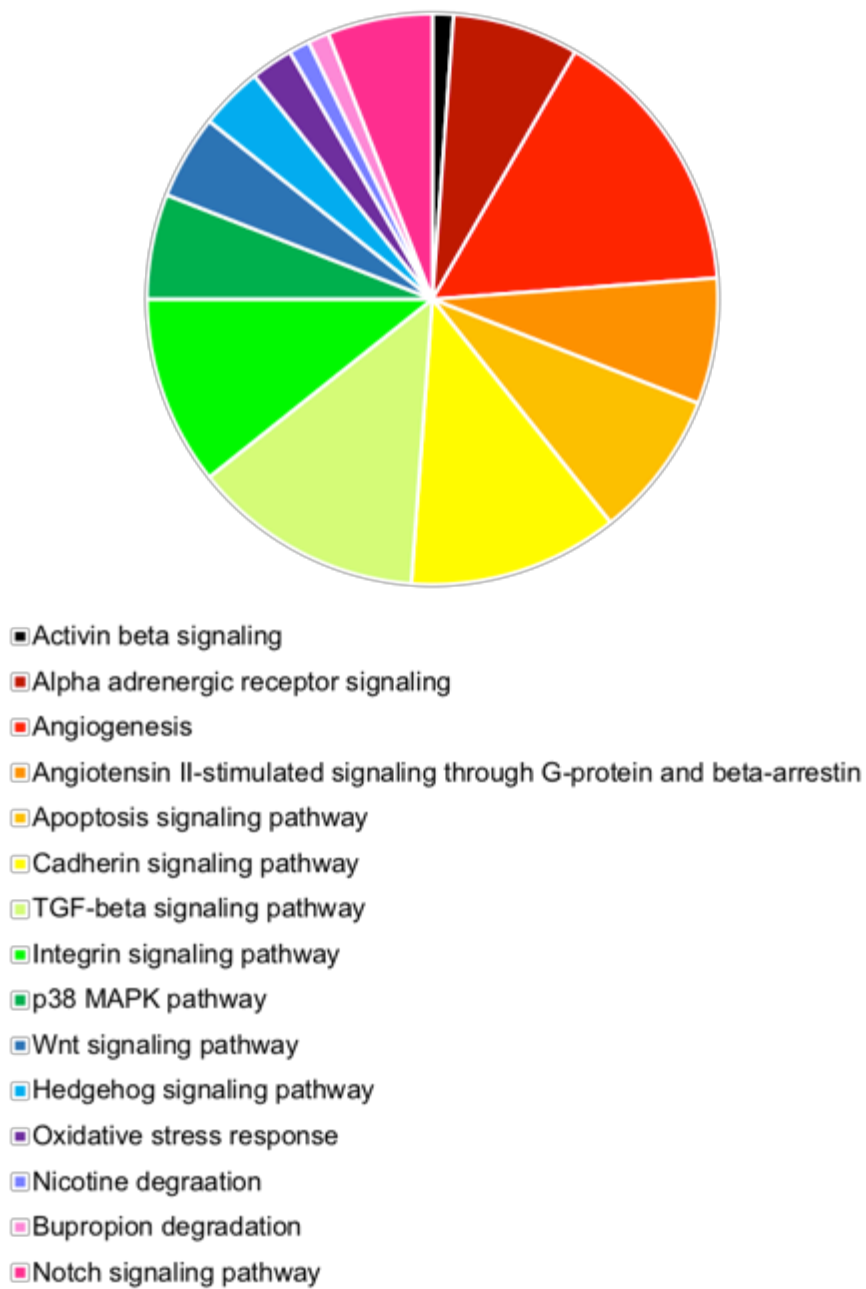


**Figure 5.8 Representative percentage of number of genes and their associated gene-target and respective pathway.**

MF<sup>C1242Y</sup> SMCs were then screened using the carefully selected subset of compounds to identify MMP-reducing agents. As previously described, MF<sup>C1242Y</sup> SMCs were seeded into a 24-well plate format and treated with the selection of 100 compounds and supernatant of each condition was collected for MMP activity measurement. MF<sup>C1242Y</sup> SMCs treated with losartan and SB203580 respectively were used as positive controls and DMSO was used as a negative control. Each compound was used at a single concentration of 1 $\mu$ M. DMSO was used at 0.1% and losartan was used at 1 $\mu$ M whilst SB203580 was used at 5 $\mu$ M. Results yielded 18 compounds to be non-cytotoxic at 1 $\mu$ M and all 18 compounds reduced MMP activity more strongly than MF<sup>C1242Y</sup> SMCs treated with DMSO. In addition, out of the 18-compound subset, eight were identified to repeatedly reduce MMP activity to levels lower than the positive controls, losartan and SB203580 (Figure 5.9).

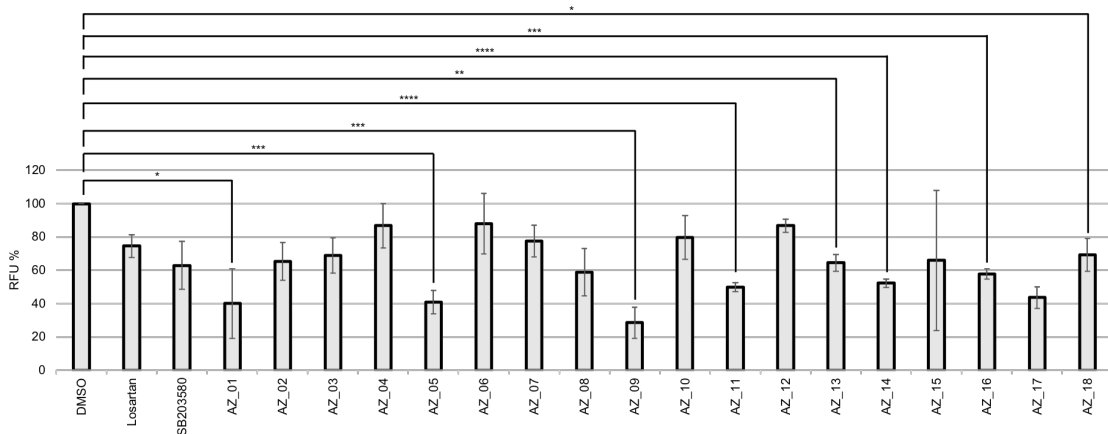


**Figure 5.9 A subset of non-cytotoxic AZ compounds reproducibly reduces MMP activity in MF<sup>C1242Y</sup> NC-SMC compared to DMSO-treated controls.**

Supernatant from MF<sup>C1242Y</sup> NC-SMCs treated with 100 compounds issued from the AZ phenotypic library was collected to measure for MMP activity. Eighteen compounds (AZ\_01-AZ18) were non-cytotoxic at a treatment concentration of 1 $\mu$ M over the course of the five-day treatment protocol. 8 out of 18 compounds reduced MMP activity significantly compared to DMSO-treated negative controls. On average, all compounds reduced MMP activity more strongly than losartan-treated positive controls. Error bars are representative of n=3; means  $\pm$  SEM; \*p  $\leq$  0.05, \*\* p  $\leq$  0.01, \*\*\* p  $\leq$  0.001 and \*\*\*\*p  $\leq$  0.0001.

## Development of novel therapies for Marfan Syndrome using a human iPSC-derived disease model

In order to apply an unbiased approach, the identity of each compound was only described after the assay was performed. Here, the subgroup of eight compounds primarily belonged to signalling pathways previously known to be involved in driving MFS syndrome. However, one compound targeting *PSEN1*, the gene encoding Presenilin 1, was revealed to also possess MMP-activity reducing potential (Table 5.2). Interestingly, mutations in presenilin-1, known to cause familiar Alzheimer's disease as a result of aberrant APP cleavage, can also impact the precision of Notch cleavage cascade and lead to determinantal effects<sup>132</sup>. There have been studies suggesting that Notch signalling is upregulated in tissue sections of thoracic aortic dissection although immunofluorescence staining revealed complex patterns of Notch signalling in the disease samples<sup>133</sup>

AZ label	Gene target
AZ_01	ACVR2B
AZ_05	KDR
AZ_09	MAPK1
AZ_11	MAPK14
AZ_13	PSEN1
AZ_14	TGFBR1
AZ_16	MAPK8
AZ_18	MAPK8

**Table 5.2 Summary of MMP activity-reducing non-cytotoxic AZ compounds and their respective gene targets.**

Notch signalling was measured in DMSO and compound treated MF MF<sup>C1242Y</sup> SMCs using a 4xCST promoter luciferase vector, but results remained inconclusive. Therefore, our goal was to screen a larger selection of compounds from the phenotypic library and for this we set up a medium-throughput assay using a selection of 1000 compounds. MMP activity was also measured in control samples, which included untreated CRISPR-corrected neural crest (NCs) progenitor cells, untreated CRISPR-corrected NC-SMCs, and untreated Marfan-uncorrected NC-SMCs. As expected, MMP activity was reduced in both progenitors (NC) and mature (SMCs) cell stages of CRISPR-corrected cell lines and elevated in Marfan-uncorrected SMCs. This set of conditions was incorporated in the list of samples in order to validate the reliability of the assay. (Figure 5.10).

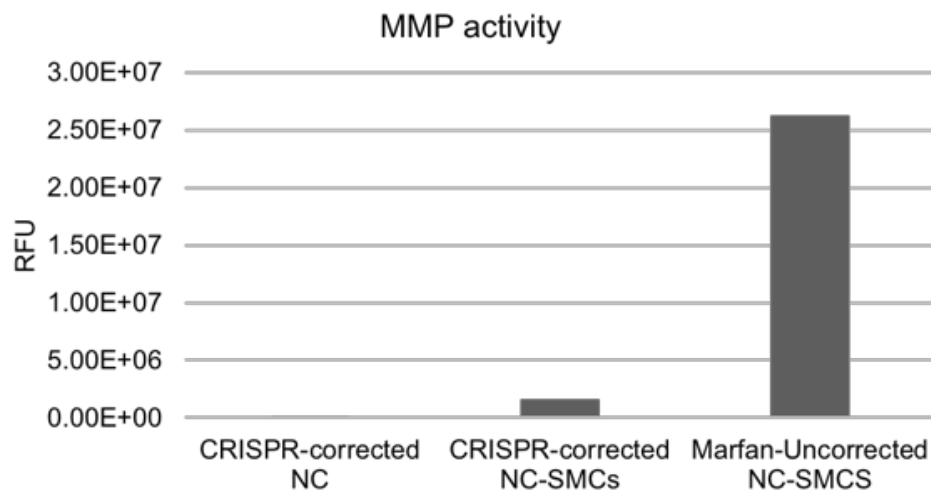


**Figure 5.10 MMP activity is reduced in CRISPR-corrected lineages and elevated in Marfan-uncorrected lineages.**

CRISPR-targeted MF<sup>C1242Y</sup> NC-SMCs were corrected for the point mutation C1242Y (CRISPR-corrected). The targeted counterpart remains uncorrected (Marfan-uncorrected). MMP activity was measured in CRISPR-corrected NC progenitors and mature CRISPR-corrected and Marfan-uncorrected NC-SMCs as a set of control conditions to validate the reliability of the assay. Data shown is n=1.

## 5.5 Expanding the drug-screen assay to 1000 compounds using a read-out based on MMP activity

As was previously alluded to, the phenotypic library is composed of a well-annotated 14,000 set of compounds with each small molecule having associated primary and secondary targets with a pIC<sub>50</sub> value. The library of SMIs is designed so that multiple compounds hit gene targets belonging to the same pathway, which constitutes the power of this particular drug library. Due to significant overlap in gene targets, we were able to limit the compound selection to one thousand molecules whilst still maintaining a broad spectrum of all the gene targets. Similar to the 100-subset approach, MF<sup>C1242Y</sup> SMCs were plated in a 24-well format, left to attach for 48 hours and then treated with the set of 1000 compounds according to the same treatment plan previously described. MMP activity was measured for all 1000 compounds in duplicates and results were compared to MF<sup>C1242Y</sup> NC-SMCs treated with 0.5% DMSO, losartan (1µM), SB203580 (5µM) respectively.

In addition, both the Marfan-uncorrected and the CRISPR-corrected NC-SMCs cell-line as well as untreated MF<sup>C1242Y</sup> NC-SMCs were included as an internal control for the assay. As expected, MF<sup>C1242Y</sup> NC-SMCs treated with losartan and SB203580 showed reduced MMP activity levels similar to CRISPR-corrected SMCs. Whilst MF<sup>C1242Y</sup> NC-SMCs treated with DMSO had elevated proteolytic activity comparable to Marfan-uncorrected and untreated MF<sup>C1242Y</sup> NC-SMCs. Following the treatment protocol, solely the supernatant of non-cytotoxic conditions was collected for further investigation. The proteolytic profile of each condition was recorded through MMP activity measurements and all 1000 compounds showed highly variable levels of MMP activity (Appendix 8.4).

Results demonstrated that thirty-six compounds treated at 1µM successfully reduced MMP activity, did not provoke cytotoxicity and showed a trend in increased proliferation in MF<sup>C1242Y</sup> NC-SMCs. Here, I use a higher concentration of 1µM for all treatment conditions necessary to achieve 50% inhibition to not risk missing any potential targets. The potential false-positive uncovered in the initial screen will further be validated using secondary phenotypic assays to verify their true ability to reverse the disease features in our MFS model. In addition, 36% of this subset of compounds were either equally as effective as losartan or more effective at reducing MMP activity (13 out of 36 non-cytotoxic compounds). Furthermore, it is worthy to note that all non-cytotoxic

compounds reduced MMP activity more strongly than DMSO-treated MF<sup>C1242Y</sup> controls. Finally, 2 out of 36 compounds were known to directly target MMP2 (C\_AZ\_09 and C\_AZ\_10), which provide internal controls for the validity of the assay. Additionally, GSK3 $\beta$  was a recurrent gene-target and 3 out of 36 compounds were found to target GSK3 $\beta$  as their primary annotated target (A\_AZ\_09, D\_AZ03 and D\_AZ07) (Figure 5.11).

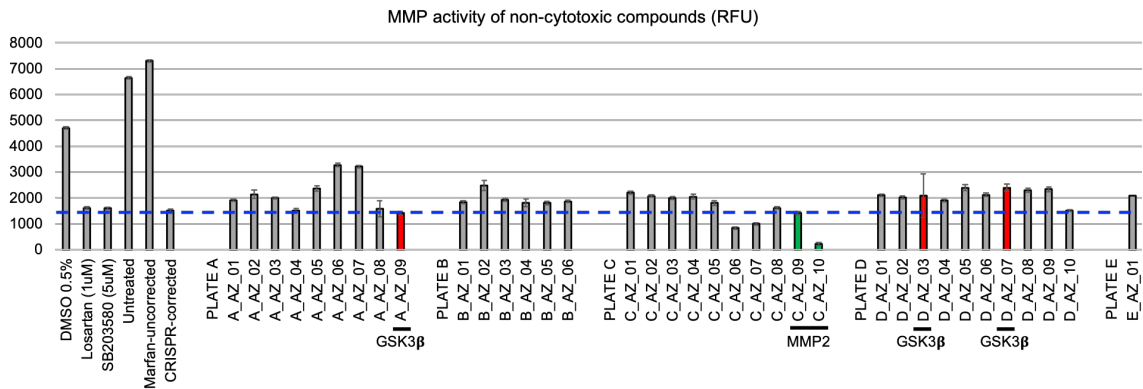


**Figure 5.11 AZ compounds selected based on toxicity, MMP activity reduction potential and proliferation.**

Supernatant of MF<sup>C1242Y</sup> NC-SMCs treated with a subset of one thousand compounds at a concentration of 1  $\mu$ M selected from the AstraZeneca phenotypic library was collected to measure for MMP activity. Control samples included MF<sup>C1242Y</sup> NC-SMCs treated with DMSO 0.5%, losartan 1  $\mu$ M and SB203580 5 $\mu$ M as well as untreated MF<sup>C1242Y</sup>, Marfan-uncorrected and CRISPR-corrected NC-SMCs. Here, the subset of MMP reducing agents showed a trend in increasing proliferation in MF<sup>C1242Y</sup> NC-SMCs as well as being non-cytotoxic. MMP2-targeting compounds (green) were highlighted to validate the assay and GSK3 $\beta$ -targeting compounds (red) were highlighted for further investigation. The blue dashed line indicates the threshold of MMP activity for samples treated with losartan 1 $\mu$ M. Data shown is the average of 2 biological replicates (n=2).

## Development of novel therapies for Marfan Syndrome using a human iPSC-derived disease model

These compounds were selected to further investigate the potential role of GSK3 $\beta$  in MF<sup>C1242Y</sup> NC-SMCs. Each GSK3 $\beta$ -targeting compound showed signs of increasing proliferation in MF<sup>C1242Y</sup> NC-SMCs over the course of the treatment protocol and compound D\_AZ\_03 provoked changes in morphology whereby the SMCs revealed a more elongated profile, which could potentially be promising in re-establishing a healthier SMC morphological profile. Furthermore, all GSK3 $\beta$  inhibitory molecules are highly potent inhibitors of GSK3 $\beta$  as the pIC50 are all above 8, meaning that 10nM is required for 50% inhibition of GSK3 $\beta$  (Table 5.3). Each small inhibitory molecule targeting GSK3 $\beta$  is also able to target a specific subset of known secondary targets, of which the top ten gene hits are listed in (Table 5.4). GSK3 $\beta$  has not yet been described in the literature to be involved in MFS pathophysiology; thus, I decided to further investigate this gene target and its potential role in our *in vitro* disease model.

AZ compound	Gene target	Proliferation		Notes	pIC50
		Day 2	Day 5		
A_AZ_09	GSK3 $\beta$	+	+		8.2
D_AZ_03	GSK3 $\beta$	+	++	Elongated morphology	8.56
D_AZ_07	GSK3 $\beta$	-	++		9.54

**Table 5.3 Information on GSK3 $\beta$  small molecule inhibitors**

<b>A_AZ_09</b>	<b>pIC50</b>	<b>D_AZ_03</b>	<b>pIC50</b>	<b>D_AZ_07</b>	<b>pIC50</b>
GSK3B	8.2	GSK3B	9.5	GSK3B	8.5
BMPR1B	7.9	CLK1	7.6	GSK3A	8.5
STK3	7.9	DYRK3	7.6	CDK3	8.3
STK4	7.9	HIPK2	7.6	SIK2	8.2
GSK3A	7.8	IRAK1	7.6	CDK2	7.9
MAP4K3	7.8	AAK1	7.6	CDK5	7.9
CSNK1G1	7.7	EIF2AK2	7.6	SIK3	7.2
MAP4K1	7.6	DYRK1A	7.6	CDK5R1	7.1
TNIK	7.6	YSK4	7.6	AURKC	6.7
ACVRL1	7.6	GSK3A	7.6	CDK1	6.5

**Table 5.4 List of secondary targets of GSK3 $\beta$  inhibitory AZ compounds and respective pIC50**

## 5.6 GSK3 $\beta$ target validation

### 5.6.1 A short introduction to GSK3 $\beta$

GSK3 $\beta$  is a well-known partner of the Wnt pathway where it plays the role of a multifaceted kinase that triggers  $\beta$ -catenin destabilisation but also mediates crosstalk between a diversity of signalling pathways and  $\beta$ -catenin-independent downstream from Wnt<sup>134</sup>. The transcription factor  $\beta$ -catenin is a major effector of the canonical Wnt signalling pathway. In the absence of Wnt ligand, cytoplasmic  $\beta$ -catenin interacts with APC and Axin scaffold proteins, which form a complex and direct  $\beta$ -catenin phosphorylation by kinases CKI and GSK3 $\beta$ . Phosphorylated  $\beta$ -catenin is subsequently labelled for ubiquitination and degraded. When Wnt is present, the ligand binds to a Frizzled family receptor and co-receptor LRP-family member, which prevents the APC/Axin/CK1/GSK3 $\beta$  complex from degrading  $\beta$ -catenin. As a result,  $\beta$ -catenin is free to accumulate in the cytoplasm, translocate to the nucleus and activate Wnt-responsive genes (Figure 5.12). Following this hypothesis, I suggested that GSK3 $\beta$ , a central component of the developmentally important Wnt pathway, is overactive in our Marfan *in vitro* disease system and, as a result, leads to the downregulation of Wnt target genes.

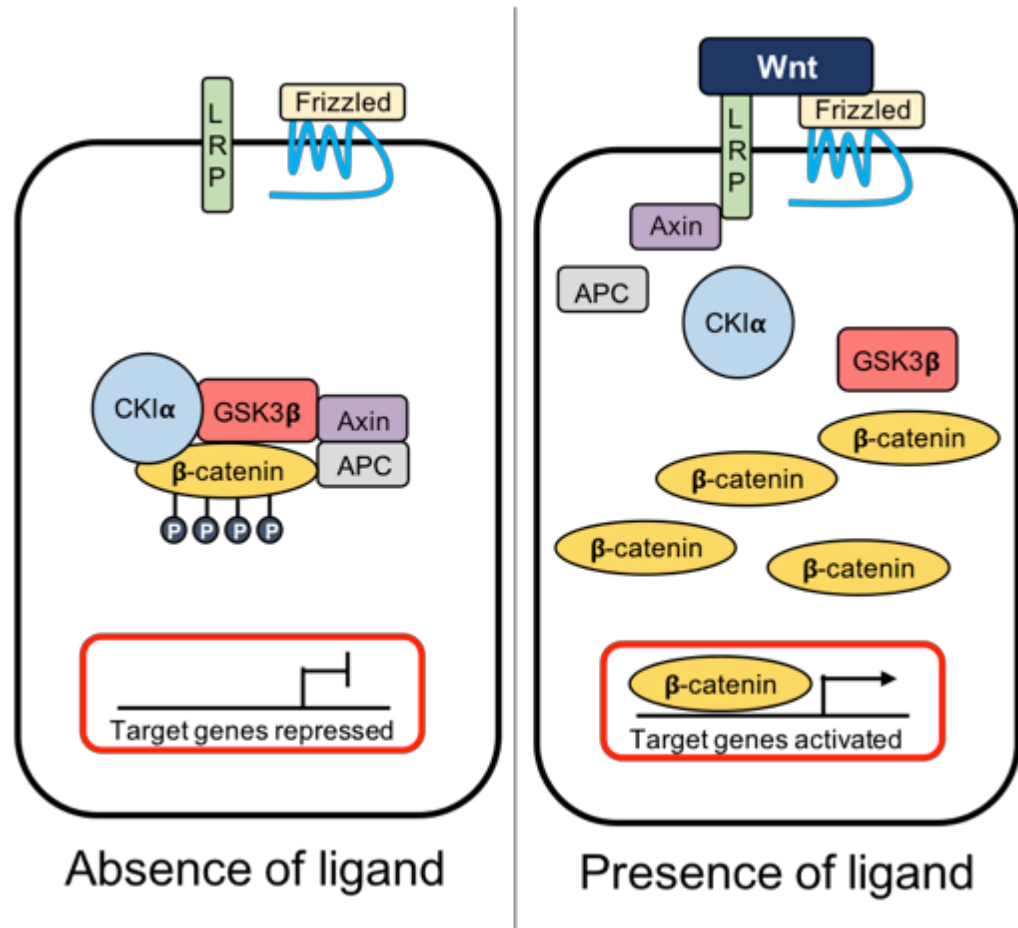


**Figure 5.12 Canonical Wnt pathway**

The transcription factor  $\beta$ -catenin is a major effector of the canonical Wnt signalling pathway. In the absence of Wnt, cytoplasmic  $\beta$ -catenin interacts with APC and Axin scaffold proteins and is phosphorylated by kinases CKI and GSK3 $\beta$ . Phosphorylated  $\beta$ -catenin is subsequently ubiquitinated and degraded. In presence of Wnt ligand, Wnt binds to the Frizzled family receptor and co-receptor LRP-family member.  $\beta$ -catenin is no longer degraded by the APC/Axin/CKI/GSK3 $\beta$  complex and will translocate to the nucleus to activate Wnt-responsive genes.

## 5.6.2 GSK3 $\beta$ is abnormally expressed in Marfan-uncorrected NC-SMCs

### 5.6.2.1 GSK3 $\beta$ is overexpressed at the molecular level in Marfan-uncorrected NC-SMCs

As GSK3 $\beta$  inhibition is shown to be a putative strategy for restoring MMP activity, I expected expression of mRNA levels of this gene to be upregulated in Marfan-uncorrected NC-SMCs compared to their isogenic controls. In order to evaluate the transcription regulation of *GSK3 $\beta$*  in our disease model, I used quantitative PCR to measure the expression *GSK3 $\beta$*  at mRNA levels. As controls, I also measured the GSK3 homologous isoform encoded by a separate gene, *GSK3 $\alpha$* , and *TGF- $\beta$*  as negative and positive controls respectively. Results show that Marfan-uncorrected NC-SMCs express elevated levels of *GSK3 $\beta$*  compared to their CRISPR-corrected counterparts. However, *GSK3 $\alpha$*  mRNA remained unchanged between both cell-lines whilst, as expected, *TGF- $\beta$*  expression levels were increased in Marfan-uncorrected NC-SMCs compared to CRISPR-corrected NC-SMCs (Figure 5.13). Figure legend is on over-leaf on page 163.

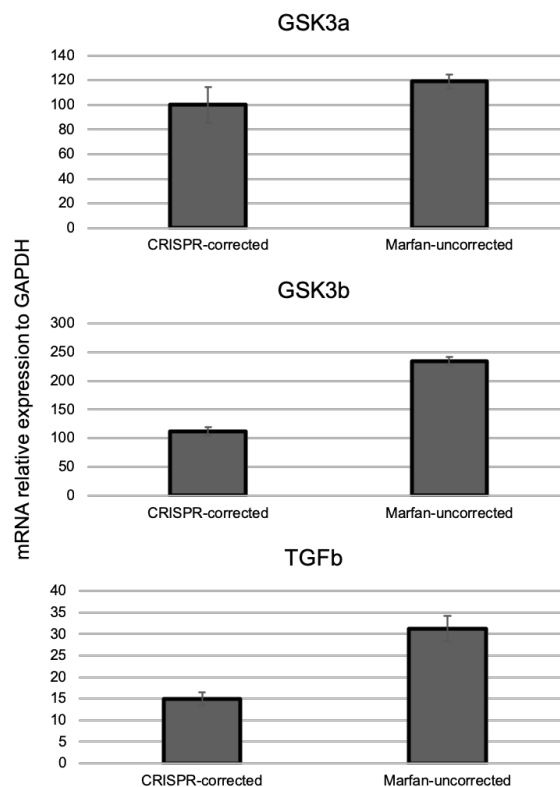


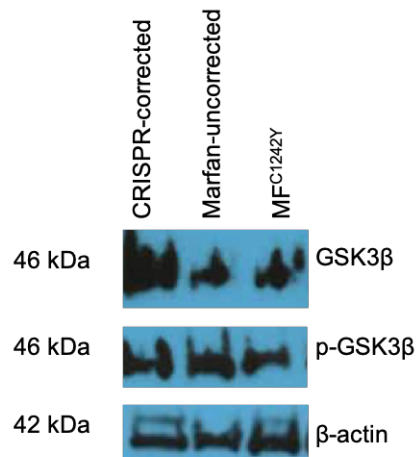
**Figure 5.13 Marfan-uncorrected express elevated mRNA levels of GSK3 $\beta$**

RT-qPCR mRNA levels of GSK3 $\alpha$ , GSK3 $\beta$ , and TGF- $\beta$  in CRISPR-corrected and Marfan-uncorrected NC-SMCs measured at serum 2 weeks. All expression levels are relative to housekeeper GAPDH mRNA expression. Data shown is the mean  $\pm$  SEM of 3 technical replicates (n=1).

5.6.2.2 Marfan-uncorrected NC-SMC produced less GSK3 $\beta$

In order to further investigate the GSK3 $\beta$  dysregulation in our disease system, I extracted protein samples of total GSK3 $\beta$  and phosphorylated GSK3 $\beta$  (p-GSK3 $\beta$ ) from Marfan-uncorrected NC-SMCs and CRISPR-corrected NC-SMCs. Unexpectedly, after two weeks in serum, protein levels of total GSK3 $\beta$  appeared to be lower in Marfan-uncorrected NC-SMCs and untargeted Marfan NC-SMCs compared to their CRISPR-corrected counterpart. Protein levels of p-GSK3 $\beta$ , the inactivated form of GSK3 $\beta$ , were of equal intensity in all cell-types, which may suggest that Marfan NC-SMCs harbour an abnormality at the level of expression, secretion and/or activity the GSK3 $\beta$  enzyme (Figure 5.14). As my hypothesis is based on GSK3 $\beta$  inhibition being beneficial to reverse some of the disease characteristics, abnormally low levels of total GSK3 $\beta$  may potentially suggest that it is sufficient to promote a signalling dysregulation in Marfan-uncorrected NC-SMCs. Nevertheless, it is important to state that this set of data presents an interpretation challenge caused by the quality of the western blots and additional experiments require repetition in order to fully interpret these preliminary results.

(A)



(B)

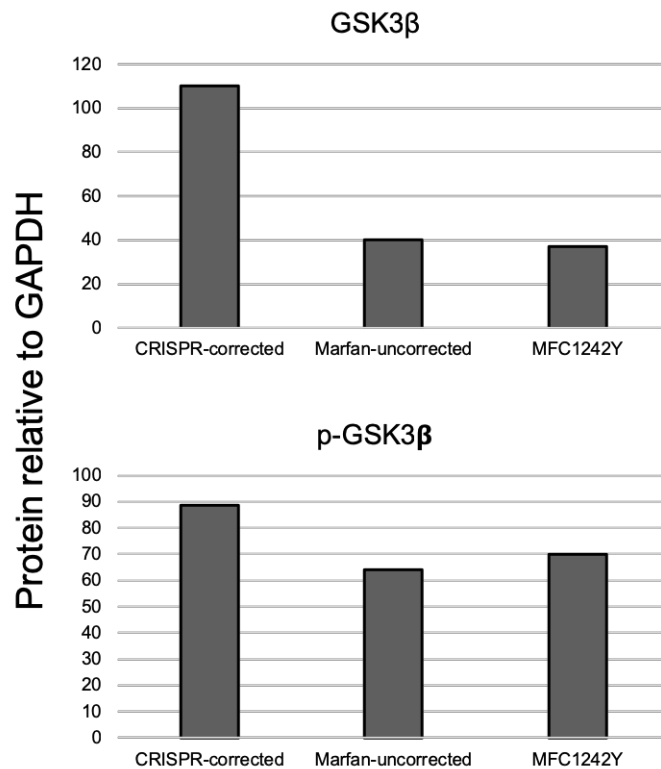


**Figure 5.14 Marfan-uncorrected NC-SMCs express reduced levels of GSK3β**

Whole cell lysates were extracted from Marfan-uncorrected, CRISPR-corrected and untargeted MFC<sup>1242Y</sup> NC-SMCs to measure protein levels of total and phosphorylated GSK3β (p-GSK3β) at serum 2 weeks. (A) Western blot representation of GSK3β (46kDA), p-GSK3β (46kDA) and β-actin (42kDa). (B) Quantification of band intensity relative to GAPDH expression levels. Data shown is the n=1.

### 5.6.3 GSK3 $\beta$ inhibition restores MMP activity and cell-death in Marfan-uncorrected NC-SMCs

#### 5.6.3.1 GSK3 $\beta$ inhibition reduces MMP activity in Marfan-uncorrected NC-SMCs

As previously demonstrated, GSK3 $\beta$  inhibition reduces MMP activity in Marfan-uncorrected NC-SMCs. In order to verify GSK3 $\beta$  specificity, a miniature drug screen was designed to measure the effect of a panel of GSK3 $\beta$  inhibitors on MMP activity. The small molecule inhibitors included two GSK3 $\beta$  inhibitors (GSK3 $\beta$  inh1 and GSK3 $\beta$  inh2) and Chiron, an extremely potent inhibitor of GSK3 $\beta$ . Chiron is the most selective GSK3 $\beta$  inhibitor reported so far and blocks GSK3 $\beta$  and GSK3 $\alpha$  at an IC<sub>50</sub> of 6.7nM and 10nM respectively. Here, my results show that treatment with both GSK3 $\beta$  inhibitors and Chiron reduces MMP activity in Marfan-uncorrected NC-SMCs after a 24h and 48h treatment period. Furthermore, a PIK3C2G inhibitor, previously reported in my medium-throughput drug-screen to have a minor effect on MMP reduction, was used as an internal control for the assay. *PIK3C2G* encodes a protein belonging to the phosphoinositide 3-kinase (PI3K) family and plays a variety of roles including regulation of cell proliferation and cell survival. Blocking PIK3C2G mildly inhibited MMP activity after 48h treatment and had no effect after 24h treatment. Lastly, losartan was used as a positive control and, as expected, MMP activity was reduced after five days of treatment (Figure 5.15).

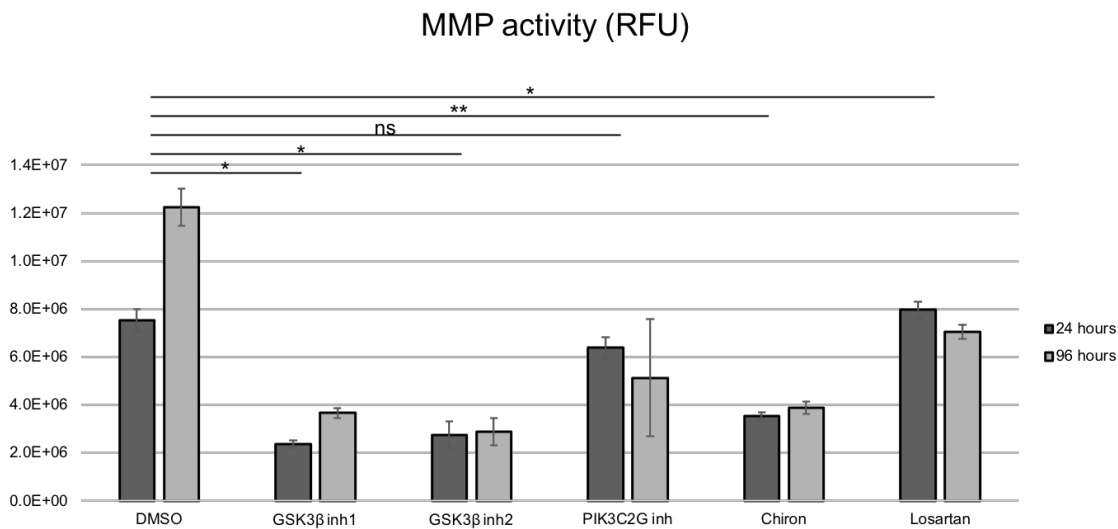


**Figure 5.15 GSK3β inhibition reduces MMP activity in Marfan-uncorrected NC-SMCs at 24h and 96h treatments.**

Marfan-uncorrected NC-SMCs were treated with GSK3β small molecule inhibitors (GSK3β inh1, GSK3β inh2 and Chiron), positive control Losartan and negative control DMSO for 24 hours and 96 hours. Supernatant was collected at 24 hours and 96 hours respectively to assay for MMP activity. MMP activity was measured based on MMP-specific substrate cleavage, which upon cleavage releases a fluorescent signal measured in relative fluorescent units (RFU). All results are representative of n=3; means ± SEM; \*p ≤ 0.05, \*\* p ≤ 0.01, and ns, non-significant.

### 5.6.3.2 GSK3 $\beta$ inhibition reduces cell-death in Marfan-uncorrected NC-SMCs

As described earlier, Marfan NC-SMCs display a severe apoptotic profile. In order to investigate if GSK3 $\beta$  inhibition can restore this particular phenotypic characteristic of our Marfan *in vitro* model, I measured the level of apoptosis in our system treated with compounds inhibiting GSK3 $\beta$ . Here, Marfan-uncorrected and CRISPR-corrected NC-SMCs were treated for 96h with the panel of small molecule inhibitors previously used to assay for MMP activity. Terminal deoxynucleotidyl transferase (TdT) dUTP Nick-End (TUNEL) labelling was employed to detect apoptotic cells, which involves detecting TUNEL-positive cells and identifying the population of cells having undergone extensive DNA degradation during the late stages of apoptosis. This method is specific to labelling DNA breaks. Here, my results show that GSK3 $\beta$  inhibitor 1 was uniquely successful in restoring cell-death levels back to those displayed by CRISPR-corrected NC-SMCs. GSK3 $\beta$  inhibitor 2 and Chiron had little effect on reducing the number of TUNEL-positive cells in Marfan-uncorrected NC-SMCs. This suggests that the signalling pathways governing apoptosis in our Marfan system may not exclusively be acting through GSK3 $\beta$  specifically. As a control, SB203580, a p38 MAP kinase inhibitor, was used to reduce apoptosis (Figure 5.16). Therefore, these results suggest the possibility of alternative components of the Wnt pathway potentially driving the excessive cell-death feature present in our disease model for MFS.

Development of novel therapies for Marfan Syndrome using a human iPSC-derived disease model

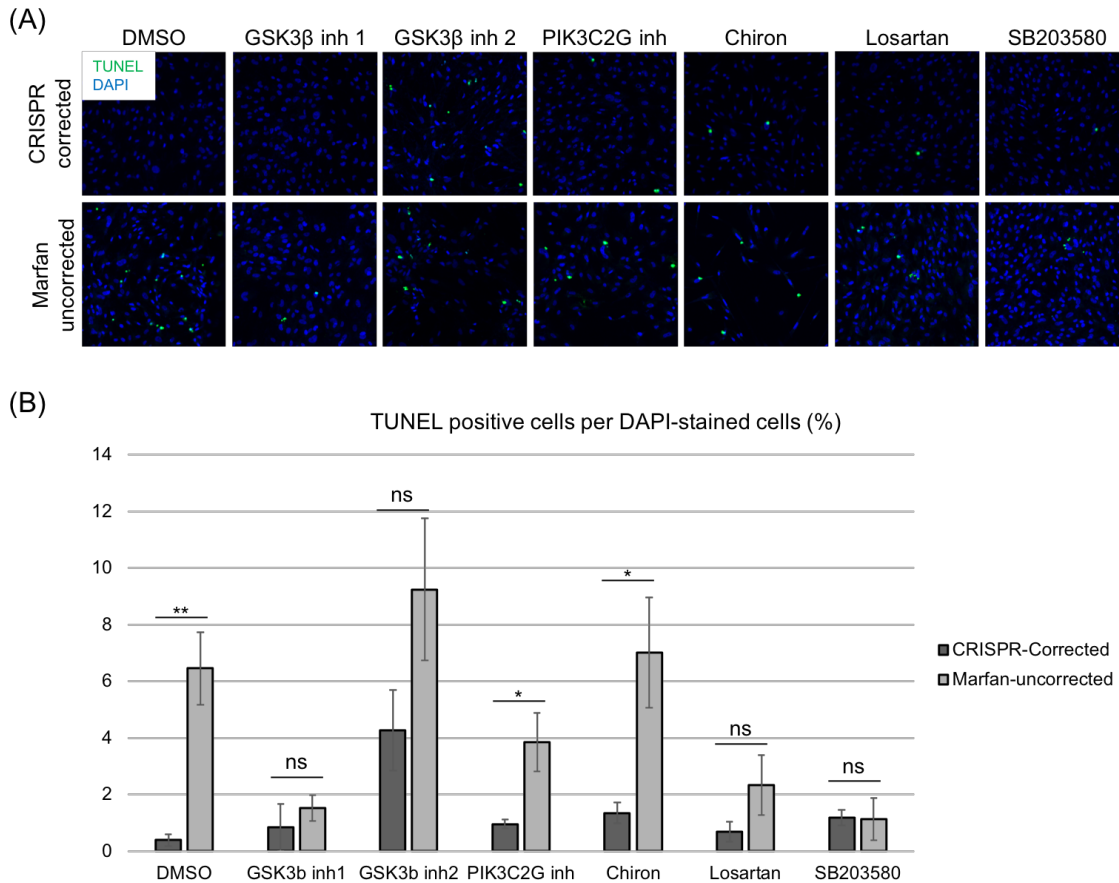


**Figure 5.16 GSK3 $\beta$  inhibitor 1 reduces TUNEL-positive cells in Marfan-uncorrected NC-SMCs at 96 hours post-treatment.**

Marfan-uncorrected NC-SMCs were treated with GSK3 $\beta$  small molecule inhibitors (GSK3 $\beta$  inh1, GSK3 $\beta$  inh2 and Chiron), Losartan, positive control SB203580 and negative control DMSO for 96 hours. (A) Samples were fixed at 96 hours post-treatment and labelled for TUNEL-positive cells. TUNEL (green) and DAPI (blue). (B) The ratio of TUNEL positive cells to total DAPI-labelled cells was quantified. All results are representative of n=3; means  $\pm$  SEM; \* $p \leq 0.05$ , \*\*  $p \leq 0.01$ , and ns, non-significant. Image magnification is 10X.

#### 5.6.4 Abnormal $\beta$ -catenin signalling in Marfan-uncorrected NC-SMCs

As previously described, GSK3 $\beta$  is part of a complex that targets  $\beta$ -catenin for degradation by phosphorylation. Therefore, in our system, I expected to detect lower levels of total  $\beta$ -catenin in Marfan-uncorrected NC-SMCs compared to CRISPR-corrected isogenic controls.

##### 5.6.4.1 Cytoplasmic and nuclear levels of $\beta$ -catenin

$\beta$ -catenin is known to shuttle between the cytoplasmic and nuclear compartments in order to initiate transcription of Wnt-target genes. Therefore, I investigated the ratio of  $\beta$ -catenin levels in both cellular compartments in healthy versus Marfan CRISPR-targeted NC-SMCs. Protein was extracted from whole cell lysates for both cytoplasmic and nuclear compartments respectively. My results showed that, although there was no difference in  $\beta$ -catenin protein levels in the cytoplasm and the nucleus in both cell types, Marfan-uncorrected NC-SMCs exhibited lower total levels of  $\beta$ -catenin protein compared to CRISPR-corrected NC-SMCs. U2AF65 was used to recognise the nuclear fraction and my results show that both nuclear and cytoplasmic samples are distinct from each other (Figure 5.17). The lower levels of total  $\beta$ -catenin in Marfan-uncorrected NC-SMCs would suggest that the transcription of Wnt-target genes is comprised and potentially reduced. This result is seemingly consistent with the decreased levels of significantly differentially expressed Wnt-pathway target genes identified in my RNA-seq data.

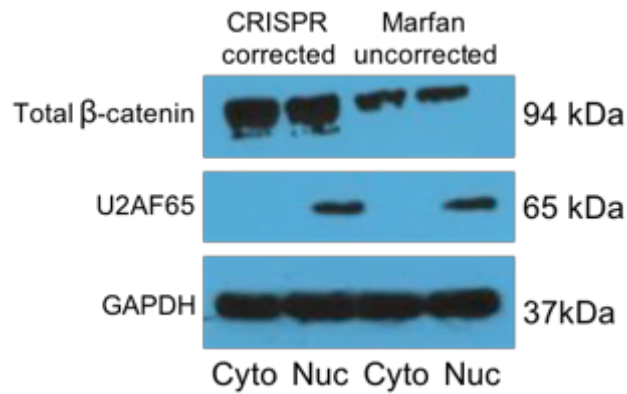


**Figure 5.17 Marfan-uncorrected NC-SMCs exhibit low levels of total β-catenin in both cellular compartments.**

Whole cell lysates were extracted from Marfan-uncorrected and CRISPR-corrected NC-SMCs to measure protein levels of total β-catenin at serum 2 weeks in cytoplasmic (Cyto) and nuclear (Nuc) compartments. Western blot representation of β-catenin (94 kDa), U2AF65 (65kDa) and GAPDH (37kDa).

#### 5.6.4.2 β-catenin activity measured by luciferase promoter activity

Finally, I measured Wnt/β-catenin signalling by luciferase activity using a TOP-flash reporter, which is a luciferase reporter plasmid that contains two sets of three copies of the wild-type TCF binding regions. Active canonical Wnt signalling induces the translocation of β-catenin into the nucleus, which will then bind to the TCF/LEF transcription factor complex to further activate Wnt target genes. Here, the measure of increased luciferase activity corresponds to an increase in β-catenin activity. Marfan-uncorrected and CRISPR-corrected NC-SMCs were transfected with the TOP-flash luciferase reporter plasmid and total lysates were collected at 24h post-transfection.

Additionally, CRISPR-corrected NC-SMCs were treated with Chiron, a Wnt activator, as a positive control for β-catenin activity and lysates were collected 4h post-transfection. My results show that at 4h post-transfection, Chiron treatment does, as expected, cause an induction in luciferase activity and therefore β-catenin activity. Unexpectedly, my results at 24h post-transfection show that Marfan-uncorrected NC-

SMCs exhibit a drastic increase in  $\beta$ -catenin activity compared to CRISPR-corrected NC-SMCs (Figure 5.18). However, these preliminary results that describe increased  $\beta$ -catenin activity in Marfan-uncorrected NC-SMCs is not aligned with the previously detected low protein levels of  $\beta$ -catenin nor my RNA-seq data analysis, which indicated Wnt-target genes to be significantly downregulated in Marfan-uncorrected NC-SMCs. Nevertheless, previous results showing low GSK3 $\beta$  protein levels could potentially suggest that the main inhibitor of  $\beta$ -catenin activity is lost in Marfan-uncorrected NC-SMCs, thus allowing abnormally high  $\beta$ -catenin signalling in our MFS system. However, it is important to note that these preliminary studies are the result of a single set of experiments and there is a need to repeat these experiments to draw any further mechanistic conclusions.

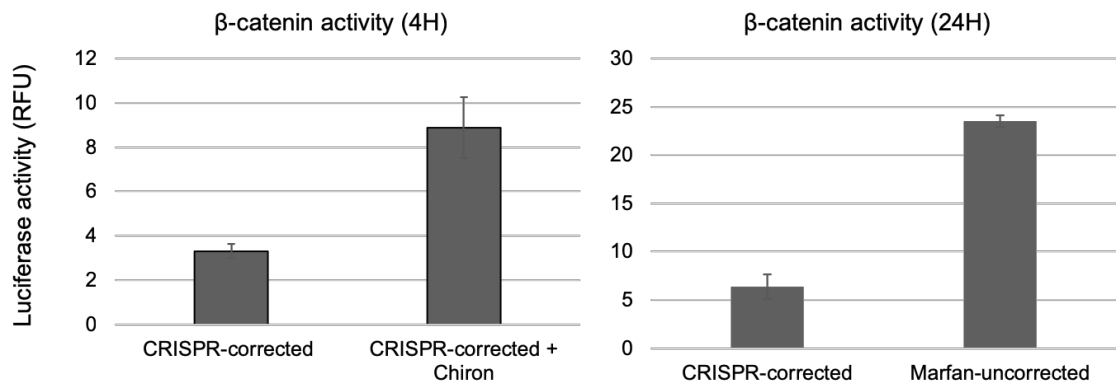


**Figure 5.18  $\beta$ -catenin activity measured by luciferase activity at 4h and 24h post-transfection.**

Whole cell lysates were extracted from Marfan-uncorrected, CRISPR-corrected and Chiron-treated CRISPR-corrected NC-SMCs to measure the activation of luciferase promoter plasmid, which harbours promoter motifs for  $\beta$ -catenin binding. Luciferase activity is measured by relative fluorescent units (RFU). Luciferase activity was measured at 4 hours post-transfection in untreated CRISPR-corrected and Chiron CRISPR-corrected SMCs whilst luciferase activity in Marfan-uncorrected was measured 24 hours post-transfection. Data shown is the mean of 3 technical replicates (n=1).

### 5.6.5 A hypothesised GSK3 $\beta$ mechanistic model in Marfan Syndrome

A dysregulation in GSK3 $\beta$  expression and activity is apparent in Marfan NC-SMCs when compared to isogenic CRISPR-corrected NC-SMCs. The current understanding of Marfan Syndrome was that TGF- $\beta$  signalling pathway governed aortic aneurysm development and was responsible for many disease characteristics displayed *in vitro*. However, recent work from our lab identified novel disease drivers, p38 and KLF4, as driving pathological features distinct to those down-stream of the TGF- $\beta$  pathway. The recent working model demonstrated that p38 and KLF4 inhibition restores apoptotic rates in Marfan-uncorrected NC-SMCs whereas blocking TGF- $\beta$  was unable to correct the cell-death feature. Several reports exist demonstrating that high levels of phosphorylated AKT, a serine/threonine kinase, are linked to promoting abdominal aneurysm formation<sup>135,136</sup>. Although, the involvement of AKT in aortic aneurysm formation has previously been described, its prominent role in regulating GSK3 $\beta$  activity remains to be established in driving the pathological features of MFS *in vitro*. AKT plays a mechanistic role whereby it is able to phosphorylate GSK3 $\beta$  at the serine residue (Ser9) and subsequently quench its kinase activity. The phosphoserine behaves similarly to a pseudo-substrate and will block the phosphate-binding pocket in GSK3 $\beta$ , preventing any further interaction of the kinase with primed substrates, such as  $\beta$ -catenin.

In this work, I suggest that abnormal MMP activity is downstream of GSK3 $\beta$  and inhibiting the latter restores MMP activity to healthy levels. However, the dysfunctional apoptotic profile may be regulated by a different mechanism, which could explain why abnormal cell-death was only rescued using one of the GSK3 $\beta$ -targeting inhibitors (Figure 5.19 and Figure 5.20). Therefore, the work presented here highlights a novel role for GSK3 $\beta$  as a potential pathological driver in our *in vitro* disease model for Marfan Syndrome and further studies are required to validate the exact GSK3 $\beta$ -dependent pathological mechanism.

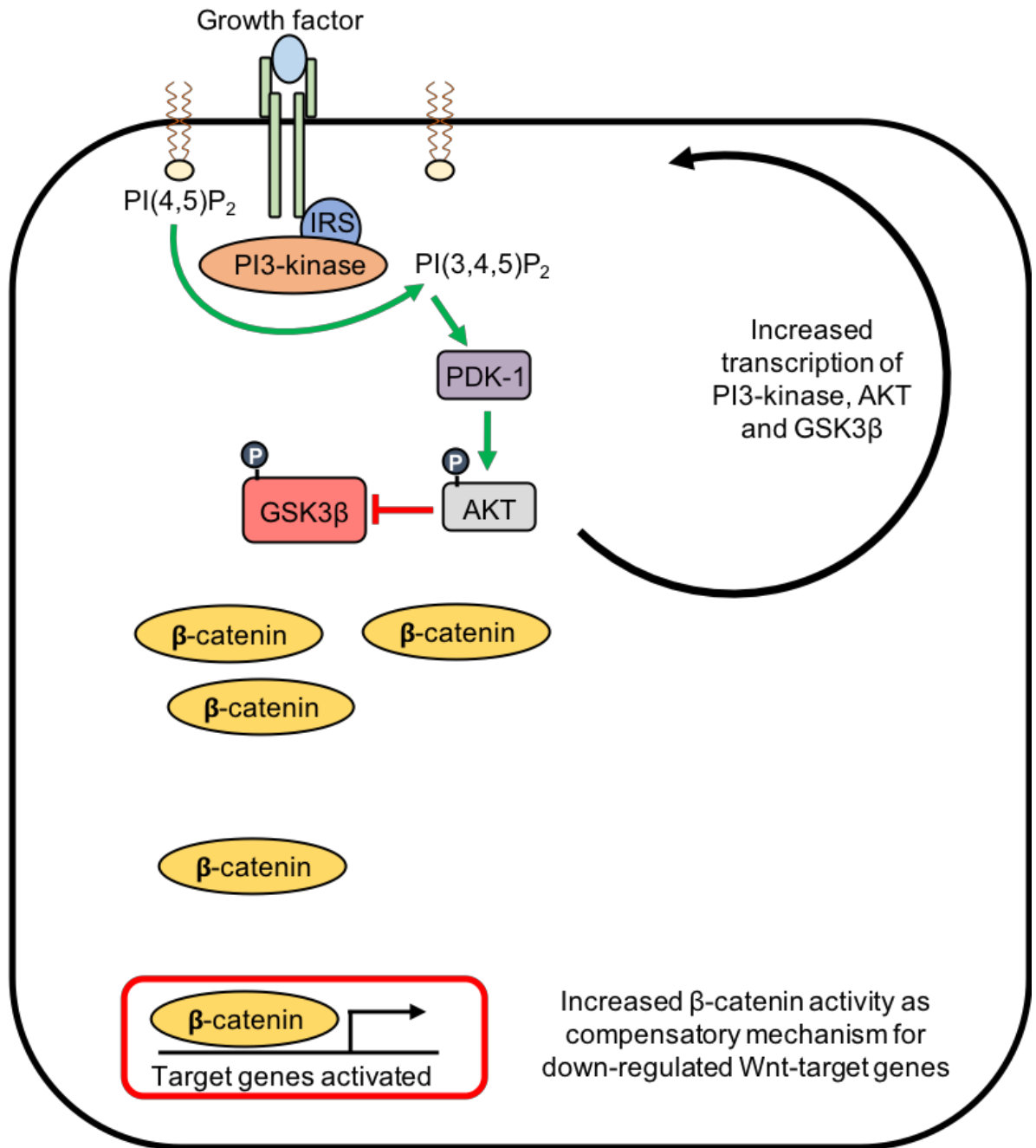
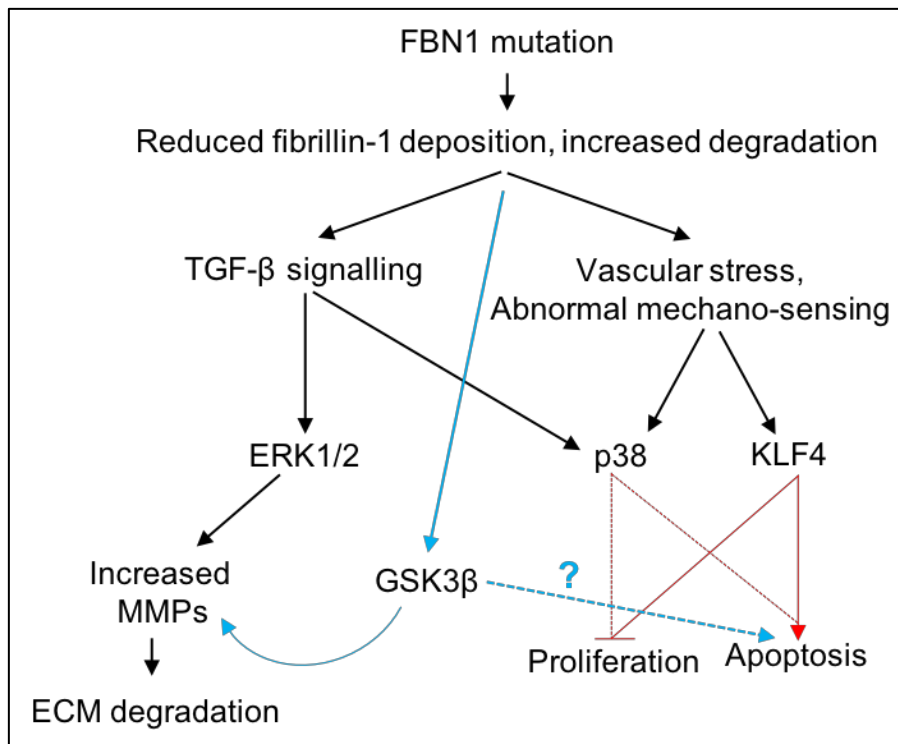


Figure 5.19 GSK3β dysregulation working model in MFS.



**Figure 5.20 MFS disease model downstream of pathogenic FBN1 mutation.**

FBN1 mutation causes reduction in fibrillin-1 deposition in the extracellular matrix and increased degradation. Matrix degradation is suggested to be TGF- $\beta$ -dependent whilst SMC apoptosis is governed by disease drivers, p38 and KLF4. Additionally, GSK3 $\beta$  shows potential to reduce MMP activity and apoptotic features in Marfan-uncorrected NC-SMCs. We suggest that GSK3 $\beta$  acts potentially downstream of the fibrillin-1 mutation and participates in driving MMP activity (blue lines). Furthermore, GSK3 $\beta$  may also regulate apoptosis through an alternative pathway (blue dotted line with blue question mark).

## 5.7 Conclusions

In this chapter, I show that our MF<sup>C1242Y</sup> NC-SMCs *in vitro* system for Marfan Syndrome can be exploited to develop a phenotypic assay for drug screening. Here, I demonstrated that a single concentration of drug treatment can successfully identify MMP-reducing compounds and shed light on the respective signalling pathways that may be involved in MFS pathogenesis. Both subsets of compounds used for the 100- and 1000-compound screen respectively were used at a 1 $\mu$ M treatment concentration. Most MMP-reducing compounds had an associated pIC<sub>50</sub> value greater or equal to 8, meaning that 10nM is sufficient to inhibit 50% of the respective gene-target. Although this 100-fold difference in concentration means that the screen may have enabled the selection of false positives, the MMP-reducing agents are further validated using secondary phenotypic screens. For therapeutic purposes, however, it will be important to execute a dose-dependent assay to determine the minimal compound concentration necessary to achieve the same reduced in MMP levels.

Using our *in vitro* disease system for Marfan Syndrome, I suggest that GSK3 $\beta$  expression contributes to the abnormal proteolytic and matrix-degradation profile displayed by MFS smooth muscle cells. There is no previous recorded role for GSK3 $\beta$  in contributing to MFS and thoracic aneurysm pathology. Additional validation of the target shows that inhibiting GSK3 $\beta$  results in reproducible reduction of MMP activity and partial apoptotic restoration. The compounds used in this study have a primary target and additional secondary targets, which will be targeted with a lesser affinity than the primary target. Therefore, the results demonstrating reduced cell-death using only one of the GSK3 $\beta$  inhibitors could be due to an off-target effect and necessitate further investigation.

Unexpectedly, my preliminary results show that our disease model exhibits reduced GSK3 $\beta$  protein expression despite GSK3 $\beta$  inhibition proving to be beneficial in restoring some of the phenotypic features. It is important to note that these are preliminary studies and that further experimental efforts need to be effectuated to harness precisely the GSK3 $\beta$ -dependent signalling pathways that govern the phenotypic abnormalities and characterise our MFS disease model. Taking all these results into account, there is still a need to screen the entire compound library available and further efforts are required to miniaturise the phenotypic assay for high-throughput conditions.

# 6 DISCUSSION AND FUTURE DIRECTIONS

## 6.1 Gene-correcting therapy for MFS

In this thesis, we have demonstrated that our patient iPSC-derived *in vitro* disease model for Marfan Syndrome (MFS) can be exploited to develop potential novel therapies. As previously highlighted, there is no current available cure for MFS, a multi-system connective tissue disorder.  $\beta$ -blocker therapy remains the first-line therapy for prevention of aortic complications and patients often have to resort to surgical intervention in the case of aneurysm formation. Here, we investigate the possibility of removing a faulty exon in a MFS patient iPSC line differentiated into SMCs using antisense oligonucleotide (AON)-mediated exon-skipping technology. During messenger RNA splicing, AONs flank the region of interest and coax the splicing machinery to exclude the targeted exon, maintain an open reading frame and allow the expression of a truncated but presumably functional protein. This approach provides patients with a mutation-specific, thus potentially personalised, therapy.

Over the last three decades, exon-skipping has become a powerful method to correct diseases, with a special focus on Duchenne Muscular Dystrophy (DMD), and substantial efforts have been applied towards the development of AONs as a therapeutic tool<sup>137–140</sup>. As a result, exon-skipping spurred the development of numerous pharmaceuticals, which have been tested in patients. A small Phase 1-2a clinical study showed that systemic administration of Drisapersen, an AON targeting dystrophin restoration, showed abundant expression of dystrophin in a body-wide manner and modest improvement in motor-function tests<sup>141</sup>. However, Phase III results failed to show marked clinical benefit of Drisapersen over placebo, ascribed to insufficient dystrophin rescue and uptake of the drug in the desired tissues<sup>142</sup>.

In 2016, Eteplirsen, designed for exon 51 deletion in dystrophin, was granted accelerated approval by the US Food and Drug Administration (FDA). Unfortunately, the majority of the trial data resulted in variable efficacy, which was owed to genetic background differences amongst patients and poor dystrophin expression in the myriad of skeletal muscles of the body<sup>143</sup>. Therefore, the efficacy of AON-mediated therapeutics is limited by insufficient faulty protein rescue and functional improvements in all tissues affected. Nevertheless, earlier evidence in mice revealed that a modest increase in dystrophin levels is sufficient to promote motor function and survival and X-linked dilated cardiomyopathy patients exhibit as low as 30% dystrophin, which is sufficient to

avoid muscular dystrophy<sup>144</sup>. Therefore, similar to DMD, the availability of the fibrillin-1 coding sequence raises hopes to intervene in MFS pathophysiology at its genetic root using AON technology.

The particular mutation analysed in this work is a missense mutation located in exon 30, which is predicated to impair the folding of the final fibrillin-1 protein. Unlike DMD, MFS-causing mutations are found to span the entire fibrillin-1 gene and there is no particular genotype-phenotype correlation recorded<sup>145</sup>. Up to now, mutations in exon 30 have not been reported to cause exon-skipping and disease despite other exon-skipping mutation clusters leading to the most severe form of Marfan Syndrome, neonatal Marfan syndrome (nMFS). Two hotspots are responsible for nMFS and comprise of a clustering of missense mutations, which cause the skipping of exonic regions 24-27, 31 and 32<sup>56</sup>. Therefore, it is feasible that, in our disease platform, the removal of a single faulty exon 30 will not aggravate the disease features and potentially prove to be therapeutically beneficial.

Here, the deletion of exon 30, which codes for a calcium binding EGF (cbEGF) domain, in fibrillin-1 is suggested to restore the functionality of the protein. Indeed, Lynne Sakai's work demonstrated that the in-frame deletion of the first hybrid domain of fibrillin-1 did not affect the microfibril network, showing that fibrillin-1 molecules are not required to assemble in perfect and identical register to form a functional component of the extracellular matrix (ECM)<sup>70</sup>. My data shows that skipping of this particular exon in *FBNI* is possible using a cocktail of AONs and the skipping efficiency is enhanced by two-fold (40% to 80% on average) when combined with a scramble AON modified with a 5'-fluorescein group. Similarly, Annemieke Aartsma-Rus showed efficient nuclear uptake of fluorescently-labelled AONs, which result in 60-80% exon-specific skipping levels in human dystrophin using primary human myoblasts<sup>146</sup>. Taken together, both the skipping efficiency of an AON cocktail and their stable back-bone configuration enable this tool to be considered for therapy.

In the context of translation medicine, it is important to consider the stability of AONs after a single transfection to determine the efficacy of exon-skipping. Here, my results show AONs remain stable for at least 6 days in patient iPSC derived NC-SMCs post-transfection. However, the variability of elevated skipping amounts across experiments made it challenging to conclude the effect of AON-mediated exon skipping on the functionality of MF<sup>C1242Y</sup> NC-SMCs. Although AONS of a given chemistry are expected to have comparable pharmacokinetic and pharmacodynamic properties, the

clinical behaviour of a particular AON may vary according to chemical modifications and sequence composition. Oliver Danos's lab showed that AON delivery for DMD correction showed improved exon skipping *in vitro* and *in vivo* but observed the accumulation of RNA by-products, which may indicate a level of saturation of the cellular processing capacity<sup>147</sup>. Hence, it is possible that the level and variability of skipping efficiency, caused by AON composition and processing, is potentially insufficient to reverse or reduce the key aspects of MFS pathology. Additionally, contrary to DMD, MFS may necessitate the removal of the faulty exon from the totality of *FBNI* transcripts in order to remedy the adverse effects caused by the mutation.

AON-based therapies face an additional challenge whereby this type of treatment requires to be re-administered throughout the patient's life and often results in poor tissue uptake. Therefore, innovative exon-deletion strategies have been developed involving permanent genetically-based corrections. Gene-editing tools, such as CRISPR/Cas9, offer promising technologies capable of precisely and permanently correcting the genetic basis of hereditary diseases. The flexibility and ease of construction of the CRISPR/Cas9 system makes it an attractive approach for targeting human iPSC lines. Studies have shown that genetically-engineered patient cells transplanted into immunodeficient mice restored dystrophin expression *in vivo*<sup>148</sup> and CRISPR/Cas9 technology achieves therapeutically beneficial levels of dystrophin in a mouse model of DMD postnatally<sup>149</sup>.

With the help of Dr Felipe Serrano, a CRISPR/Cas9-modified iPSC MFS cell-line was generated to remove exon 30, which contains the cysteine substitution. However, in our hands, the positively-edited human iPSC lines were unable to differentiate into NC progenitors and mature SMCs. Our control CRISPR-targeted but MFC<sup>1242Y</sup> uncorrected line was also incapable of proper differentiation, suggesting a possible off-target effect caused by the action of the Cas9 enzyme. There are a number of variables, which may be altered to optimise our current strategy in order to generate patient-corrected iPSC capable of successfully differentiating into SMC lineages of interest. Redesigning gRNAs and optimising the screening process for predicted off-target effects may yield higher efficiency of cutting in the precise loci of interest, avoiding unwanted genomic modifications. Additionally, varying the ratio of guide to donor may preferentially produce homozygously-targeted clones uniquely edited in exon 30 of *FBNI*. Finally, a further series of targeting experiments are required to determine the optimal conditions required to generate clones capable of differentiating appropriately; allowing us to

## Development of novel therapies for Marfan Syndrome using a human iPSC-derived disease model

determine if skipping exon 30 is beneficial or detrimental in our *in vitro* MFS disease model. Despite the positively-skipped hiPSC showing major difficulties in differentiating towards NC-SMC, CRISPR/Cas9 technology holds promise for correcting the disease-causing exon in our model of MFS and could potentially improve the vascular pathology displayed *in vitro* by mature SMC.

The CRISPR/cas9 system allows modifications of the genome using programmable nucleases and offers an attractive strategy for precisely correcting disease-causing mutations. Eric N Olson's group designed a CRISPR/Cas9-mediated correction strategy, termed "Myoediting", to deliver gene-editing components by adeno-associated virus (AAV) in postnatal muscle tissues of mdx mice, a murine model for DMD<sup>119</sup>. Here, they demonstrated effective delivery of dystrophin-restoration components to cardiac and skeletal muscle, which resulted in increased dystrophin expression up to 12 weeks post-injection. This approach was validated in a human system where precise CRISPR/Cas9-mediated correction restored dystrophin expression in DMD patient iPSC-derived myoblasts<sup>150</sup>. Furthermore, an encouraging study showed positively gene-edited muscle tissues using the CRISPR/Cas9 AAV delivery system in a canine model of DMD<sup>151</sup>. More recently, the CRISPR/Cas9 system was harnessed to develop a technology that controls gene splicing, efficiently induces exon-skipping and hardware permanent modifications in the genome. Here, CRISPR-SKIP was demonstrated to produce exon skipping at therapeutically significant levels after a single treatment, which is especially attractive for tackling the variety of human diseases<sup>152</sup>. Thus, genomic editing allows the permanent removal of the disease-causing mutation and this tactic is potentially applicable to the wide spectrum of mutation-harboring exons found in MFS patients.

However, it is of interest to note that large deletions and more complex genomic rearrangements have recently been identified in human differentiated cell lines targeted with CRISPR/Cas9<sup>153,154</sup>. Although sensitive detection methods have been developed to address off-target activity of this particular gene-editing technology, extensive on-target genomic damage is shown to be a common outcome in differentiated human cell lines. In the clinical context, it is important to consider that the lesions resulting from CRISPR/cas9 may be frequent, extensive and undetectable. When taken together with previous reports in the literature, it is possible that exon 30 removal in fibrillin-1 orchestrated by CRISPR/Cas9 induced detrimental genomic rearrangements hindering iPSC differentiation. Extensive molecular analysis is required to fully understand the impact of our gene-editing strategy targeting the fibrillin-1 gene. Substantial efforts have

been made to address the off-targets issue and a recent tool was developed to reliably identify and quantify off-targets provoked by gene-editing nucleases in whole organisms<sup>155</sup>. Therefore, it is warranted to comprehensively screen the effects of CRISPR/Cas9-mediated genomic modifications, which may occur beyond the scope of *in silico* predictions and provoke pathogenic consequences, before considering any form of patient administration.

In parallel to gene-editing, additional progress has been made in devising treatments based on gene-replacement. Conceptually, substituting the mutated protein with a normal one would provide a potential early-stage treatment for genetic diseases. Similar challenges have been encountered when attempting to replace the mutated dystrophin gene with a healthy counterpart, which are due to the enormous size of the gene and achieving effective distribution to the target muscles throughout the body.

As previously eluded to, AAV vectors have been proven superior for muscle gene transfer and a single intravenous injection of AAV results in whole-body muscle transduction *in vivo*<sup>137,156-158</sup>. However, a major hurdle remains to apply AAV for gene-replacement therapy as the maximal packaging capacity of an AAV virus is 4.4-kb. Similar to the 14-kb dystrophin cDNA, the fibrillin-1 protein is encoded by a 9.3-kb coding sequence much too large for effective packaging in AAV constructs. In the context of DMD, the issue was addressed by the generation of a series of mini-dystrophin genes weighing less than 4-kb that retain the essential set of functions needed to protect muscle from disease progression. Under the control of a muscle-specific promoter, these specific sequences are readily packaged into AAV vectors<sup>159,160</sup>. The mini-gene treatment restored myofiber morphology and increased dystrophin expression in murine models of DMD. This attractive novel approach has recently been brought into clinical trial by Pfizer, who has initiated a Phase 1b clinical trial for its mini-dystrophin gene therapy candidate in young patients suffering from DMD using AAV-based technology<sup>161</sup>.

Finally, the modular flexibility of dystrophin enables the genetic sequence to be modified and largely reduced, whilst still allowing the protein to retain significant function. Although microfibril fragments have been reported to themselves lead to pathogenic events through MMP upregulation<sup>162</sup>, the high number of tandemly repeated cbEGF domains may allow a certain plasticity within the coding sequence to modulate the size of the final protein secreted. Mini-fibrillin-1 genes may be an area worthy of investigation as there currently have been no cases reporting AAV-packaging of fibrillin-1 for replacing the faulty protein and restoring a functional ECM network. Considering

### **Development of novel therapies for Marfan Syndrome using a human iPSC-derived disease model**

all the recent advancements made for hereditary disease treatment, targeting the root cause of MFS syndrome using alternative gene-editing and gene-replacement strategies may offer novel means of therapeutic progression for MFS syndrome.

## 6.2 Transcriptome Profiling for Pathway Analysis in Human iPSC-derived Complex Disease Models

In MFS, the downstream pathological mechanisms of the fibrillin-1 mutations remain poorly understood. Therefore, there is a need for human-based disease models that recapitulate the pathological features of MFS in order to identify the disease-causing signalling pathways. The availability of MFS patient-sourced human iPSCs have enabled the study of disease progression and have also offered a platform for site-specific gene-editing. In this work, the rescued phenotype, displayed by the isogenic iPSC-derived SMC lines, is solely accounted for by the positively-edited point-mutation using CRISPR-targeting technology. Up to now, studies attributed canonical and non-canonical aberrant TGF- $\beta$  signalling as the main drivers of MFS. However, emerging evidence has disputed this theory, shifting the focus away from abnormal TGF- $\beta$  activity as being the exclusive cause for MFS disease manifestation<sup>71,73–75,163</sup>.

In order to identify novel disease drivers for MFS, RNA sequencing was utilised to capture the differences in signalling mediators between CRISPR-corrected and Marfan-uncorrected iPSC-derived SMCs. The completion of the Human Genome Project has enabled transcriptomics to evolve as a gold-standard reference tool in the study of human disease. By definition, transcriptomics allows the access to all transcribed RNA species at a particular developmental stage and under certain physiological or pathological conditions<sup>164</sup>. The complete landscape of all transcribed RNA species gives insight on the gene expression regulation and genome plasticity differences between samples of physiological and pathological origin. In this thesis, the work described attempts to disclose the key alternations in biological processes that participate in MFS manifestation and to discover novel disease markers useful for clinical therapy.

My findings demonstrated that our disease platform can predict variations in gene expression signatures at the transcriptomic level between MFS and isogenic NC-SMCs. Although the number of samples used to perform the analysis is relatively limited (n=2), previously identified disease-drivers such as, KLF4 and MMPs, were highlighted as significantly elevated in MFS NC-SMCs compared to their healthy counterparts in my transcriptomics study. This finding reinforced the ability of our disease model to serve as an investigatory platform capable of uncovering the biological causes that underlie the

## Development of novel therapies for Marfan Syndrome using a human iPSC-derived disease model

differences in gene expression. Using pathway analysis, I was able to identify a set of signalling pathways that are predicted to have a statistically significant association with the selection of differentially expressed genes between both samples at early (PTd12) and late (serum 2 weeks) stages of differentiation. My pathway analysis results highlighted significant differences in PI3K/Akt and Wnt signalling, suggesting a dysregulation in genetic modulators involved in those specific pathways at both stages of SMC maturation.

As previously mentioned, abdominal aneurysm formation is potentially triggered by abnormal Wnt-signalling and accumulation of respective downstream targets, such as  $\beta$ -catenin, which is thought to act as protective mechanism to counter the progressive loss of SMCs<sup>126,165,166</sup>. Previous studies have shown that abnormal Wnt signalling may play a role in abdominal aneurysm development<sup>167</sup> and atherosclerosis<sup>166</sup> progression. Within the context of MFS pathophysiology, SMC display high apoptotic rates associated with loss of aortic integrity, which may contribute to aneurysm development.  $\beta$ -catenin, a distal component of the highly conserved Wnt pathway, was reported to accumulate after vascular injury; suggesting a protective role in promoting SMC survival<sup>165</sup>. Although additional studies are required to characterise the role of Wnt signalling in MFS, my data suggests a potential role for abnormal Wnt activity and its respective partners in contributing to MFS disease progression. Therefore, these findings illustrate the relevance of using patient-specific iPSC lines to model complex diseases and compare them to their genetically engineered isogenic control line to identify novel pathogenic signalling pathways, which opens up possibilities for drug discovery.

Currently, differentiated iPSCs are conventionally grown in 2D monolayers, which lack many of the functions central to mimicking an accurate pathophysiological environment<sup>168</sup>. Novel biomaterials have enabled the production 3D scaffolds to mimic the organ architecture and seed relevant cell types to mimic the native biological tissue. However, these systems remain to be optimised due to cell-survival and precise methods to integrate vascular perfusion and mechanical forces have been suggested as an intermediate approach to model disease in 2D formats. To fully capture all disease-driving signalling pathways, it is important to consider the complex interplay between cell and ECM, whilst integrating the biological cues that influence vessel behaviour. Under normal conditions, the SMCs embedded in the medial lamellar units of the aorta vessel wall play a mechano-sensing role, whereby they are responsible for establishing, maintaining and restoring local mechanical homeostasis in the vasculature<sup>169,170</sup>. The resident SMCs perceive the mechanical loads and stimuli that are transmitted through

ECM constituents, intracellular structures and cell-to-matrix receptors<sup>171</sup>. Local changes in blood flow exert a significant tension on the ECM, which plays a protective role and shields the SMCs and other aortic wall cell types from high stresses<sup>172,173</sup>. Defects in force-sensing proteins affect the contractile nature of SMCs and are often linked to a panel of aneurysmal diseases. In the context of MFS, patients exhibit microfibril quality deterioration, ECM remodelling and SMC loss, which largely contribute to the increasing stiffness of the aortic wall and to disease progression. Recently, altered mechanical stimuli has been put forward to play a causal role in driving MFS pathogenicity<sup>174</sup>. Therefore, a number of biological cues remains to be incorporated into our *in vitro* disease system to recapitulate the abnormal mechanical stress-response and dysregulated contractility featured by patient SMCs.

In some of my previous work, I showed that mechanically-stretched MFS SMCs using cyclic stretching exhibited a higher density of focal adhesions and stress fibres. In culmination with increased MMP activity, these features were exacerbated in the MFS phenotype displayed *in vitro* compared to healthy SMCs<sup>28</sup>. The application of stretch to our *in vitro* system strives to recreate a more biologically-accurate environment that may help unveil the complexity of signalling abnormalities caused by defective fibrillin-1. In this thesis, the samples sequenced for transcriptomic analysis were issued from static SMC cultures. Nevertheless, a number genes coding for subunits of ion channels were identified to be differentially expressed in MFS SMCs. This abnormal ion channel signature may contribute to contractile defects and suggests abnormal SMC mechanistic behaviour. Different studies report conflicting results regarding the use of channel blockers in reducing aneurysm progression. Administration of amlodipine, a calcium-channel blocker (CCB), was shown to ablate aortic dilatation in MFS mice whilst a more recent consortium study demonstrated that different categories of CCBs exacerbated aortic tearing in an identical mouse model<sup>163,175</sup>. These opposing results have ramifications for MFS patients, to whom are regularly prescribed various classes of CCB agents. Therefore, the potentially pathogenic role played by the spectrum of ion channel subunits remains to be explored and may provide a therapeutic avenue for vasculopathies.

One of the limitations of the study presented in this thesis is the lack of information regarding differences in protein signatures between healthy and MFS SMCs. Although transcriptomic analyses give an overview of changes at the mRNA level, these do not necessarily correlate with fluctuations in protein expression. Vascular SMCs produce and sustain various components of the ECM, which is important for the structural

## Development of novel therapies for Marfan Syndrome using a human iPSC-derived disease model

support of the aortic wall. MFS patients exhibit a compromised ECM whereby matrix proteins endure severe proteolysis, a pathological event that cannot be detected at the level of transcribed mRNA and leads to aneurysmal complications. An initial proteomic study showed that aortic samples collected from MFS patients exhibit increased calpain expression and activity, which leads to histological changes and detrimental ECM remodelling<sup>176</sup>. Dr Manuel Mayr's group have developed an extraction method that captures soluble, newly synthesised and degradation protein products<sup>177</sup>. This novel and sensitive approach enables to define the ECM composition differences between aneurysmal aortas and healthy subjects. Thus, our work would benefit from a proteomics study comparing the ECM produced by normal and diseased SMCs in order to identify pathogenic protein differences and potentially highlight therapeutic targets.

The advent of high-throughput profiling has led to the development of tools capable of extracting meaning from long lists of differentially expressed genes (DEG) and proteins. Many approaches address this challenge by grouping individual genes into smaller sets of related genes or proteins, creating large knowledge-based datasets that associate a biological process or component (e.g. a signalling pathway) to an individual gene known to be involved in a specific biological story. In this study, Ingenuity Pathway Analysis (IPA) was the primary search-tool used to generate an array of biological pathways associated with the cluster of genes identified as differentially expressed between CRISPR-corrected and Marfan-uncorrected NC-SMCs. IPA is a comprehensive software that identifies pathways, which are potentially impactful in a condition by correlating pathway information issued from at least one database with gene expression patterns found in the condition of interest. Although the databases queried by IPA are extensive, they still present some outstanding limitations, which include those of an annotation nature<sup>178</sup>. Annotation difficulties take into account inaccuracies within the databases and omitting the detailed role of a gene in a specific condition, timepoint or cell-type. Therefore, it is important to note that non-specific genes can possibly introduce a bias in the analysis and, as a result, allocate a higher significance to a certain pathway.

Patient-specific iPSC technology became attractive when it became apparent that rodent models were insufficient to fully recapitulate human clinical pathophysiology. The fundamental differences between species has contributed to poor translation of potential drugs from rodents to human and, therefore, has led to failures of many clinical trials over the years. Despite human iPSC providing a valuable drug discovery platform, concerns around genetic instability of iPSC lines and variability in their differentiation

potential towards different cell fates remains a challenge to the disease modelling community. Marked variability in iPSC differentiation potential has been reported where transcriptomic signatures acknowledged genetic heterogeneity amongst donor cell lines to be the main contributor towards transcription differences<sup>179</sup>. Although surprising, several lines of evidence report a high intra-patient variability between functional cell phenotypes derived from the same patient iPSC during separate differentiations<sup>180,181</sup>. In light of our findings, this uncovered differentiation bias within a single iPSC line could explain the transcriptional variability of significantly differentiated genes within samples generated from the same MFS patient-derived iPSC cell-line and respective isogenic control. To address this issue, we suggest the following experimental procedures (i) increase the number of differentiations of a single patient-derived iPSC lines to be RNA-sequenced in the aim of reducing the skewed differentiation potential and (ii) compare the transcriptomic profiles of MFS patients harbouring different missense mutations to identify the common pathophysiological processes underlying MFS that can be targeted therapeutically.

Taking all these observations together, there is a need to study the transcriptomic profiles of MFS SMCs cultured in a more biologically-relevant *in vitro* system and evaluating the complementary proteomes to gain a more comprehensive view of the pathological mechanisms underlying aortic dilation. Ongoing efforts in our lab are currently aiming to analyse the transcriptomes of stretched and static SMCs derived from MFS patient iPSC lines harbouring different mutations to uncover additional non-TGF- $\beta$ -mediated disease drivers.

## 6.3 Improving Drug screening of Complex Disease Platforms for Pre-clinical Purposes

The ability of our model to mimic the disease characteristics exhibited in MFS patients presents a platform capable of identifying novel signalling pathways and molecular mechanisms involved in disease progression. Here, I report that MMP activity is a reliable feature of the disease model and constitutes a feasible read-out for low- to medium-throughput drug screening. Although, the over-arching goal of this study is to identify pathways involved in a spectrum of phenotypic abnormalities, it remained necessary to select a single robust disease characteristic to instigate the preliminary drug-screen. As previously described, disease-specific human iPSC can recapitulate pathophysiological mechanisms and serve as an investigatory platform to identify novel pathways. The challenge lies in adapting these disease models for screening purposes. To the best of our knowledge, there has been a lack of high-throughput drug screens dedicated to screening large libraries of compounds aimed at reversing the pathological features of MFS exhibited *in vitro*. In this body work, our MFS disease model is employed to develop a low- to medium-throughput screen based on abnormal proteolysis whereby positive hits are investigated to unravel the pathological mechanisms leading to aneurysm formation.

The abnormal proteolysis exhibited in our MFS *in vitro* system is reflected in patients and constitutes a feature of the disease, which potentially may be interesting for therapeutic intervention. Therefore, a phenotypic collection of 14,000 annotated molecules, which target a range of 1,200 human genes, was screened for its ability to reduce MMP activity in MFS SMCs. The power of this phenotypic library stems from it being designed to hit many overlapping targets. A recurrent positive target identified from the drug screen will inform as to which pathways should be further explored for target deconvolution. For practical reasons pertaining to executing a low- to medium-throughput drug screen in-house, it was challenging to screen the entire compound library. Therefore, a smaller subset of compounds, which exemplified a broad representation of all target genes, was selected for the drug screen.

Results obtained from an initial 100-compound screen and, subsequently upscaled to 1000 compounds, showed that successful MMP-reducing compounds

targeted genes involved in pathways previously described to be involved in MFS pathogenesis, such as TGF- $\beta$  and p38 MAP kinase signalling pathways. However, out of 1000 compounds screened, GSK3 $\beta$  was a recurrent positive target for reducing MMP activity, which led us to believe that GSK3 $\beta$ -dependent signalling pathways may participate in MFS physiopathology. Further validation showed that the dysregulated apoptotic profile in MFS SMCs could be reversed through GSK3 $\beta$  inhibition. Additional studies are required to further characterise the role of GSK3 $\beta$  in MFS pathogenicity, which would include evaluating the GSK3 $\beta$  signatures in MFS iPSC-derived SMCs harbouring other mutations and in MFS SMCs derived from different embryonic origins. Furthermore, the library remains to be investigated in its entirety and follow-up efforts are needed to miniaturise our complex disease phenotypic screen to a scale, which is befitting of high-throughput screening machinery.

Additional novel targets were extracted from the MMP-reducing list of compounds, such as an array of ion channels subunits. Ion channels and GSK3 $\beta$  have not been explicitly described in the literature as being linked to MFS development although there is evidence Wnt inhibition reduces aneurysm formation. Sclerostin, a Wnt inhibitor, was recorded to reduce the formation of angiotensin-II induced abdominal aortic aneurysm and atherosclerosis<sup>167</sup>. Although my preliminary studies suggest that GSK3 $\beta$  inhibition potentially yields a positive effect on MFS pathophysiology, it is worth noting that the previous research cited using Sclerostin was conducted on abdominal aneurysm whereas the focus of my study is on SMCs derived from patients that develop complications in the region of the thoracic aorta. The origin of SMCs populating these distinct aortic regions may cause the SMCs to respond differently to the modulation of Wnt signalling and require different treatment procedures. Thus, the impact on SMC origin and mutation type on treatment requirements remains to be further investigated.

The work in this thesis primarily focused on exploring the pathogenic role of a single positive hit, GSK3 $\beta$ , issued from the drug-screen as this gene-target correlated with important dysregulated pathways identified in the respective transcriptomic analysis. However, other sets of compounds, including ion-channel inhibitors, revealed themselves as putative MMP-reducing agents. As previously mentioned, ECM provides a scaffold for quiescent contractile SMCs to mature and disruption of the contractile apparatus can lead to aneurysm growth and different arterial pathologies<sup>171,172,182</sup>. As the field for aortopathies is moving towards arterial mechanics, ion channels represent highly attractive target for drug discovery. Ion channels are pore-forming proteins that allow the

## Development of novel therapies for Marfan Syndrome using a human iPSC-derived disease model

movement of ions across the membranes of SMCs and participate in crucial functions of the vasculature, including mobilizing ions for regulating contractile activity and vascular tone. SMCs exhibit a plethora of ion channels, which include potassium ( $K^+$ ) channels, intracellular  $Ca^{2+}$  release channels and many more<sup>183</sup>.

Previous studies have recorded the importance of  $K^+$  channel activity in regulating vascular tone and blood vessel diameter<sup>184</sup>. Altered  $K^+$  channel protein expression in SMCs is known to compromise the ability of the vessel to adapt properly to mechanistic forces. Information from our drug screen revealed that inhibition of a subset of  $K^+$  subunits was able to significantly reduce MMP activity. Due to the restricted tools able to measure ion channel biophysical characteristics, very few studies have explored the impact of  $K^+$  channel function in vascular disease and ion channels remain an under-exploited target class. However, rising improvements in state-of-the-art sensor technologies have enabled the development of automated electrophysiology instruments, which provide ways to screen ion channel specific-compounds in high-throughput conditions<sup>185</sup>. A recent study, focusing on  $K^+$  channel activity, developed a cell-based assay for high-throughput screening using a novel fluorescent dye, FluxOR<sup>TM</sup>. Here, the dye-based assay identified specific inhibitors of  $K^+$  channel subunits and showed that the read-out can easily be incorporated in a high-throughput workflow whilst maintaining pharmacological fidelity<sup>186</sup>. Therefore, these novel approaches have reenergised ion channel-focused drug discovery and it remains an interesting area of investigation for potentially correcting the contractile and proteolytic abnormalities in SMCs issued from MFS patients.

Our disease model is currently based on a single cell-type, which may limit the true efficacy of drugs identified by our phenotypic screen. The absence of other vascular cell-types in our model may render important disease-causing signalling pathways elusive. A co-culture system incorporating SMCs with other vascular cells, such as endothelial cells, will improve the range of physiological conditions and may more accurately replicate the MFS disease environment. Endothelial cells are known to participate in the regulation of circulatory functions through mechanical stimuli partially governed by stretch-activated mechanosensors<sup>187</sup>. Piezo1, a large transmembrane stretch-activated ion-channel, was recently identified as a pivotal mediator for mechanical stimuli in the vascular architecture<sup>188</sup>. Several reports suggested a role for Piezo1 in regulating mechanotransduction in endothelial cells<sup>188,189</sup>. Therefore, integrating different vascular cell-types into our SMC-based MFS disease model may enable a cell-to-cell

communication process that could potentially improve the drug discovery pipeline for MFS.

Finally, the identification of a single therapeutic target may be insufficient to reverse all phenotypic abnormalities displayed by our disease model. In the past, patient clinical trials have failed to demonstrate efficacy of a single drug treatment<sup>80</sup>. Therefore, it may be useful to consider treating our MFS model with a combination of compounds that can further be developed for therapeutic purposes. Employing a drug-cocktail strategy offers several advantages, which include (i) modulating the dose of each individual compound to patient-approved administration levels (ii) adapting the drug-cocktail to a specific MFS mutation category (iii) provide a pre-clinical platform complementary to *in vivo* drug testing. There is evidence stating that the type of MFS mutation may respond to different treatments. Several follow-up sub-studies to the losartan clinical trial conducted in 2014 showed that segregating patients according to their mutation type may define a patient category that is more responsive to losartan than others<sup>81,82</sup>. Therefore, it may prove to be insightful to design drug-screen tools according to the mutation category exhibited by the MFS patients in order to identify appropriate treatment strategies.

## 6.4 Future Directions

This thesis attempts to address the need to develop innovative approaches to identify and intervene upon novel pathological mediators in MFS using a patient iPSC-derived *in vitro* disease model. Previous research using mice models have been failed to translate the treatments aimed at reversing aortic aneurysm progression to the clinic. Therefore, using patient material to model a disease *in vitro* offers a biologically-relevant system to study disease development and investigate therapeutic strategies. Our patient-derived MFS model recapitulates the majority of disease features exhibited by patients and provides a reliable platform to predict the effectiveness of medical strategies.

As previously described, MFS is caused by mutations in *FBNI*, a gene coding for an extracellular matrix protein called fibrillin-1. The mutant protein, either by loss-of-function or by detrimentally interacting with the endogenous wild-type microfibrils, is thought to negatively impact the structure of the connective tissue fibres. This detrimental effect potentially contributes to the weakening of the vessel wall and enables aneurysm formation. Additionally, fibrillin-1 plays a bioregulatory role by binding to growth-factors (e.g. TGF- $\beta$ ), cell-surface receptors and other matrix proteins. Therefore, defective fibrillin-1 is suggested to release TGF- $\beta$  in the environment, driving abnormal TGF- $\beta$  activity and contributing to MFS pathogenicity. Although TGF- $\beta$  signaling is potentially responsible for participating in disease development, emerging evidence has contested its role as sole disease-driver both in animal models and in the clinic.

In this thesis, the work demonstrates that our human MFS disease model can be harnessed to unveil novel pathological signaling pathways and, subsequently, to develop alternative therapeutic strategies. Here, I explore the possibility of interfering directly at the root-cause by removing the mutation using exon-skipping technology. My results show that removing the faulty exon is feasible using antisense oligonucleotides (AON)-mediated exon skipping and CRISPR-based gene editing. However, in our system, AON-targeting methods generated variable levels of skipping and it was difficult to assess whether these tools truly were able to reverse or restore the phenotypic characteristics of our disease model. Gene-correction tools, such as CRISPR/Cas9 technology, have been employed to treat other complex genetic disease (e.g. DMD) and offer an alternative approach to robustly remove the faulty exon from the genome. However, CRISPR-edited

NC-derived SMCs were unable to fully differentiate and mature *in vitro*, suggesting an off-target effect caused by the design of our gene-editing components. Additional efforts need to be effectuated to optimise a CRISPR-based gene-correction strategy in order to fully evaluate the effect of removing a mutation-containing exon from the final translated fibrillin-1 protein and, subsequently, on the pathophysiology of MFS.

Additionally, I developed a pair of unbiased and complementary methods to identify novel pathways that cause disease. For this, our model was exploited to investigate novel pathogenic signatures using a phenotypic drug assay based on reversing the abnormal proteolytic profile in our MFS system. My in-house drug screen was designed to capture compounds capable of inhibiting MMP activity, a prominent disease feature exhibited by our model and in patients. For practical purposes, a selection of compounds from a drug library designed for high-throughput screening was picked for testing in our system. Out of 1000 compounds, a subset was identified to reproducibly reduce MMP activity in MFS NC-SMCs, which included the gene target GSK3 $\beta$ . Although GSK3 $\beta$  has been reported to participate in abdominal aortic aneurysm progression, via the Wnt signaling pathway<sup>167</sup>, there are no studies, to my knowledge, claiming a GSK $\beta$ -dependent effect in thoracic aortic aneurysm development. Interestingly, my RNA sequencing analysis complements these findings as putative abnormal expression was highlighted in the GSK $\beta$ /Wnt, PI3K/AKT and ion channel signalling pathways. In the future, the significant overlap in results will allow me to prioritise these mechanisms for further investigation. Therefore, the role of GSK $\beta$  as a novel gene target remains to be thoroughly validated using a spectrum of phenotypic assays. Finally, my results demonstrate that it is feasible to exploit *in vitro* platforms of complex diseases to design a phenotypic assay capable of capturing novel signaling pathways that may participate in MFS pathogenicity.

Despite our MFS disease model being able to recapitulate the majority of patient features, several limitations require attention in order to improve drug discovery in *in vitro* systems for vascular disease. Emerging mechanistic data is contesting the pathological hyperactive TGF- $\beta$  theory and the field is starting to consider alternations in myogenic tone, extracellular matrix contraction and fluid pressure, as aggravating factors in aortopathies<sup>190</sup>. Thus, it is becoming urgent to model the initial stages of aneurysm formation, which one of the causes is suggested to be

## Development of novel therapies for Marfan Syndrome using a human iPSC-derived disease model

the result of a tear in the intimal layer of the vessel. This further triggers intralamellar fluid infiltration and expansion of the vessel area. Various approaches may help to improve our disease model by integrating different biological cues, such as additional vascular cell-types (e.g. endothelial cells) using co-culture technology and applying mechanical forces (e.g. stretch) and fluid dynamics to replicate the physiological environment of SMCs.

Improving the model system of complex aortopathies will enable to reveal the pathological mechanisms that underlie MFS and offer a more reliable platform for the development of new diagnostic technologies. In the future, optimised disease models will offer the possibility of studying a spectrum of MFS mutations and widen the patient landscape for therapeutic investigation. Human *in vitro* data can serve as a pre-clinical platform, which potentially is able to complement drug discovery studies performed in animal models to better inform clinical trials. As a result, the work presented in this thesis may contribute to the scientific research ideal of personalised medicine and have implications in the development of therapeutic strategies for MFS and a wide spectrum of aortic pathologies.

# 7 REFERENCES

## Development of novel therapies for Marfan Syndrome using a human iPSC-derived disease model

1. Deglincerti, A. *et al.* Self-organization of the in vitro attached human embryo. *Nature* **533**, 251–254 (2016).
2. Carlson, B. M. *Human embryology and developmental biology.* (Elsevier/Saunders, 2014).
3. Seidelmann, S. B., Lighthouse, J. K. & Greif, D. M. Development and pathologies of the arterial wall. *Cell. Mol. Life Sci.* **71**, 1977–1999 (2014).
4. Wagenseil, J. E. & Mecham, R. P. Vascular extracellular matrix and arterial mechanics. *Physiol. Rev.* **89**, 957–89 (2009).
5. Hellström, M. *et al.* Lack of pericytes leads to endothelial hyperplasia and abnormal vascular morphogenesis. *J. Cell Biol.* **153**, 543–53 (2001).
6. Yancopoulos, G. D. *et al.* Vascular-specific growth factors and blood vessel formation. *Nature* **407**, 242–248 (2000).
7. Loughna, S. & Sato, T. N. Angiopoietin and Tie signaling pathways in vascular development. *Matrix Biol.* **20**, 319–25 (2001).
8. Uemura, A. *et al.* Recombinant angiopoietin-1 restores higher-order architecture of growing blood vessels in mice in the absence of mural cells. *J. Clin. Invest.* **110**, 1619–1628 (2002).
9. Peter Carmeliet. *Mechanisms of angiogenesis and arteriogenesis.* (2000).
10. Kumar, M. S. Combinatorial Control of Smooth Muscle-Specific Gene Expression. *Arterioscler. Thromb. Vasc. Biol.* **23**, 737–747 (2003).
11. Sun, Z., Martinez-Lemus, L. A., Hill, M. A. & Meininger, G. A. Extracellular matrix-specific focal adhesions in vascular smooth muscle produce mechanically active adhesion sites. *Am. J. Physiol. Cell Physiol.* **295**, C268-78 (2008).
12. Owens, G. K., Kumar, M. S. & Wamhoff, B. R. Molecular regulation of vascular smooth muscle cell differentiation in development and disease. *Physiol. Rev.* **84**, 767–801 (2004).
13. Campbell, J. H. & Campbell, G. R. Smooth Muscle Phenotypic Modulation—A Personal Experience. *Arterioscler. Thromb. Vasc. Biol.* **32**, 1784–1789 (2012).
14. Kieny, M., Mauger, A., Chevallier, A. & Sengel, P. [Origin of cutaneous smooth muscles in birds (author's transl)]. *Arch. Anat. Microsc. Morphol. Exp.* **68**, 283–90 (1979).

15. Gadson, P. F., Rossignol, C., McCoy, J. & Rosenquist, T. H. Expression of elastin, smooth muscle alpha-actin, and c-jun as a function of the embryonic lineage of vascular smooth muscle cells. *In Vitro Cell. Dev. Biol. Anim.* **29A**, 773–81 (1993).
16. Jiang, X. *Fate of the mammalian cardiac neural crest.* (2000).
17. Waldo, K. L. *et al.* Secondary heart field contributes myocardium and smooth muscle to the arterial pole of the developing heart. (2005). doi:10.1016/j.ydbio.2005.02.012
18. Milan Esner<sup>1</sup>, Sigolène M. Meilhac<sup>1,\*</sup>, Frédéric Relaix<sup>1</sup>, Jean-François Nicolas<sup>1</sup>, Giulio Cossu<sup>2,3, 4</sup> and Margaret E. Buckingham<sup>1, †</sup>. Smooth muscle of the dorsal aorta shares a common clonal origine with skeletal muscle of the myotome. *Development* 737–749 (2005). doi:10.1242/dev.02226
19. Wasteson, P. *et al.* Developmental origin of smooth muscle cells in the descending aorta in mice. *Development* **135**, 1823–32 (2008).
20. Majesky, M. W. Developmental basis of vascular smooth muscle diversity. *Arterioscler. Thromb. Vasc. Biol.* **27**, 1248–58 (2007).
21. HAIMOVICI, H. & MAIER, N. Fate of Aortic Homografts in Canine Atherosclerosis. *Arch. Surg.* **89**, 961 (1964).
22. Sinha, S. & Santoro, M. M. New models to study vascular mural cell embryonic origin: implications in vascular diseases. doi:10.1093/cvr/cvy005
23. Dietz, H. C. *et al.* Marfan syndrome caused by a recurrent de novo missense mutation in the fibrillin gene. *Nature* **352**, 337–339 (1991).
24. Van Hemelrijk, C., Renard, M. & Loeys, B. The Loeys–Dietz syndrome: an update for the clinician. *Curr. Opin. Cardiol.* **25**, 546–551 (2010).
25. Malfait, F. *et al.* The 2017 international classification of the Ehlers-Danlos syndromes. *Am. J. Med. Genet. Part C Semin. Med. Genet.* **175**, 8–26 (2017).
26. Nataf, P. & Lansac, E. Dilation of the thoracic aorta: medical and surgical management. *Heart* **92**, 1345–1352 (2006).
27. Leroux-Berger, M. *et al.* Pathologic calcification of adult vascular smooth muscle cells differs on their crest or mesodermal embryonic origin. *J. Bone Miner. Res.* **26**, 1543–1553 (2011).
28. Granata, A. *et al.* An iPSC-derived vascular model of Marfan syndrome identifies

- key mediators of smooth muscle cell death. *Nat. Genet.* **49**, 97–109 (2017).
29. Wolinsky, H. & Glagov, S. Comparison of abdominal and thoracic aortic medial structure in mammals. Deviation of man from the usual pattern. *Circ. Res.* **25**, 677–86 (1969).
  30. Ruddy, J. M., Jones, J. A., Spinale, F. G. & Ikonomidis, J. S. Regional heterogeneity within the aorta: Relevance to aneurysm disease. *J. Thorac. Cardiovasc. Surg.* **136**, 1123–1130 (2008).
  31. Halloran, B. G., Davis, V. A., McManus, B. M., Lynch, T. G. & Baxter, B. T. Localization of Aortic Disease Is Associated with Intrinsic Differences in Aortic Structure. *J. Surg. Res.* **59**, 17–22 (1995).
  32. Groenink, M. *et al.* The influence of aging and aortic stiffness on permanent dilation and breaking stress of the thoracic descending aorta. *Cardiovasc. Res.* **43**, 471–80 (1999).
  33. Zorina S. Galis, J. J. K. Matrix Metalloproteinases in Vascular Remodeling and Atherogenesis The Good, the Bad, and the Ugly. *Circ. Res.* 251–262 (2002). doi:10.1161/hh0302.105345
  34. Dietz, H. C. *et al.* The skipping of constitutive exons in vivo induced by nonsense mutations. *Science* **259**, 680–3 (1993).
  35. Loeys, B. L. *et al.* The revised Ghent nosology for the Marfan syndrome. *J. Med. Genet.* **47**, 476–85 (2010).
  36. Faivre, L. *et al.* The new Ghent criteria for Marfan syndrome: what do they change? *Clin. Genet.* **81**, 433–442 (2012).
  37. Sakai, L. Y., Keenes, D. R., Glanvilles, R. W. & Bachingerss, H. P. *THE JOURNAL OF BIOLOGICAL CHEMISTRY Purification and Partial Characterization of Fibrillin, a Cysteine-rich Structural Component of Connective Tissue Microfibrils\**. **266**, (1991).
  38. von Kodolitsch, Y., Rybczynski, M., Robinson, P. N. & Godfrey, M. in *Marfan Syndrome: A Primer for Clinicians and Scientists* 45–69 (Springer US, 2004). doi:10.1007/978-1-4419-9013-6\_5
  39. Nienaber, C. A. & Clough, R. E. Management of acute aortic dissection. *Lancet* **385**, 800–11 (2015).

40. Halpern, B. L., Char, F., Murdoch, J. L., Horton, W. B. & McKusick, V. A. A prospectus on the prevention of aortic rupture in the Marfan syndrome with data on survivorship without treatment. *Johns Hopkins Med. J.* **129**, 123–9 (1971).
41. Shores, J., Berger, K. R., Murphy, E. A. & Pyeritz, R. E. Progression of Aortic Dilatation and the Benefit of Long-Term  $\beta$ -Adrenergic Blockade in Marfan's Syndrome. *N. Engl. J. Med.* **330**, 1335–1341 (1994).
42. Ose, L. & McKusick, V. A. Prophylactic use of propranolol in the Marfan syndrome to prevent aortic dissection. *Birth Defects Orig. Artic. Ser.* **13**, 163–9 (1977).
43. Sakai, L. Y., Keene, D. R. & Engvall, E. Fibrillin, a new 350-kD glycoprotein, is a component of extracellular microfibrils. *J. Cell Biol.* **103**, 2499–509 (1986).
44. Handford, P. . Fibrillin-1, a calcium binding protein of extracellular matrix. *Biochim. Biophys. Acta - Mol. Cell Res.* **1498**, 84–90 (2000).
45. Ramirez, F. & Pereira, L. The fibrillins. *Int. J. Biochem. Cell Biol.* **31**, 255–9 (1999).
46. Ramirez, F., Sakai, L. Y., Dietz, H. C. & Rifkin, D. B. Fibrillin microfibrils: multipurpose extracellular networks in organismal physiology. *Physiol. Genomics* **19**, 151–4 (2004).
47. Ramirez, F. & Dietz, H. C. Fibrillin-Rich Microfibrils: Structural Determinants of Morphogenetic and Homeostatic Events. *J. Cell. Physiol* **213**, 326–330 (2007).
48. Pereira, L. *et al.* Pathogenetic sequence for aneurysm revealed in mice underexpressing fibrillin-1. *Proc. Natl. Acad. Sci. U. S. A.* **96**, 3819–23 (1999).
49. Robertson, I. B. *et al.* Latent TGF- $\beta$ -binding proteins. *Matrix Biol.* **47**, 44–53 (2015).
50. Horiguchi, M., Ota, M. & Rifkin, D. B. Matrix control of transforming growth factor- $\beta$  function. *J. Biochem.* **152**, 321–9 (2012).
51. Jones, J. A., Spinale, F. G. & Ikonomidis, J. S. Transforming growth factor-beta signaling in thoracic aortic aneurysm development: a paradox in pathogenesis. *J. Vasc. Res.* **46**, 119–37 (2009).
52. Dietz, H. C. & Pyeritz, R. E. Mutations in the human gene for fibrillin-1 (FBN1) in the Marfan syndrome and related disorders. *Hum. Mol. Genet.* **4 Spec No**, 1799–

809 (1995).

53. Dietz, H. C., Loeys, B., Carta, L. & Ramirez, F. Recent progress towards a molecular understanding of Marfan syndrome. *Am. J. Med. Genet. C. Semin. Med. Genet.* **139C**, 4–9 (2005).
54. Lafyatis, R. Transforming growth factor  $\beta$ —at the centre of systemic sclerosis. *Nat. Rev. Rheumatol.* **10**, 706–719 (2014).
55. Milewicz, D. M., Pyeritz, R. E., Crawford, E. S. & Byers, P. H. Marfan syndrome: defective synthesis, secretion, and extracellular matrix formation of fibrillin by cultured dermal fibroblasts. *J. Clin. Invest.* **89**, 79–86 (1992).
56. Tiecke, F. *et al.* Classic, atypically severe and neonatal Marfan syndrome: twelve mutations and genotype–phenotype correlations in FBN1 exons 24–40. (2001).
57. Palz, M. *et al.* Clustering of mutations associated with mild Marfan-like phenotypes in the 3' region of FBN1 suggests a potential genotype-phenotype correlation. *Am. J. Med. Genet.* **91**, 212–21 (2000).
58. Liu, W. *et al.* Mutant fibrillin-1 monomers lacking EGF-like domains disrupt microfibril assembly and cause severe marfan syndrome. *Hum. Mol. Genet.* **5**, 1581–1587 (1996).
59. Barnett, C. P. *et al.* Central nervous system abnormalities in two cases with neonatal Marfan syndrome with novel mutations in the fibrillin-1 gene. *Am. J. Med. Genet. Part A* **152A**, 2409–2412 (2010).
60. Aoyama, T., Tynan, K., Dietz, H. C., Francke, U. & Furthmayr, H. Missense mutations impair intracellular processing of fibrillin and microfibril assembly in Marfan syndrome. *Hum. Mol. Genet.* **2**, 2135–40 (1993).
61. Pereira, L. *et al.* Targetting of the gene encoding fibrillin–1 recapitulates the vascular aspect of Marfan syndrome. *Nat. Genet.* **17**, 218–222 (1997).
62. Ramirez, F. & Sakai, L. Y. Biogenesis and function of fibrillin assemblies. *Cell Tissue Res.* **339**, 71–82 (2010).
63. Judge, D. P. *et al.* Evidence for a critical contribution of haploinsufficiency in the complex pathogenesis of Marfan syndrome. *J. Clin. Invest.* **114**, 172–81 (2004).
64. Ng, C. M. *et al.* TGF-beta-dependent pathogenesis of mitral valve prolapse in a mouse model of Marfan syndrome. *J. Clin. Invest.* **114**, 1586–92 (2004).

65. Kaartinen, V. & Warburton, D. Fibrillin controls TGF- $\beta$  activation. *Nat. Genet.* **33**, 331–332 (2003).
66. Neptune, E. R. *et al.* Dysregulation of TGF- $\beta$  activation contributes to pathogenesis in Marfan syndrome. *Nat. Genet.* **33**, 407–411 (2003).
67. Kang, J. S., Liu, C. & Derynck, R. New regulatory mechanisms of TGF- $\beta$  receptor function. *Trends Cell Biol.* **19**, 385–394 (2009).
68. Yamashita, M. *et al.* TRAF6 mediates Smad-independent activation of JNK and p38 by TGF-beta. *Mol. Cell* **31**, 918–24 (2008).
69. Habashi, J. P. *et al.* Losartan, an AT1 antagonist, prevents aortic aneurysm in a mouse model of Marfan syndrome. *Science* **312**, 117–21 (2006).
70. Charbonneau, N. L. *et al.* In vivo studies of mutant fibrillin-1 microfibrils. *J. Biol. Chem.* **285**, 24943–55 (2010).
71. Cook, J. R. *et al.* Dimorphic effects of transforming growth factor- $\beta$  signaling during aortic aneurysm progression in mice suggest a combinatorial therapy for Marfan syndrome. *Arterioscler. Thromb. Vasc. Biol.* **35**, 911–7 (2015).
72. Chen, X. *et al.* TGF- $\beta$  Neutralization Enhances AngII-Induced Aortic Rupture and Aneurysm in Both Thoracic and Abdominal Regions. *PLoS One* **11**, e0153811 (2016).
73. Wang, Y. *et al.* TGF-beta activity protects against inflammatory aortic aneurysm progression and complications in angiotensin II-infused mice. *J. Clin. Invest.* **120**, 422–32 (2010).
74. Choudhary, B. *et al.* Absence of TGFb Signaling in Embryonic Vascular Smooth Muscle Leads to Reduced Lysyl Oxidase Expression, Impaired Elastogenesis, and Aneurysm. doi:10.1002/dvg.20466
75. Wei, H. *et al.* Aortopathy in a Mouse Model of Marfan Syndrome Is Not Mediated by Altered Transforming Growth Factor b Signaling. doi:10.1161/JAHA
76. Atlas, S. A. The Renin-Angiotensin Aldosterone System: Pathophysiological Role and Pharmacologic Inhibition. *J. Manag. Care Pharm.* **13**, 9–20 (2007).
77. Wang, C., Qian, X., Sun, X. & Chang, Q. Angiotensin II increases matrix metalloproteinase 2 expression in human aortic smooth muscle cells via AT1R and ERK1/2. *Exp. Biol. Med.* **240**, 1564–1571 (2015).

## Development of novel therapies for Marfan Syndrome using a human iPSC-derived disease model

78. Orsborne, C., Chaggar, P. S., Shaw, S. M. & Williams, S. G. The renin-angiotensin-aldosterone system in heart failure for the non-specialist: the past, the present and the future. *Postgrad. Med. J.* **93**, 29–37 (2017).
79. Holm, T. M. *et al.* Noncanonical TGF $\beta$  signaling contributes to aortic aneurysm progression in Marfan syndrome mice. *Science* **332**, 358–61 (2011).
80. Lacro, R. V. *et al.* Atenolol versus Losartan in Children and Young Adults with Marfan's Syndrome. *N. Engl. J. Med.* **371**, 2061–2071 (2014).
81. Milleron, O. *et al.* Marfan Sartan: a randomized, double-blind, placebo-controlled trial. *Eur. Heart J.* **36**, 2160–2166 (2015).
82. Franken, R. *et al.* Beneficial Outcome of Losartan Therapy Depends on Type of FBN1 Mutation in Marfan Syndrome. *Circ. Cardiovasc. Genet.* **8**, 383–388 (2015).
83. Pera, M. F. & Trounson, A. O. Human embryonic stem cells: prospects for development. *Development* **131**, 5515–25 (2004).
84. Carver, J. *et al.* An in-vitro model for stromal invasion during implantation of the human blastocyst. *Hum. Reprod.* **18**, 283–290 (2003).
85. Shahbazi, M. N. *et al.* Self-organization of the human embryo in the absence of maternal tissues. *Nat. Cell Biol.* **18**, 700–708 (2016).
86. Pera, M. F. *et al.* What if stem cells turn into embryos in a dish? *Nat. Methods* **12**, 917–919 (2015).
87. Thomson, J. A. *et al.* Embryonic stem cell lines derived from human blastocysts. *Science* **282**, 1145–7 (1998).
88. Takahashi, K. *et al.* Induction of Pluripotent Stem Cells from Adult Human Fibroblasts by Defined Factors. *Cell* **131**, 861–872 (2007).
89. Vallier, L., Alexander, M. & Pedersen, R. A. Activin/Nodal and FGF pathways cooperate to maintain pluripotency of human embryonic stem cells. *J. Cell Sci.* **118**, 4495–4509 (2005).
90. Vallier, L. *et al.* Signaling Pathways Controlling Pluripotency and Early Cell Fate Decisions of Human Induced Pluripotent Stem Cells. *Stem Cells* **27**, 2655–2666 (2009).
91. Pauklin, S. & Vallier, L. Activin/Nodal signalling in stem cells. *Development* **142**, 607–619 (2015).

92. Brons, I. G. M. *et al.* Derivation of pluripotent epiblast stem cells from mammalian embryos. *Nature* **448**, 191–195 (2007).
93. Vallier, L., Touboul, T., Chng, Z., Brimpari, M. & Hannan, N. Early Cell Fate Decisions of Human Embryonic Stem Cells and Mouse Epiblast Stem Cells Are Controlled by the Same Signalling Pathways Early Cell Fate Decisions of Human Embryonic Stem Cells and Mouse Epiblast Stem Cells Are Controlled by the Same Signalling Pathways. *PLoS ONE* **4**(6): e6082. (2009). doi:10.1371/journal.pone.0006082
94. Bernardo, A. S. *et al.* BRACHYURY and CDX2 Mediate BMP-Induced Differentiation of Human and Mouse Pluripotent Stem Cells into Embryonic and Extraembryonic Lineages. *Cell Stem Cell* **9**, 144–155 (2011).
95. Cheung, C., Bernardo, A. S., Trotter, M. W. B., Pedersen, R. A. & Sinha, S. Generation of human vascular smooth muscle subtypes provides insight into embryological origin-dependent disease susceptibility. *Nat. Biotechnol.* **30**, 165–73 (2012).
96. Vitale, A. M. *et al.* Variability in the Generation of Induced Pluripotent Stem Cells: Importance for Disease Modeling. doi:10.5966/setm.2012-0043
97. Soldner, F. & Jaenisch, R. Medicine. iPSC disease modeling. *Science* **338**, 1155–6 (2012).
98. Grskovic, M., Javaherian, A., Strulovici, B. & Daley, G. Q. Induced pluripotent stem cells — opportunities for disease modelling and drug discovery. *Nat. Rev. Drug Discov.* **10**, 915 (2011).
99. Jinek, M. *et al.* A Programmable Dual-RNA-Guided DNA Endonuclease in Adaptive Bacterial Immunity. *Science (80-. ).* **337**, 816–821 (2012).
100. Schrijver, I., Liu, W., Brenn, T., Furthmayr, H. & Francke, U. Cysteine Substitutions in Epidermal Growth Factor–Like Domains of Fibrillin-1: Distinct Effects on Biochemical and Clinical Phenotypes. *Am. J. Hum. Genet.* **65**, 1007–1020 (1999).
101. Cheung, C., Bernardo, A. S., Pedersen, R. A. & Sinha, S. Directed differentiation of embryonic origin-specific vascular smooth muscle subtypes from human pluripotent stem cells. *Nat. Protoc.* **9**, 929–38 (2014).
102. Jain, R. K. Molecular regulation of vessel maturation. *Nat. Med.* **9**, 685–693

(2003).

103. Cirak, S. *et al.* Exon skipping and dystrophin restoration in patients with Duchenne muscular dystrophy after systemic phosphorodiamidate morpholino oligomer treatment: an open-label, phase 2, dose-escalation study. *Lancet (London, England)* **378**, 595–605 (2011).
104. Goemans, N. M. *et al.* Long-Term Efficacy, Safety, and Pharmacokinetics of Drisapersen in Duchenne Muscular Dystrophy: Results from an Open-Label Extension Study. *PLoS One* **11**, e0161955 (2016).
105. Amoasii, L. *et al.* Gene editing restores dystrophin expression in a canine model of Duchenne muscular dystrophy. *Science* eaau1549 (2018). doi:10.1126/science.aau1549
106. Aartsma-Rus, A. *et al.* Guidelines for antisense oligonucleotide design and insight into splice-modulating mechanisms. *Mol. Ther.* **17**, 548–553 (2009).
107. Charbonneau, N. L. *et al.* In vivo studies of mutant fibrillin-1 microfibrils. *J. Biol. Chem.* **285**, 24943–55 (2010).
108. Uchimura, T., Otomo, J., Sato, M. & Sakurai, H. A human iPSC cell myogenic differentiation system permitting high-throughput drug screening. *Stem Cell Res.* **25**, 98–106 (2017).
109. Mathur, A. *et al.* Human iPSC-based Cardiac Microphysiological System For Drug Screening Applications. *Sci. Rep.* **5**, 8883 (2015).
110. Carlson, C. *et al.* Phenotypic screening with human IPS cell-derived cardiomyocytes: HTS-compatible assays for interrogating cardiac hypertrophy. *J. Biomol. Screen.* (2013). doi:10.1177/1087057113500812
111. Goel, S. A. *et al.* High-Throughput Screening Identifies Idarubicin as a Preferential Inhibitor of Smooth Muscle versus Endothelial Cell Proliferation. *PLoS One* **9**, e89349 (2014).
112. McGettrick, A. J., Knott, V., Willis, A. & Handford, P. A. Molecular effects of calcium binding mutations in Marfan syndrome depend on domain context. *Hum. Mol. Genet.* **9**, 1987–1994 (2000).
113. Aartsma-Rus, a. *et al.* Therapeutic modulation of DMD splicing by blocking exonic splicing enhancer sites with antisense oligonucleotides. *Ann. N. Y. Acad.*

- Sci.* **1082**, 74–76 (2006).
114. Aoki, Y. *et al.* Bodywide skipping of exons 45-55 in dystrophic mdx52 mice by systemic antisense delivery. *Proc. Natl. Acad. Sci. U. S. A.* **109**, 13763–8 (2012).
  115. Aartsma-Rus, A. *et al.* Theoretic applicability of antisense-mediated exon skipping for Duchenne muscular dystrophy mutations. *Hum. Mutat.* **30**, 293–299 (2009).
  116. Aartsma-Rus, A. *et al.* Review Development of Exon Skipping Therapies for Duchenne Muscular Dystrophy: A Critical Review and a Perspective on the Outstanding Issues. doi:10.1089/nat.2017.0682
  117. Aartsma-Rus, A. & van Ommen, G.-J. B. Antisense-mediated exon skipping: a versatile tool with therapeutic and research applications. *RNA* **13**, 1609–24 (2007).
  118. van Putten, M. *et al.* Preclinical Studies on Intestinal Administration of Antisense Oligonucleotides as a Model for Oral Delivery for Treatment of Duchenne Muscular Dystrophy. *Mol. Ther. Acids* **3**, e211 (2014).
  119. Long, C. *et al.* Postnatal genome editing partially restores dystrophin expression in a mouse model of muscular dystrophy. *Science* **351**, 400–3 (2016).
  120. Fava, M. *et al.* Role of ADAMTS-5 in Aortic Dilatation and Extracellular Matrix Remodeling. *Arterioscler. Thromb. Vasc. Biol.* **38**, 1537–1548 (2018).
  121. MacDonald, B. T., Tamai, K. & He, X. Wnt/ $\beta$ -catenin signaling: components, mechanisms, and diseases. *Dev. Cell* **17**, 9 (2009).
  122. Yu, J. S. L. & Cui, W. Proliferation, survival and metabolism: the role of PI3K/AKT/ mTOR signalling in pluripotency and cell fate determination. (2016). doi:10.1242/dev.137075
  123. Zhang, Y. *et al.* Patient iPSC-Derived Neurons for Disease Modeling of Frontotemporal Dementia with Mutation in CHMP2B. *Stem Cell Reports* **8**, 648–658 (2017).
  124. Huang, Y. *et al.* Transcriptome Analysis of Induced Pluripotent Stem Cell (iPSC)-derived Pancreatic  $\beta$ -like Cell Differentiation. *Cell Transplant.* **26**, 1380–1391 (2017).
  125. Ovchinnikova, E. *et al.* Stem Cell Reports Article Modeling Human Cardiac Hypertrophy in Stem Cell-Derived Cardiomyocytes. (2018). doi:10.1016/j.stemcr.2018.01.016

126. Krishna, S. M. *et al.* Wnt Signaling Pathway Inhibitor Sclerostin Inhibits Angiotensin II-Induced Aortic Aneurysm and Atherosclerosis. *Arterioscler. Thromb. Vasc. Biol.* **37**, 553–566 (2017).
127. BRADE, T., MANNER, J. & KUHL, M. The role of Wnt signalling in cardiac development and tissue remodelling in the mature heart. *Cardiovasc. Res.* **72**, 198–209 (2006).
128. van Gijn, M., Daemen, M. J. A. P., Smits, J. F. M. & Blankesteyjn, W. M. The wnt-frizzled cascade in cardiovascular disease. *Cardiovasc. Res.* **55**, 16–24 (2002).
129. Al-Majed, A.-R. A., Assiri, E., Khalil, N. Y. & Abdel-Aziz, H. A. Losartan: Comprehensive Profile. *Profiles Drug Subst. Excipients Relat. Methodol.* **40**, 159–194 (2015).
130. Catalioto, R.-M. *et al.* Angiotensin II-induced responses in vascular smooth muscle cells: inhibition by non-peptide receptor antagonists. *Eur. J. Pharmacol.* **280**, 285–292 (1995).
131. Caballero, R., Delpón, E., Valenzuela, C., Longobardo, M. & Tamargo, J. Losartan and its metabolite E3174 modify cardiac delayed rectifier K(+) currents. *Circulation* **101**, 1199–205 (2000).
132. Andersson, E. R. & Lendahl, U. Therapeutic modulation of Notch signalling — are we there yet? *Nat. Publ. Gr.* **13**, (2014).
133. Zou, S. *et al.* Notch Signaling in Descending Thoracic Aortic Aneurysm and Dissection. *PLoS One* **7**, e52833 (2012).
134. Wu, D. & Pan, W. GSK3: a multifaceted kinase in Wnt signaling. *Trends Biochem. Sci.* **35**, 161–8 (2010).
135. Ghosh, A. *et al.* Phosphorylation of AKT and abdominal aortic aneurysm formation. *Am. J. Pathol.* **184**, 148–58 (2014).
136. Yu, J., Liu, R., Huang, J., Wang, Lixin & Wang, W. Inhibition of Phosphatidylinositol 3-kinase suppresses formation and progression of experimental abdominal aortic aneurysms. *Sci. Rep.* **7**, 15208 (2017).
137. Duan, D. Systemic AAV Micro-dystrophin Gene Therapy for Duchenne Muscular Dystrophy. *Mol. Ther.* (2018). doi:10.1016/J.YMTHE.2018.07.011
138. Shimizu-Motohashi, Y., Murakami, T., Kimura, E., Komaki, H. & Watanabe, N.

- Exon skipping for Duchenne muscular dystrophy: a systematic review and meta-analysis. *Orphanet J. Rare Dis.* **13**, 93 (2018).
139. Lim, K. R., Maruyama, R. & Yokota, T. Eteplirsen in the treatment of Duchenne muscular dystrophy. *Drug Des. Devel. Ther.* **Volume11**, 533–545 (2017).
  140. Aartsma-Rus, A. & Krieg, A. M. FDA Approves Eteplirsen for Duchenne Muscular Dystrophy: The Next Chapter in the Eteplirsen Saga. *Nucleic Acid Ther.* **27**, 1–3 (2017).
  141. Goemans, N. M. *et al.* Systemic Administration of PRO051 in Duchenne’s Muscular Dystrophy. *N. Engl. J. Med.* **364**, 1513–1522 (2011).
  142. Crunkhorn, S. New exon-skipping strategy rescues dystrophin. *Nat. Rev. Drug Discov.* **14**, 236–237 (2015).
  143. Lim, K. R., Maruyama, R. & Yokota, T. Eteplirsen in the treatment of Duchenne muscular dystrophy. *Drug Des. Devel. Ther.* **Volume11**, 533–545 (2017).
  144. Neri, M. *et al.* Dystrophin levels as low as 30% are sufficient to avoid muscular dystrophy in the human. doi:10.1016/j.nmd.2007.07.005
  145. Franken, R. *et al.* Diagnosis and genetics of Marfan syndrome. *Expert Opin. Orphan Drugs* **2**, 1049–1062 (2014).
  146. Aartsma-Rus, A. *et al.* Targeted exon skipping as a potential gene correction therapy for Duchenne muscular dystrophy. *Neuromuscul. Disord.* **12**, S71–S77 (2002).
  147. Eckenfelder, A. *et al.* The Cellular Processing Capacity Limits the Amounts of Chimeric U7 snRNA Available for Antisense Delivery. (2012). doi:10.1038/mtna.2012.24
  148. Ousterout, D. G. *et al.* Multiplex CRISPR/Cas9-based genome editing for correction of dystrophin mutations that cause Duchenne muscular dystrophy. *Nat. Commun.* **6**, 6244 (2015).
  149. Long, C. *et al.* Postnatal genome editing partially restores dystrophin expression in a mouse model of muscular dystrophy. *Science* **351**, 400–3 (2016).
  150. Li, H. L. *et al.* Precise Correction of the Dystrophin Gene in Duchenne Muscular Dystrophy Patient Induced Pluripotent Stem Cells by TALEN and CRISPR-Cas9. *Stem Cell Reports* **4**, 143–154 (2015).

## Development of novel therapies for Marfan Syndrome using a human iPSC-derived disease model

151. Amoasii, L. *et al.* Gene editing restores dystrophin expression in a canine model of Duchenne muscular dystrophy. *Science* eaau1549 (2018). doi:10.1126/science.aau1549
152. Gapinske, M. *et al.* CRISPR-SKIP: programmable gene splicing with single base editors. *Genome Biol.* **19**, 107 (2018).
153. Kosicki, M., Tomberg, K. & Bradley, A. Repair of double-strand breaks induced by CRISPR–Cas9 leads to large deletions and complex rearrangements. *Nat. Biotechnol.* **36**, 765 (2018).
154. Boroviak, K., Fu, B., Yang, F., Doe, B. & Bradley, A. Revealing hidden complexities of genomic rearrangements generated with Cas9. *Sci. Rep.* **7**, 12867 (2017).
155. Akcakaya, P. *et al.* In vivo CRISPR editing with no detectable genome-wide off-target mutations. *Nature* (2018). doi:10.1038/s41586-018-0500-9
156. Gregorevic, P. *et al.* Systemic delivery of genes to striated muscles using adeno-associated viral vectors. *Nat. Med.* **10**, 828–834 (2004).
157. Wang, Z. *et al.* Adeno-associated virus serotype 8 efficiently delivers genes to muscle and heart. *Nat. Biotechnol.* **23**, 321–328 (2005).
158. Yue, Y. *et al.* A Single Intravenous Injection of Adeno-associated Virus Serotype-9 Leads to Whole Body Skeletal Muscle Transduction in Dogs. *Mol. Ther.* **16**, 1944–1952 (2008).
159. Wang, B., Li, J. & Xiao, X. *Adeno-associated virus vector carrying human minidystrophin genes effectively ameliorates muscular dystrophy in mdx mouse model.*
160. Harper, S. Q. *et al.* Modular flexibility of dystrophin: Implications for gene therapy of Duchenne muscular dystrophy. *Nat. Med.* **8**, 253–261 (2002).
161. Pfizer. Pfizer Doses First Patient Using Investigational Mini-Dystrophin Gene Therapy for the Treatment of Duchenne Muscular Dystrophy. *Pfizer News & Media* (2018). Available at: <https://press.pfizer.com/press-release/pfizer-doses-first-patient-using-investigational-mini-dystrophin-gene-therapy-treatmen>.
162. Booms, P. *et al.* RGD-containing fibrillin-1 fragments upregulate matrix metalloproteinase expression in cell culture: A potential factor in the pathogenesis

- of the Marfan syndrome. *Hum. Genet.* **116**, 51–61 (2005).
163. Chen, X. *et al.* TGF- $\beta$  Neutralization Enhances AngII-Induced Aortic Rupture and Aneurysm in Both Thoracic and Abdominal Regions. *PLoS One* **11**, e0153811 (2016).
  164. Casamassimi, A., Federico, A., Rienzo, M., Esposito, S. & Ciccodicola, A. Transcriptome Profiling in Human Diseases: New Advances and Perspectives. *Int. J. Mol. Sci.* **18**, (2017).
  165. Wang, X. *et al.* A Role for the-Catenin/T-Cell Factor Signaling Cascade in Vascular Remodeling. (2002). doi:10.1161/hh0302.104466
  166. Mill, C. & George, S. J. Wnt signalling in smooth muscle cells and its role in cardiovascular disorders. *Cardiovasc. Res.* **95**, 233–240 (2012).
  167. Krishna, S. M. *et al.* Wnt Signaling Pathway Inhibitor Sclerostin Inhibits Angiotensin II-Induced Aortic Aneurysm and AtherosclerosisHighlights. *Arterioscler. Thromb. Vasc. Biol.* **37**, 553–566 (2017).
  168. Liu, C., Oikonomopoulos, A., Sayed, N. & Wu, J. C. Modeling human diseases with induced pluripotent stem cells: from 2D to 3D and beyond. (2018). doi:10.1242/dev.156166
  169. Roccabianca, S., Ateshian, G. A. & Humphrey, J. D. Biomechanical roles of medial pooling of glycosaminoglycans in thoracic aortic dissection. *Biomech. Model. Mechanobiol.* **13**, 13–25 (2014).
  170. Humphrey, J. D. Vascular Adaptation and Mechanical Homeostasis at Tissue, Cellular, and Sub-cellular Levels. *Cell Biochem. Biophys.* **50**, 53–78 (2008).
  171. Humphrey, J. D., Dufresne, E. R. & Schwartz, M. A. Mechanotransduction and extracellular matrix homeostasis. *Nat. Rev. Mol. Cell Biol.* **15**, 802–12 (2014).
  172. Humphrey, J. D., Schwartz, M. A., Tellides, G. & Milewicz, D. M. Role of Mechanotransduction in Vascular Biology: Focus on Thoracic Aortic Aneurysms and Dissections. *Circ. Res.* **116**, 1448–1461 (2015).
  173. Lacolley, P., Regnault, V., Segers, P. & Laurent, S. Vascular Smooth Muscle Cells and Arterial Stiffening: Relevance in Development, Aging, and Disease. *Physiol Rev* **97**, 1555–1617 (2017).
  174. Mallat, Z., Ait-Oufella, H. & Tedgui, A. The Pathogenic Transforming Growth

Factor- $\beta$  Overdrive Hypothesis in Aortic Aneurysms and Dissections: A Mirage?  
*Circ. Res.* **120**, 1718–1720 (2017).

175. Doyle, J. J. *et al.* A deleterious gene-by-environment interaction imposed by calcium channel blockers in Marfan syndrome. *Elife* **4**, (2015).
176. Pilop, C. *et al.* Proteomic Analysis in Aortic Media of Patients With Marfan Syndrome Reveals Increased Activity of Calpain 2 in Aortic Aneurysms. (2009). doi:10.1161/CIRCULATIONAHA.108.843516
177. Abdulkareem, N., Skroblin, P., Jahangiri, M. & Mayr, M. Proteomics in aortic aneurysm - What have we learnt so far? *PROTEOMICS - Clin. Appl.* **7**, 504–515 (2013).
178. Khatri, P., Sirota, M. & Butte, A. J. Ten Years of Pathway Analysis: Current Approaches and Outstanding Challenges. *PLoS Comput. Biol.* **8**, e1002375 (2012).
179. Rouhani, F. *et al.* Genetic Background Drives Transcriptional Variation in Human Induced Pluripotent Stem Cells. *PLoS Genet.* **10**, e1004432 (2014).
180. Sgodda, M. & Cantz, T. Small but significant: inter- and inpatient variations in iPSC cell-based disease modeling. *Mol. Ther.* **21**, 5–7 (2013).
181. Thatava, T. *et al.* Inpatient Variations in Type 1 Diabetes-specific iPSC Cell Differentiation Into Insulin-producing Cells. *Mol. Ther.* **21**, 228–239 (2013).
182. Karnik, S. K. *et al.* A critical role for elastin signaling in vascular morphogenesis and disease. *Development* **130**, 411–23 (2003).
183. Tykocki, N. R., Boerman, E. M. & Jackson, W. F. in *Comprehensive Physiology* **7**, 485–581 (John Wiley & Sons, Inc., 2017).
184. Sobey, C. G. Potassium channel function in vascular disease. *Arterioscler. Thromb. Vasc. Biol.* **21**, 28–38 (2001).
185. Dunlop, J., Bowlby, M., Peri, R., Vasilyev, D. & Arias, R. High-throughput electrophysiology: an emerging paradigm for ion-channel screening and physiology. *Nat. Rev. Drug Discov.* **7**, 358–368 (2008).
186. Beacham, D. W., Blackmer, T., O'Grady, M. & Hanson, G. T. Cell-Based Potassium Ion Channel Screening Using the FluxORTM Assay. *J. Biomol. Screen.* **15**, 441–446 (2010).
187. Chien, S. Mechanotransduction and endothelial cell homeostasis: the wisdom of

- the cell. *Am. J. Physiol. Circ. Physiol.* **292**, H1209–H1224 (2007).
188. Ranade, S. S. *et al.* Piezo1, a mechanically activated ion channel, is required for vascular development in mice. *Proc. Natl. Acad. Sci. U. S. A.* **111**, 10347–52 (2014).
189. Li, J. *et al.* Piezo1 integration of vascular architecture with physiological force. *Nature* **515**, 279–282 (2014).
190. Mallat, Z., Tedgui, A. & Henrion, D. Role of Microvascular Tone and Extracellular Matrix Contraction in the Regulation of Interstitial Fluid. *Arterioscler. Thromb. Vasc. Biol.* **36**, 1742–1747 (2016).

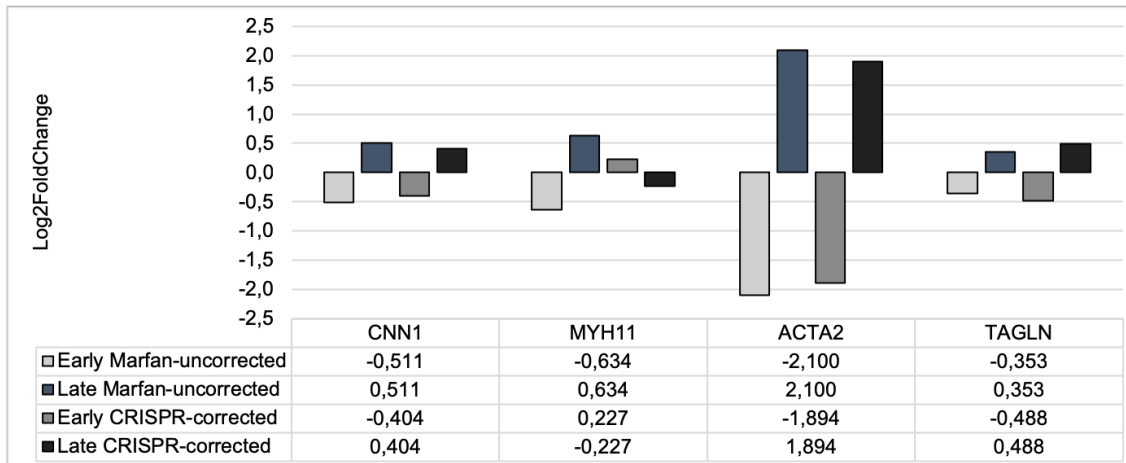
# 8 APPENDICES

**APPENDIX 8.1 TABLE OF SIGNIFICANTLY DIFFERENTIALLY EXPRESSED GENES COMPARING MARFAN-UNCORRECTED AND CRISPR-CORRECTED NC-SMCs AT BOTH EARLY AND LATE STAGES OF DIFFERENTIATION RESPECTIVELY**

Early MF vs CTL	LogFC2	padj
PLA2G3	-7,548604988	0,002840767
ADAMTSL2	-7,144328526	0,004140246
KCNQ2	-5,449397558	0,039319564
MYCN	-5,145515043	0,03365281
KCNH2	-4,734424236	0,00045092
NKD1	-4,694389622	1,04E-11
FZD10	-4,591532818	0,000586902
COL2A1	-4,544530934	0,001641424
KANK4	-4,494445961	0,002156502
MMP8	-4,26061698	0,00848782
ITGA8	-3,865717462	2,65E-07
CD200	-3,848953423	4,50E-06
CDHR1	-3,801947909	3,74E-19
NKAIN4	-3,732251473	2,40E-06
CACNA1G	-3,41121977	0,019314834
CD24	-3,396959034	0,017380956
COL8A2	-3,258086774	1,27E-05
PCDH19	-3,243382787	1,44E-07
COL9A3	-3,181113104	6,71E-05
ADAMTS16	-3,061289703	5,75E-10
WNT11	-3,022517124	0,001121708
ADAMTS4	-2,982596467	4,73E-12
ACTA1	-2,911654205	0,012404468
WISP1	-2,798261821	0,000291992
PIK3IP1	-2,758604535	2,64E-15
PIK3AP1	-2,682359796	0,032372924
FOXO1	-2,589577386	7,68E-09
GNA14	-2,50783799	0,005830677
CD40	2,55471452	0,029420049
CD44	2,663340685	2,28E-09
CD55	2,859708946	0,000242912
KLF4	2,923230615	9,25E-14
CAMK2N1	3,374377388	9,59E-07
CDH4	3,720041788	2,40E-10
MMP1	4,313937105	0,007271787
KCNQ5	6,273675741	3,35E-06
CD70	7,656479775	0,009936217
CDCP1	7,656479775	0,009936217

Late MF vs CTL	Log2FC	p-adj
MMP8	-6,402050769	9,32E-05
ATP8B4	-6,1963284	0,033300946
KCNH2	-5,314450709	1,69E-05
ATP6V0A4	-4,997911021	0,000609685
MYLPF	-4,664711993	0,024908383
MYL1	-4,332523745	0,028461651
MMP9	-4,098837219	6,96E-06
COL2A1	-3,932314832	0,010221391
MYL7	-3,547723167	0,000308956
CDHR1	-3,454520214	2,89E-18
MYL4	-3,286005676	1,64E-05
KCNJ2	-3,190302027	0,000588057
KCNJ15	-3,160465989	0,037447311
FZD10	-3,149956578	0,012755804
NKD1	-3,096405069	5,72E-07
GNA14	-3,029824016	0,000425209
PIK3AP1	-3,006816516	0,015585338
MYOM1	-3,004987028	0,011088276
ATP2B3	-2,973625611	0,049026401
COL13A1	-2,968546931	3,64E-06
KCNJ6	-2,960808157	0,001112399
PIK3IP1	-2,872848317	1,41E-16
MYOM3	-2,759941231	0,022291458
PCDHB12	-2,72787624	0,014896411
GPR183	-2,693284933	0,001430648
PLCB4	-2,662679303	7,24E-08
WISP1	-2,572387212	0,001345315
KCNT2	2,912231361	2,54E-13
ITGB4	3,233369762	0,012262333
GPRC5A	3,260007012	4,52E-06
WISP3	4,072360812	0,000173056
VCAM1	5,012323544	0,000303744
COL21A1	5,325910953	0,003902124
KCNQ5	7,92946659	0,000138489

## APPENDIX 8.2 DIFFERENTIAL EXPRESSION OF SMC GENES COMPARING EARLY AND LATE DIFFERENTIATION STAGES FOR BOTH MARFAN-UNCORRECTED AND CRISPR-CORRECTED NC-SMCs RESPECTIVELY



## APPENDIX 8.3 PERCENTAGE OF GENE TARGETS IN SELECTION OF PATHWAYS FOR 100-COMPOUND PILOT SCREEN

<b>Pathway from Panther Database</b>	<b>Gene targets (%)</b>
Activin beta signalling pathway (P06210)	1%
Alpha adrenergic receptor signalling pathway (P00002)	6%
Angiogenesis (P00005)	18%
Angiotensin II-stimulated signalling through G proteins and beta-arrestin (P05911)	5%
Apoptosis signalling pathway (P00006)	15%
Cadherin signalling pathway (P00012)	10%
TGF-beta signalling pathway (P00052)	13%
Integrin signalling pathway (P00034)	9%
p38 MAPK pathway (P05918)	6%
Wnt signalling pathway (P00057)	7%
Hedgehog signalling pathway (P00025)	2%
Oxidative stress response (P00046)	1%
Nicotine degradation (P05914)	1%
Notch signalling pathway (P00045)	5%

